Inference of River Hydrodynamics and Ice Processes from Close-Range Remote Sensing

Saber Ansari

Thesis submitted in partial fulfillment of the requirements for the degree of

Doctorate in Philosophy Civil Engineering

Under the auspices of the Ottawa-Carleton Institute for Civil Engineering

Academic advisors: Prof. Colin Rennie, Prof. Shawn Clark, and Prof. Ousmane Seidou

uOttawa

Abstract

The use of new technologies for monitoring and data collection in earth sciences and river engineering has transformed our understanding of river processes, leading to improved management and preservation of these vital resources. Remote sensing, particularly close-range remote sensing, has emerged as a useful tool for acquiring essential data for river studies. It offers the advantage of large-scale, long-term data collection options, enabling researchers to explore hard to access or hazardous areas and providing a wealth of information to enhance decision-making processes. The importance of remote sensing in earth sciences and river engineering lies in its ability to monitor and collect data on various river hydrodynamics and river processes, such as river ice formation, which significantly influence river characteristics. In cold regions, river ice processes affect hydraulics, sediment transport, water quality, and morphology. The application of close-range remote sensing both using aerial and fixed shore-based imagery in river ice monitoring and data collection has facilitated improved insights into these processes, contributing to better river management and the mitigation of potential hazards.

This thesis focuses on the development and application of close-range remote sensing techniques to enhance our understanding of river hydrodynamics and river ice processes. This thesis led to novel applications of close-range remote sensing along two axes: river ice detection and quantification and water survey/ discharge measurement.

Two algorithms for river ice segmentation and river flow estimation based on artificial intelligent techniques were developed and evaluated in the first axe. The first algorithm is IceMaskNet, a novel river ice detection and segmentation algorithm based on an improved version of the Mask R-CNN. The algorithm has been successfully applied to both aerial and fixed shore-based imagery for river ice detection and classification, achieving average detection and segmentation accuracies of 95% and 91% on aerial imagery. Additionally, the algorithm has been adapted for use on oblique shore-based, low-quality image data, with a detection accuracy of 90% and a segmentation accuracy of 86%.

IceMaskNet can be used on aerial imagery to generate quantifiable data and provide insights for an extensive portion of a freezing river. It can also be used on shore-based imagery to gather long-term, near-range observation in comprehending river ice processes. The effectiveness of the developed algorithm was demonstrated in a case study on the Dauphin River where ice categories and ice quantities where extracted over four winters. By employing cost-effective trail cameras along the Dauphin River, a vast collection of oblique, shore-based, and low-quality image data were used to extract quantified river ice data. The comprehensive data and insights derived from this extensive database highlight the potential of close-range monitoring to revolutionize our understanding of river ice processes and their impacts on river systems. IceMaskNet was also

adapted, and trained over a set of sea ice imagery to produce an algorithm to identify and segment different sea ice types interacting with bridge piers.

The second part of this study was devoted to the development of new tools for water survey and discharge measurement, such as surface velocimetry. In recent years, number of image-based surface velocimetry techniques have emerged, utilizing aerial or shore-based imagery for estimating surface velocity and river discharge. While these methods show great potential in supplementing or even replacing traditional river discharge measurements, they come with high operational costs and require significant user expertise to produce high-quality and satisfactory results. In response to this need, we developed RivQNet, a novel river velocimetry scheme that processes close-range non-contact water surface images using artificial intelligence techniques. The proposed method yields accurate and dense spatial distributions of surface velocities, outperforming conventional optical flow methodologies. Moreover this method requires less amount of user input to estimate surface velocity. RivQNet was further validated with common standard measurement methods and compared with conventional optical flow, Large scale Particle Imagery (LSPIV) and Space Time Image Velocimetry (STIV) methodologies, w

ith a significantly higher estimation accuracy than both LSPIV and STIV, with approximately 25% and 15% higher accuracy respectively for LSPIV and STIV.

In conclusion, this thesis demonstrates the value of close-range remote sensing in advancing our understanding of river ice processes and hydrodynamics. The development of novel algorithms, such as IceMaskNet and RivQNet, represents a significant contribution to the field of river engineering and water resources management. The comprehensive data and insights derived from the extensive database of oblique shore-based imagery emphasize the significance of long -term close-range monitoring in gaining a better understanding of river ice processes and hydrodynamics. The developed algorithms can be utilized across a range of applications and settings, benefiting water resources researchers, water survey authorities, and industries engaged in environmental and river engineering projects.

Acknowledgement

Throughout my PhD, I've been privileged to be encircled by an exceptional cadre of professionals, institutions, and loved ones, all of whom were instrumental in molding both my academic pursuits and personal resilience.

Leading my academic direction were my esteemed supervisors, Prof. Colin Rennie, Prof. Shawn Clark and Prof. Ousmane Seidou. Their expertise, unwavering support, and nurturing mentorship have been the touchstone of my academic journey. Prof. Rennie, I was truly grateful to have had you as an exceptional supervisor and mentor. Working with you deeply shaped my scientific understanding and personal growth and I will always be grateful for that.

I extend profound gratitude to my examiners: Prof. Mark Loewen, Prof. Hossein Bonakdari, Dr. Elizabeth Jamieson, and Prof. Majid Mohammadian. Their meticulous feedback and astute critiques have enriched my research, pushing me to strive for excellence.

My research was greatly enhanced by collaborations and support from esteemed institutions and their representatives. The contributions from the University of Manitoba, Water Survey Canada-Environment and Climate Change Canada, and National Research Council Canada were paramount. A special mention goes to Simon Fraser University, particularly Prof. Jeremy Venditti and Dr. Eva Kwoll (Now Prof. at university of Victoria). Furthermore, the financial support from NSERC was invaluable in elevating my research endeavors.

In the heart of the lab and field work, the tireless efforts of Mark Lapointe – University of Ottawa, and Alexander Wall – University of Manitoba were consistently inspiring. Their technical expertise, coupled with their persistent commitment, ensured smooth progress in the research. Special thanks to Alain Goulet – ECCC for his help throughout extensive field work campaigns. I learnt a lot from you Alain.

Throughout this research, I received invaluable assistance from some outstanding volunteer students from uOttawa: Gianmarco Maggiore, Dana Pothier and Yifei Zhang. Additionally, coop students Nicolas Chan, Albert Zombre, Alison Nandram, and Kim Alain Kazenga, along with French exchange students Yann Nebout, Tristan Rouvière, Tom AgeneauView, Rahmouna Benahmida, and Honorine Jaquerod, played significant roles. I extend my deepest gratitude to each of you; your contributions greatly enhanced this work.

At uOttawa, alongside research, I also forged meaningful friendships. A heartfelt thank you to my friends and colleagues: Iman, Sean, Kate, Sanaz, Mehran, Soheil, Parna, Hamidreza, Rouzbeh, Sepideh, Katie, Jacob, Amanj,. Also thanks to my friends beyond uOttawa for their support and encouragement, Reza, Salar, Ali and Nasim. Ali, our conversations about AI has always been inspiring.

On a personal note, thanks to my parents, Alireza and Gohar. While my departed father, Alireza, instilled in me a lasting foundation of strength and resilience, my mother, Gohar, has been an unwavering source of love, and continued to be a pillar of strength, although from a long distance.

Maman sorry for being away for so long. Thanks to my sister, Sanam, has been a constant source of motivation and joy. Additionally, I'm deeply thankful to my aunt Nadereh, and my cousins Nazli and Reza, for their presence and support. I am also profoundly grateful to my in-laws: Tahereh, Farzad, Farnaz, Navid, Golnaz, Ali, Niki and Nila, thanks for your warmth and kindness.

The tapestry of my life wouldn't be complete without the unwavering love and support of my beloved wife, Behnaz. Her faith in me has been my anchor, her love my guiding light. Behnaz, we've weathered many challenges together. Every time I found myself in need, whether grappling with a technical issue or seeking emotional solace, you were my steadfast anchor, always by my side. Words cannot express the depth of my love for you!

This journey has been a mosaic of experiences. I am eternally grateful for the richness, color, depth, and vibrancy each tile, each individual brought to this mosaic.

Table of Contents

List of Figures

List of Tables

Symbols and abbreviations

C	Coherency value
g	Gray level
$I(x,y)$	Image intensity
$\omega^{(b)}$	Bias potential
$\omega^{(u)}$	Unary potential
$\omega^{(p)}$	Pairwise potential
p_{ij}	Number of pixels that belong to class i
p_{ii}	Number of pixels in category i correctly classified
ω	Training parameter
k	total number of classes in the model
m_{ij}	Viewing angle coordinates
$\underline{\tau}$	Shift amount vector
$f(\underline{x})$	Three-dimensional image intensity distribution
x_0 and y_0	Projection center
Ψ	joint feature function
P	Prediction accuracy rate
S_x - S_y	STI axis
X	Superpixel matrix
y	Prediction label field
F	Focal length
℃	Degrees Celsius
AI	Artificial Intelligence
ADCP	Acoustic Doppler Current Profiler
ADV	Acoustic Doppler Velocimeter
CIS	Canadian Ice Services
CNN	Convolutional Neural Networks
COCO	Common Objects in Context
DEM	Digital Elevation Model
DPM	Deformable Part-based Model
DDOF	Degree Days of Freezing
DNN	Deep Neural Networks
FCN	Fully convolutional network
FN	False negative
FP	False positive
FRWSC	Fairford River Water Control Structure
GHz	Gigahertz
GCP	Ground Control Points
GPU	Graphical Processing Unit
ICP	Image Control Points
IoU	Intersection over Union
JI	Jaccard Index
LiDAR	Light Detection and Ranging
LSPIV	Large Scale Particle Image Velocimetry

mAP	Mean average precision
MAPE	Mean Absolute Percentage Error
Mx My	Interrogation area size
PIV	Particle Image Velocimetry
PTV	Particle tracking velocimetry
R	Recall rate
R-CNN	Regions with Convolutional Neural Networks
RGB	Red Green Blue
ReLU	Rectifier Linear Unit
ResNet	Residual Learning Network
RMSE	Root Mean Square Error
ROI	Region of Interest
RoIPool	Region of Interest Pool
RPAS	Remotely Piloted Aircraft Systems
RPN	Region Proposal Network
TP	True positive
TDD	Thaw Degree Days
VGG	Visual Geometry Group
SVM	Support Vector Machine
STI	Space Time Image
STIV	Space Time Image Velocimetry
SVM	Support Vector Machine

1. Introduction

1.1 Background

Rivers, as naturally flowing water bodies, empty into lakes, wetlands, reservoirs, and oceans. They are crucial components of surface water systems, acting as intricate hydro-bio-geomorphic networks with interactions shaped by watershed properties. These waterways are indispensable to the environment, driving ecological processes and transporting nutrients along their course. They serve as life sources for numerous global ecosystems and have been critical for human existence throughout history. Many thriving cities worldwide were established near rivers, which facilitated trade, exploration, cultural exchange, and leisure activities. Additionally, rivers supply water for consumption and irrigation. The emergence of water engineering was driven by the need for human communities to supply irrigation water for agriculture. Presently, hydraulic engineering encompasses numerous applications, such as providing water resources for human activities (e.g., drinking, agriculture, and industry), flood control, and hydroelectric power generation. Therefore, examining watershed climatology, geomorphology, hydrology, river hydrodynamics, and sediment transport is crucial for river engineering and effective water resources management.

Field investigations, data collection, and monitoring are crucial elements in understanding and managing water resources, particularly concerning river systems. They contribute to an improved understanding of spatial and temporal river dynamics, enhanced decision-making, accurate predictions and modeling of future river behavior, and effective evaluation of management strategies. To collect accurate river discharge information, various approaches can be employed, including direct measurement techniques and remote sensing. Direct measurement techniques, such as current metering and flow gauging, provide highly accurate data but can be labor intensive. Remote sensing, using satellite, aerial and terrestrial imagery, offers large-scale and/or long-term data collection options for monitoring inaccessible, hard to access or hazardous areas.

The advancement of various technologies has significantly improved field investigations and experimentation (Aberle, 2017). For instance, acoustic Doppler technology has allowed for more comprehensive studies of river flow and hydrodynamics (Venditti *et al.*, 2014), while the development of water quality sensors has contributed to a deeper understanding of water quality and mixing processes in rivers (Pilechi *et al.*, 2015).

Remote sensing offers significant value to the earth science community as a primary data source, obtained from a distinct perspective. Although the raw electromagnetic radiation captured

by sensors requires meticulous calibration to convert these observations into usable scientific information, remote sensing platforms deliver high-quality primary data across various spatial, temporal, and spectral scales (Gleason and Durand 2020). Hydrology and hydrometry have traditionally embraced the use of remote sensing (Calmant, *et al.*, 2008; Lettenmaier, *et al.*, 2015; Döll, et al., 2016). Remote sensing applications in earth sciences have enabled large-scale monitoring of rivers and their watersheds (e.g., Bastiaanssen, 1998; Rango, 1994; Govender, *et al.* 2007). The introduction of optical cameras has further enhanced our knowledge of river processes.

The introduction of optical cameras and their use in earth sciences has furthered our knowledge of river processes. Aerial photogrammetry, initially employed for geodesy and mapping, marked the beginning of close-range photogrammetry applications. It subsequently served as a qualitative assessment tool for various river flow processes (e.g., Hirpa et al., 2013; Smith, 1997b; Fonstad and Marcus, 2005). The advancement of image processing and computer vision technology, in conjunction with artificial intelligence techniques and affordable imaging instruments, has accelerated the adoption of the use of aerial and terrestrial imaging known as close-range sensing in earth sciences. Furthermore, it is possible to obtain quantified data through the application of image processing and computer vision techniques. However, employing close-range photogrammetry can present challenges, such as managing large volume of collected imagery data, requiring expertise in image processing and computer vision, and potentially needing high-specification computers for photogrammetry data processing.

These technological innovations present valuable opportunities for leveraging shore-based imagery in flood protection monitoring and enhancing our understanding of river processes. The implementation of close-range photogrammetry is a relatively straightforward and cost-effective method, which makes it an attractive option for many researchers and practitioners. Furthermore, close-range sensing enables long-term and continuous data collection, providing a wealth of information for further analysis and decision-making.

This research aims to develop simpler, faster, and more accurate data extraction methods to investigate river ice processes and river hydrodynamics across multiple field experiments. The resulting algorithms could potentially benefit a wide range of users, including water resources researchers, water survey authorities, and industries engaged in environmental and river engineering projects.

1.2 Objectives

The primary aim of this study is to create innovative methodologies for measuring and deepening our understanding of dynamic river processes by leveraging cost-effective close-range photogrammetry techniques, computer vision and artificial intelligence technologies. By doing so, the research seeks to advance the field of river hydrodynamics and ice processes monitoring while minimizing costs and maximizing efficiency. The specific objectives of this research endeavor encompass the following:

1. Integrate artificial intelligence (AI) and machine learning algorithms into close-range photogrammetry processes to further improve data analysis and interpretation.

2. Developing an artificial intelligence (AI) based river ice detection, and characterization tool using aerial and fixed-camera photogrammetry.

3. Perform a case study to confirm the effectiveness of the developed river ice characterization algorithm and obtain long-term quantitative data from shore-based oblique images.

4. Creating a rapid, precise, and dependable framework for discharge measurement utilizing close-range photogrammetry and artificial intelligence techniques with minimal user data input requirement.

5. Evaluating the practicality and effectiveness of the developed techniques through real-world field experiments and case studies, ensuring their applicability across various river environments and scenarios.

1.3 Contributions and Novelty of the Study

This research aims used innovative AI techniques using close-range photogrammetry to develop tools that enhance the understanding of river hydrodynamics. Simultaneously, the study will further explore river ice processes and river hydraulics through various field studies and data collection.

We developed a novel AI based algorithm (named IceMaskNet) for river ice detection and characterization into different ice classes using aerial imagery, marking a first in the field. This innovative approach is complemented by the additional training and use of the algorithm to classify

and characterize river ice through shore-based imagery. Furthermore, the groundbreaking investigation of river ice processes using quantified data extracted from long-term shore-based imagery adds a new dimension to the study of these phenomena. Furthermore, a unique model is developed to identify and categorize various sea ice types utilizing images captured from cameras mounted on a bridge. Results of this research can be used to explore the diverse types of sea ice loads exerted on bridge piers.

The second portion of this research centered on creating the creation of an AI-driven algorithm to measure surface velocity using aerial or oblique shore-based imagery. The devised algorithm, named RivQNet, is founded on an innovative deep learning-based optical flow method. RivQNet requires minimal user input data to execute surface velocity and discharge calculations compared to traditional image-based surface velocity algorithms. Furthermore, this algorithm delivers significantly higher accuracy compared to standard Large Scale Particle Image Velocimetry (LSPIV) and Space Time Image Velocimertry (STIV) methods. RivQNet can also provide denser surface velocity estimates at reduced computational expense. Due to its lower computational costs and minimal user input requirements, this algorithm emerges as a promising candidate for a fully automated surface and discharge measurement method.

Lastly, this study provides a comprehensive dataset for close-range photogrammetry of open channel flow and river ice monitoring, enriching the available resources for researchers and practitioners in the field. These groundbreaking contributions expands the knowledge and understanding of river processes, paving the way for more effective management strategies and innovative solutions for water resources challenges.

1.4 Outline of the thesis

In order to tackle the objectives outlined in Section 1.2, this thesis presents a series of investigations that explore various developed algorithms and their respective uses. To facilitate this, the thesis has been organized into the subsequent chapters:

- Chapter 2.0 presents a comprehensive overview of the cutting-edge developments in three primary subsections. The first subsection delves into the utilization of close-range monitoring techniques for effective river ice monitoring and data collection. The second subsection offers a thorough background and insight into deep learning, emphasizing its applications in object detection and image segmentation. Lastly, the third subsection explores the principles and implementation of surface velocimetry through the use of close-range imagery using various existing algorithms.

- Chapter 3.0 presents the methods for monitoring and gathering data on river and sea ice using close-range imagery. This chapter is divided into three sections: firstly, the implementation of deep learning to create an AI-driven algorithm for detecting and categorizing various river ice types through aerial images. Secondly, it discusses long-term shore-based monitoring using an AI-trained algorithm and the data acquired. Lastly, it explains an algorithm for identifying different kinds of sea ice. The first section has been published as a journal paper, the second section has been drafted for submission as a journal paper, and the third section has been published as a conference paper.
- Chapter 4.0 focuses on the utilization of AI and near-field imagery in surface velocimetry. The first section introduces RivQNet, an AI-driven algorithm designed for surface velocimetry and discharge measurements. In the second section, RivQNet is compared with other established surface velocimetry algorithms, such as LSPIV and STIV. Additionally, the last section discusses the application of optical flow methods in surface velocimetry within a steep bedrock canyon. The first section has been published as a journal paper, and the second and third sections have been published as conference papers.
- Chapter 5.0 Summarizes the thesis by outlining the developed algorithms for both surface velocimetry and river ice processes. Future works are also proposed to tackle challenges faced during algorithm development and to improve the created algorithms further.

2. Literature Review

2.1 River ice and close-range non-intrusive sensing

The cyclical occurrence of ice in rivers and lakes significantly impacts numerous aspects of life for those residing in colder regions. Ice engineering emerged as a critical field of study in the 19th century, with its appearance in literature dating back to the early 20th century (Ashton, 1986; Zare, 2017). Since then, river ice research has made considerable advancements, exploring various dimensions of river ice and its influence on diverse river features. Key research areas in ice engineering include ice mechanics (e.g. Assur, 1980; Dempsey, 2000; Siyal et al., 2017), river ice hydraulics (e.g. Smith et al., 1997; Ettema 2002; Guo, 2002; Ghareh Aghaji Zare et al., 2016; Nyantekyi-Kwakye et al., 2021; Lees et al., 2023), computational modeling of river ice (Beltaos, 1993; Shen, and Liu, 2000), river ice jams (e.g. Beltaos, 1995; Prowse and Beltaos, 2002; Nafziger et al., 2016 and 2019), and the impact of river ice on water quality (e.g. Ranjie and Huimin, 1987; Chambers, et al. 1993 and Biron and Buffin-Bélanger and Martel, 2018). Although a vast body of research has been conducted to better comprehend the various aspects of river ice, numerous questions remain unresolved due to the challenging and potentially hazardous nature of river ice investigations.

Close-range photogrammetry, which leverages aerial or oblique terrestrial imagery, has emerged as a valuable tool for data collection in earth sciences (e.g., Barker *et al*., 1997; Kaufmann, 2012; Westoby *et al.*, 2012). Technological advancements and the development of artificial intelligence-based computer vision algorithms have expanded the use of these techniques in earth science and engineering for precise data collection. River ice engineering has also adopted close-range photogrammetry, beginning with a study by Bourgault (2008) on the Saint Lawrence River. This approach can be used for marine navigation, monitoring, and predicting or preventing ice jam-induced floods. Coupling close-range photogrammetry with in-situ instruments can further enhance the analysis of river ice processes.

In a founding study by Ansari et al. (2017), close-range photogrammetry was applied to extract quantifiable data from shore-based imagery of the Lower Nelson River in Manitoba, Canada. The researchers developed an automated pipeline using image processing techniques. Subsequent research by Kalke and Loewen (2018) employed a machine-learning algorithm based on support vector machines to detect and classify two types of river ice. This work signified an essential effort in using machine learning for river ice detection and classification.

Another study (Ansari et al., 2019) utilized machine learning algorithms for river ice segmentation by applying a fast superpixel segmentation algorithm. Simoes and Clark (2019) conducted research to quantify border ice growth on the Assiniboine River using shore-based imagery. Singh et al. (2019) developed a deep learning algorithm to detect river ice from a downward-looking camera mounted on a bridge. Pei et al., (2023) employed the algorithm created by Singh to train a model for detecting river ice from the shore. This method executes the ice detection process on orthorectified images. In the third chapter of this study, the enhanced use of deep learning algorithms for river ice detection is emphasized, presenting IceMaskNet - a fast and relatively precise river ice detection and characterization algorithm (Ansari et al., 2023) applied to aerial imagery for river ice detection. Furthermore, this algorithm was utilized to train two models to identify and categorize various river ice classes using shore-based oblique images and for sea ice segmentation.

2.1.1 River ice processes

A complete river ice cover process encompasses freeze-up, stabilization, and break up. River ice is a dynamic and intricate phenomenon, shaped by the interplay of various meteorological, hydrological, mechanical, and thermal factors. As a result, it can differ for rivers with distinct characteristics (Turcotte and Morse, 2011). River ice processes typically commence with the formation of frazil ice, which consists of small ice particles that can develop in turbulent supercooled water. Frazil ice particles can attach to objects in the water, such as sediments or other ice particles, creating frazil flocs and clusters. As more frazil particles adhere to one another, and depending on the river's turbulence intensity and the objects at the core of the ice particles, they can gain buoyancy in the water column and rise to the surface, forming frazil pans.

Depending on the river's mixing power, floating ice particles can form frazil ice pans or slush ice (Zare, 2017). Frazil ice pans typically exhibit a round shape with elevated edges resulting from collisions on the water surface. Frazil slush possesses a mushy and unconsolidated texture. Frazil flocs can also adhere to the river bed or submerged objects, such as vegetation, to create anchor ice. Border ice, another type of ice cover attached to riverbanks, forms thermally or through frazil accretion.

Flow velocity is often regarded as a primary factor in river ice formation, as it significantly affects frazil ice production in high flow and turbulent conditions. Conversely, in low flow conditions with reduced turbulence intensity, thermal growth of river ice can occur. Thin, smooth ice cover that forms around river margins and banks is called border ice. River ice cover formation

continues as ice pans and other ice types accumulate in calmer river sections or on existing border ice, narrowing the river cross-section (Figure 2-1 c&d). The relatively consolidated ice cover then propagates upstream through further ice floe accumulation at its leading edge. Various factors influence ice cover propagation and thickness, with the balance of induced forces such as ice cover weight and water and wind drag being the most crucial. Figure 2-2 offers a simplified illustration of river ice processes. Ice cover thickening can also be mechanical, with frazil ice pans accumulating beneath the ice cover surface.

The final stage of the ice cover process is ice decay and breakup, typically occurring in late winter and early spring. Ice breakup varies significantly among rivers and, like the formation stage, is a complex phenomenon influenced by numerous hydrothermal and hydromechanical processes (Zare, 2017). River ice breakup comprises pre-breakup, drive, and wash (Beltaos, 1995). The pre-breakup phase begins with melting snow on ice cover and land before temperature rise, leading to early spring freshets. These processes affect breakup through thermal exchange among water, ice, and air, as well as by increasing flow discharge, velocity, and water levels (Beltaos, 1993). Breakup mainly includes surface melt and decay, occurring through convection, conduction, and radiation. Once surface snow cover melts, radiation penetrates deeper into the ice sheet, causing internal melt and ice strength loss. Melt also occurs at the ice sheet's base due to heat conduction between ice and water, with hydro-technical factors potentially affecting heat transfer. Even slightly higher water temperatures and high-water velocity can promote heat transfer, leading to further melt and ice cover weakening. Heat transfer rates can vary for ice covers with different roughness conditions; a rougher ice cover may have a higher heat transfer rate than a smooth one (Ashton, 1986; Beltaos, 1993).

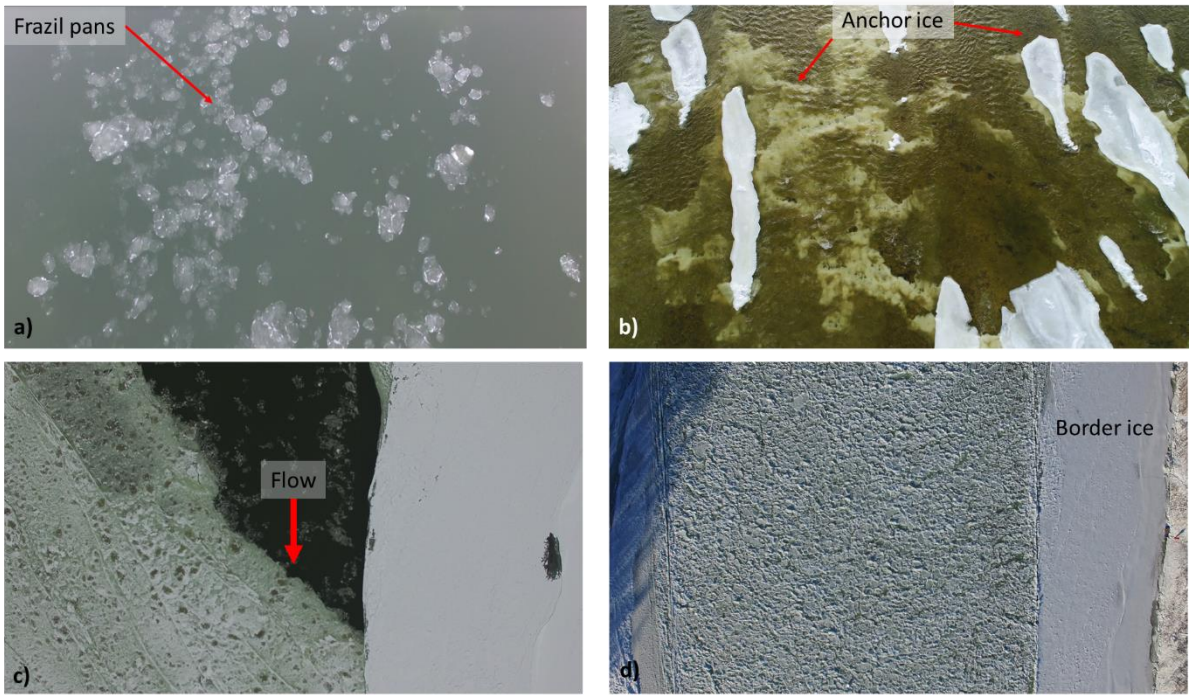

Figure 2-1 River ice types at Dauphin River a) frazil pans b) anchor ice, c) ice pans accumulated in a constriction d) complete ice cover concentration

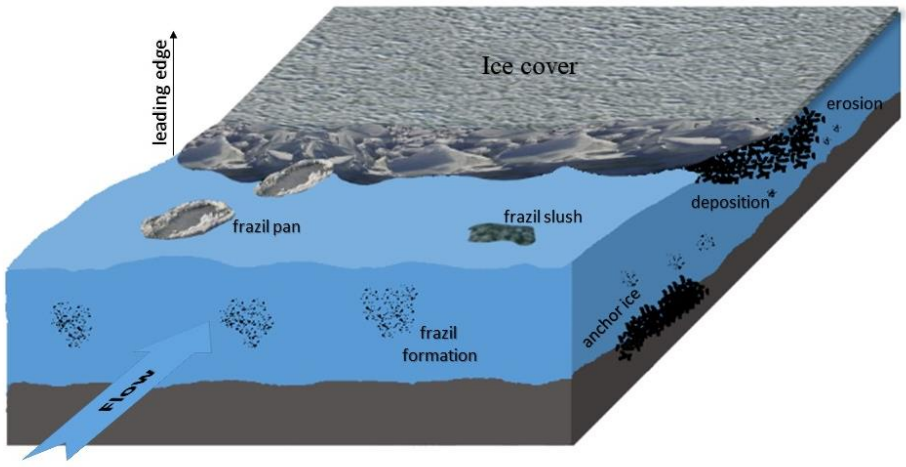

Figure 2-2 River ice processes

The breakup of river ice can occur abruptly or progressively, influenced by multiple factors discussed earlier. As a result, the spatial and temporal weakening and disintegration of ice cover during the breakup stage can vary across different river sections, depending on aspects like river morphology, groundwater input, and the distribution of precipitation and ice conditions (Beltaos, 1995; Beltaos and Burrell, 2003). The deteriorated and released ice cover then begins to move downstream in broken pieces. These freed ice can obstruct specific river sections, leading to the formation of stationary ice accumulations called ice jams. Elevated water levels caused by ice jams can trigger severe flooding events (Beltaos, 1995; Beltaos, 2013). Researchers have explored numerous meteorological, hydraulic, and geomorphological processes involved in ice jam formation and the resulting floods (Beltaos, 1995; Calkins, 1983; Turcotte et al. 2019; Daly and Vuyovich, 2007).

2.2 Deep learning in object detection and image segmentation

Artificial intelligence and computer vision techniques have been used in this research work as the basis for the development of river ice characterization and surface velocimetry algorithms. Image segmentation and object detection are two closely related areas of research in computer vision that sometimes involve the same or similar kinds of tasks. In object classification, object recognition is only performed on specific and previously labeled objects in the image. An example of object labelling is the designation of bounding boxes around specific objects. An image segmentation algorithm has pixel-wise accuracy and can segment the whole image even if the segmented objects are not known or specifically of interest. In other words, in image segmentation, the algorithm groups the pixels that are in the same category together. An overview and recent advances of both methodologies are briefly presented in the next subsections.

2.2.1 Deep learning models

The application of neural networks started to form in the 1940s (Pitts and McCulloch, 1947 and Zhao *et al.*, 2019). Deep models are neural networks with deep structures that mimic the human brain system. The availability of large databases of annotated data along with the development of high-performance computing devices and the concurrent advances in the design of the network structures and training strategies led to vast improvements in the application and the development of deep learning algorithms.

Deep learning achieved great potential with the introduction of Convolutional Neural Networks (CNNs) in the late 1980s (Lecun *et al.*, 1998). Application of CNNs facilitated the use of machine learning on image processing, specifically in object detection and image segmentation tasks. Figure 2-3 illustrates a typical CNN architecture known as VGG 16, which is a CNN model proposed by (Simonyan and Zisserman, 2014). This model achieved 92.7% accuracy and was one of the winners of the ImageNet, which is an image database with over 14 million images in 1000 classes (Deng, et al., 2009).

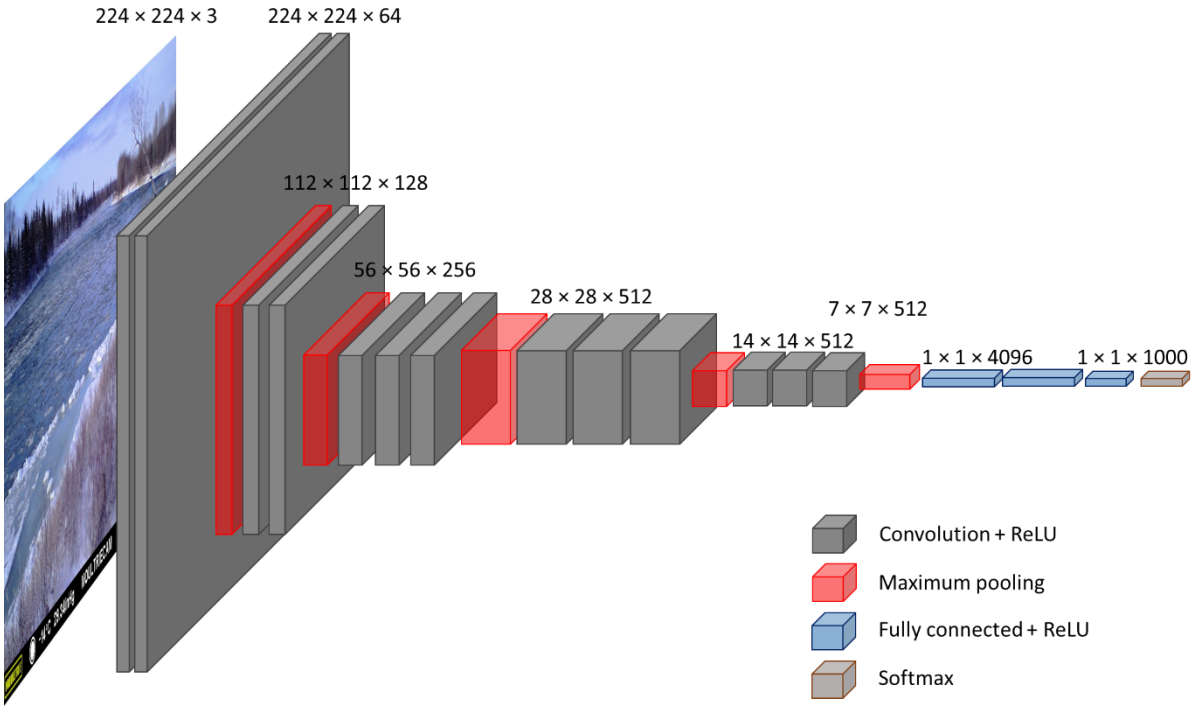

Figure 2-3 VGG 16 architecture adopted from Deng et al. 2009

In the example above, the input is an RGB image in a 3D matrix representing pixel intensities. The input of this architecture may be for instance a (224 × 224 × 3) tensor, and the resultant is a vector with a size of 1000 values. The input image first is passed through a set of a convolutional layer where filters are used for feature extraction (a very small receptive field of 3 × 3). The result is two layers with 64 channels of 3 × 3 filters and similar padding (size). Then, a maximum pooling[1] of pool size 2 × 2 with a stride[2] of (2 × 2) is applied to reduce the amount of information.

[1] Maximum pooling is an operation to calculate the maximum or largest value in each patch of each feature map.
[2] A component of the CNN utilized to compress the image data.

The result is 2 convolutional layers of (112 × 112 × 128), followed by another maximum pooling of 2 × 2 pool and stride size which results in 3 convolutional layers of 256 channel of 3 × 3 filter and same padding (56 × 56 × 256). This procedure continues until we get a 7 × 7 × 512 feature map as the output of the CNN. The final step is to pass the results to the fully connected layer. The fully connected input layer takes the previous layers and flattens them and converts them to one vector. Finally, a softmax[3] probability function is used for classification. A Rectifier Linear Unit (ReLU)[4] is in all the hidden layers to prevent negative values to be transferred to the next layer. In CNNs pooling operations such as maximum pooling, average pooling, L2 pooling, and local contrast normalization (maximum pooling in VGG16) is used to decrease the information used in the network (Kavukcuoglu *et al.*, 2009).

Convolutional neural networks often outperform the traditional neural networks due to their hierarchical learning nature and their deeper architecture. Moreover, the CNN architecture provides the ability for multi-task optimization, as employed in Fast Region-based convolutional networks, R-CNN (Zhao *et al.*, 2019). Convolutional neural networks have been widely used in various computer vision fields, such as image classification and segmentation.

2.2.2 Object detection

Object detection is the task of determining and locating a specific object in an image, and classifying of the detected object. Traditional object detection algorithms are built on basic feature extraction, detection, and clustering algorithms. Rapid progress in the development of machine learning and deep learning algorithms introduced robust object recognition tools that can learn high-level and deeper features. Traditional object detection algorithms mainly consist of the three different steps of region selection, feature extraction, and classification (Zhao *et al.*, 2019). Region selection is often performed using a scanning procedure of the whole image with a sliding window (filter) over an image. This stage can be a very time-consuming task when there is a large number of images. Semantic feature extraction (the second stage in object detection procedures) is the extraction of the image meaningful features. Traditional methods using manual feature design (i.e. design and select appropriate feature descriptors by a human expert), utilize basic feature descriptors for object identification; however, complexity induced to object detection due to different shapes, illumination conditions, and background makes the old-fashioned procedures difficult and underperforming. Classification of the extracted features is the next step in object detection. Various classifiers have been used for this purpose, such as Support Vector Machine

[3] An activation function that in CNN is used mostly for the output layer and for multiclass classification.
[4] An activation function defined as y = max(0,x).

(SVM) (Cortes and Vapnik, 1995) and Deformable Part-based Model (DPM) (Felzenszwalb *et al.*, 2009).

The emergence of Deep Neural Networks (DNNs) (Krizhevsky *et al.* 2012; Holden *et al.*, 2006) and their application in machine learning and object detection is considered as a significant advance in this field (Zhao *et al.*, 2019). A more recent and robust development is the advent of Region-based Convolutional Neural Networks (R-CNNs) (Girshick *et al.*, 2014). Unlike the traditional object detection algorithms, deep neural network (DNN) based training algorithms perform object detection training without manual feature design (Lecun *et al.* 2015). The development of different methods of R-CNN, such as fast R-CNN (Girshick, 2015) and Faster R-CNN (Ren *et al.*, 2017), have led to improvements in object detection by increasing their accuracy and reducing computational complexity.

2.2.3 Image segmentation

Image segmentation is one of the most critical and challenging fields in computer vision. Basic clustering techniques of the base image information such as contours and edges were the traditional methods of image segmentation, e.g., Prowse and Marsh, 1989 and Thomee *et al.*, 2008. Clustering techniques have continuously been improved and have been widely used in scene segmentation for various applications; for instance, a modeling technique using a Markov process (Geman and Geman, 1984) or a mixed method of contour detection and a hierarchical approach (Arbeláez *et al.*, 2011). Clustering techniques have also been used in ice detection in satellite images (Banfield and Raftery, 1992). Recently improved image segmentation techniques can be divided into three different categories, as described in detail below. While all three categories need annotated data for training, the weakly supervised segmentation model does not only rely on annotated images. In this case, annotation means manually identifying and classifying objects of interest in the images.

Region-based semantic segmentation

R-CNN is a region-based semantic segmentation pipeline that performs semantic segmentation using object detection algorithms (Girshick *et al.*, 2014). R-CNN utilizes a selective search pipeline to extract object proposals (Uijlings *et al.*, 2013) and then builds convolutional features for each one of the extracted features. The final step is classification using a support vector machine (SVM). R-CNNs can be used for object detection as well as more complicated tasks of image segmentation.

Fully convolutional network (FCN) - based semantic segmentation

FCN based semantic segmentation algorithms have been constructed based on the traditional CNNs (Long *et al.* 2015). In this method, the segmentation is performed without any region proposal extraction. FCNs act similar to the CNNs; however, in FCNs, after the first series of convolutional layers, another set of CNNs is performed in reverse order. This is to recreate the original image size with pixels that are classified as the predefined classes. Figure 2-4 illustrates the general architecture of the FCN based semantic segmentation pipelines. Although the results of the FCN based methods are promising, they are computationally expensive, and have poor segmentation prediction quality because of the propagation of the images through several convolutional and pooling layers. Several attempts have been made to address this issue with the application of multiscale resolution sub-networks (Eigen and Fergus, 2015) or combining coarse high-level information with fine low level data (Long, *et al.*, 2015).

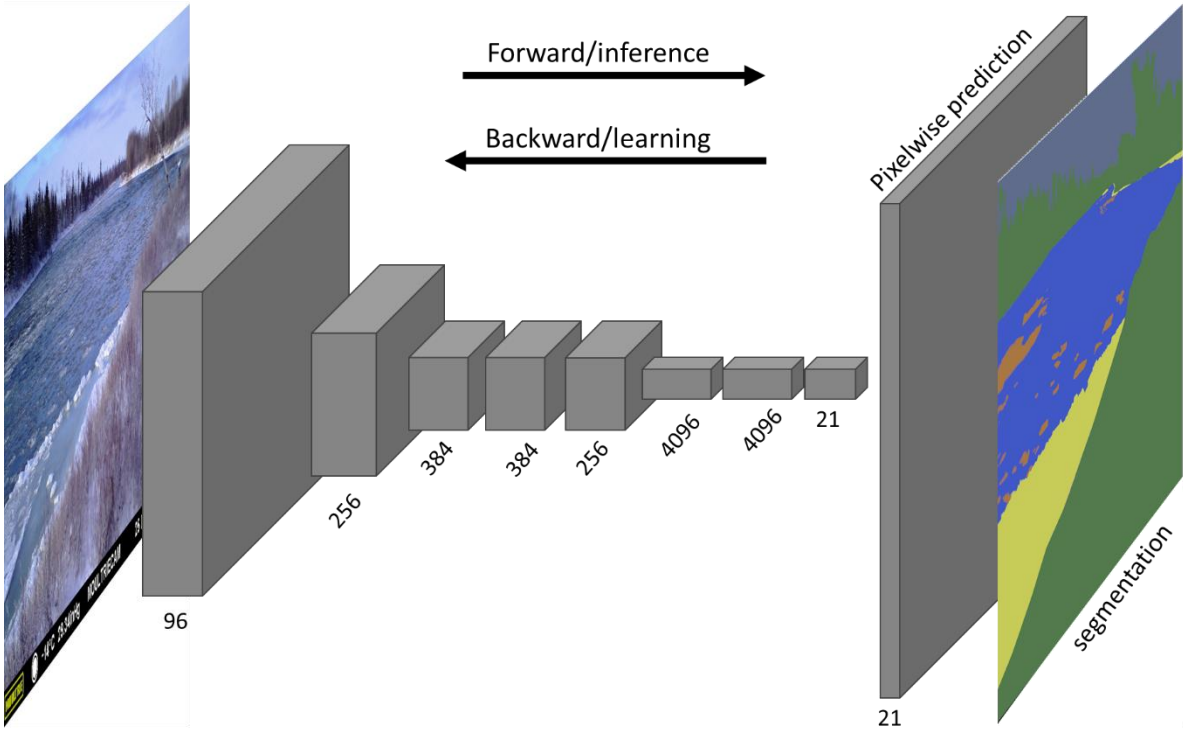

Figure 2-4 Fully convolutional neural network based image segmentation adapted from Long, (Shelhammer and Darrell, 2015)

Weakly supervised segmentation

One of the significant challenges in the training of the image segmentation models is labeling and annotating the images. Weakly supervised segmentation algorithms that only utilize a bounding box (Dai, He and Sun, 2015) or even image-level labels (Guo *et al.,* 2018) have been introduced recently. One of the outstanding achievements in this field is the method presented by (Papandreou *et al.,* 2015) in which an expectation maximization approach was used to train the convolutional networks based on a combination of both the bounding box labeling and image-level labeling. There have also been some attempts to increase the accuracy of the bounding box annotation with the application of recursive training methodology (Khoreva *et al.,* 2017). An important drawback of the image-level labeling is that in this method, object location is ignored. Further research works have recently been conducted to improve image-level supervision methods dealing with the problem of object localization (Bearman *et al.,* 2016; Wei *et al.,* 2016; Saleh *et al.,* 2016; Jin *et al.* 2017).

2.3 Surface velocimetry

Measuring discharge, a critical component of streamflow data, is essential for informed decision-making in both environmental and economic contexts. Hydrographs play a significant role in managing water resources, mitigating flood risks, designing hydraulic structures, and conducting environmental and fish habitat research. Consequently, accurate and dependable flow data are crucial for minimizing expenses and ensuring sound decisions in water resource management and environmental applications (McMillan *et al.,* 2017). This concept can be further emphasized by discussing the impact of over- and underestimation of flow data on design parameters. For most hydraulic structures, overestimation may result in excessive construction costs, while underestimation could increase the likelihood of failure.

Numerous tools and techniques have been developed for measuring open channel flow, including mechanical gauging devices, acoustic instruments, and non-contact measurement technologies. Progress in electronics and remote sensing technologies has expanded the use of these methods in earth sciences and engineering. Although in situ acoustic instruments are now commonly employed for discharge measurement, basic mechanical stream gauging devices, which were developed over a century ago, continue to be used (Costa *et al.,* 2000). However, some hydrometric stations have adopted new acoustic, radar, and remote sensing technologies as in-line measuring devices. For instance, certain gauge stations now utilize acoustic instruments with an index velocity method for measuring discharge. The relatively slow adoption of these novel measurement techniques is primarily due to their high costs, the need for specialized expertise, and the uncertainty surrounding their results.

During the 1990s, numerous research experiments explored the use of non-contact methods for observing and measuring flow fields through satellite imagery (Smith et al., 1996; Smith, 1997). While some of these studies focused on flow observations and flood inundation monitoring, others aimed to extract quantified flood flow field data, such as the research conducted by Bates and De Roo (2000) and Horritt and Bates (2001). Satellite imagery based discharge estimation often involves indirect flow measurement techniques, such as using altimeters to determine river width, stage, and slope (Kouraev et al., 2004; Durand *et al.,* 2016), or hydraulic models (Bjerklie et al., 2003). Despite recent advancements in discharge measurement using satellite imagery, its practical application is limited due to factors such as low accuracy (resulting from satellite imagery resolution), high costs, and constraints in satellite imagery timing and frequency.

Close-range photogrammetry is another form of non-contact discharge measurement. Significant advancements in image acquisition and the emergence of high-quality, powerful cameras at more affordable prices have contributed to the rapid growth of close-range photogrammetry in earth sciences (Barker *et al.,* 1997; Clark and Hardegree, 2005; Bourgault, 2008; Kaufmann, 2012; Westoby *et al.,* 2012; Jędrzychowski and Kujawski, 2014; Tauro *et al.,* 2016). Various photogrammetry techniques for surface velocimetry are described in detail below:

2.3.1 Particle tracking velocimetry (PTV) and particle image velocimetry (PIV)

Particle Tracking Velocimetry (PTV) and Particle Image Velocimetry (PIV) are two traditional imaging techniques that have evolved over time. These methods have been employed in both laboratory and field experiments, such as those conducted by Cowen and Monismith (1997) and Raffel et al. (2018). Both approaches involve tracking individual particles (PTV) or groups of particles or features in images, known as patterns (PIV), between consecutive frames. The differences between the two methods result in distinct applications, as well as varying outcomes in terms of seeding concentration, spatial resolution, and field averaging results (Aberle et al., 2017). Since PTV focuses on tracking individual particles (tracers), it can be applied at lower seeding concentrations than PIV (Adrian, 1991). This distinction is where the errors of the two techniques become more noticeable. Due to the fact that PIV considers a larger field of view, inconsistencies in particle concentration can impact the results. Overall, tracer concentration is crucial in both methods, as a sufficient, desirable concentration is needed for accurate estimations.

In PIV, a designated interrogation area must be defined for velocity measurement, and the accuracy of the results heavily depends on the size of this area. The tracking process in PIV occurs within the bounds of the specified interrogation area, making it vital to define an area with a

uniform velocity distribution (Adrian, 1991). In contrast, PTV does not require uniform velocity distribution, as it tracks individual tracers. Generally, PTV methods are better suited for high gradient velocities (Aberle, 2017).

The steps used in PTV can be summarized as below:

1- Thresholding to detect particles
2- Tracking corresponding particles in consequent frames
3- Calculating velocities based on tracked tracers
4- Eliminating erroneously calculated velocities

The steps used in PIV includes:

1- Defining the interrogation regions over the image
2- Calculation of the displacement within the interrogation regions using statistical methods and application of the 2-D correlation of interrogation windows in consecutive images.
3- Division of the measured displacement in each window to time (derived from frame rate).
4- Elimination of erroneously calculated velocities

Advancements in PIV methodologies for calculating displacement within interrogation regions across consecutive images in video footage have been driven by enhancements in correlation functions, which have evolved alongside improvements in camera and optic technology. Traditionally, cross-correlation and auto-correlation functions have been employed to identify and calculate displacement between two frames. Pattern changes or particle displacements are determined using statistical methods, such as 2D correlations. Two primary 2-dimensional correlation functions can be utilized in PIV methods: autocorrelation and cross-correlation functions (Raffel *et al.,* 2018). Autocorrelation involves correlating a signal with itself and is mainly used in PIV for high image density flow conditions. In contrast, cross-correlation is predominantly employed in low-density image mode (Fujita *et al.*, 1998). It is worth noting that various correlation functions have been developed and introduced based on the specific application of PIV methods in determining flow velocities (Sveen, 2013; Aberle, 2017).

A specific pattern in an interrogation area within an image is considered to track and calculate displacement, which leads to velocity calculation. The utilized cross-correlation function is as follows:

(2-1)

$$R_{ab} = \frac{\sum_{i=1}^{MX}\sum_{j=1}^{MY}\{(a_{ij} - \overline{a_{ij}})(a_{ij} - \overline{b_{ij}})\}}{\sqrt{\sum_{i=1}^{MX}\sum_{j=1}^{MY}(a_{ij} - \overline{a_{ij}})^2 \sum_{i=1}^{MX}\sum_{j=1}^{MY}(b_{ij} - \overline{b_{ij}})}}$$

In this equation, the MX and MY are the two indicators of the interrogation area size and a_{ij} and b_{ij} is the gray intensity of the interrogation area. a_{ij} and $b_{ij}$are the image intensities of two frame intervals.

There is a vast debate on selection criteria for the tracers and selection of the interrogation zone in PTV and PIV methods. In PIV while the selection criteria should be consistent with the dominating flow, a tracer particle-image diameter size of 1.0 to 4.0 pixels is recommended. This size range in PTV is between 1.8 to 2.4 pixels (Cowen and Monismith, 1997; Westerweel, 1999; Prasad *et al.*, 1992).

2.3.2 Large scale particle image velocimetry (LSPIV)

Advancements in electronics, optics, and computer science has facilitated the development and application of PTV and PIV imaging techniques for measuring hydraulic flow characteristics. Initially, these methods could only be applied in laboratory settings. In the early 1990s, researchers such as Lloyd *et al.*, (1995) and Ettema *et al.*, (1997) introduced the application of PIV for river flow measurements. These studies demonstrated the use of PIV in smaller areas to minimize distortion errors. However, later research by Fujita and Aya (2000) presented large-scale particle image velocimetry (LSPIV), which focused on a more extensive area for flow measurements (Aberle, 2017). The methodologies for river flow velocity measurements using PIV and LSPIV are similar. In LSPIV's three-dimensional environment, the primary focus is on the flow's free surface. Identifying common trackable features that represent river flow allows LSPIV to measure surface flow velocity. These trackable features can include surface ripples and drifting materials in the river flow. In conventional PIV, three major parameters are crucial: seeding, illumination, and the employed image processing techniques. In LSPIV, recorded images require additional processing to rectify distortion caused by oblique imagery. Despite significant progress in finding a reliable solution for illumination over the water surface, this issue remains a major challenge in LSPIV.

Similar to PIV, the main steps of LSPIV consist of:

1- Recording sequence of images (video footage) from an oblique angle.

2- Ortho-rectification of the images. This is conducted using a mapping relationship.

There are several methods for rectification of the images. Some earlier versions of the LSPIV use ground control points (GCPs) to obtain more accurate results (Fujita *et al.*, 1998; Muste *et al.*, 2004). However, later some other methods using camera specifications were used for this purpose (Härer *et al.*, 2013; Ansari *et al.*, 2017).

3- Image processing. This is mainly regarding the quality of the images and to deal with the illumination problems in the image.

4- Image stabilization; another challenging criterion of imagery techniques for field flow measurement is to rectify the movements of the cameras due to wind and field conditions.

5- Pattern recognition and application of the basic conventional PIV methods.

6- Displacement calculation. Once the features were detected and tracked then the next step is to calculate the displacement between the tracked features in the sequence of a set of images.

7- Velocity calculations. Considering the frame rate in the video file

In this section, a brief review of the popular methods used in each of the main steps is presented.

2.3.2.1 Rectification

An accurate mapping relation is essential for rectification of the acquired images. Considering that the 2-dimensional coordinates in an image plane are presented by (x,y) and the 3-dimensional real-world coordinates of the same images are (X, Y, Z) the conventional direct linear transformation (Chen *et al.*, 1994) was used by several researchers (Fujita and Aya, 2000; Aberle, *et al.* 2017). The elevation coefficients (A B and C) can be estimated by solving six different equations corresponding to the ground control points (GCPs).

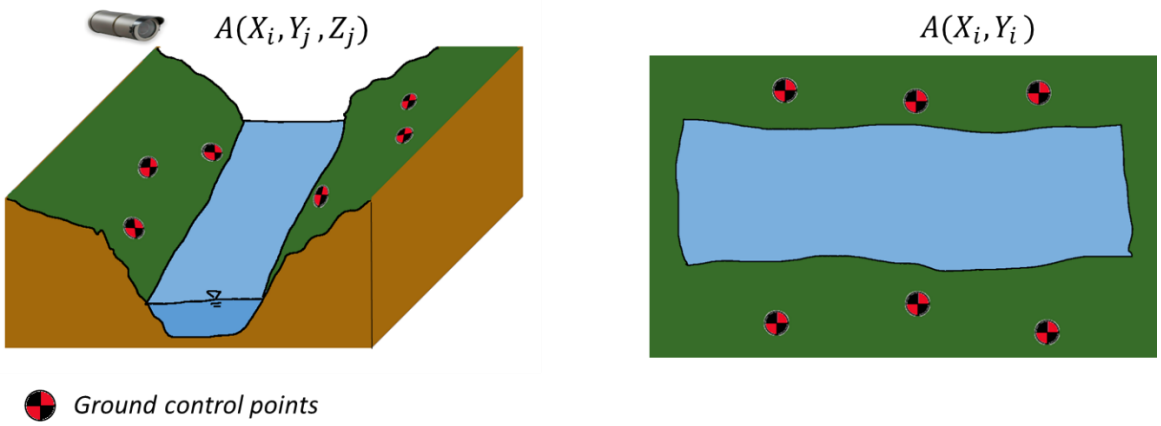

Figure 2-5 Camera and GCP coordinates in the site and after rectification

Locating at least four GCP points is essential to solving the two equations above to perform the image transformation to real-world coordinates. In other words, at least six (x,y) pixels with known (X,Y,Z) locations are required to solve the A_i, B_i, and C_i coefficients in Equations 2-2 and 2-3. Using the GCPs, a grid having the step size ΔX and ΔY is produced, that are the real coordinates.

$$x = \frac{A_1X + A_2Y + A_3Z + A_4}{C_1X + C_2Y + C_3Z + 1} \tag{2-2}$$

$$y = \frac{B_1X + B_2Y + B_3Z + B_4}{C_1X + C_2Y + C_3Z + 1} \tag{2-3}$$

As an alternative to rectification calculations using Ground Control Points (GCPs), if the extrinsic and intrinsic camera coordinates are known, the following two equations can be applied:

$$x - x_0 = -f\left[\frac{m_{11}(X - X_0) + m_{12}(Y - Y_0) + m_{13}(Z - Z_0)}{m_{31}(X - X_0) + m_{32}(Y - Y_0) + m_{33}(Z - Z_0)}\right] \tag{2-4}$$

$$y - y_0 = -f\left[\frac{m_{21}(X - X_0) + m_{22}(Y - Y_0) + m_{23}(Z - Z_0)}{m_{31}(X - X_0) + m_{32}(Y - Y_0) + m_{33}(Z - Z_0)}\right] \tag{2-5}$$

In these equations, x_0 and y_0 represent the projection center and (X_0, Y_0, Z_0) is the camera coordinates. f is the focal length and m_{ij} are viewing angle coordinates; this will yield a

transformation matrix between camera coordinates and the real-world coordinates of the main point. The next step is to consider water surface plane and to substitute the water surface elevation equation into equation 2-4 and 2-5:

Water surface plane equation can be stated as:

$$Z = D_1 X_s + D_2 Y_s + D_3 \tag{2-6}$$

This leads to the following equations:

$$X_s = \frac{c_1 x + c_2 y + c_3}{p_1 x + p_2 y + p_3} \tag{2-7}$$

$$Y_s = \frac{q_1 x + c_2 y + q_3}{p_1 x + p_2 y + p_3} \tag{2-8}$$

The coefficients of these equations are as follows:

$$\begin{aligned}
c_1 &= (B_2C_3 - B_3C_2)D_3 + (B_3 - B_4C_3)D_2 + (B_2 - B_4C_2) \\
c_2 &= -\{(A_2C_3 - A_3C_2)D_3 + (A_3 - A_4C_3)D_2 + (A_2 - A_4C_2)\} \\
c_3 &= (A_3B_4 - A_4B_3)D_2 + (A_2B_3 - A_3B_2)D_3 + (A_2B_4 - A_4B_2) \\
p_1 &= (B_3C_2 - B_2C_3)D_1 + (B_1C_3 - B_3C_1)D_2 + (B_1C_2 - B_2C_1) \\
p_2 &= (A_2C_3 - A_3C_2)D_1 + (A_3C_1 - A_1C_3)D_2 - (A_1C_2 - A_2C_1) \\
p_3 &= (A_3B_2 - A_2B_3)D_1 + (A_1B_3 - A_3B_1)D_2 + (A_1B_2 - A_2B_1) \\
q_1 &= -\{(B_1C_3 - B_3C_1)D_3 + (B_3 - B_4C_3)D_1 + (B_1 - B_4C_1)\} \\
q_2 &= (A_1C_3 - A_3C_1)D_3 + (A_3 - A_4C_3)D_1 + (A_1 - A_4C_1) \\
q_3 &= -\{(A_3B_4 - A_4B_3)D_1 + (A_1B_3 - A_3B_1)D_3 + (A_1B_4 - A_4B_1)\}
\end{aligned} \tag{2-9}$$

2.3.2.2 Feature detection and tracking

The next important step in LSPIV is the detection and tracking of similar patterns within the water surface. The interrogation areas should be constructed to perform the feature tracking within each subsection. Once the small interrogation subsections are constructed, feature detection and tracking should be performed. Similar to the conventional PIV, this is conducted using the cross-correlation function:

(2-10)

$$R_{ab} = \frac{\sum_{i=1}^{M}\sum_{j=1}^{N}\{(a_{ij} - \overline{a_{ij}})(a_{ij} - \overline{b_{ij}})\}}{\sqrt{\sum_{i=1}^{M}\sum_{j=1}^{N}(a_{ij} - \overline{a_{ij}})^2 \sum_{i=1}^{M}\sum_{j=1}^{N}(b_{ij} - \overline{b_{ij}})^2}}$$

Once the surface velocity is calculated, river discharge can also be estimated using the known bathymetry utilizing the velocity-area method.

The LSPIV has been widely used in research for river flow discharge measurements. In several comparison studies over LSPIV and other conventional measurement techniques, it was shown that this method has an approximate error of 10% which is less than common mechanical current meters (Muste *et al.*, 2004). However, there are several deficiencies regarding this method, which led to the development of other methods, such as STIV. These shortcomings can be listed as:

1- In terms of calculations, this method requires a higher amount of disk space on a computer, and real-time infield estimation with this method is not an easy procedure.

2- Image perspective distortion has a higher effect on the results achieved by this method, and the near-field yields considerably better results compared to the far end. Moreover, the accuracy of the estimated velocity differs spatially.

3- A study conducted by (Kim, 2006) showed 27 elemental error sources in LSPIV, the most important ones are categorized to illumination, seeding, recording, transformation, and processing.

4- The main drawback of this method is its reliance on tracers, which might not always be available in the field.

5- Measurement at sections with lower velocity is not feasible using this method and might lead to unacceptable errors.

2.3.3 Space-time image velocimetry (STIV)

LSPIV was introduced as a robust method for river flow velocity and discharge estimation. However, due to the deficiencies mentioned in the last section and also to improve the non-contact river measurement techniques, another method known as Space-Time Image Velocimetry (STIV) was introduced by the initiators of the LSPIV (Fujita *et al.* 2007). The main attempt in STIV was to reduce the error sources and the aspects of the calculation method affecting the estimation result. In STIV a uniform velocity distribution can be estimated, which is independent of the camera view angle and also the resolution of the image. It should be noted that the calculated velocity with this method is an averaged flow velocity and not an instantaneous velocity.

The steps required to apply this method consist of (Fujita *et al.* 2007):

1- Establish a search line aligned with the flow direction, which will be utilized to create the space-time image (STI). The STI is formed by analyzing the alterations in brightness along the chosen search line over time. Ensure that the line encompasses a diverse range of brightness or color within a series of images (Figure 2-6).
2- Once the searching line is defined by the user the STI is produced. STI is an image which is formed by the bright pixels along the line occurring throughout the consecutive images.
3- As shown in Figure 2-6, the pattern consists of bright inclined lines. By calculating the angle of this inclination, we can estimate the velocity.
4- This angle can be calculated using the following equations originated from pattern recognition in computer vision. In the following equations $\boldsymbol{g}$ is the gray level intensity.

$$tan2\varphi = \frac{2J_{xt}}{J_{tt} - J_{xx}} \tag{2-11}$$

$$J_{xx} = \int_A \frac{\partial g}{\partial x}\frac{\partial g}{\partial x} dxdt \tag{2-12}$$

$$J_{xt} = \int_A \frac{\partial g}{\partial x}\frac{\partial g}{\partial t} dxdt \tag{2-13}$$

$$J_{tt} = \int_A \frac{\partial g}{\partial t}\frac{\partial g}{\partial t} dxdt \tag{2-14}$$

5- One of the advantages of this method is defining a coherency value. This is a measure of the coherence of the image pattern. This makes it possible to select a brighter line to define the orientation. The coherency value is defined as:

$$C = \frac{\sqrt{(J_{tt} - J_{xx})^2 + 4J_{xt}^2}}{J_{xx} + J_{tt}} = \frac{\lambda_1 - \lambda_2}{\lambda_1 + \lambda_2} \tag{2-15}$$

6- The coherency value calculated with equation 2-16 allows a more clear angle definition using the coherency level as a weighting function:

$$\bar{\varphi} = \frac{\int \varphi C(\varphi) d\varphi}{\int C(\varphi) d\varphi} \tag{2-16}$$

7- Translation of the image pixel coordinates to real-world coordinates should also be performed. This will lead to a unit length scale for a horizontal STI axis S_x (m/pixel) and also the vertical component, corresponding to time S_y (s/pixel). Finally, equation 2-17 should be used to estimate the velocity.

$$U = \frac{S_x}{S_t} tan\bar{\varphi} \tag{2-17}$$

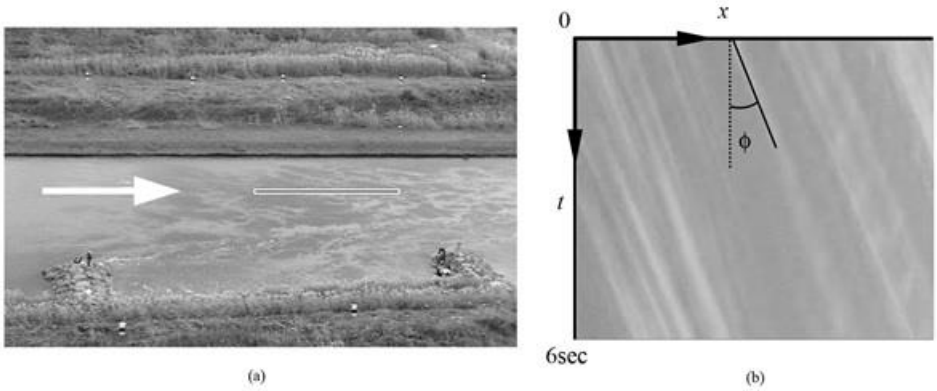

Figure 2-6 Sample image for STIV methods and the searching line defined by the user (Tsuji et al., 2019)

The STIV method has been used for several years, and the results are highly acceptable compared to the previous LSPIV method. However, the one drawback of this method is that the user has to identify the search lines. This limits the automatic estimation of the flow discharge measurements. Moreover, the flow direction is also defined by the user, which is sometimes difficult in places such as meandering flow. To solve the shortcomings, the space-time volume velocimetry has been introduced.

2.3.4 Optical flow

2.3.4.1 Optical flow constraint equation

The optical flow technique involves examining the movement of objects within a sequence of consecutive images. By identifying pixels associated with both the moving objects and the static background in these images, the motion can be analyzed. This approach has various applications, including determining the quantity and direction of moving objects, as well as detecting the objects in motion.

By defining a function named **Optical Flow**, for every pixel, the velocity vector and its intensity and direction are defined ($\boldsymbol{v} = (\boldsymbol{u}, \boldsymbol{v})$). A brief description of the optical flow concept will be provided herein.

Supposing that the image intensity is defined by *I(x,y)*, and the intensity in the image is a function of time, then the intensity of the image at a point slightly away can be defined as:

$$I(x + dx, y + dy, t + dt) = I(x, y, t) + \frac{\partial I}{\partial x}dx + \frac{\partial I}{\partial y}dy + \frac{\partial I}{\partial t}dt + \cdots. \quad (2\text{-}18)$$

Considering that an object in part of the image is at position (x,y) in the image at a time t and that by a time *dt* later this object has a movement through a distance in reality and in the image *(dx,dy)*. Moreover, supposing that otherwise the pixel intensity of that part of the image remains constant and uniform i.e. background. Then, we would have the following:

$$I(x + dx, y + dy, t + dt) = I(x, y, t) \quad (2\text{-}19)$$

$$\frac{\partial I}{\partial x}dx + \frac{\partial I}{\partial y}dy + \frac{\partial I}{\partial t}dt + \cdots = 0 \quad (2\text{-}20)$$

By dividing by time (dt), we would have:

$$\frac{dx}{dt} = u, \qquad \frac{dy}{dt} = v \quad (2\text{-}21)$$

The above-mentioned equations show the pixel velocity in two different directions. Thus if we divide this in the limit that *dt* tends to zero, then we would have:

$$-\frac{\partial I}{\partial t} = \frac{\partial I}{\partial x}u + \frac{\partial I}{\partial y}v \quad (2\text{-}22)$$

The latter equation is called ***optical flow constraint equation.***

In the mentioned equations, $\frac{\partial I}{\partial t}$ is the speed of pixel intensity change, while $\frac{\partial I}{\partial x}$ and $\frac{\partial I}{\partial y}$ describe the spatial gradient of pixel intensity across the picture.

This equation with two unknown variables is difficult to solve. Various methods have been presented to solve these equations and analyze the pixel motion, i.e., 1) intensity-based differential methods, 2) multiconstraint methods, 3) frequency-based methods, 4) correlation-based methods, 5) multiple motion methods, 6) temporal refinement methods. Herein, two of these methods are described for application of the OF method.

2.3.4.2 Lucas-Kande method

Lucas Kande method (Lucas and Kanade, 1981) is a widely used differential method for optical flow estimation in computer vision. In this method, the neighboring pixels of the image are considered to have constant pixel intensity and considering this assumption, the optical flow constraint equation is solved by the ***least square fit method***. This method is less sensitive to the image noise compared to the pointwise solution. However, since this method considers local pixel intensity, it fails to perform robustly in the interior uniform regions of the image. If for instance a 3×3 patch around the point is considered, and the equation for 9 points is solved using the least square fit method, then the final solution would be two equations with two unknown problems as below:

$$\begin{bmatrix} u \\ v \end{bmatrix} = \begin{bmatrix} \sum_i f_{x_i}^2 & \sum_i f_{x_i} f_{y_i} \\ \sum_i f_{x_i} f_{y_i} & \sum_i f_{y_i}^2 \end{bmatrix}^{-1} \begin{bmatrix} -\sum_i f_{x_i} f_{t_i} \\ -\sum_i f_{y_i} f_{t_i} \end{bmatrix}$$

Where:

$$f_x = \frac{dI}{dx}, \quad f_y = \frac{dI}{dy}, \quad f_t = \frac{dI}{dt} \tag{2-23}$$

2.3.4.3 Horn-Schunck method

Similar to the Lucas-Kanade method, Horn-Schunck is another technique for estimating velocity using gradient constraints. In this approach, the velocity field is determined by minimizing a function across the image (Thota *et al.*, 2013). The algorithm is based on the assumption that the flow throughout the entire image is smooth. This implies that, to account for brightness variations due to shading effects, the method initially assumes a flat imaged surface and uniform incident illumination (Horn and Schunck, 1981). The pixel intensity across the image is considered constant, without any spatial brightness discontinuity. As a result, the gradient constraint is

combined with a global smoothness functional to constrain the velocity field. Consequently, the estimated velocity field is represented by equation 2-24.

$$V(X,t) = (u(X,t), v(X,t)) \tag{2-24}$$

The flow is then formulated as a global energy functional that should be minimized. The two-dimensional image streams can be shown as the following:

$$E = \iint (I_x u + I_y v + I_t)^2 dxdy + \alpha \iint \left\{ (\frac{\partial u}{\partial x})^2 + (\frac{\partial u}{\partial y})^2 + (\frac{\partial v}{\partial x})^2 + (\frac{\partial v}{\partial y})^2 \right\} dxdy \tag{2-25}$$

Where $\frac{\partial u}{\partial x}$ and $\frac{\partial u}{\partial y}$ are the spatial derivatives of the optical velocity components, and α is the regularization term within the functional. The magnitude of α reflects the influence of the smoothness term (Thota *et al.*, 2013); it is suggested by Horn and Schunck (1981) to consider this value equal to 100 for better results. In the Horn-Schunck method equation 2-25 is minimized using the following functions:

$$u_{x,y}^{k+1} = \bar{u}_{x,y}^{k} - \frac{I_x \left[I_x \bar{u}_{x,y}^{k} + I_y \bar{v}_{x,y}^{k} + I_t \right]}{\alpha^2 + I_x^2 + I_y^2} \tag{2-26}$$

$$v_{x,y}^{k+1} = \bar{v}_{x,y}^{k} - \frac{I_x \left[I_x \bar{u}_{x,y}^{k} + I_y \bar{v}_{x,y}^{k} + I_t \right]}{\alpha^2 + I_x^2 + I_y^2} \tag{2-27}$$

Where $\left[u_{x,y}^{k}\ v_{x,y}^{k}\right]$ is the estimation for pixel velocity at *(x,y)*, and $\left[\bar{u}_{x,y}^{k}\ \bar{v}_{x,y}^{k}\right]$ denotes the neighbourhood average of $\left[u_{x,y}^{k}\ v_{x,y}^{k}\right]$. *k* denotes the number of iterations.

3. River ice inference using close-range remote sensing

3.1 IceMaskNet: River Ice Detection and Characterization Using Deep Learning Algorithms Applied to Aerial Photography

Preprint of an article printed in Cold Regions Science and technology © ELSEVIER
https://doi.org/10.1016/j.coldregions.2021.103324

3.1.1 Introduction

The presence of ice is one of the unique aspects of cold region hydrology. Ice in rivers and lakes of cold areas can influence streamflow behaviour and watershed response during winter. River ice cover processes can also affect the socio-economic activities of these regions. Hence understanding river ice and its processes is crucial for the management of water systems. There have been several studies on the effects of ice on rivers of these regions, such as hydraulic characteristics (e.g., Zare *et al.,* 2016), water quality (e.g., Tang *et al.,* 2016), the morphology of the rivers (e.g., Smith, 1979), channel stability (e.g., Ettema and Zabilansky, 2004) and sediment transport (e.g., Beltaos and Burrell, 2016; Kalke *et al.*, 2017;).

River ice processes often initiate with frazil ice production (Beltaos, 2013). Formation of the suspended frazil ice (small ice crystals) usually starts in turbulent open water sections that are super-cooled. Frazil ice consists of small ice crystals that are suspended in water and flow downstream. When frazil crystals are actively growing they will flocculate, forming frazil flocs that will float to the water surface and form slush ice. Ice pans are formed when the floating slush ice is exposed to cold air for a prolonged duration and gains strength through thermal ice growth. Frazil pans often appear circular in nature since their collisions with one another (or with border ice or other objects) on the water surface round off any sharp edges. Frazil ice pans floating downstream can adhere together and form bigger ice rafts (Beltaos, 2013).

Ice conveyance will continue downstream until a stable ice cover can initialize. This can happen in several different ways, one of which is when the moving ice encounters an already established solid ice cover. A stable ice cover can also occur whenever the surface ice concentration becomes high enough to prevent downstream ice movement. Narrow river sections, islands, encroaching solid border ice (i.e., stationary ice growing laterally outwards from the river bank), and slower sections of the river can all promote stable ice cover formation (Beltaos, 2013). Anchor ice is another form of river ice that forms when frazil particles adhere to objects in the bottom or the banks of the river. Anchor ice is known to affect sediment transport during the winter (Kempema and Ettema, 2011).

Understanding river ice processes requires intensive winter data collection. Recent studies have shown that close-range photogrammetry can be used for monitoring and quantitative data collection (Ansari *et al.,* 2017; Kalke and Loewen, 2018; Ansari *et al.,* 2019a; Simoes and Clark, 2019). Quantifying the surface ice concentration in rivers is necessary for a better understanding of river processes. Moreover, the information extracted can also be used to validate river ice numerical dynamic models (e.g., Shen *et al.,* 2000; Zare *et al.,* 2015; Lindenschmidt, 2017; and Wazney *et al.,* 2019b). Utilization of close-range and aerial photogrammetry in earth science and engineering has recently gained attraction with the emergence of high-tech and cost-effective cameras and Remotely Piloted Aircraft Systems (RPAS). At the same time, rapid progress and development of computer vision methods has enabled quantitative analysis of the data collected using close-range photogrammetry. Ansari et al. (2017) used photogrammetry and image processing techniques to develop a robust automatic river ice quantification pipeline. This was the first attempt in this field for quantitative data extraction from shore-based imagery. However, the algorithm was costly to run primarily in the river-ice detection step. Moreover, the algorithm did not perform any classification of river ice types. Kalke and Loewen, (2018) utilized Support Vector Machines (SVMs), to detect and classify floating ice pieces as either released anchor ice or frazil ice pans (two classes) from drone imagery and cameras installed on a bridge. Their work was an important attempt to apply machine learning methods in river ice detection and classification. Application of a fast superpixel segmentation algorithm was another attempt made by Ansari et al. (2019b) to employ machine learning algorithms for the segmentation of shore-based river ice imagery. The goal of the segmentation procedure was to detect and delineate each distinct object of interest (here different types of ice) in an image. Singh et al. (2019), the first attempt to utilize deep learning for river ice segmentation, utilized four different deep learning algorithms (Deeplab, UNet, SegNet and DenseNet) to detect two different types of river ice from downlooking cameras mounted on a bridge.

One of the most challenging problems in computer vision has been automatic object detection and semantic image segmentation. Similarly, ice detection under various circumstances is a fundamental problem in river ice monitoring and the development of an automated algorithm of quantified river ice classification. In computer vision, object detection and semantic segmentation are the two crucial and rapidly improving fields that have a variety of applications. The most popular machine learning algorithms in this field currently are the Region-based Convolutional Neural Networks, R-CNN (Girshick *et al.,* 2014), Fast R-CNN (Girshick, 2015), Faster R-CNN (Ren *et al.,* 2017) and Single Shot Multibox Detector, SSD (Liu *et al.,* 2016). The improvements of baselines, Fast/Faster R-CNN (Girshick, 2015) and (Ren *et al.,* 2017) and Fully Convolutional

Neural Networks (FCN) (Long *et al.*, 2015) have led to advances in object detection and semantic segmentation respectively (He *et al.*, 2017).

In the present study, a novel deep learning framework, Mask R-CNN, was employed for river ice detection and segmentation. This framework combines both the object detection and segmentation in one network (He *et al.*, 2017). Most of the previously developed image segmentation algorithms are based on candidate regions such as (Pinheiro *et al.*, 2015) and (Li *et al.*, 2017). Mask R-CNN is an image detection and segmentation algorithm with a pixel-wise accuracy that has accurate instance segmentation products. The robust Mask R-CNN algorithm previously has successfully been utilized in various studies such as in nuclei segmentation (Vuola *et al.*, 2019), in lesion detection (Sorokin, 2018), in segmentation of oral diseases (Anantharaman *et al.*, 2019) and in remote sensing (Zhang *et al.*, 2018).

In this study, Mask R-CNN was improved and utilized to develop a generalized algorithm, named IceMaskNet, to automatically perform accurate and fast detection and characterization of river ice from aerial imagery. IceMaskNet can recognize open water patches and five types of ice with high accuracy. To the best of our knowledge, IceMaskNet is the first computer vision pipeline capable of performing fast and accurate river ice detection and characterization into six different classes from aerial imagery taken in different flight altitudes and various camera angles.

3.1.2 Data and Methodology

3.1.2.1 Study area

This study was conducted on the Dauphin River located in central Manitoba, north of Winnipeg, Canada. Lake Manitoba connects to Lake St. Martin through Fairford River and Lake Pineimuta, and the Dauphin River then connects Lake St. Martin to Lake Winnipeg (Figure 3-1). This water system and water levels of Lake Manitoba have been controlled by the Fairford River Water Control Structure (FRWSC) since 1961. To prevent flooding at Lake St. Martin due to the ice formation on the Dauphin River, the FRWSC typically restricts flow to 100 (m^3/s) in the winter. Dauphin River is approximately 52 km long. The slope of the first 40 km of this river is about 0.029%. With an abrupt change of slope, the lower 12 km section has a slope of 0.16%, almost 5.5 steeper than the upper reach (Wazney *et al.*, 2019a). The steeper section promotes dynamic river ice processes that warrant extensive monitoring.

A comprehensive study has been conducted on the Dauphin River since 2014. This study consisted of various monitoring efforts to observe river ice processes. These attempts include the installation of several trail cameras along the river for shore-based monitoring and the deployment

of pressure loggers and acoustic instruments. Moreover, several RPAS flights have also been conducted to collect aerial imagery footage for observations of river ice freeze-up processes.

3.1.2.2 Data acquisition

Aerial imagery of the Dauphin River taken mostly during freeze-up was used in this study. Figure 3-2 illustrates the deployed DJI Phantom 4 RPAS along with some sample images and their locations along the river. The aerial footage was collected at various dynamic and important sections of the river from November to March of three consecutive years (2017 to 2020). The specifications of the DJI Phantom 4 RPAS camera used for aerial imagery are provided in Table 3-1. Images used for training were single images taken during different RPAS flights and extracted frames of a series of varying flight recorded video footage. There were about 115 images used for the training, validation and testing. The dataset was divided into 80 percent for training and 20 percent for validation and testing. River ice in these images was annotated into six different classes; frazil pan, broken ice, frazil slush, border ice, ice cover, and open water. It should also be mentioned that the number of occurrences for each class used for training are as following: Frazil Slush: 2871, Open water: 1276, Border Ice: 963, Ice Cover: 1958, Frazil Pan: 956, Broken: 938.

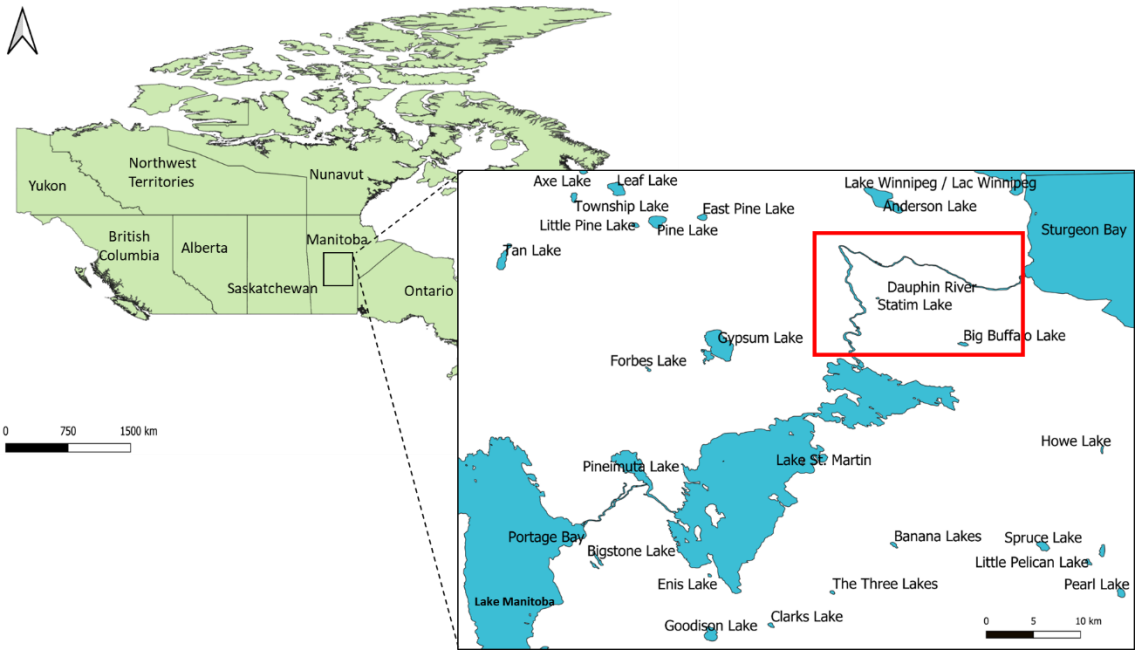

Figure 3-1 Lake Manitoba-Lake Winnipeg water system and Dauphin River

Figure 3-3 illustrates the six different classes separately. While the border ice often has a smoother uniform texture (Figure 3-3a), broken pieces are smaller pieces of ice with sharper edges (Figure 3-3d). Broken ice can be further separated into pieces of anchor ice, border ice, or just crushed pan ice. Frazil slush, on the other hand, has a more slushy texture with more water in between the pieces (Figure 3-3b). Frazil pans look more similar to broken pieces of ice, but they have rounded and upward turned edges (Figure 3-3c). Open water has a more smooth and uniform texture compared to ice cover or border ice (Figure 3-3e). Ice cover is a class that is defined for the images taken from the stable ice cover condition with open water patches. Ice cover has a very similar texture to the border ice cover, but it has a different shape and size in the image (Figure 3-3f).

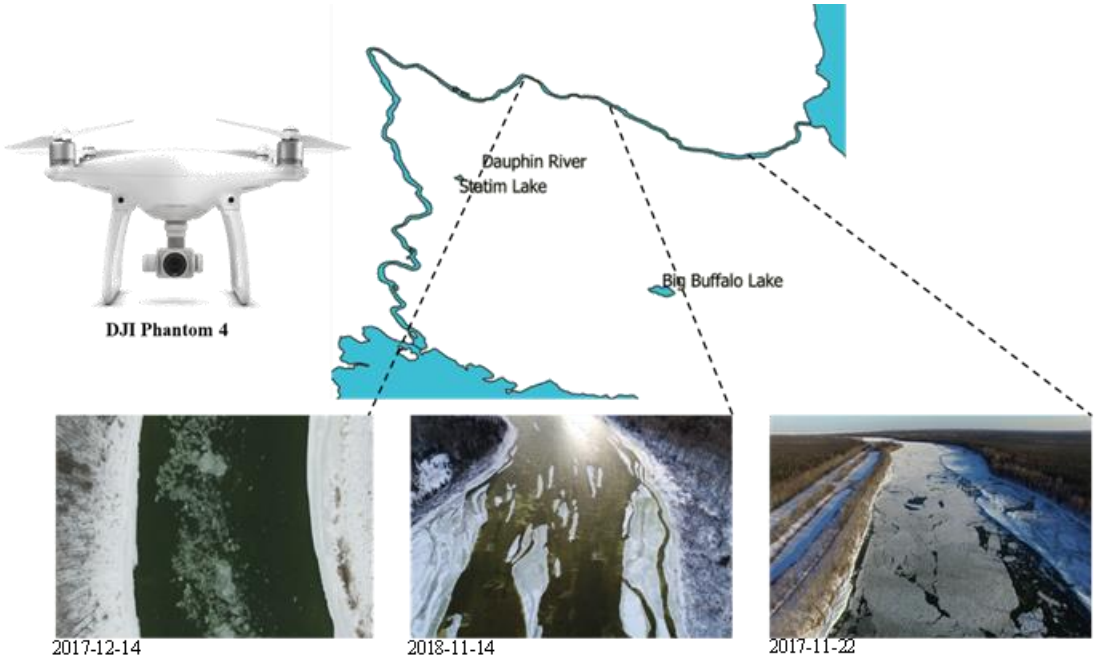

Figure 3-2 The Dauphin River and sample aerial imagery at three different locations

Table 3-1 DJI Phantom 4 camera specifications

Sensor	1” CMOS (20 Megapixels)
Lens	FOV 84° 8.8 mm/24 mm
Image Size	3:2 Aspect Ratio: 5472 × 3648 4:3 Aspect Ratio: 4864 × 3648 16:9 Aspect Ratio: 5472 × 3078
Still Image Resolution	4864 x 3648, 5472 x 3078, 5472 x 3648
Video Recorder Resolutions	1280 x 720 (720p), 1920 x 1080 (1080p), 2720 x 1530, 3840 x 2160 (2160p), 4096 x 2160

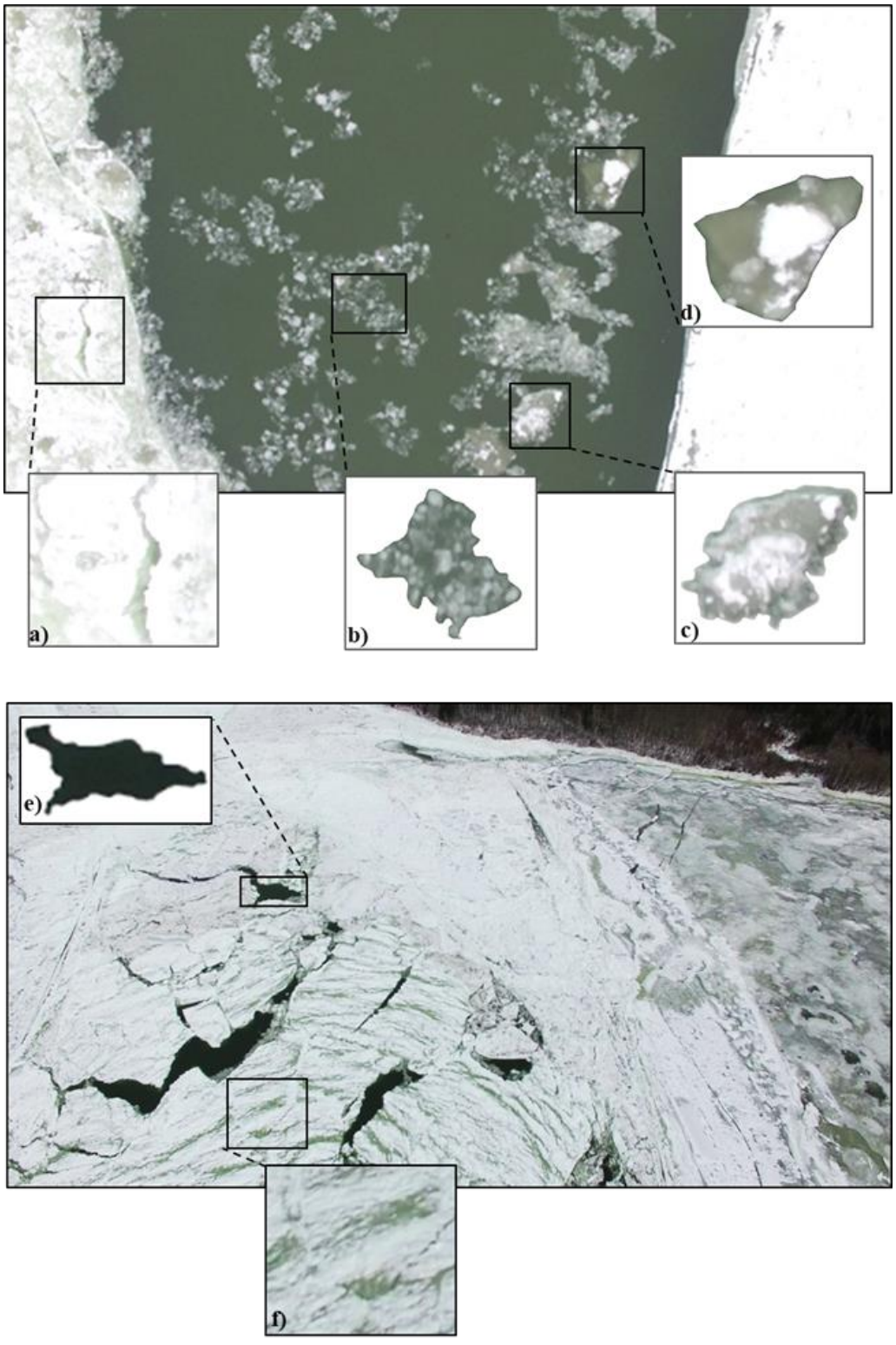

Figure 3-3 Comparison between six different classes defined for the IceMaskNet a) Border Ice; b) Frazil Slush; c)Frazil Pan; d)Broken Ice; e) Open Water; f) Ice Cover

3.1.2.3 IceMaskNET Algorithm framework

The developed automated river ice segmentation algorithm, illustrated in Figure 3-4, is based on a modified design of the Mask R-CNN framework. The collected aerial images were divided into three categories of training, validation, and testing. All three data sets were then labeled based on the six previously defined classes. As will be explained below, the original Mask R-CNN framework was improved for the river ice recognition task by changing the backbone structure of the framework. The annotated training and validation images were fed to the improved Mask R-CNN for the training and validation process, and the test images were used for statistical testing of the accuracy of the trained model. The resulting trained, validated, and tested model would be available to be used to recognize and classify river ice in images not previously seen by the model.

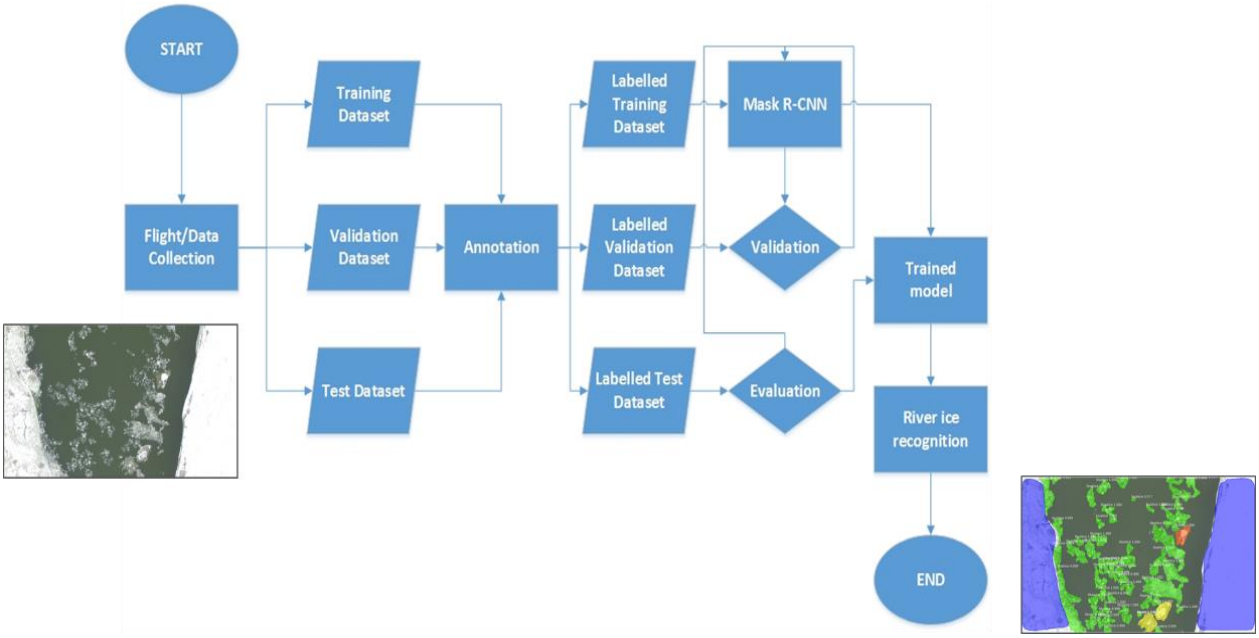

Figure 3-4 IceMaskNet algorithm pipeline for river ice recognition

Mask R-CNN

The Mask R-CNN algorithm is a Faster R-CNN based method with a third added output of an object mask. The added object mask in the Mask R-CNN is the class label, and the bounding box defining the specific region of the object mask enables more precise object detection and image segmentation (He *et al.*, 2017). The core of the Faster R-CNN includes two stages: specifying a Region Proposal Network (RPN), which involves defining rectangular "candidate box" regions within the image with identified features, and classification of the features within a candidate box

using Region of Interest Pool (RoIPool) and bounding box regression (He *et al.*, 2017; Ren *et al.*, 2017).

The Mask R-CNN framework consists of 5 different steps (He *et al.*, 2017): [i] a backbone convolutional neural network for feature extraction, i.e., Residual Learning Network (ResNet) [ii] improvement of the representation of different kinds of ice at various scales by object detection using the Feature Pyramid Networks (FPN) approach (Tsung-yi *et al.*, 2017), [iii] generation of regions of interests using Region Proposal Network (RPN), [iv] Region of Interest (RoI) classification and bounding box regression for improved accuracy, [v] RoIAlign for ice mask prediction with pixel-wise accuracy. A more detailed explanation of the framework is presented in the following section (Figure 3-5).

In Mask R-CNN, a mask of an object encodes the spatial distribution of the object in the image that is addressed by a pixel-to-pixel correspondence by convolutions. In each layer, the $m \times m$ mask preserves its spatial layout without collapsing to a single vector (He *et al.*, 2017). RoIAlign is used next in Mask R-CNN to extract a small feature map from each RoI. The RoI pooling layer in Fast R-CNN uses maximum pooling inside any region of interest to extract small feature maps with a size of $H \times W$. RoI maximum pooling involves quantization by dividing the $h \times w$ RoI window to $H \times W$ sub-windows of $h/H \times w/W$ size. After quantization the maximum pooling procedure is performed (Girshick, 2015). The quantization in RoI pooling could affect the pixel-wise accuracy of the mask prediction. In Mask R-CNN this problem is addressed by RoIAlign, which is a robust alignment of the extracted features without any quantization. A bilinear interpolation is utilized to compute the input features, which are then aggregated using a maximum

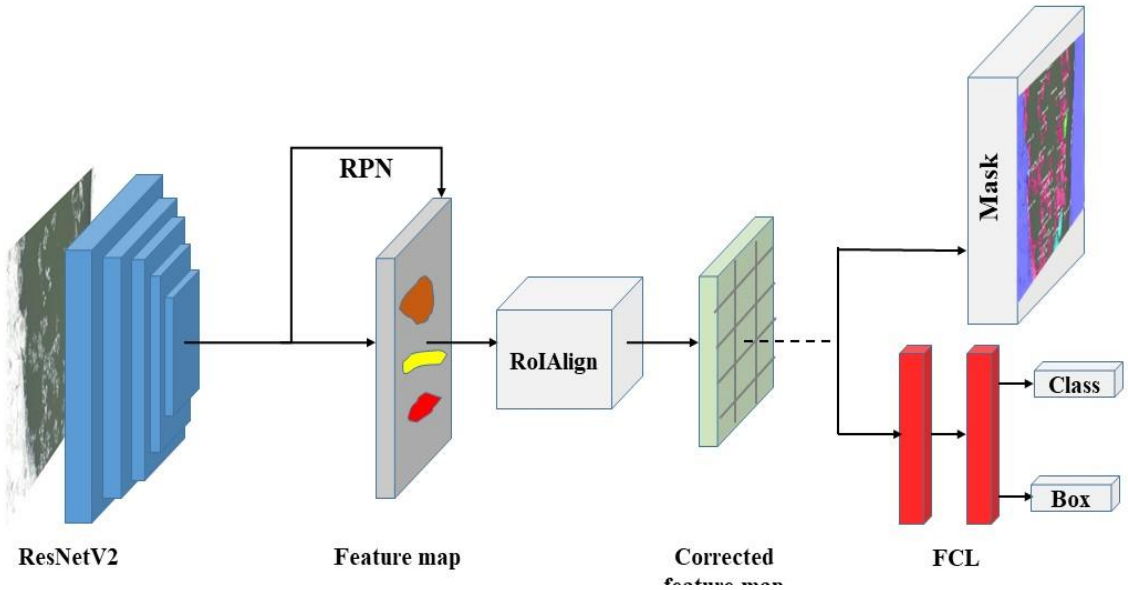

Figure 3-5 Mask R-CNN framework used for river ice recognition

or averaging procedure (He *et al.*, 2017). Figure 3-5 illustrates the Mask R-CNN framework used in the IceMaskNet algorithm for river ice detection and characterization.

Improved Mask R-CNN

The Mask R-CNN framework originally employed a Residual Learning Network with 101 layers, ResNet101, as the backbone network structure of the framework for feature extraction. ResNet101 with 101 layers is too deep for river ice characterization. Hence to enhance the detection accuracy and training speed of the developed algorithm for river ice characterization, Mask R-CNN was modified by utilizing the ResNetV2 with 50 layers as the backbone architecture. In ResNetV2, the residual connection of the network was improved by the addition of a Batch Normalization (BN) and ReLU (Rectified Linear Units), prior to the activation of the convolution (He *et al.*, 2016). This is illustrated in Figure 3-6. These modifications further improved the generalization performance of the framework.

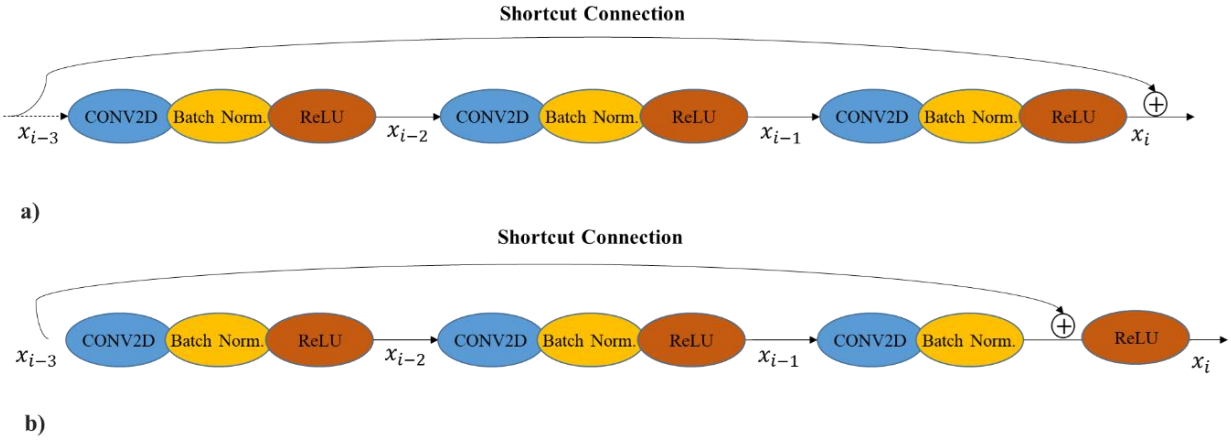

Figure 3-6 ResNet backbone structure, a) ResNet structure used originally in the Mask R-CNN b) ResNetV2 structure used in IceMaskNet

3.1.2.4 Application

The Mask R-CNN convolutional neural network used for river ice segmentation was implemented on Keras, an open-source neural network library in Python, (Chollet, 2015) and Tensorflow, an open-source software library for dataflow and differentiable programming (Abadi, et al., 2015). The river ice aerial imagery training was conducted on a pre-trained model based on the COCO (Common Objects in Context) dataset (Lin *et al.*, 2014). For an easier model optimization and to achieve optimal GPU (Graphical Processing Unit) performance, the NVDashboard (RAPIDS,

2019), an interactive real-time visualization tool built with JupyterLab (Kluyver et al. 2016) and Bokeh server (Bokeh Developement Team, 2018) was utilized. Training was conducted on a GPU empowered unit with the characteristics detailed in Table 3-2.

Table 3-2 Characteristics of the machine used for training

CPU	Intel(R) Core(TM) i7K 8700K (6-Core/12-Thread, 12MB Cache, up to 4.7GHz
Memory	32GB Dual Channel DDR4 at 2666MHz (2X16GB) (370-ADUD)
GPU	NVIDIA(R) GeForce(R) GTX 1080 Ti with 11GB GDDR5X (490-BEDE)
Hard Disk	256GB M.2 PCIe Solid State Drive (400-AVIX)

To reduce the number of labeled images and to increase the model generalization, data augmentation techniques of random flips were utilized to increase the variety of the training data. To observe and optimize the model prior to its application, the model was trained for 100 epochs to achieve a full learning curve. Figure 3-7 illustrates the results of the optimization process. The class (Figure 3-7a) and mask (Figure 3-7b) training and validation procedure results indicate that the training and validation losses both decrease until they reach their lowest at the 27th epoch. Both the training and validation loss calculations were performed using the methodologies introduced in He et. al., 2017 and Girshick et. al., 2015. The training and validation loss shown in Figure 3-7a and b show that the training stops at the 27th epoch, and the model starts to memorize rather than to learn. In other words, after the 27th epoch, the model begins overfitting. Therefore the Mask R-CNN trained for 27 epochs should be selected. There are two reasons for the convergence of the model at the 27th epoch. The first is the small number of images used for training, and the second reason is due to conducting the training process on a pre-trained weighted model. The optimized model was employed for river ice segmentation to the six different classes used for this study.

3.1.2.5 Performance assessment

The test data set was used to evaluate the results separately for detection and segmentation accuracy and also for each one of the six defined classes. The detection performance of the algorithm was tested using the Precision-Recall (PR) curve, which yielded the mean average

precision (mAP). Mean average precision is the area under the Precision-Recall curve and utilized to quantify detection accuracy (Girshick, 2015). Precision (P) and recall (R) are defined based on the following equations:

$$P = \frac{TP}{TP + FP} \tag{3-1}$$

$$R = \frac{TP}{TP + FN} \tag{3-2}$$

Where P is the prediction accuracy rate and R is the recall rate; TP, true positive, is the correct number of pixels classified correctly; FP, false positive, is the number of pixels classified that does not exist; and FN, false negative, is the number of pixels classified incorrectly.

The Jaccard Index (JI), also known as Intersection over Union (IoU), is another evaluation index (Jaccord, 1908). IoU evaluates the performance of the network by the comparison of the overlap degree between the ground truth and prediction. In other words, the Jaccard Index measures the intersection over the union of the labeled segments and the missed values for each class (Csurka *et al.,* 2013). In this study, multi-class segmentation is conducted; hence, the mean of the IoU or (MIoU) is defined as:

$$MIoU = \frac{1}{k+1}\sum_{i=1}^{k}\frac{p_{ii}}{\sum_{j=0}^{k} p_{ij} + \sum_{j=0}^{k} p_{ji} - p_{ii}} \tag{3-3}$$

where k is the total number of classes in the model, p_{ij} is the number of pixels that belong to class i, but classified as category j; p_{ii} is the number of pixels in category i correctly classified, and p_{ji} are misjudged pixels. The MIoU is used as a metric for mask accuracy, which represents the accuracy of the classification into different ice types.

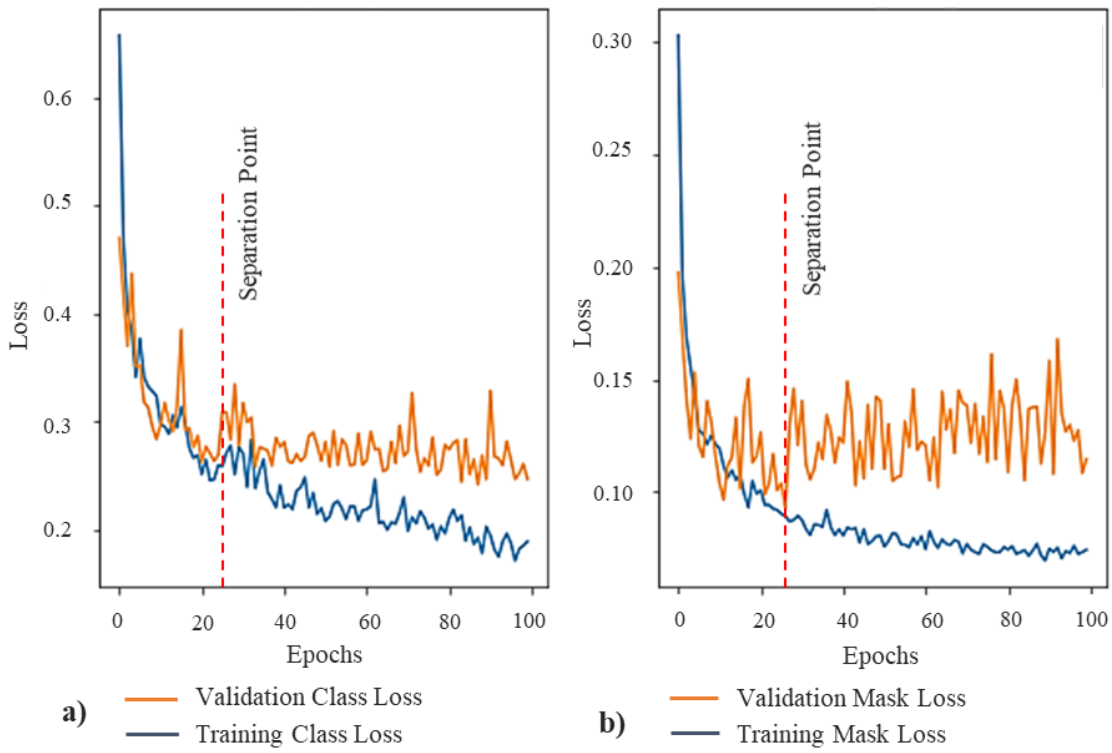

Figure 3-7 Mask R-CNN optimization process; a) Class loss; b) Mask loss

3.1.3 Results and discussion

3.1.3.1 Qualitative performance assessment

Sample results of the river ice recognition algorithm applied to aerial RPAS imagery are shown in Figure 3-8 and 9. The set of images in the left column (Figure 3-8 a, c, e & g; Figure 3-9a &c) show the original images, and the column on the right (Figure 3-8 b, d, f & h; (Figure 3-8 b & d) shows the predicted classified results. It can be seen that the developed algorithm was able to detect, segment, and classify open water and five different classes of river ice (in total, six defined classes in river imagery). The first row images (Figure 3-8 a & b) show downward looking footage from an early stage of river ice processes. In this figure, along with the border ice on the river banks, frazil slush, broken ice sheets, and frazil ice pans were detected. The other three rows of the images show other sections of the river where the river ice cover has formed and ice categories recognized in this set include: border ice, ice cover, frazil slush, and open water. It should be mentioned that while in the first row image set, the water has not been defined as a target class; in the other set where the ice concentration is higher, the open water is of interest for recognition.

The second set of sample images shown in Figure 3-9 focuses on the application of IceMaskNet on oblique aerial imagery. It should be mentioned that in images with higher oblique angle we have defined a region of interest (RoI) for annotation which excludes around 12 percent from the top of the image, this was considered to reduce the annotation imposed error to the model as it is much difficult to differentiate between different types of ice in a further distance.

IceMaskNet can operate fast enough to be used as an instant segmentation tool for online processing of drone imagery. The average speed of the analysis is eight frames per second. Results also show that despite being presented images with various field of view angles and different illumination and shade conditions in the RPAS footage, the model was able to perform the river ice recognition task accurately. This indicates that there is no need for image quality enhancements, even with the observed noise or poor quality images. The presented highly generalized algorithm is also able to accurately detect and classify same class objects (river ice) with a different texture, position, orientation, and location. An excellent example of this is the recognition of the two classes of border ice and ice cover; although these two classes often share similar texture characteristics (Figure 3-3 a & f) and are located close to each other, they can accurately be recognized in the images using the IceMaskNet. It should also be mentioned that in this version of the IceMaskNet we have not considered classes such as “snow on ice” or “water on ice” that can be used for studying different conditions of river ice, these classes can be consider for a further enhancement of the algorithm.

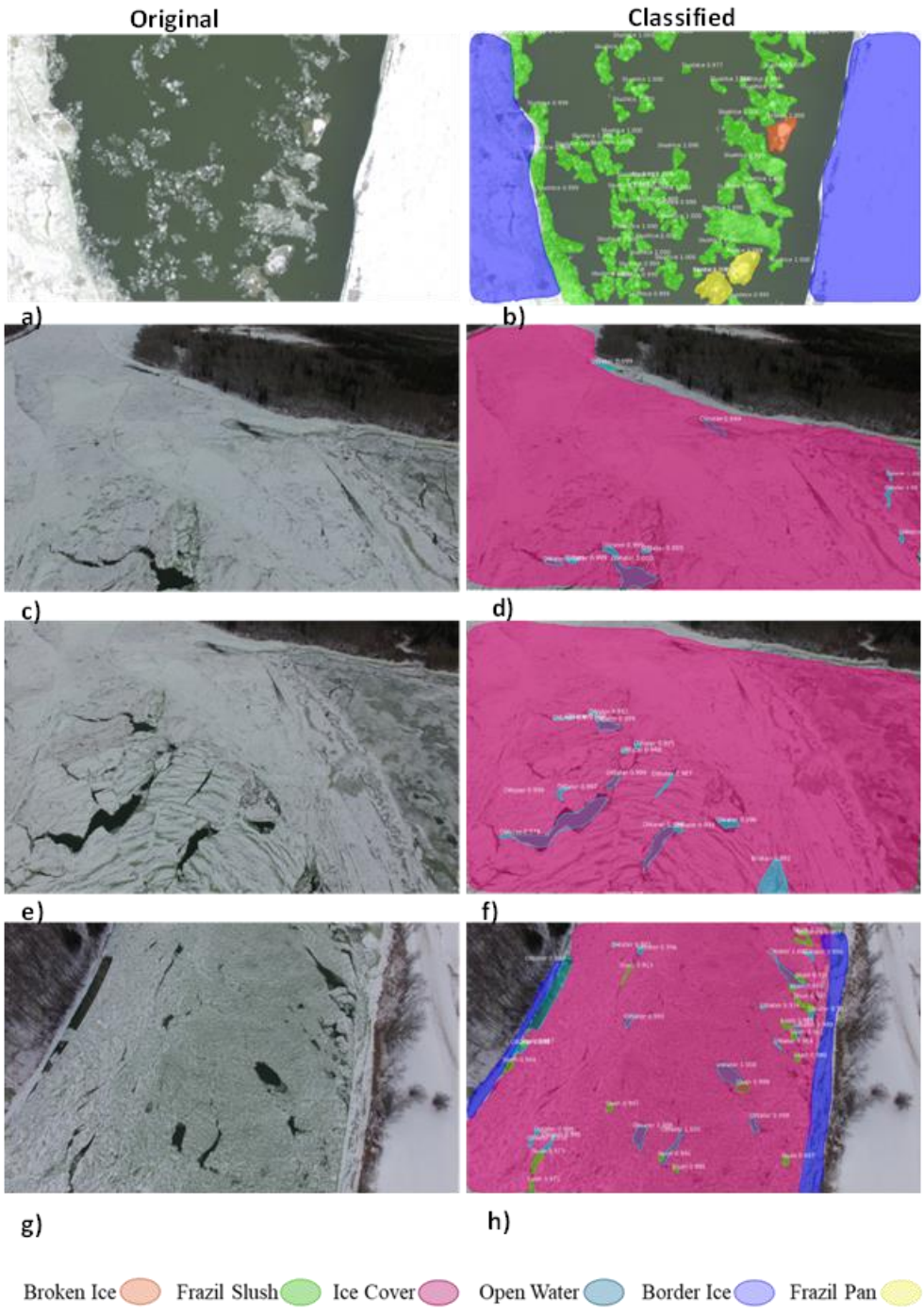

Figure 3-8 Sample results of the IceMaskNet river ice recognition algorithm

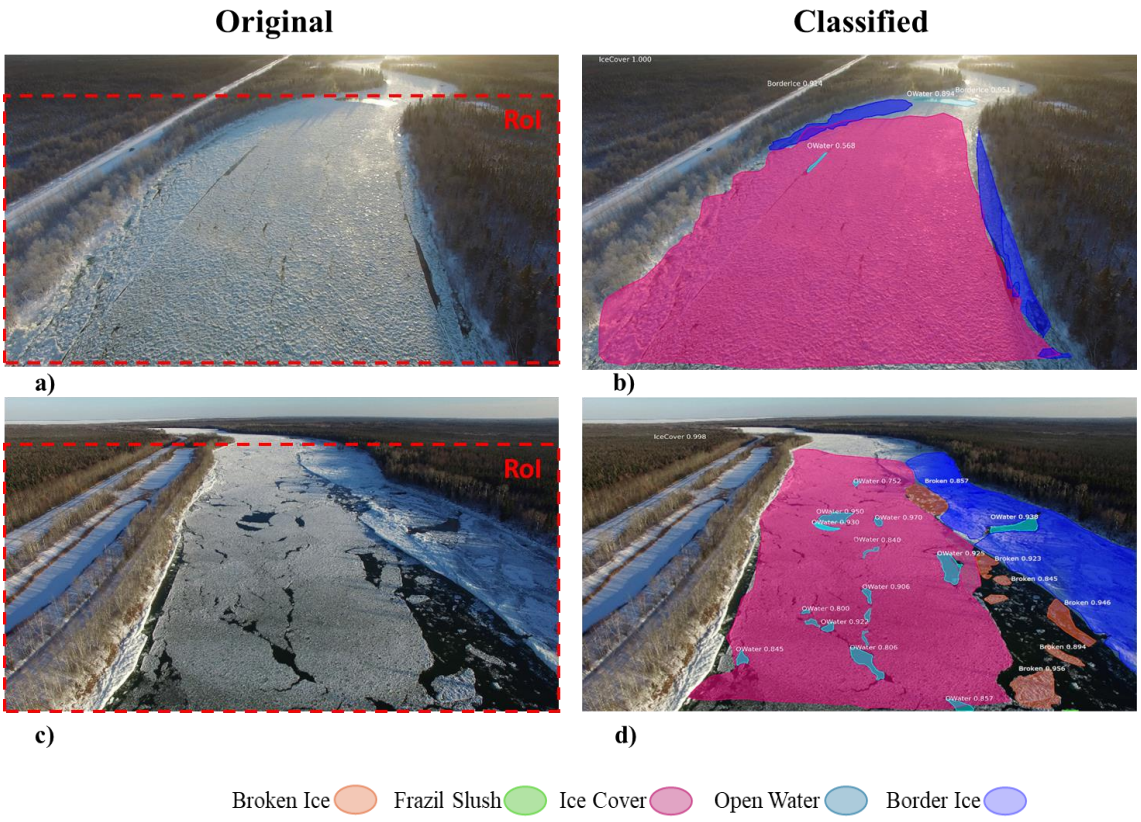

Figure 3-9 Sample results of the IceMaskNet river ice recognition algorithm applied on oblique aerial imagery

3.1.3.2 Quantitative performance assessment

Based on the evaluation parameters mentioned in section 2.5, the average pixel accuracy of the detection and segmentation is 95 and 91 percent, respectively. Table 3-3 shows the confusion matrix over all defined classes and the respective model sensitivity to detect each class. Detailed evaluation for each one of the defined classes is presented in Table 3-4. Results show that the broken ice class has the highest detection rate and mask accuracy, while the ice cover class has the lowest detection accuracy. This is also observable from the sample results presented in Figure 3-8 and 9. The main reasons for these types of errors are the smaller number of labeled images for training and possible inconsistencies in the labeling annotation task. Although all the images have been annotated by experienced people in the field, the annotation task can be challenging, especially when the object is further away in the field of view of the camera.

Table 3-3 IceMaskNet accuracy assessment through confusion matrix

	Broken Ice	Frazil Slush	Ice Cover	Open Water	Border Ice	Frazil Pan
Broken Ice	97.20	1.30	0.00	0.00	0.00	1.50
Frazil Slush	0.90	95.80	0.00	1.80	0.00	1.40
Ice Cover	0.50	1.00	92.70	1.80	4.00	0.00
Open Water	0.00	1.70	1.20	94.70	1.90	0.50
Border Ice	0.00	0.00	5.90	0.00	94.10	1.10
Frazil Pan	1.40	0.20	0.20	1.70	0.00	96.50

Table 3-4 Performance of the IceMaskNet for river ice recognition

Classes	Broken Ice	Frazil Slush	Ice Cover	Open Water	Border Ice	Frazil Pan	Mean
Detection Accuracy (%)	*97.22*	*95.85*	*92.73*	*94.68*	*94.13*	*96.46*	*95.18*
Mask Accuracy (%)	*94.30*	*90.20*	*87.34*	*92.87*	*89.02*	*92.57*	*91.05*

In order to further verify the reliability of the trained model and the annotated data used for training and testing 5 fold cross validation was used. The annotated images were divided into 5 subsets one for each of the 5 subsets as a test set. Results of this cross validation is shown in Table 3-5.

Table 3-5 Results of 5-fold cross validation trials (%)

Models	Fold 1	Fold 2	Fold 3	Fold 4	Fold 5	Average
Model 1	94.87	95.54	95.64	95.78	94.9	95.35
Model 2	95.84	95.1	96.05	95.25	94.54	95.36
Model 3	95.31	95.38	94.01	95.61	95.48	95.16
Model 4	95.51	95.61	95.43	95.43	95.23	95.44
Model 5	95.29	94.87	95.64	95.19	94.35	95.07

3.1.4 Conclusions

Close-range photogrammetry is becoming an attractive data acquisition option as a result of continuous advances in computer vision, and increasing availability of low-cost photogrammetry devices. The use of aerial imagery has recently gained traction with the advent of small RPAS in earth science and engineering. This study presented IceMaskNet, a robust real-time river ice detection, and characterization algorithm. IceMaskNet was developed based on an improved version of a high accuracy instance segmentation algorithm, the Mask R-CNN. The proposed algorithm can perform fast and high accuracy river ice recognition into the classes of open water, broken ice, frazil pan, frazil slush, border ice, and ice cover. IceMaskNet approached a detection accuracy of 95 percent and a segmentation accuracy of 91 percent. The developed algorithm can be used to extract river ice concentrations for different river ice classes using aerial photogrammetry. The extracted results can then be used in river ice studies, to improve numerical model accuracy or in hazard prevention.

3.2 River Ice Detection and Characterization Using Oblique Shore-based Photography

Preprint of an article submitted to Cold Regions Science and Technology © ELSEVIER

3.2.1 Introduction

River ice constitutes a vital element of the cryosphere, substantially affecting global hydrological systems, particularly in the Northern Hemisphere, where it influences 58% of total river length through seasonal ice cover (Bennett & Prowse, 2010; Prowse *et al.,* 2007). This ice presence significantly alters flow properties (e.g., Zare *et al.,* 2015; Ghareh Aghaji Zare *et al.,* 2016), river chemistry and biology (Prowse *et al.,* 2006, 2007), water quality (Prowse *et al.,* 2001; Hosseini *et al.,* 2017), and river morphology as well as fish habitats (Prowse & Culp, 2003; Huusko *et al.,* 2007; Hosseini *et al.,* 2017; Hu *et al.,* 2022). Despite the extensive body of research on river ice processes in large rivers (Beltaos, 2012), our understanding of this phenomenon continues to evolve.

River ice formation typically begins with the production of frazil ice, primarily in fast-flowing sections, or stationary ice that often forms in slower regions of the river, such as along riverbanks (Beltaos, 2013). In turbulent, super-cooled open water locations, frazil ice crystals form. As frazil ice crystals grow and adhere, they clump together to form floating frazil flocs that rise to the water's surface, creating slush ice. Prolonged exposure of frazil slush to cold weather solidifies it into ice pans through thermal growth. Floating ice pans can merge to form larger ice rafts, while the accumulation of floating ice creates brash ice (Beltaos, 2013). Ice cover refers to a substantial amount of ice on a water surface expanse and can be unconsolidated or stable. Unconsolidated ice often originates from brash ice and remains loose and floating. Stable ice cover is formed from the packing and freezing of various types of river ice (Beltaos, 2013). Narrow, constricted, and slow-flowing river sections can facilitate ice cover formation (Beltaos, 2013).

Understanding river ice processes and its various direct and indirect impacts requires rigorous, long-term and continuous monitoring and data collection. Ice monitoring techniques include in situ measurements, remote sensing and visual observations or close-range remote sensing (e.g. Bourgault *et al.,* 2008; Mermoz *et al.,* 2013; Zare *et al.,* 2013; Duguay *et al.,* 2015; Ansari *et al.,* 2017; Ghobrial and Lowewen, 2021; Ansari *et al.,* 2021). In situ measurements can be challenging, costly, and potentially dangerous, especially during freeze-up and break-up stages. Remote sensing measurements serve as an alternative data collection method, but acquiring satellite images and their analysis can also be costly, with lower resolution suitable only for larger-scale projects

(Mermoz *et al.,* 2013; Ansari *et al.,* 2017). Visual ice observations comprise marine, aerial, and terrestrial types, each offering a different observer perspective (MANICE 2005). Close-range remote sensing has been employed as a qualitative approach to investigate ice conditions (MANICE 2005). Recent advances in photogrammetry technology and computer vision techniques have made quantitative data collection possible (Bourgault *et al.,* 2008; Ansari, 2016; Ansari *et al.,* 2017; Ansari *et al.,* 2021; Simoes and Clark, 2019). As an initial effort in this research area, Ansari et al. 2017 introduced an image processing-based pipeline coded in Matlab to detect and quantify river ice using oblique shore-based imagery systems. The ice detection subroutine of the developed pipeline was expensive to run and incapable of detecting various ice types. The first algorithm to detect two different kinds of ice was developed by Kalke and Loewen (2018). They utilized Support Vector Machines (SVM) to detect and classify released broken pieces of anchor ice and frazil ice pans. In another attempt Ansari et al (2019) utilized a machine learning approach based on a fast superpixel segmentation algorithm for river ice segmentation using terrestrial photogrammetry. Recent advancements in deep learning helped further progress of river ice segmentation algorithms. Singh *et al.,* (2019) utilized different deep learning algorithms to detect two types of river ice using a downward looking camera. In continuation of Singh et al. (2019), Sola and Scott (2022) introduced an efficient shallow network for river ice segmentation for same downward looking camera image set. Ansari *et al.,* (2021) developed deep learning based methodology to detect and classify five different river ice type from aerial photography. Zhang *et al.,* (2021 and 2022) designed a deep learning based multilevel feature fusion framework to develop a semantic river ice segmentation algorithm using aerial photogrammetry.

In the past, research has predominantly focused on employing nadir angle imagery, such as images from cameras mounted on bridges (e.g., Kalke *et al.,* 2018; Sola and Scott, 2022) or aerial drone imagery (Zhang *et al.,* 2020; Ansari *et al.,* 2020 & 2021), for developing ice classification algorithms. While this approach has proven useful, it is insufficient for long-term monitoring of surface river ice detection and concentration quantification, particularly during the freeze-up period. To address this limitation, Ansari *et al.,* 2019 developed a machine learning algorithm to leverage a fast superpixel segmentation algorithm to detect and classify river ice from oblique shore-based images. Although this algorithm produced satisfactory results, it was computationally intensive. In a more recent study, Pei et al. (2023) investigated the use of oblique river surface images captured at extended focal lengths and processed using deep learning algorithms. Pei et al. (2023) developed a hybrid image processing algorithm comprising several stages, including image classification, rectification, segmentation, and extraction of river ice properties, to compute surface ice concentrations, as well as ice pan size and shape properties. The algorithm contained separate

sections for ice cover image detection and ice pan image detection. For the former, a thresholding algorithm coupled with morphological operations was employed while for the latter, a trained UNet model based on a dataset of nadir images with two different classes was used. In this methodology, the images are orthorectified to a bird's eye view, before they are passed through a trained ice pan detection UNet model for pan ice detection and classification. Overall, the findings of Pei *et al.,* (2023) study demonstrate the potential of using oblique images of river surfaces for long-term monitoring of surface ice conditions, and the development of the algorithm represents an important step forward in this area of research. Pei et al. (2023) developed an approach that is based on a UNet model trained on annotated nadir imagery, but the method requires orthorectification of each image prior to performing detection. As a result, this approach may be computationally expensive, and the algorithm is limited to detecting and classifying only three different ice classes: "slushy pan," "crusty pan," and "no ice." In contrast, the present study proposes a new approach that uses annotated shore-based imagery, which enables the algorithm to detect and classify river ice without the need for prior orthorectification. Nevertheless, orthorectification remains an essential component of the algorithm for delivering quantifiable results. In this approach orthorectification is applied to select images which represent a subset of the image dataset. Once the rectification matrix is determined, it is utilized to access various detected categories of river ice. The presented algorithm is trained based on the shore-based imagery and has the potential to decrease computational expenses and broaden the scope of detectable ice classifications beyond three kinds previously identified by Pei et al. This article uses a four-year (2015-2019) field monitoring effort on the Dauphin River, using close-range remote sensing methods.

3.2.2 Methodology

3.2.2.1 Study area

The study was conducted on the Dauphin River located in central Manitoba, 250 km north of Winnipeg (Figure 3-10). The Dauphin River discharges from Lake St. Martin to Lake Winnipeg, in a lake-river system, i.e., Lake Manitoba – Fairford River – Lake St. Martin – Dauphin River – Lake Winnipeg (Figure 3-10). Dauphin River is approximately 52 km long with an approximate gross drainage basin area of 82,300 km2 (Water Survey of Canada, 2021). The Dauphin River is characterized with a mild average slope of 0.00029 for the first 40 km and an abrupt slope increase to 0.0016 in the final 11.2 km to Lake Winnipeg (Clark and Wall 2016). Average river discharge during freeze-up is about 100 m3/s with a river width range of 110 to 160 m. The upper section of the river features multiple winding channels and a broader top width accompanied by low-lying banks, while in contrast, the lower section is considerably more linear and possesses steeper banks

(Clark and Wall 2016). Due to the steeper slope in the lower section, the open water velocity in specific regions surpasses 1.5 meters per second (Wazney et. al., 2018). In the lower section of the river, the turbulent and fast-flowing water has the capacity to generate significant amounts of frazil ice during the freeze-up period. Historically, this phenomenon has resulted in the development of hanging ice-dam at the outlet to Lake Winnipeg, where the frazil ice accumulates beneath the lake's thermal ice cover (KGS Group and North/South Consultants, 2014, Wazney *et al.*, 2018).

This study is part of a comprehensive investigation for better understanding of dynamic river ice processes in Dauphin River. River ice investigations in the Dauphin River were initiated in 2015 comprising various long- and short-term monitoring and data collection campaigns, including installation of pressure loggers, acoustic instruments, and close-range remote sensing – using both shore-based and aerial imagery.

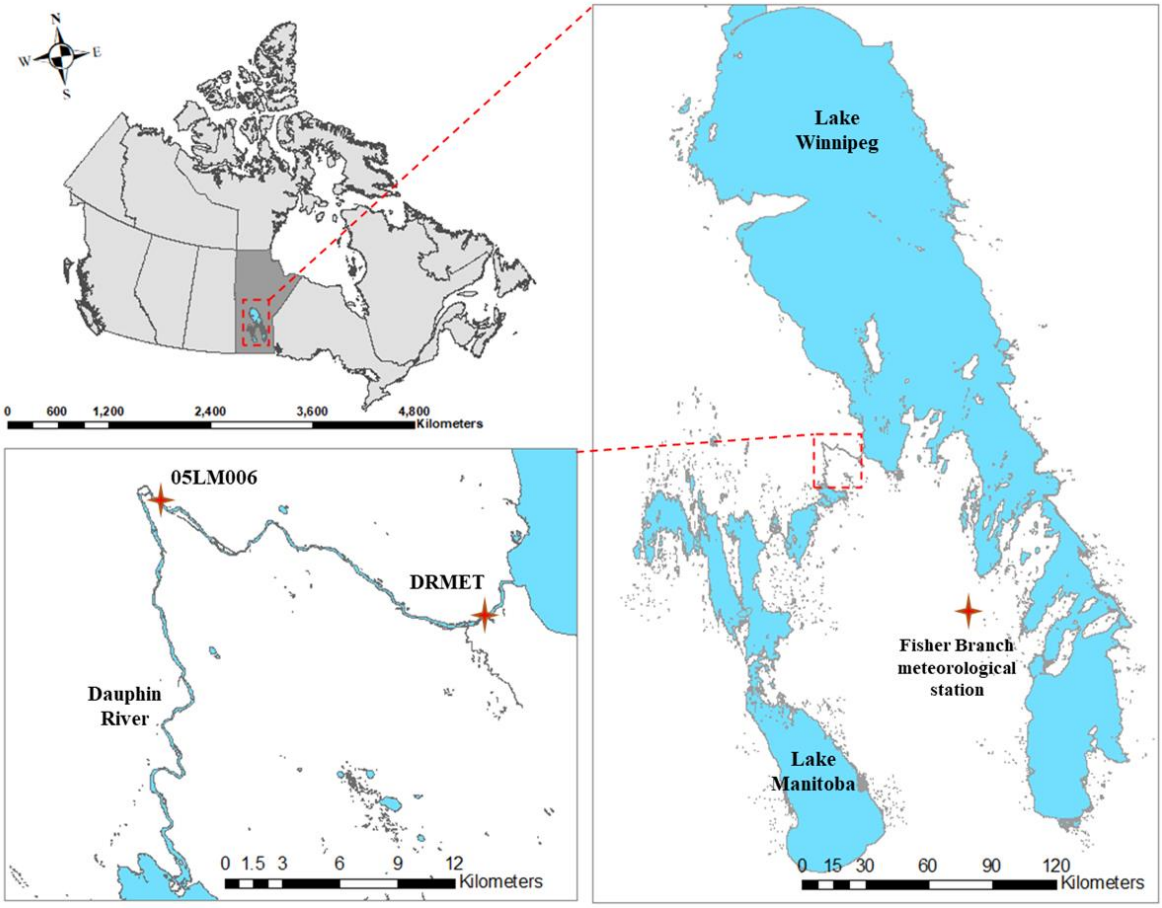

Figure 3-10. Study area map. Dauphin River, the Fisher branch Meteorological station and Water Survey Canada gauge 05LM006

3.2.2.2 Data

In this investigation, a database comprising oblique, shore-based images was utilized, which were obtained from trail cameras stationed for long-term winter surveillance of fluvial ice phenomena. These cameras were mounted on tree trunks at various sites on the left bank (north side) of the river, primarily to conduct a qualitative examination of ice conditions during freeze-up and breakup phases. Figure 3-11 illustrates the Dauphin River research area and the camera locations. In a prior study, Wazney et al. (2018) observed compelling dynamic ice processes, especially during the freeze-up stage, which encouraged the adoption of oblique imagery from trail cameras for quantitative evaluation in the present study. To ensure consistent data acquisition during crucial freeze-up and breakup phases, the cameras were maintained twice per winter season. Nonetheless, unforeseen field circumstances resulted in the loss of some data at certain locations. Table 3-6 presents a summary of the site coordinates for close-range sensing, as well as the monitoring duration and the number of images used in this investigation. The cameras utilized in this study were Moultrie Digital Game Cameras, equipped with an onboard memory card for data gathering. Data collection frequency summarized in Table 3-6 varied due to the objectives of other concurrent projects. Figure 3-12 shows the riverbed profile of the Lower Dauphin River, the open water profile (discharge=200 m^3/s), and the camera locations utilized in this study. The camera at DRLL04 is situated in a section with an estimated slope of 0.0025 and a river width of 100 meters, suggesting a relatively fast flowing segment of the river. The DRLL05 camera is positioned in a river section with an approximate slope of 0.0022 and a width of 157 meters, indicating that while not as steep and narrow as DRLL04, DRLL05 remains a fast-flowing portion of the river. DRLL06 is found at the end of one sharp slope and the beginning of another, with a relative slope and river width of 0.0034 and 134 meters, respectively. Cameras at DRLL06a and DRLL06b are situated in areas with mild slopes and river widths of 345 meters for DRLL06a and 108 meters for DRLL06b, which is located at a narrowing. The DRLL07 camera is placed in a river section with a slope of 0.0016 and a width of 208 meters, and an island can be seen in the right corner of the image from this location. Cameras at DRLL08 and DRLL08a are in close proximity to the mouth of Lake Winnipeg, with a river slope of 0.0023 at both locations and a shared river width of 146 meters. Despite the relatively steep slope at DRLL08 and 08a, the water surface slope is quite mild due to the backwater effect caused by Lake Winnipeg. Finally, the DRLL10 camera is located at the mouth of Lake Winnipeg, with a river width of 108 meters and nearly horizontal water surface slope.

Meteorological data for this study were obtained from two sources: the DRMET meteorological station and the Environment Canada station situated at Fisher Branch, which is

approximately 100 km from the Lower Dauphin River (refer to Figure 3-10). Generally, the air temperature measurements at Fisher Branch corresponded well with those recorded at DRMET (Wazney *et al.*, 2018). Air temperatures during the winter seasons from 2015-2016 to 2018-2019 are depicted in Figure 3-13. The average air temperatures during the freeze-up period (defined as the month of December in this study) were -8.21°C, -14.24°C, -15.7°C, and -11.6°C, respectively, for these four winters, respectively. For this investigation, river discharge data were acquired from an Environment and Climate Change Canada discharge and water level gauge situated at Dauphin River (Gauge 05LM006). This station is positioned approximately 25 km upstream of Lake Winnipeg (see Figure 3-10). Figure 3-14 displays the daily average measured discharge at station 05LM006. It is evident that the 2018-2019 season had notably lower discharge compared to the other years under analysis.

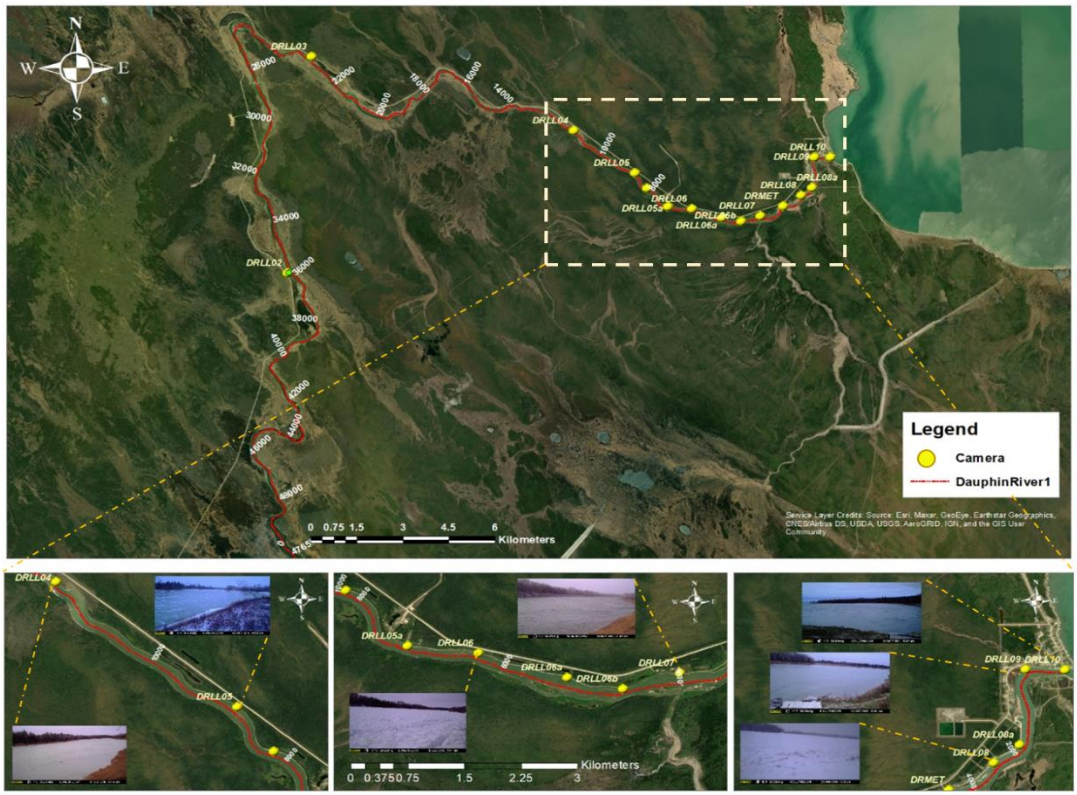

Figure 3-11 Camera locations along the Dauphin River along with sample oblique imagery acquired from trail cameras

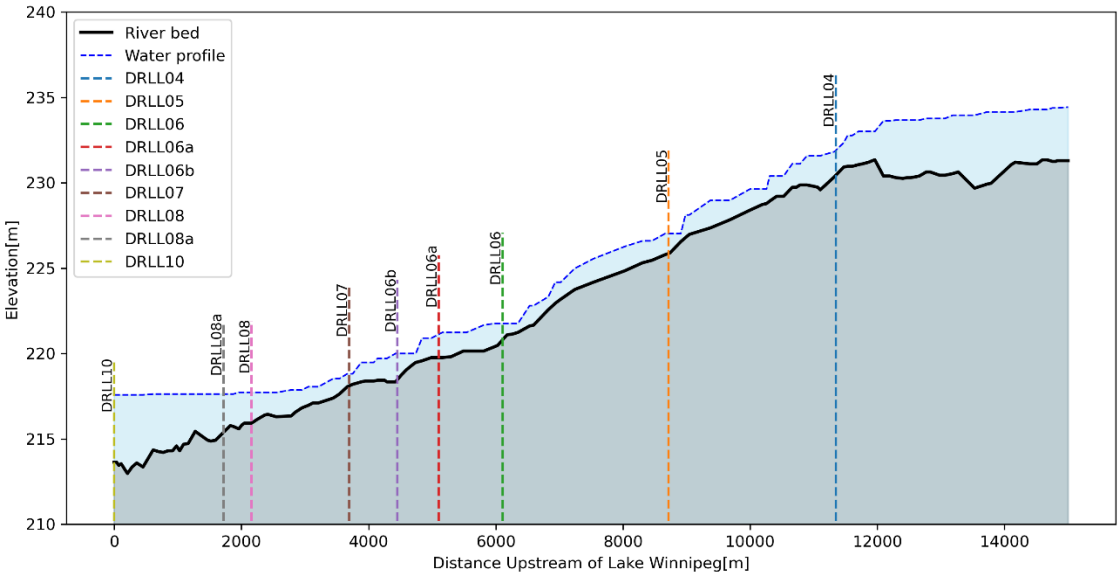

Figure 3-12 Lower Dauphin River bathymetry along with open water profile and camera locations

Table 3-6 Close-range remote sensing sites and image availability along the Dauphin River– Letters after numbers represent duration of the imagery in months (JA: January; MR: March; AP: April; MY: May; JN: June; OC: October; NV: November; DE: December;)

Year 2015-16			Year 2016-17			Year 2017-18			Year 2018-19		
DRLL04	555 NV-JA	60 min	DRLL03	2404 NV-JN	60 min	DRLL03	[3512 NV-DE][1802 AP]	5 min	DRLL03	3996 MR-MY	15 min
DRLL05	2394 NV-MA	60 min	DRLL04	[8766 DE] [4285 MR-AP]	[3 min] [15min]	DRLL04	4448 AP	5 min	DRLL05	1718 OC-NV	15 min
DRLL06	445 NV-DE	60 min	DRLL06	[577 MR] [444 NV-DE]	[15 min] [60 min]	DRLL05	[782 OC-NV] [6104 NV-DE] [7065 AP-MY]	[15 min] [5min]	DRLL07	1487 OC-NV	15 min
DRLL08	677 NV-JA	60 min				DRLL06	19042 OC-MY	5 min			
DRLL10	717 NV-JA	60 min				DRLL06a	15922 OC-NV + AP	15 min			
						DRLL06b	9490 OC-AP	[60 min] [15min]			
						DRLL07	10939 OC-MY	15 min			
						DRLL08	9298 NV-MY	15 min			
						DRLL08a	9029 OC-MY	15 min			

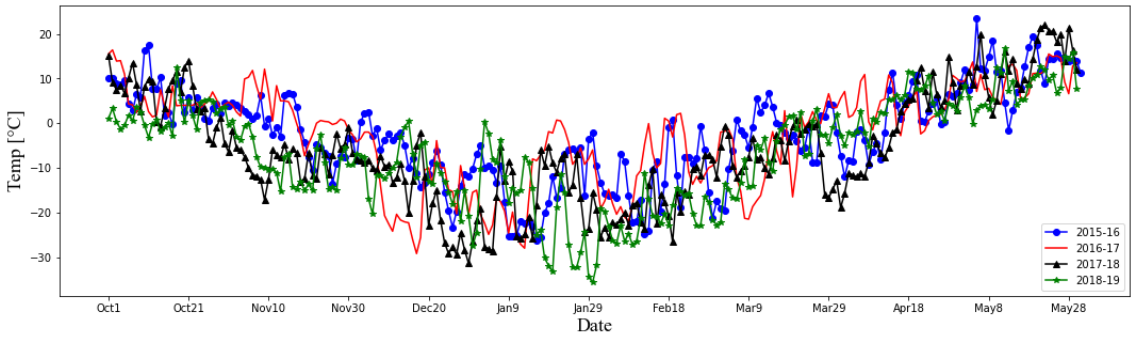

Figure 3-13 Air temperatures during the four analyzed winters (2015-2019)

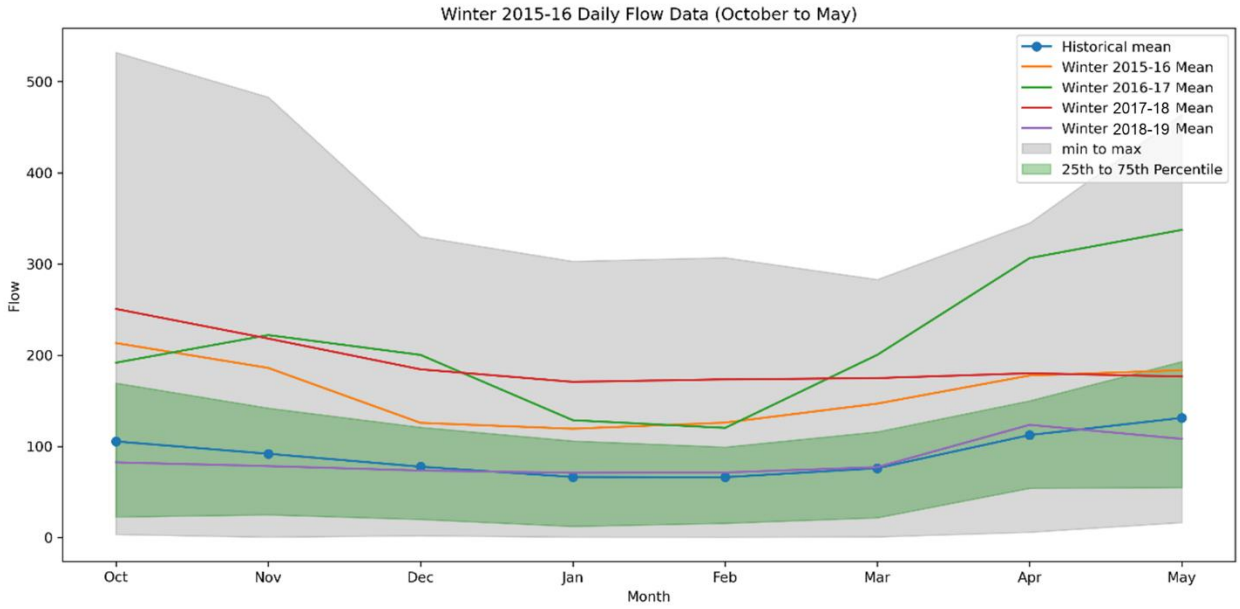

Figure 3-14 Discharge records for four analyzed winters (2015-2019) measured at Environment and Climate Change Canada gauge station 05LM006

The oblique shore-based image dataset was obtained at different locations across the river and over the course of four distinct winters and comprises 125,898 images. From these, a total of 1,795 images, captured using various cameras and spanning different years, were annotated using a manual annotation software i.e. “VGG-Image annotator” (Dutta and Zisserman 2019) Figure 3-15 shows sample annotated images. The annotated images were employed for training, validation, and testing purposes. The dataset was partitioned, with 80% allocated for training and the

remaining 20% for validation and testing. The oblique shore-based dataset enables the identification of four distinct river ice types and open water, which were annotated accordingly: "BorderIce" for border ice, "IceCover" for complete ice cover, "FrazilSlush" for frazil slush, "Ice" for frazil pan and surface collar ice (i.e. surface ice formed around a rock in shallow regions), and "OWater" for open water. The various ice classes are demonstrated in Figure 3-16. Border ice, characterized by a smooth uniform surface, forms along river banks (Figure 3-16c, e and i). Frazil slush displays a heterogeneous texture interspersed with water (Figure 3-16a). Open water exhibits a smoother texture compared to ice cover (Figure 3-16f and h). The ice cover class encompasses images of fully formed ice cover, which shares a similar texture with border ice but differs in shape and size (Figure 3-16c). Frazil pans, are characterized by their rounded boundaries and float on the water surface (Figure 3-16b). It is essential to highlight that annotating this specific ice class in the available dataset was quite challenging, particularly when the river surface was densely covered with frazil slush ice. Therefore, in instances where the river surface exhibited a high density of frazil slush along with some dispersed frazil pans that were difficult to distinguish between the two different classes, the entire scene was annotated as frazil slush. Surface collar ice, also labeled as “Ice” is thermal ice formation around objects (e.g. rocks) (Figure 3-16g). Separating surface collar ice as a separate class caused lower segmentation accuracy and thus was labeled as “Ice” similar to frazil pan.

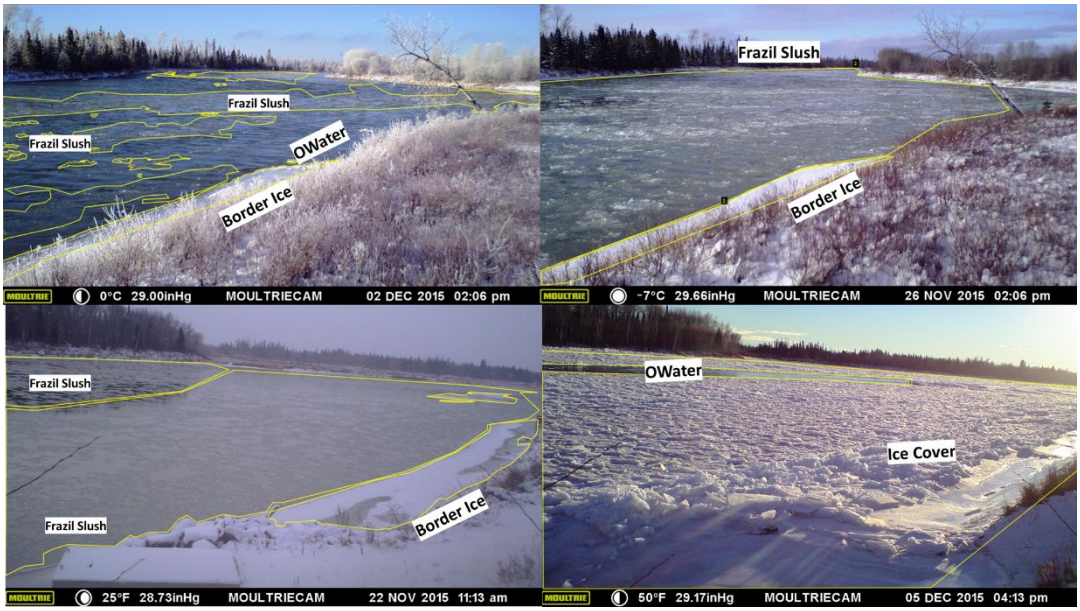

Figure 3-15 Sample manually annotated images using VGG-Via software

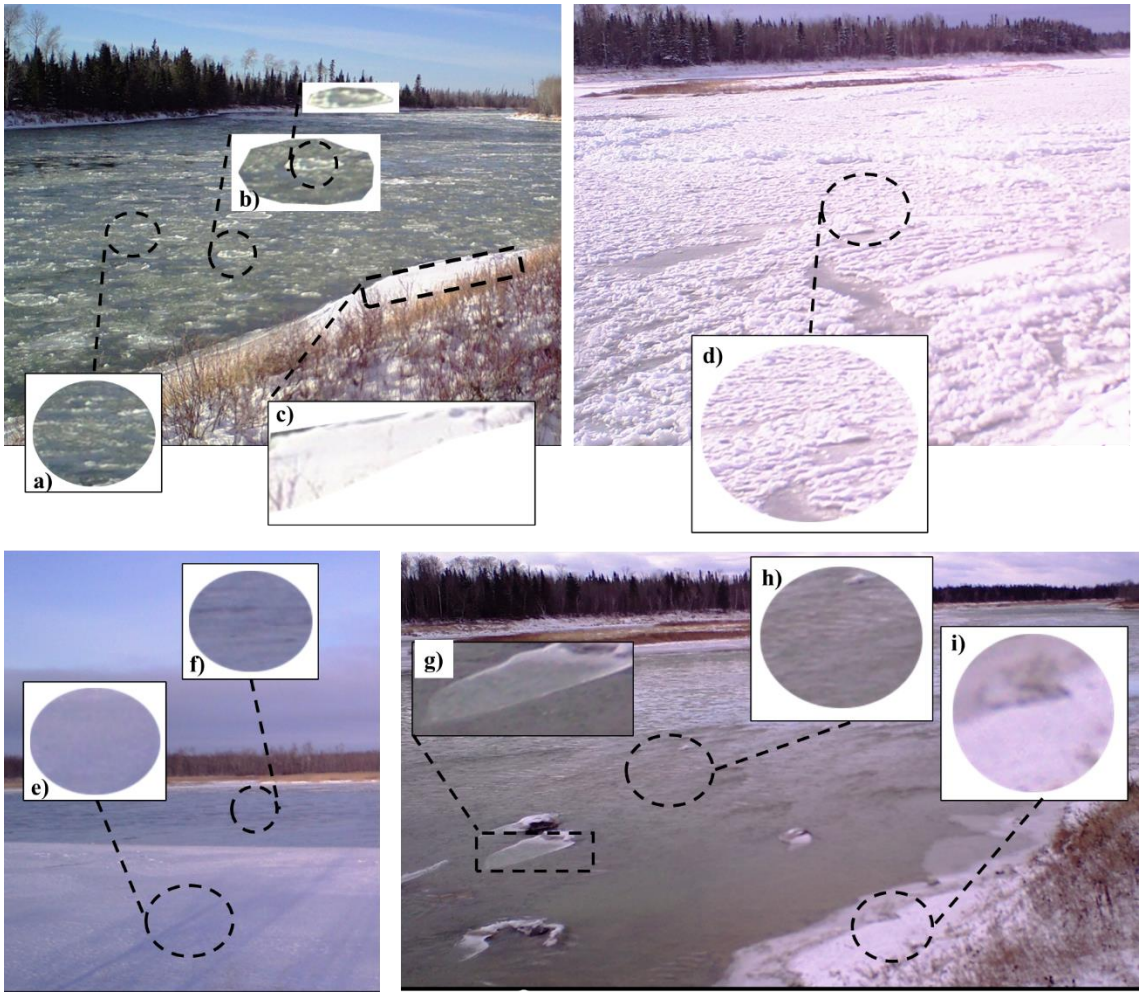

Figure 3-16 Comparison between different classes of river ice. a) slush ice, b) pan ice in dense slush ice, c) border ice, d) ice cover, e) border ice, f) open water, g) surface collar ice, h) open water, i) border ice

3.2.2.3 IceMaskNet for oblique imagery

IceMaskNet, an algorithm designed for the segmentation of river ice using aerial imagery, was implemented for river ice detection and classification using oblique shore-based imagery. IceMaskNet employs a modified Mask R-CNN framework for river ice detection and characterization. The algorithm pipeline for river ice segmentation is depicted in Figure 3-17 and comprehensively discussed in Ansari et al. (2021). A set of oblique shore-based imagery was collected at various monitoring stations along the Dauphin River, with different angles and fields of view, and divided into training, testing, and validation categories. The images were annotated based on the defined classes of "Border Ice," "Ice Cover," "Frazil Slush," "Ice," and "Open Water."

IceMaskNet was trained on the training and validation datasets, and the accuracy of the trained model was evaluated using a test dataset. The final trained and validated IceMaskNet was utilized to analyze the entire dataset of four consecutive years, and an orthorectification approach was employed in conjunction with the trained model to quantify different segmented river ice classes to extract quantified river ice data.

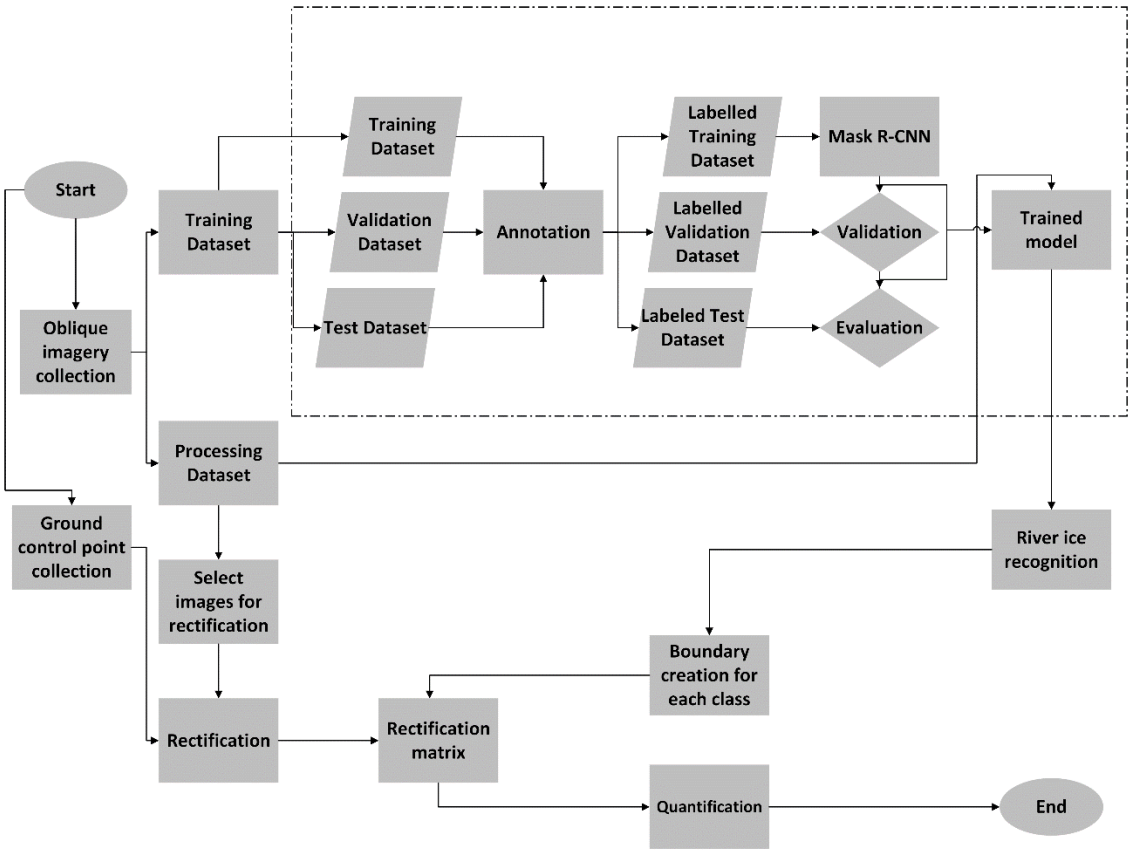

Figure 3-17 River ice detection and quantification algorithm using shore-based oblique imagery

IceMaskNet utilizes a Mask-RCNN convolutional neural network structure implemented on Tensorflow and Keras, open-source software libraries for dataflow and differentiable programming (Ansari *et al.*, 2021). The IceMaskNet model was previously trained, first on the COCO dataset and then on aerial river ice segmentation imagery (Ansari et al. 2021). Herein, the IceMaskNet model training was fine-tuned for oblique shore-based river ice segmentation. The model was trained using a machine with a graphical processing unit (GPU) as detailed in Table 3-7. To optimize the training process, the NVDashboard (Team R.D., 2018), an interactive real-

time visualization tool built with (Kluyver *et al.*, 2016) and Bokeh server (Bokeh Development Team, 2014) was employed. Additionally, data augmentation techniques were utilized to increase the diversity of the training data and improve generalization.

Table 3-7 Characteristics of the machine used for training

CPU	Intel(R) Core™ i7K 8700 K (6-Core/12-Thread, 12MB Cache, upto 4.7 GHz
Memory	32GB Dual Channel DDR4 at 2666 MHz(2X16GB)(370-ADUD)
GPU	NVIDIA(R) GeForce(R) GTX 1080 Ti with 11GB GDDR5X(490-BEDE)
Hard Disk	256GB M.2 PCle Solid State Drive(400-AVIX)

To assess the accuracy of the results, the test data set was utilized to evaluate detection and segmentation performance for each of the six predefined classes. Precision (P) and Recall (R) defined in equations 3-1 and 3-2 were employed to evaluate the detection performance of the algorithm. The mean average precision (mAP) was computed as the area under the Precision-Recall curve, as described by Girshick (2015). Precision-recall is used to evaluate the performance of a classification model. Precision (P) also known as positive predictive value, is the ratio of true positive (TP- the number of correctly classified pixels) and false positive (FP- the number of pixels incorrectly classified as a member of a class) predictions as shown in equation 3-1. In other words precision measures the model's accuracy in identifying only the relevant instances out of all the predicted instances as positive (Girshick 2015). Recall or sensitivity or true positive rate, is the ratio of the true positive predictions to sum of true positive and false negative (FN- is the number of pixels incorrectly classified as not a member of a class). Recall measures the model's ability to identify all the relevant instances (positive class) from the actual positive instances.

$$P = \frac{TP}{TP + FP} \tag{3-5}$$

$$R = \frac{TP}{TP + FN} \tag{3-6}$$

The Jaccard Index (JI), also referred to as Intersection over Union (IoU), is a widely used evaluation metric in computer vision applications (Jaccard, 1908). IoU is employed to evaluate the performance of neural networks by measuring the degree of overlap between predicted and ground truth segmentation maps. Fundamentally, the Jaccard Index calculates the ratio of the intersection to the union of the labelled segments and the missed values for each class (Csurka *et al.*, 2013).

As this study involves multiclass segmentation, the mean IoU (MIoU) is determined by averaging the IoU across all classes:

$$MIoU = \frac{1}{k+1}\sum_{i=1}^{k}\frac{p_{ii}}{\sum_{j=0}^{k} p_{ij} + \sum_{j=0}^{k} p_{ji} - p_{ii}} \tag{3-7}$$

where k corresponds to the total number of classes considered in the model; p_ij is the number of pixels that belong to class i, but classified as category j; the variable p_ii represents the number of pixels in category i that are accurately classified, and p_ji refers to the number of pixels that belong to category j but are erroneously classified as class i. The MIoU metric is employed to evaluate the precision of masks and quantifies the accuracy of categorizing different ice types.

Figure 3-18 displays the results of the river ice recognition algorithm when applied to fixed oblique imagery along the Dauphin River. The left-hand column images (Figure 3-18 a, c, e & g) present the original photos, while those on the right (Figure 3-18 b, d, f & h) illustrate the predicted classified results. These results show that the algorithm successfully identified, segmented, and classified open water and four distinct categories of river ice (five defined classes in river imagery). The first row of images (Figure 3-18 a & b) shows footage taken by the trail camera at DRLL02 on December 8, 2016, during the early stages of river ice formation. In these images, the algorithm identifies open water and border ice along the riverbank. Images captured by the trail camera at DRLL07 on November 7, 2018, are presented in Figure 3-18 c & d. The algorithm detects border ice forming due to thermal growth on riverbanks and around rocks as surface collar ice, as well as open water. Figure 3-18 e & f features an image taken at DRLL04 on November 27, 2015, wherein the algorithm detects frazil slush and border ice. Figure 3-18 g & h depicts an image captured at DRLL07 on November 10, 2018, with the algorithm recognizing complete ice cover in the camera's field of view. The sample images demonstrate the algorithm's success in detecting and distinguishing various predefined river ice classes and open water. However, a minor overlap between the identified classes exists. Although this overlap was accounted for when calculating areas, it remains an area for enhancement in future research.

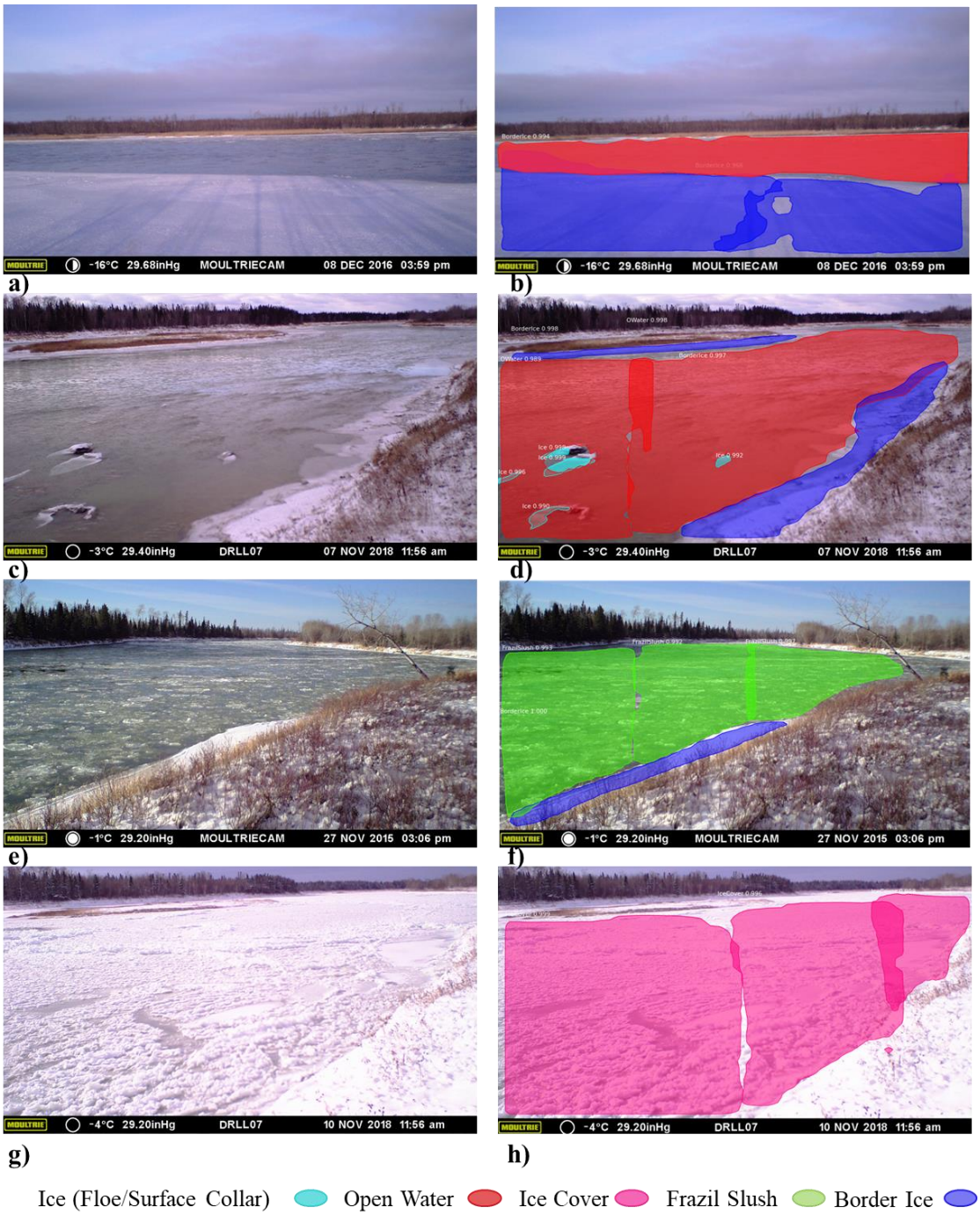

Figure 3-18 Sample results of the developed river ice detection and classification algorithm using oblique shore-based imagery

The algorithm exhibits average pixel accuracies of 90% and 86%, respectively for detection and masking. A comprehensive evaluation of each defined class is presented in Table 3-8. The results indicate that “Border Ice” and “Open Water” classes achieve the highest detection and segmentation accuracies. Conversely, the “Frazil Slush” class demonstrates the lowest accuracy among the various defined classes, with the complexity of its features being the primary reason for the reduced detection and recognition accuracy. While the annotation task was carried out by experienced individuals in this field, it is important to note that some limitations of the model can be attributed to the accuracy and consistency of the annotated training data that is due to the limited quality of the oblique imagery.

Table 3-8 Performance of the trained algorithm for river ice recognition in oblique shore-based imagery

Classes	Border Ice	Ice Cover	Frazil Slush	Frazil Floe/Ice	Open Water	Average
Detection Accuracy [%]	95	89	82	87	95	90
Mask Accuracy [%]	90	83	78	86	93	86

The developed algorithm demonstrates rapid processing capabilities, making it suitable as an instant segmentation tool for online analysis of terrestrial oblique imagery. On average, the model can process eight frames per second. Results reveal that the algorithm can effectively execute river ice recognition tasks with acceptable accuracy, even when faced with images featuring varying field of view angles, and diverse illumination and shading conditions. This suggests that image quality enhancements are not necessary, despite the presence of noise or poor-quality images. Moreover, the presented algorithm is highly generalized, enabling accurate detection and classification of different classes of river ice, irrespective of differences in texture, position, orientation, and location. For example, the recognition of “Border Ice” and “Frazil Slush” classes, which possess similar texture characteristics and are situated in close proximity, can be accurately performed using the trained algorithm, as illustrated in Figure 3-18f.

The accuracy and robustness of a segmentation and classification algorithm are intimately tied to the quality of annotations it is trained on. A well-annotated dataset empowers the algorithm to distinguish between nuanced differences in various kinds of river ice. In this work different classes of river ice were defined and a standard annotation approach was introduced. Annotations were cross validated to ensure the quality of the annotated dataset.

Although in this work the annotation procedure was conducted carefully, a number of challenges are inherent to the process. Increasing the amount of labeled data is often considered to increase the accuracy of the algorithm; however, as the scale of data grows, the constraints of manual annotation become evident. It is not just about the number of images, but also the granularity of annotation that is required. Manual annotations, while rich in qualitative insights, may not always capture the breadth of variations seen in river ice formations. Moreover, operator subjectivity may be introduced by different annotators. The present annotations were defined and performed by experts in this field or individuals trained for this purpose. Nonetheless, even experts may interpret the same ice formation differently, leading to inconsistencies in the dataset. Cognitive biases, both conscious and unconscious, can creep into the annotations, potentially skewing outcomes. The intricate nature of river ice formations, replete with overlapping and sometimes ambiguous patterns, compounds these challenges. For instance, the identification of frazil ice, which can manifest in varied thickness and distributions, often confounds many specialists due to its dynamic nature in river systems. Likewise, considerable disagreement can arise when differentiating between surface intruded anchor ice and surface ice, given their often-overlapping physical characteristics. Such discrepancies in annotations can mean that the hand-labeled data might deviate from the actual phenomenon, potentially undermining the precision of supervised machine learning models. Thus, to minimize subjective operator errors, all the manually annotated images in the present work were checked by the lead author. Specifically, to ensure a robust annotation framework, the following steps were employed:

a) Standardization of Annotation Protocols: The keystone of consistent annotation is a standardized guideline, adhered to universally by annotators. Such a foundation minimizes subjective biases and disparities.
b) Training & Validation: It's crucial for annotators to undergo comprehensive training to grasp the intricacies of river ice formations. Continual validation of their work safeguards against inconsistencies and upholds quality.
c) Quality Control and Feedback Mechanisms: Annotation is an iterative process. Regular reviews, supplemented with constructive feedback mechanisms, facilitate the refinement of the annotation quality over time.
d) Cross annotation: All annotated images were verified by a single lead operator, to provide constructive feedback and to find inconsistencies.

Another approach would have been to have the same dataset annotated multiple times by various experts, although this would have been both costly and time-intensive. To compensate for

inconsistencies originating from human annotations, different approaches have been introduced to extract an approximation of the ground truth from multi-expert annotations such as STAPLE (Warfield et al., 2004) and VoteNet (Ding et al., 2019) used in medical image segmentation. In VoteNet, for example, multiple labeled templates are registered to a target image. Once this registration is done, the labels from the templates are transferred to the target. Then these multiple label maps are fused into a single, coherent segmentation. These methods in general require multiple opinions for the same data but at the end they provide a more trustable annotation dataset. It may be possible to improve river ice characterization by employing a similar approach to generate a comprehensive and diverse dataset labelled and annotated by several experts in the field. This was not the goal of this research but can be considered as a future research work. Further, for forthcoming endeavors, it would be beneficial to undertake a study specifically focused on quantifying the errors stemming from the annotation process. This would further bolster our understanding of the nuances and implications of annotation in this field.

3.2.2.4 Orthorectification:

In this study, images were collected using trail cameras mounted on tree trunks at an oblique angle. To convert these oblique images into a quantifiable representation of the scene, orthorectification is necessary. This process corrects geometric distortions and ensures the images are aligned with real-world coordinates. Orthorectification can be carried out using at least 6 ground control points (GCPs), which are identifiable landmarks in the image with known real-world coordinates. By leveraging these control points and applying the collinearity equation (Hartley and Zisserman, 2003), the relationship between the camera, image, and ground coordinates can be established, allowing for the transformation of oblique images into orthorectified ones.

$$x - x_0 = -f\left[\frac{m_{11}(X - X_0) + m_{12}(Y - Y_0) + m_{13}(Z - Z_0)}{m_{31}(X - X_0) + m_{32}(Y - Y_0) + m_{33}(Z - Z_0)}\right] \quad (3\text{-}8)$$

$$y - y_0 = -f\left[\frac{m_{21}(X - X_0) + m_{22}(Y - Y_0) + m_{23}(Z - Z_0)}{m_{31}(X - X_0) + m_{32}(Y - Y_0) + m_{33}(Z - Z_0)}\right] \quad (3\text{-}9)$$

Where *(x,y)* is the pixel coordinates, *(X, Y, Z)* is the real-world coordinates, *f* is the focal length, and $m_{i,j}$, are the mapping coefficients including camera rotation and transformation information.

These coefficients are often referred to as the camera transform and can be determined through camera calibration procedures.

For each camera, six GCPs were surveyed to facilitate georectification. As an example, Figure 3-19 presents six unique GCPs gathered for image georectification at DRLL05. Figure 3-19a displays a representative image from DRLL05, highlighting the acquired GCPs, while Figure 3-19b exhibits the georectified image overlaid with both Image Control Points (ICP) and Ground Control Points (GCP). The calculated root mean square error (RMSE) reflecting the distance between the GCPs and ICPs indicates the precision of the georectification process; for this image, the RMSE stands at 1.02 meters.

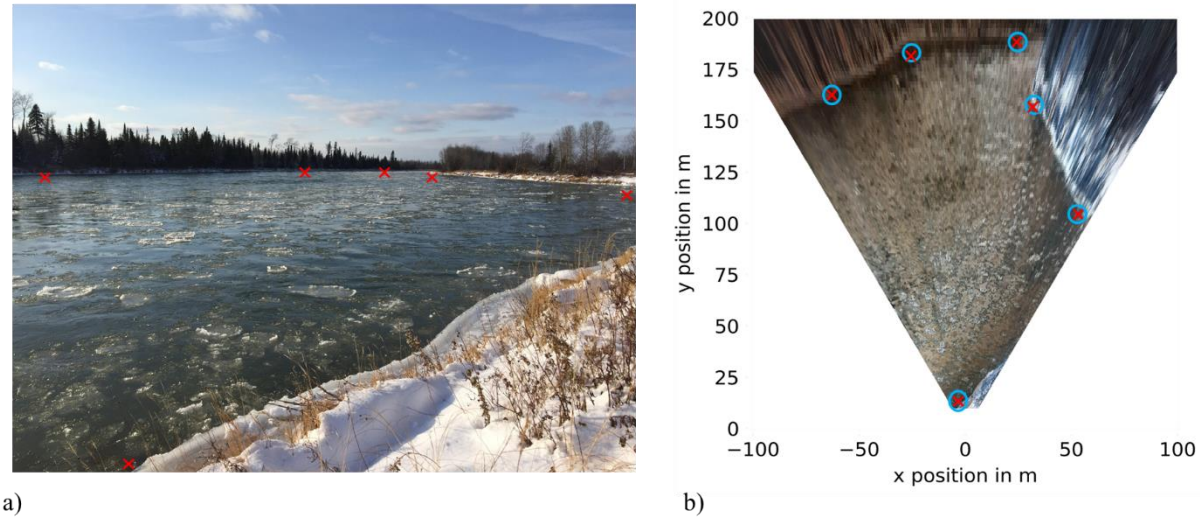

Figure 3-19 a) A sample shore-based oblique image at DRLL05 with the collected GCPs (✕) b) shows the geo-rectified image with the ICPs (○) and superimposed GCPs in bird's eye view.

This method was employed to perform orthorectification on a selection of images from each camera stationed along the Dauphin River. Orthorectification matrix represents the mathematical relation between the original image coordinates and the orthorectified image coordinates. This matrix accounts for camera orientation, focal length and sensor geometry. The orthorectification matrix, which has dimensions equivalent to the original image, illustrates the connection between camera coordinates and real-world coordinates. By utilizing the orthorectification matrix, estimations can be made for each type of river ice class area, based on their known boundary

coordinates associated with specific ice classes. Once the orthorectified matrices were generated, they were used to extract quantifiable data pertaining to the different segmented river ice classes.

3.2.3 Results and discussion

The trained algorithm for river ice segmentation, classification, and quantification was applied to process and analyze a collection of shore-based oblique images captured along the Dauphin River during four consecutive winter seasons (2015-2019). The study utilized image data gathered from various locations along the river in order to examine the temporal and spatial variations in river ice regimes throughout the research period. Throughout the processing period, quantified results were obtained for various types of river ice and open water detected. These findings were plotted in conjunction with temperature data for the entire analysis duration. In the following section, the outcomes for each winter season will be interpreted individually.

- ***Winter 2015-16***

In this analysis, images from five trail cameras (i.e., DRLL04, DRLL05, DRLL06, DRLL08, and DRLL10) along the river were employed (Table 3-6- Figure 3-11). Except for DRLL05, all images analyzed in this study were from the freeze-up period. Quantitative results are displayed in

to 24 for trail cameras DRLL04, DRLL05, DRLL06, DRLL08, and DRLL10, respectively. The data shows that river ice production, in the form of both thermal border ice growth (DRLL04, DRLL05, DRLL06, and DRLL08) and frazil ice production, begins as early as mid-November. Figure 3-25 illustrates the total ice concentration quantified at different camera locations that is plotted against degree days of freezing during the freeze-up season and thawing degree days during the breakup season. A rise in air temperature in early December halted frazil ice production, but border ice volume remained largely unaffected. Substantial ice growth, including both frazil ice generation and thermal border ice growth, was observed starting in the second week of December at 150 DDOF. The gradual increase of river ice eventually led to the formation of full ice cover on December 26th, December 19th, December 17th, November 25, and November 24th for trail cameras at DRLL04, DRLL05, DRLL06, DRLL08, and DRLL10, respectively; which demonstrates the typical ice front progression from downstream to upstream.

A quantitative examination of the imagery gathered along the Dauphin River, as detailed in section 3, reveals that ice production typically begins in nearly all parts of the river around November 19th, once air temperatures fall below freezing. At DRLL10, near Lake Winnipeg's mouth, frazil ice observed flowing into the lake from upstream quickly transitions to a full ice cover on November 24th, persisting for the entire season until breakup. Around 2.2 km upstream

at DRLL08, frazil ice appears simultaneously on November 19th, followed by a shifting smooth cover on November 25th that transforms into a rough, thick ice cover just one day later.

During December 2015, air temperatures rose above freezing from December 1st to December 15th, impacting all trail cameras and ice production. An open water patch emerged at DRLL08, lasting until December 15th. As water temperatures declined after December 15th, the open water patch shrank until it vanished entirely on December 17th. DRLL08 then exhibited full ice cover for the remainder of the season.

Frazil ice formation began at DRLL06 on November 20th, with concentrations increasing from November 20th to December 2nd, when air temperatures began to rise. No ice was observed from December 2nd to December 15th. Complete ice cover commenced with compacted frazil ice on December 17th, resulting in a thin, smooth ice layer. This ice quickly became rough and thick after December 18th and remained so until observations concluded.

At DRLL05, both thermal border ice and frazil ice production began on November 19th. As seen at other locations, the increase in air temperature led to a pause in frazil production and border ice decay. Frazil ice production rapidly resumed after temperatures dropped again on December 17th and continued until a full, thin, and smooth cover formed on December 19th. On December 20th, a rise in water levels, also visible in the imagery, caused the sudden formation of an open water lead at this location. This open water patch disappeared around December 25th, but another increase in water levels resulted in the creation of a new open water patch near the left riverbank on January 9th, 2016, which persisted until the end of the observations and breakup season.

At DRLL04, conditions were more dynamic but similar to DRLL05. Frazil ice production began on November 20th, with concentrations increasing for two days between November 20th and 22nd, followed by a two-day absence of frazil ice. Border ice formation and growth continued from November 23rd. As with other sites, no ice was observed between December 3rd and December 15th due to rising air temperatures. Frazil ice particles reappeared starting December 15th, with concentrations gradually increasing. Frazil ice concentrations fluctuated from December 17th until a full, thin, and smooth ice cover formed on December 24th. This ice cover grew thicker and rougher through mechanical thickening until December 26th and remained unchanged until the end of the observations.

The findings from the two cameras at DRLL04 and DRLL05 exhibit similarities, particularly in their dynamic frazil ice production patterns. This behavior is distinct from what was observed at DRLL06, DRLL08, and DRLL10. The locations of the cameras at DRLL06 and DRLL08 correspond to milder slope sections of the river compared to those at DRLL04 and DRLL05, which likely contributes to the differences in ice production and growth patterns observed. The camera at DRLL10 is situated where the Dauphin River flows into Lake Winnipeg, which results in different hydrodynamic conditions that significantly affect frazil ice production and ice growth. The simultaneous formation of full ice cover at DRLL08 and DRLL06 and the rising water levels at DRLL05 and DRLL04 can be examined and considered related. As mentioned in Wazney et al. (2018), ice cover formations at DRLL06 and DRLL08 led to backwater and increased water levels at DRLL05, resulting in the creation of an open water patch on December 20. While the rising water levels caused the formation of an open water patch at DRLL05, the other cameras displayed an expanding ice cover. This suggests an actively consolidating zone that ceased further growth once it reached a stable state. Figure 3-29a illustrates the spatial and temporal distribution of river ice observed and quantified at five camera locations along the Dauphin River.

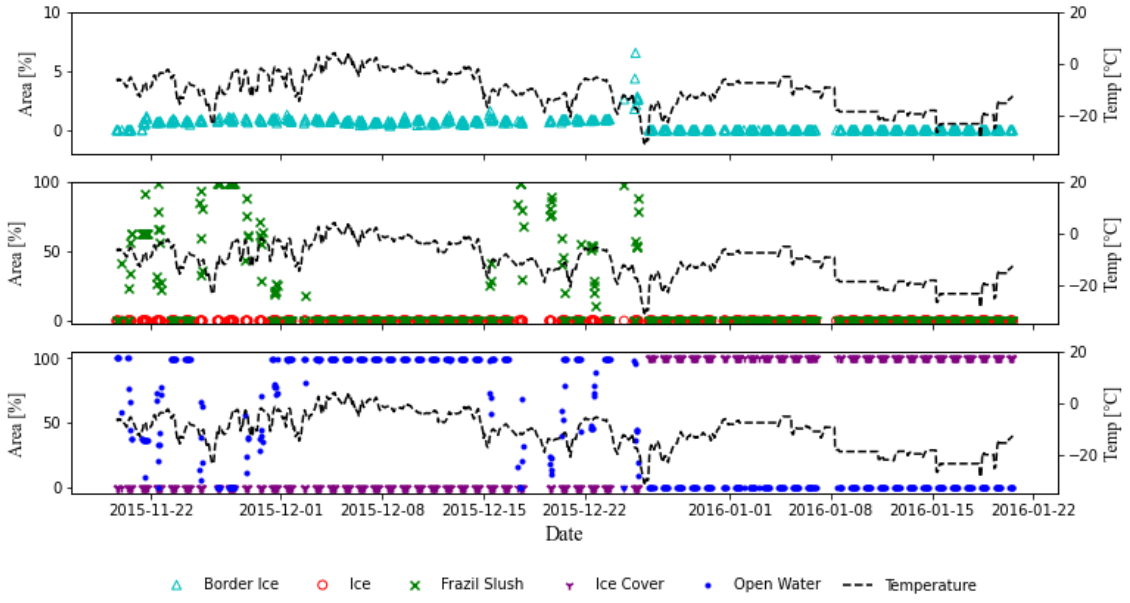

Figure 3-20 River ice concentrations of distinct ice classes, obtained from close-range imagery at DRLL04 during the 2015-16 winter, plotted with air temperature.

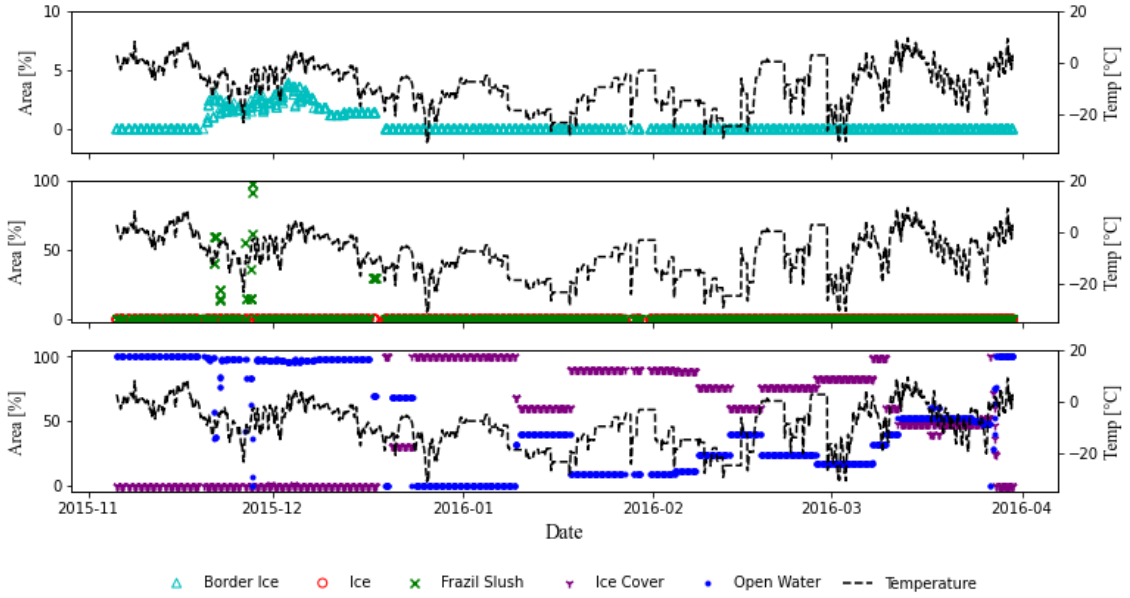

Figure 3-21 River ice concentrations of distinct ice classes, obtained from close-range imagery at DRLL05 during the 2015-16 winter, plotted with to air temperature.

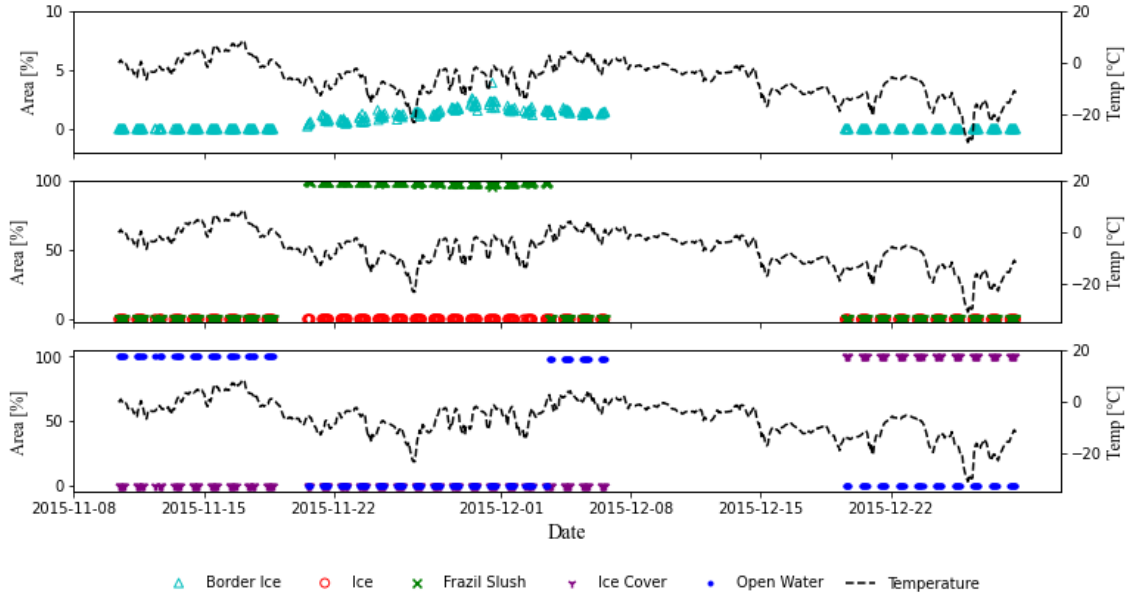

Figure 3-22 River ice concentrations of distinct ice classes, obtained from close-range imagery at DRLL06 during the 2015-16 winter, plotted with to air temperature.

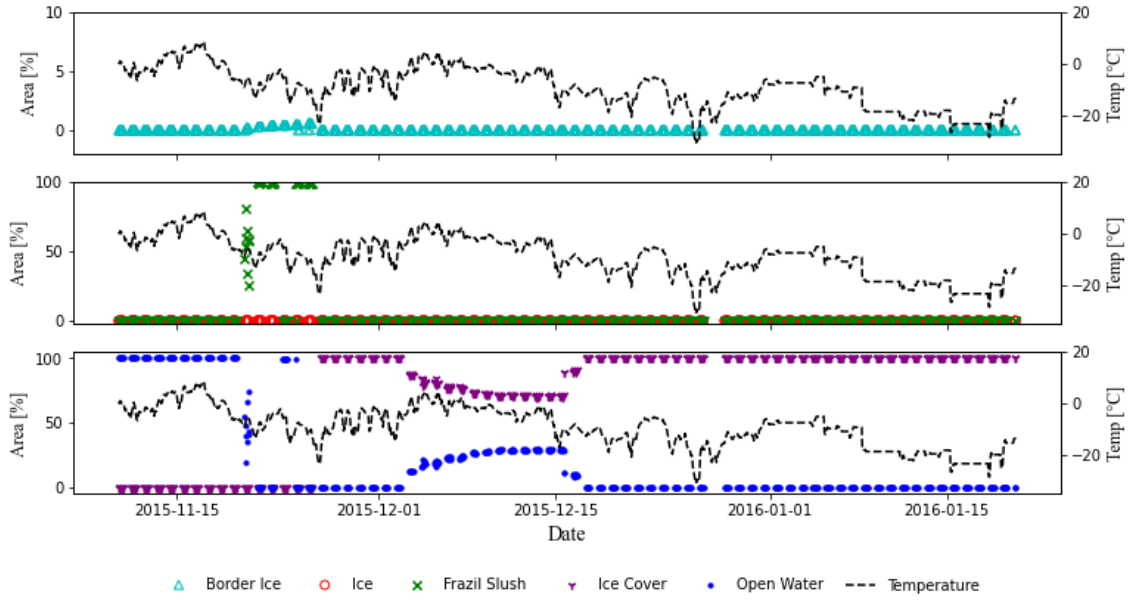

Figure 3-23 River ice concentrations of distinct ice classes, obtained from close-range imagery at DRLL08 during the 2015-16 winter, plotted with to air temperature.

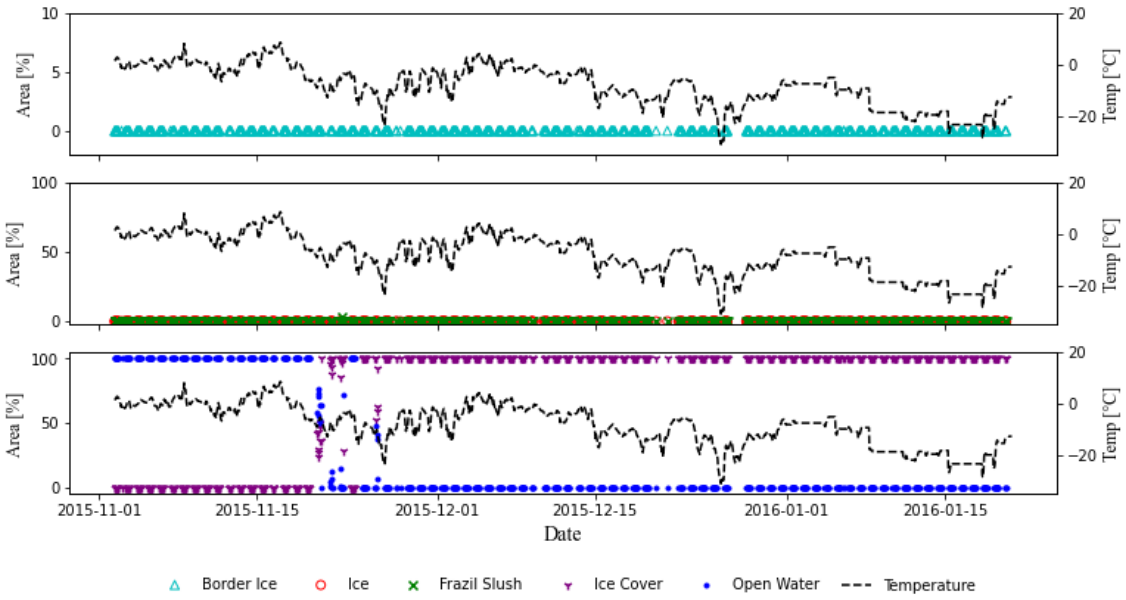

Figure 3-24 River ice concentrations of distinct ice classes, obtained from close-range imagery at DRLL10 during the 2015-16 winter, plotted with to air temperature.

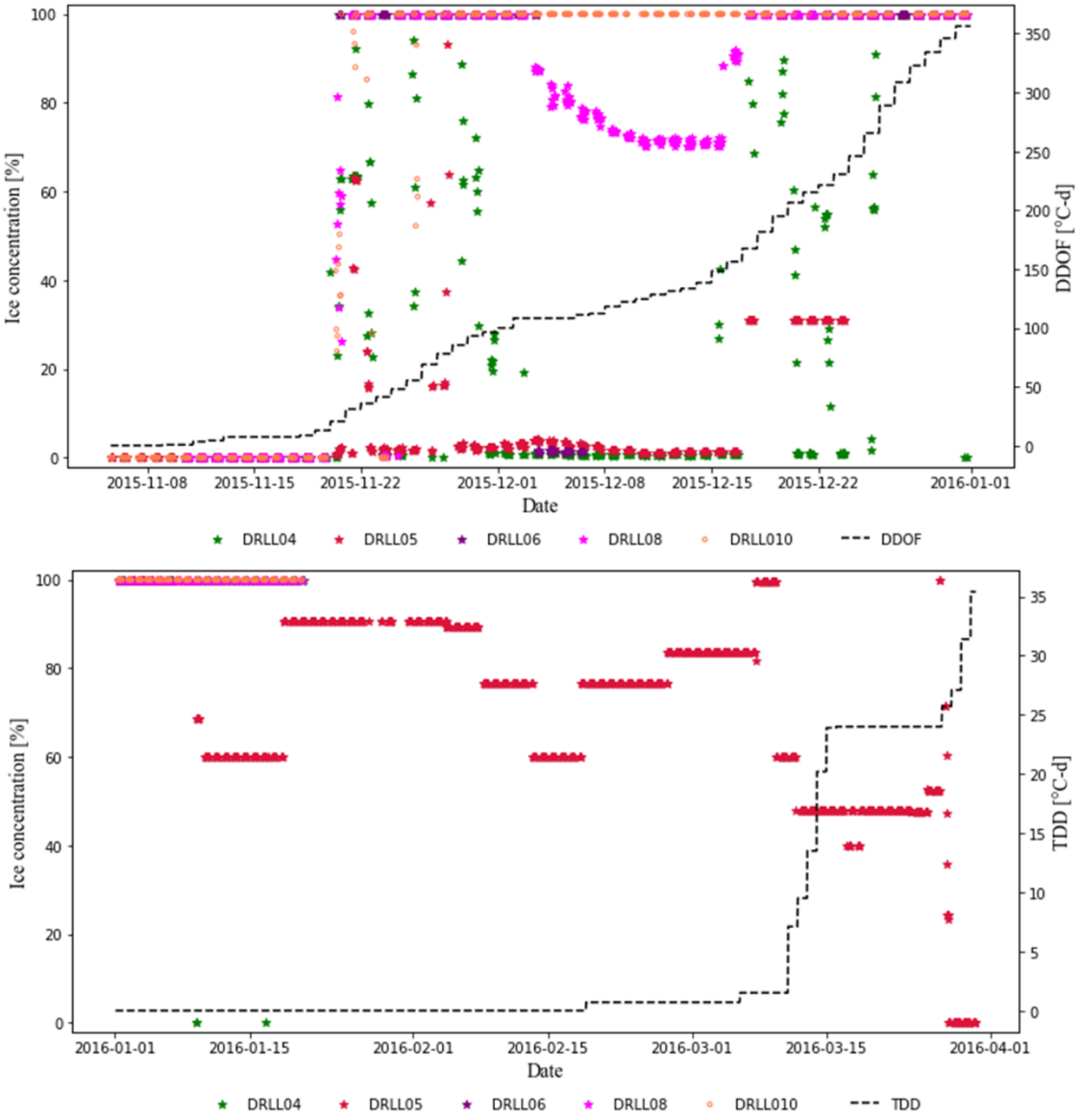

Figure 3-25 River ice concentrations observed at different monitoring stations plotted against degree days of freezing during the winter of 2015-16. The figure illustrates river ice progression along the Dauphin River.

- ***Winter 2016-17***

Data from four monitoring locations (namely, DRLL03, DRLL04, and DRLL06) were utilized in this analysis (Table 3-6). The quantified river ice concentrations at these locations are illustrated in Figure 3-30 to Figure 3-32 in the appendices, respectively to DRLL03, DRLL04, and DRLL06. The analysis of the data from DRLL03 demonstrates both thermal border ice growth and active frazil ice production. Although complete river ice never formed during the freeze-up period due to the dynamic nature of the river ice and the formation of an open water patch at this location, 100 percent river ice concentration and complete ice cover formation was observed in March 13. The break-up process and transition to complete open water occurred in less than 14 hours in early May.

Figure 3-31 presents the results of the analysis at DRLL04 from March to April, covering the break-up period. The break-up at this location transpired more gradually over a 72-hour period. Only a few days in December were observed at DRLL06, but these capture the incremental growth of river ice that led to complete coverage within 48 hours (Figure 3-32). The findings show that ice production, in the form of both thermal border ice growth and frazil ice production, commences with a significant decrease in air temperature and when the degree days of freezing reach around 80. Figure 3-26 illustrates the river ice concentration and degree days of freezing and thawing degree days at three monitoring locations, DRLL03, DRLL04, and DRLL06, during the winter of 2016-17. Spatial and temporal distribution of ice concentration in Dauphin River during 2016-17 season is presented in Figure 3-29.

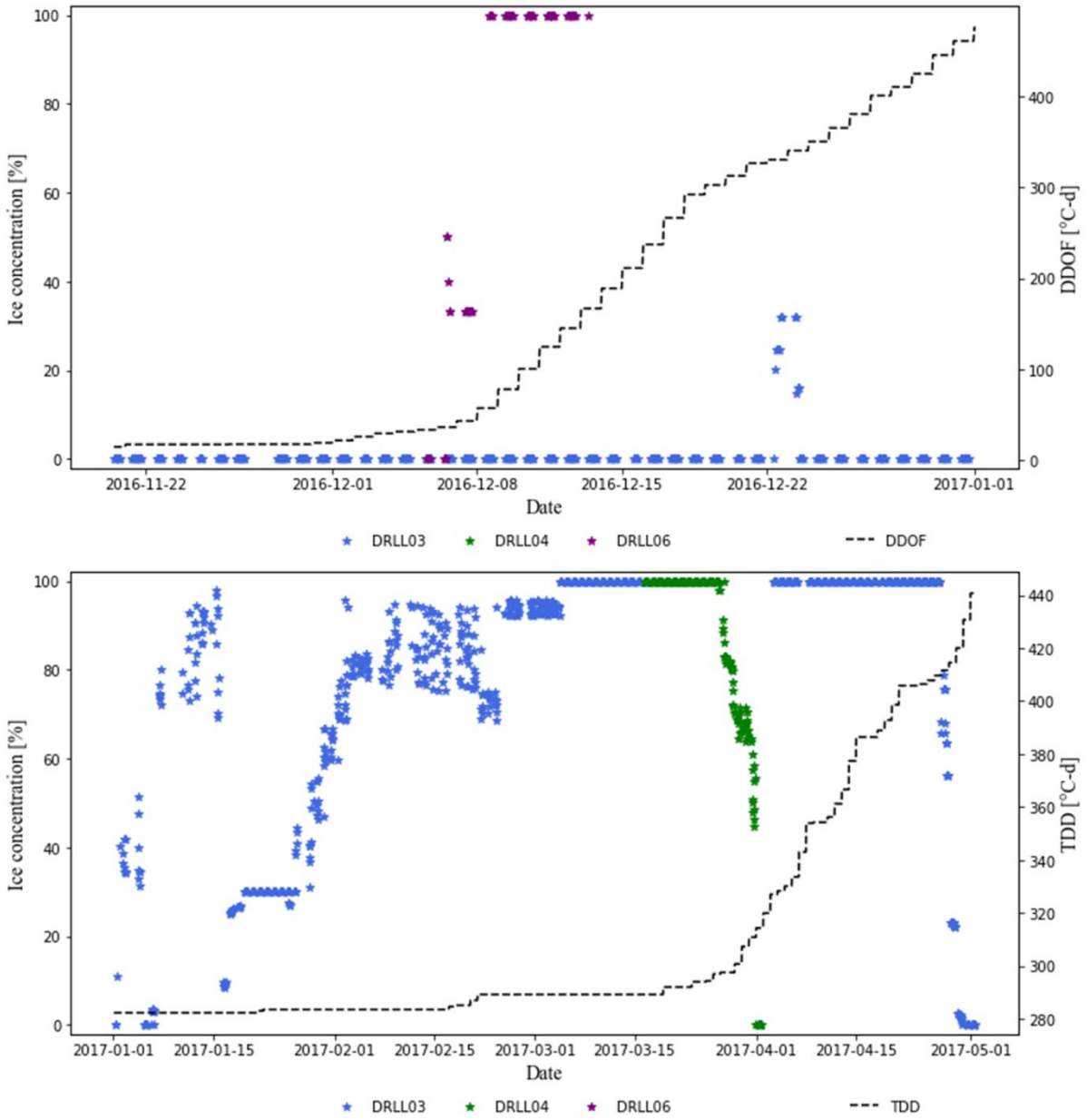

Figure 3-26 River ice concentrations observed at different monitoring stations plotted against degree days of freezing during the winter of 2016-17

- ***Winter 2017-18***

The analysis for the 2017-18 winter utilized images obtained from nine trail cameras, namely DRLL03, DRLL04, DRLL05, DRLL06, DRLL06a, DRLL06b, DRLL07, DRLL08, and DRLL08a. The results are presented in Figure 3-33 to Figure 3-41, with each figure corresponding to a specific camera. Figure 3-33 displays the results of the DRLL03 trail camera dataset, covering approximately one month (November to December 2017) and capturing the full freeze up period until December 12. The analysis revealed consistent frazil slush formation similar to previous years. Due to the camera angle and the field of view, frazil floes were also detected at this location. The available dataset from the DRLL04 trail camera covers imagery only from the break-up period (Figure 3-34). This graph shows that with the gradual air temperature increase above zero and up to 20°C, the ice cover break up occurred in 72 hours (Figure 3-34). Oblique image dataset collected from DRLL05 successfully covered both the freeze-up (October 2017 to mid-December 2018) and break-up (April to May 2018) periods (Figure 3-35). Frazil ice production was observed during the freeze-up period until the complete ice cover formation on December 5. Ice cover at this time was unconsolidated and moving down-stream. The break-up and free surface open water occurred quickly over 84 hours following a period of gradual temperature increase. The trail camera at DRLL06 had one of the most complete datasets for the duration of seven months (i.e. October 2017 to mid-April 2018); although the break-up was not observed in this camera the freeze-up and consolidation were completely covered. Similar to other cameras the frazil slush was detected and quantified in the freeze-up period on November 4 until the complete ice formation on December 06. It was discovered that a high concentration of frazil ice became trapped by thermally formed border ice, subsequently increasing the border ice's extent at this site. The growth of border ice towards the river center resulted in more frazil slush contributions, eventually leading to a complete but mobile river ice cover. This occurred around November 20, with the full ice cover forming on November 21 (Figure 3-37). Frazil ice was first spotted at the DRLL06a camera on November 4. Its concentration fluctuated until November 16, when an extremely dense frazil concentration appeared in the camera's field of view, moving downstream. This dense frazil ice incrementally contributed to the thickness and reach of the thermally developed border ice. The border ice expanded and advanced to the river center, ultimately forming a smooth, thin, and moving ice cover on November 18. The river ice cover continued to consolidate, but data for this location was unavailable beyond November 22 until April 2018. However, ice breakup was not observed at this site. The river ice processes at DRLL06b were similar to those described for DRLL06a, with the exception of the presence of border ice. Frazil ice began to emerge as early as November 4 and increased in density until a complete cover formed on November 18. Ice breakup was observed at DRLL06b; increased air temperatures led to the formation of an open water lead

at this location on April 22, which subsequently resulted in complete ice deterioration and breakup shortly thereafter. The image datasets for DRLL07 span from late October to mid-December 2017 and then continue in April 2018. Consistent with other locations, frazil ice becomes visible in the camera's field of view as early as November 4. The concentration of frazil ice fluctuated, intensifying considerably after November 9 until a complete, smooth, and mobile ice cover formed on November 16. Complete ice cover further stabilized and during the winter and in the available dataset. The image dataset at this site also captures the ice breakup period during April 2018. Breakup at this location transpires through the further enlargement of an existing open water area.DRLL08 and DRLL08a cover both the freeze up and break up (October 2017 to May 2018). In the field of view of the cameras DRLL08a no border ice was detected. Frazil slush production varied during freeze-up until the full ice cover formation on November 11 and November 8 respectively for DRLL08 and DRLL08a. On December 12 a large open water lead formed at DRLL08. Break up occurred gradually over a few hours in May 2018 respectively for DRLL08 and DRLL08a. Figure 3-27 summarizes ice concentration for all the cameras during the freeze up season plotted against the degree days of freezing and thaw degree days. Complete river ice formation for the cameras DRLL03, DRLL05, DRLL06, DRLL06a, DRLL06b, DRLL07, DRLL08, and DRLL08a occurred on December 05, December 06, November 19, November 18th, November 15th, November 9th, November 8th with the degree days of freezing of 324, 303, 314, 188, 176, 151, 104 and 87 DDOF respectively. Temporal and spatial distribution of river ice observed during 2017-18 is illustrated in Figure 3-29.

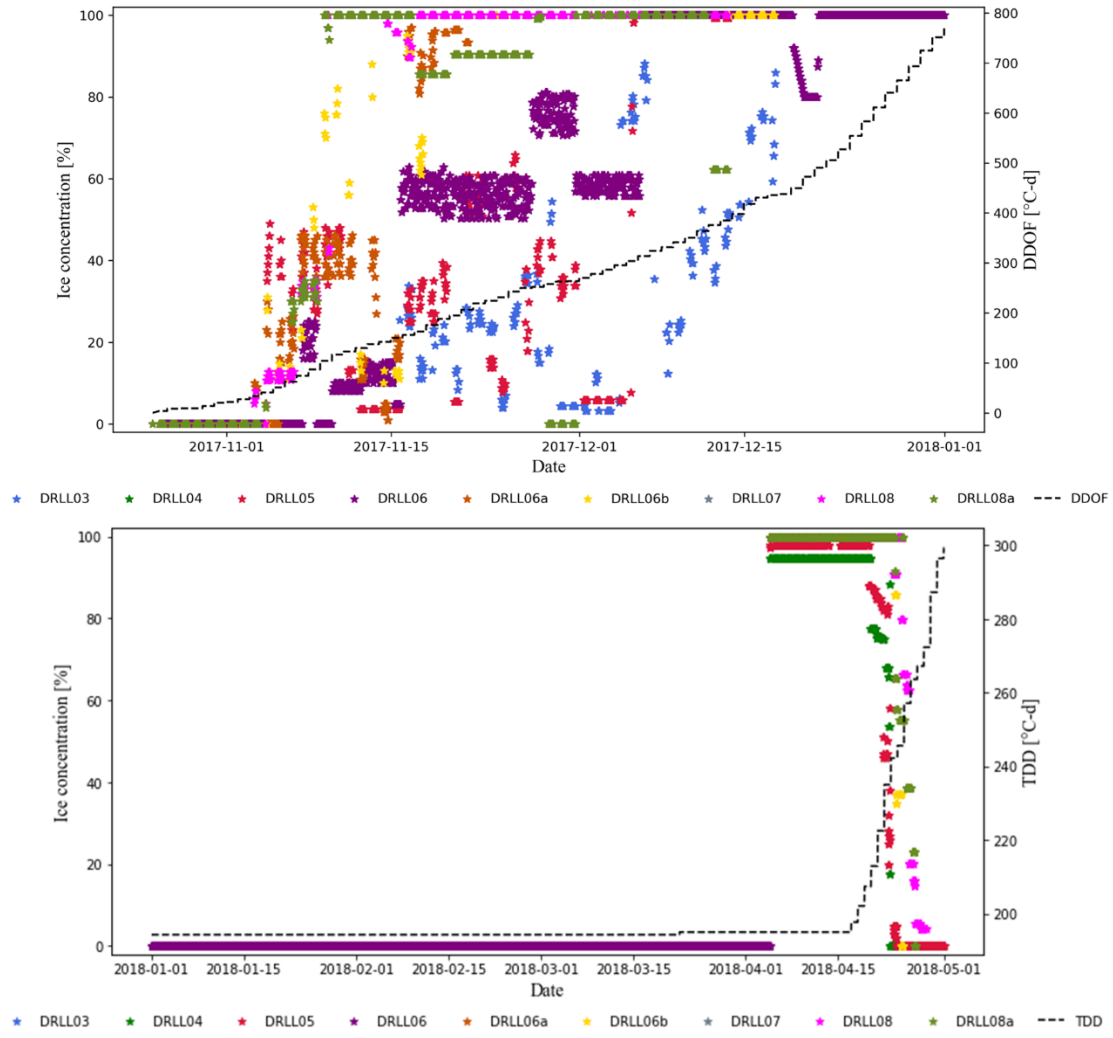

Figure 3-27 River ice concentrations observed at different monitoring stations plotted against degree days of freezing during the winter of 2017-18

- ***Winter 2018-19***

The analysis for the 2018-19 winter utilized images obtained from trail cameras at DRLL03, DRLL04, DRLL05, DRLL06 and DRLL07, respectively shown in Figure 3-42, Figure 3-43, Figure 3-44, Figure 3-45 and Figure 3-46. Analysis of the available image dataset at DRLL03 only covers break-up season (March to April 2019), and shows that a relatively gradual breakup initiated with the formation of an open water patch on the right river bank on April 11. The gradual transformation to open water continued with the expansion of the open water patch which took around 72 hours and finally complete open water formed on April 14 (Figure 3-42). The camera at DRLL04 collected imagery for the freeze up period (October 2018 to January 2019). Frazil slush production fluctuations observed in previous years did not occur in 2018-19. Rather, border ice commenced on November 9 and progressively grew towards the center of the river over a period of nine days (covering up to 38 percent of the channel), and then a complete ice cover formation rapidly occurred on November 18 (Figure 3-43). This different behavior of river ice processes can be associated to low flow conditions in 2018-19. A similar freeze-up process was observed at DRLL05, with border ice growth over 84 hours and then a complete ice cover quickly developing on November 14. The camera at DRLL07 captured both the freeze up and break up periods (October 2018 to May 2019) (Figure 3-46). River ice formation at this location was a rapid occurrence that occurred in 72 hours to a complete formation on November 9th. River ice break-up occurred over 18 days to complete open water on April 18th. Figure 3-28 summarizes river ice concentration for all cameras during freeze up and is plotted versus degree days of freezing and thawing degree days. River ice formation was observed first at DRLL07, then DRLL06, DRLL05 and DRLL04. This figure shows that while complete river ice formation in DRLL07 is a rapid occurrence (80 DDOF), river ice formation in DRLL04 is relatively gradual (200 DDOF).

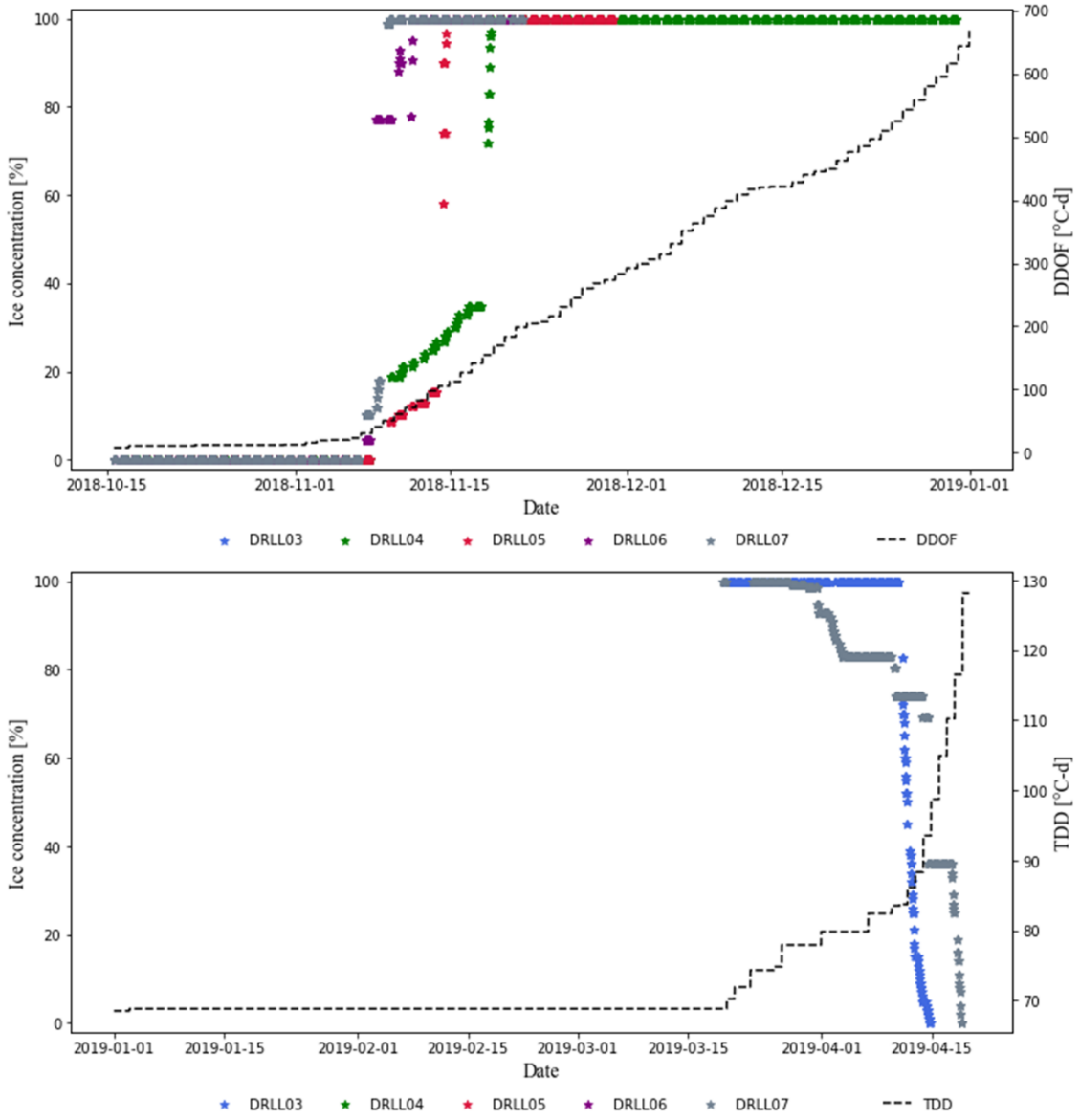

Figure 3-28 River ice concentrations observed at different monitoring stations plotted against degree days of freezing during the winter of 2018-19

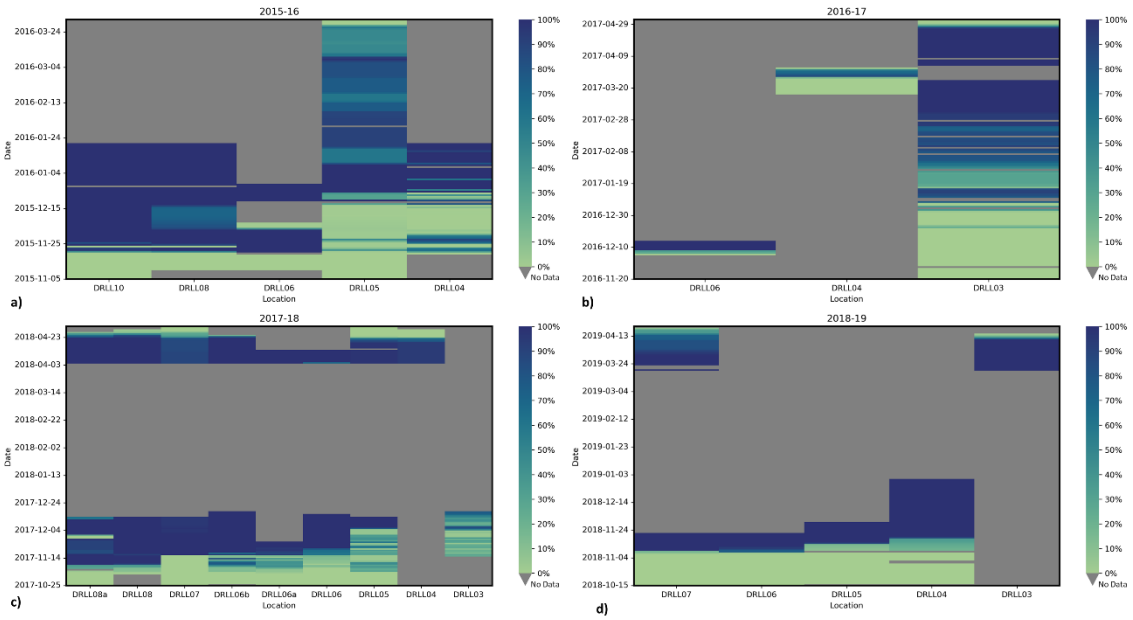

Figure 3-29 Temporal and spatial distribution of river ice extracted from oblique shore-based imagery along the Dauphin Rivera; a) year 2015-16 at DRLL10, DRLL08, DRLL06, DRLL05, DRLL04; b) year 2016-17 at DRLL06, DRLL04, DRLL03, c) year 2017-18 at DRLL08a, DRLL08, DRLL07, DRLL06b, DRLL06a, DRLL06, DRLL05, DRLL04, DRLL03; d) year 2018-19 at DRLL07, DRLL06, DRLL05, DRLL04, DRLL03

- ***Comparison of river ice processes along the Dauphin River in four consecutive winters of 2015-2019***

The typical pattern of river ice cover processes along the Dauphin River is consistent across the studied years, with some notable variations, as detailed here. River ice processes in the Dauphin River usually commence with frazil ice formation on steeper slope sections upstream, such as DRLL03, DRLL04, and DRLL05. Downstream ice formation predominantly begins with thermal ice growth, followed by the accumulation and consolidation of frazil slush and pans transported from upstream. Observations indicated that backwater effects from advancing ice cover can cause significant water level changes, occasionally resulting in the release and downstream transfer of large ice accumulations (e.g., DRLL05 in November 2015). Water level fluctuations at a given site persisted until the ice cover fully stabilized.

The average air temperatures during the freeze-up period (defined as December in this study) were -8.21°C, -14.24°C, -15.7°C, and -11.6°C for the winters between 2015 and 2019, respectively. The winter of 2016-17 had the highest flow, while 2018-19 had the lowest. The 2015-16 and 2017-18 winters experienced higher than average flows, but were still within the normal

range. Generally, complete ice cover formed more rapidly in 2018-19 when river flow was significantly lower, and the pattern of ice cover formation at different sites varied. For instance, at steeper upstream locations, ice cover formation in previous years typically began with the production of frazil and pan ice, sometimes even before border ice formation, which could be attributed to higher flow and turbulent intensities inhibiting thermal ice growth along the river banks. In contrast, during 2018-19, river ice formation at these sites started with the development and advancement of border ice towards the river's center, subsequently trapping downstream flowing frazil slush. The constriction created by the progressing border ice contributed to the rapid formation of river ice cover in these sections. Low flow conditions were also responsible for the gradual formation of open water and river ice decay during the break-up season.

3.2.4 Conclusions

This study highlights the increasing value of close-range remote sensing and monitoring for river ice process analysis, facilitated by advancements in computer vision and the growing accessibility of affordable photogrammetry devices. The research presented a novel river ice detection, segmentation, and quantification algorithm utilizing state-of-the-art deep learning techniques, specifically designed for oblique imagery. Built on an enhanced version of the highly accurate instance segmentation algorithm, Mask R-CNN, the IceMaskNet system was trained using 1795 manually annotated oblique shore-based images of the Dauphin River. The algorithm demonstrates a high degree of accuracy in detecting and segmenting various river ice categories, achieving 90% detection accuracy and 86% segmentation accuracy.

In summary, the findings indicate that river ice processes in the Dauphin River are intricate phenomena influenced by factors such as air temperature, river flow, flow velocity at specific river sections, and hydrodynamics. Although the overall pattern of ice production and river ice cover progression occurs from downstream to upstream, the timeframe for complete ice cover formation varies among different years. These variations can be ascribed to a combination of air temperature and river flow. For instance, in low flow conditions, border ice growth along river banks initiates river ice cover formation, contrasting with frazil ice formation during winters with higher flow. Consistent intermittent water level fluctuations during the freeze-up period were found to be indicators of active consolidation events, which were more pronounced during higher flow winters. It was also observed that ice cover mobilizes and moves downstream across several kilometers. An increase in ice surface elevation was noted during the studied years, indicating rapid mechanical thickening and/or water level rise. Observations during break-up periods revealed that

the formation of an open water patch on faster-flowing sections of the river typically initiates the break-up process, which occurs gradually under low flow conditions.

This study underscores the potential of close-range remote sensing as a complementary tool for improving our understanding of river ice processes during freeze-up and decay. The developed algorithm was applied in a case study to showcase its capabilities in producing quantified data and information derived from long-term shore-based monitoring. The resulting quantitative data can significantly contribute to our comprehension of river ice processes and can be employed in various applications, including enhancing numerical modelling accuracy, measuring river discharge in winter, studying river ice dynamics, and developing flood hazard prevention and mitigation strategies related to ice jams.

3.2.5 Appendices

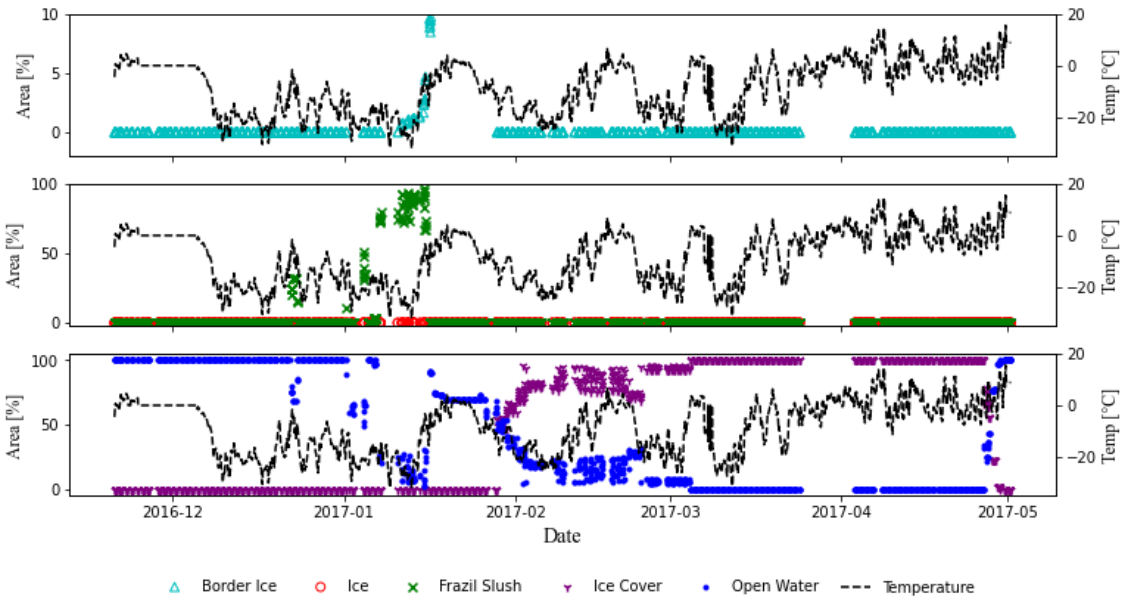

Figure 3-30 River ice concentrations of distinct ice classes, obtained from close-range imagery at DRLL03 during the 2016-17 winter, plotted with air temperature.

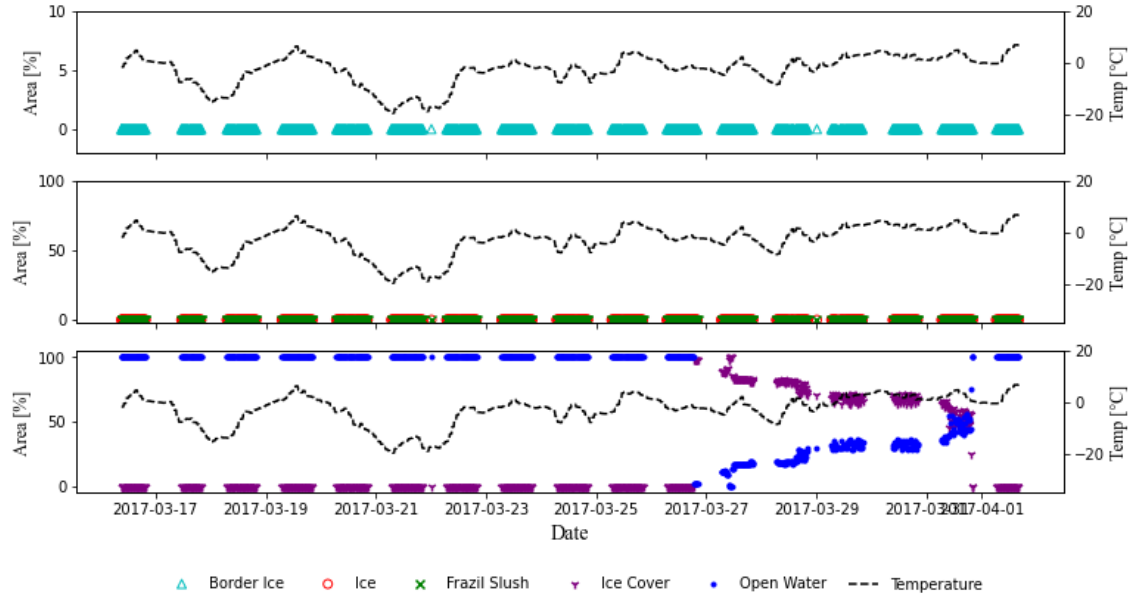

Figure 3-31 River ice concentrations of distinct ice classes, obtained from close-range imagery at DRLL04 during the 2016-17 winter, plotted with air temperature.

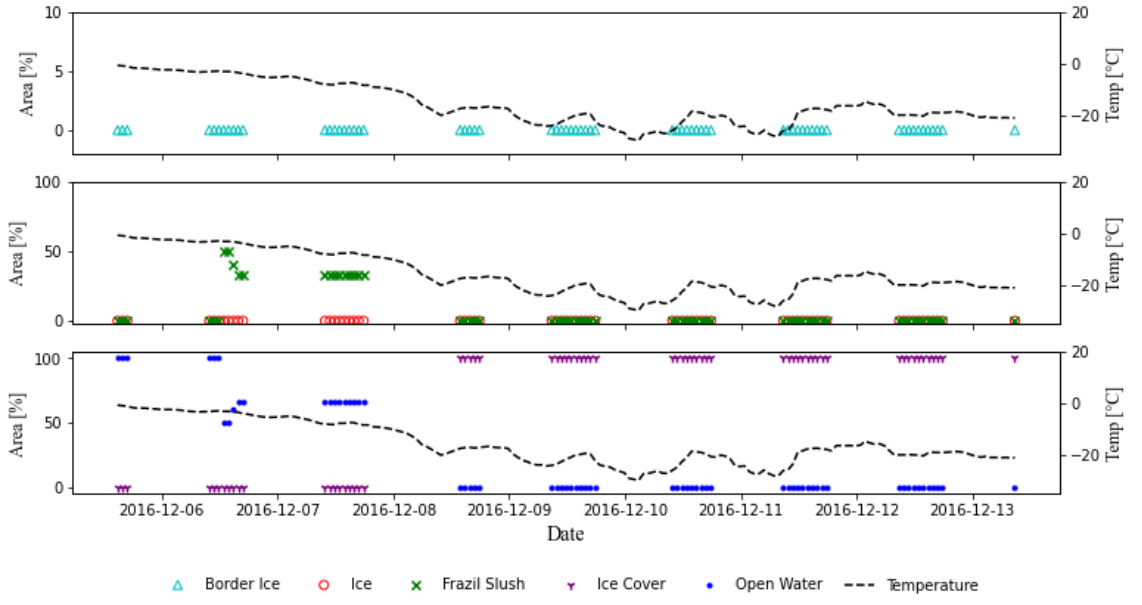

Figure 3-32 River ice concentrations of distinct ice classes, obtained from close-range imagery at DRLL06 during the 2016-17 winter, plotted with air temperature.

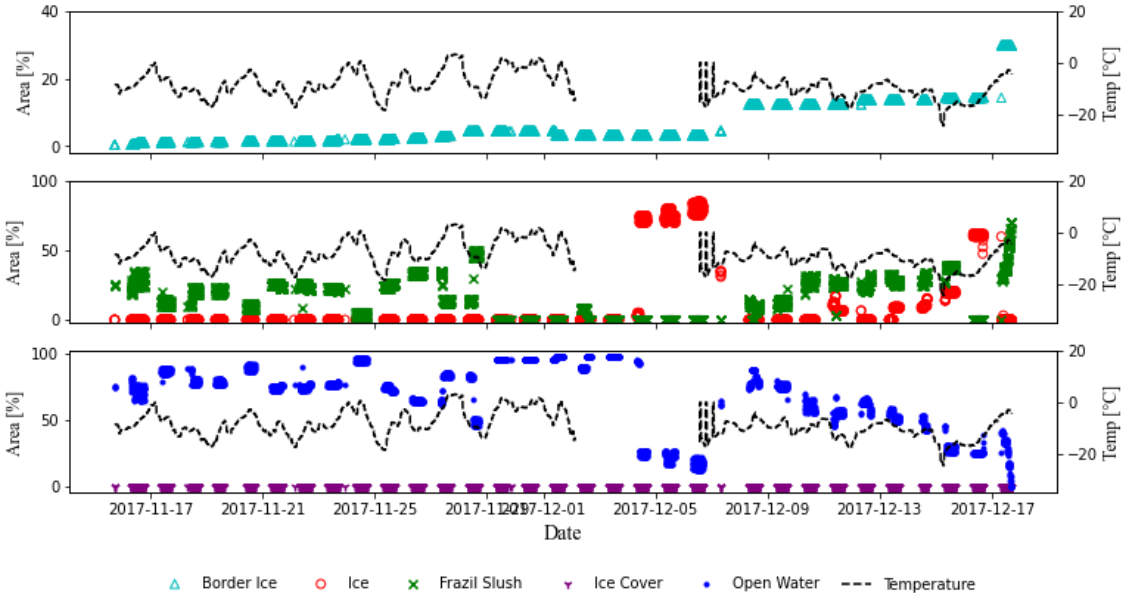

Figure 3-33 River ice concentrations of distinct ice classes, obtained from close-range imagery at DRLL03 during the 2017-18 winter, plotted with air temperature.

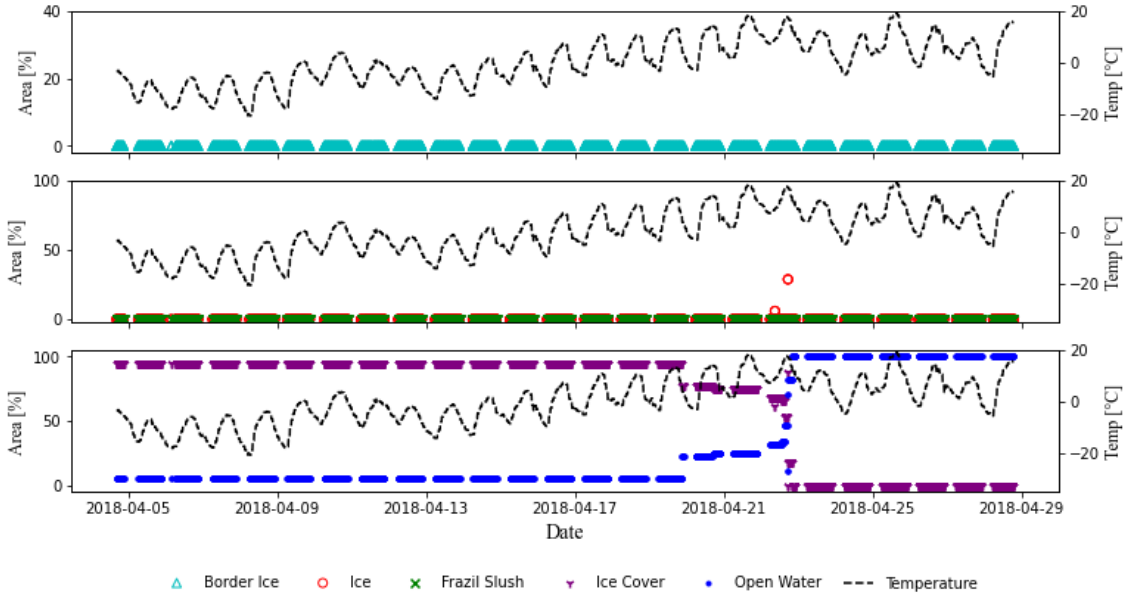

Figure 3-34 River ice concentrations of distinct ice classes, obtained from close-range imagery at DRLL04 during the 2017-18 winter, plotted with air temperature.

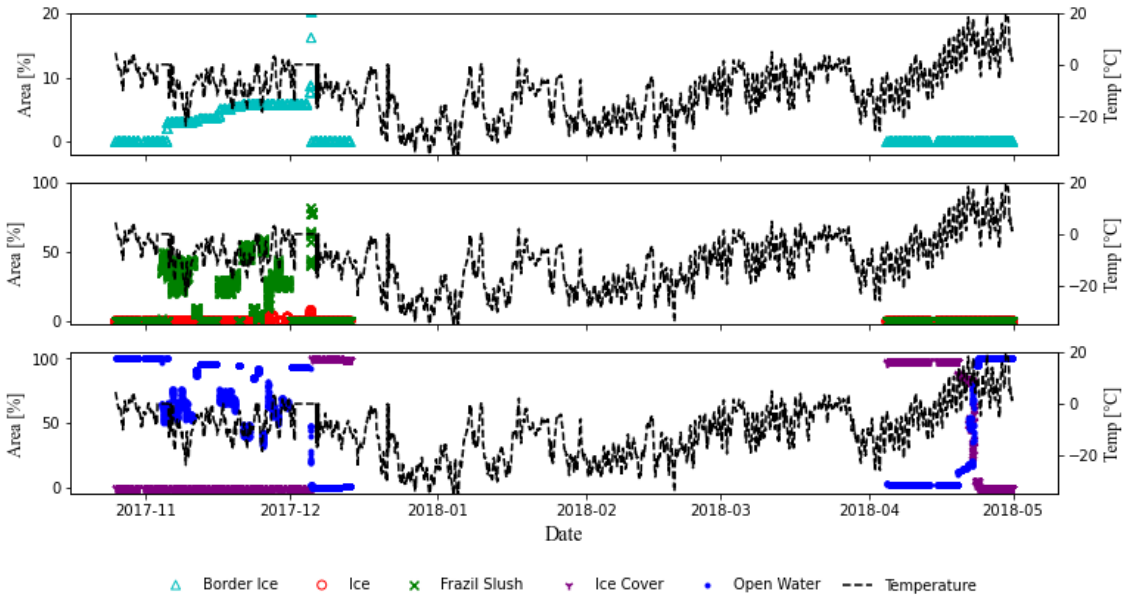

Figure 3-35 River ice concentrations of distinct ice classes, obtained from close-range imagery at DRLL05 during the 2017-18 winter, plotted with air temperature.

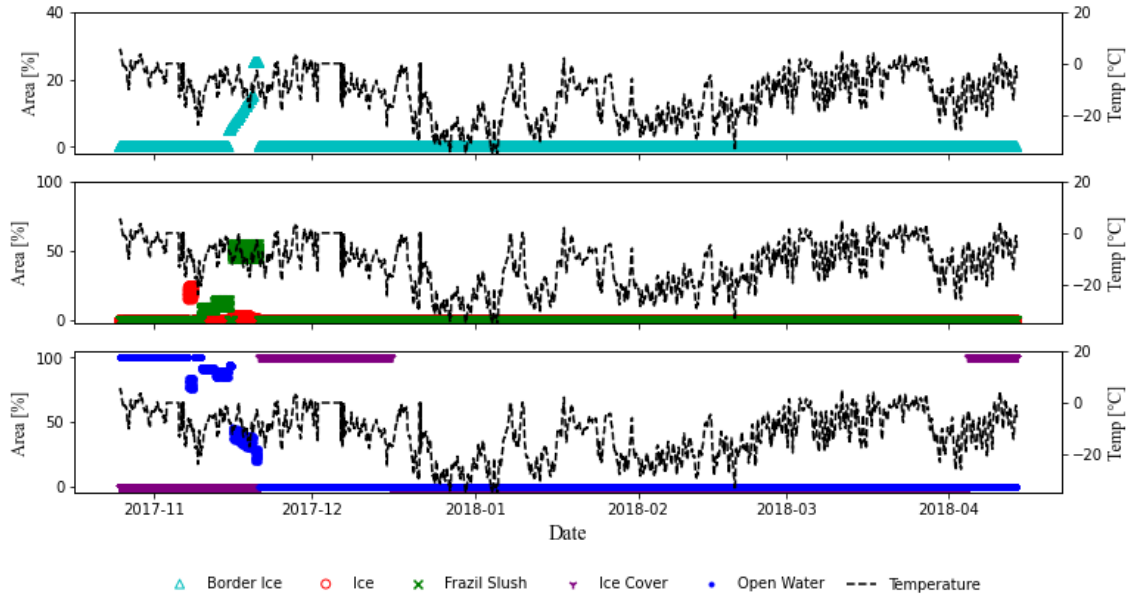

Figure 3-36 River ice concentrations of distinct ice classes, obtained from close-range imagery at DRLL06 during the 2017-18 winter, plotted with air temperature.

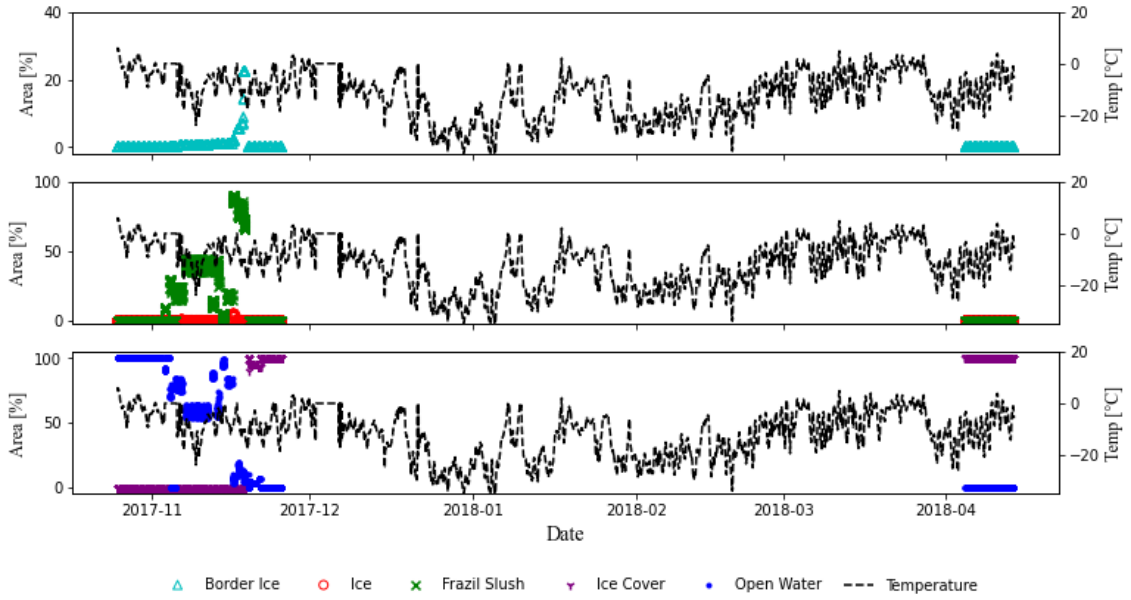

Figure 3-37 River ice concentrations of distinct ice classes, obtained from close-range imagery at DRLL06a during the 2017-18 winter, plotted with air temperature.

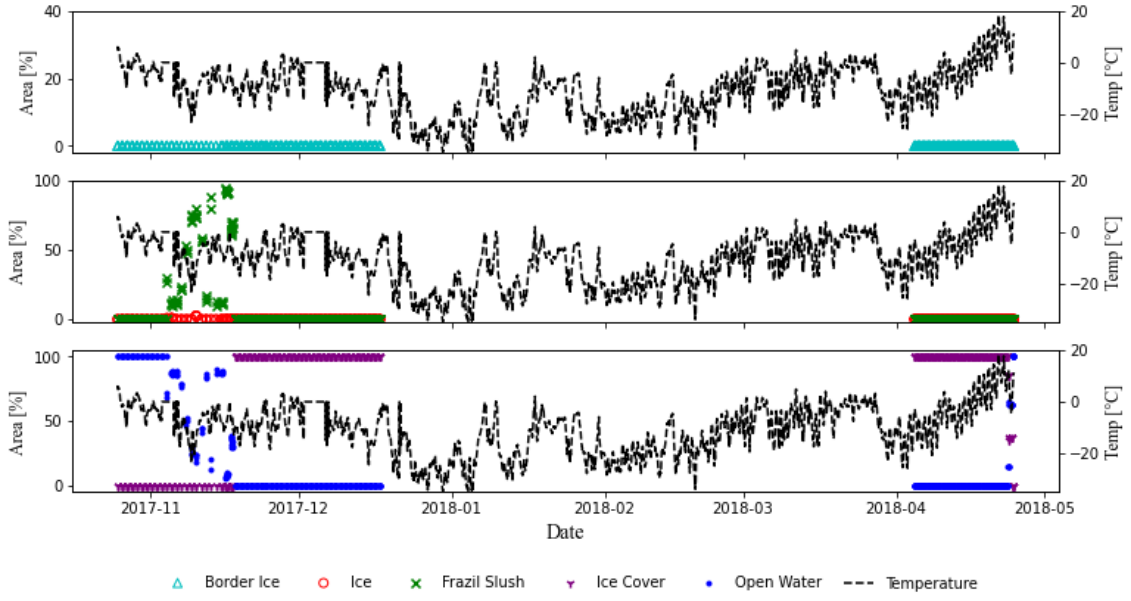

Figure 3-38 River ice concentrations of distinct ice classes, obtained from close-range imagery at DRLL06b during the 2017-18 winter, plotted with air temperature

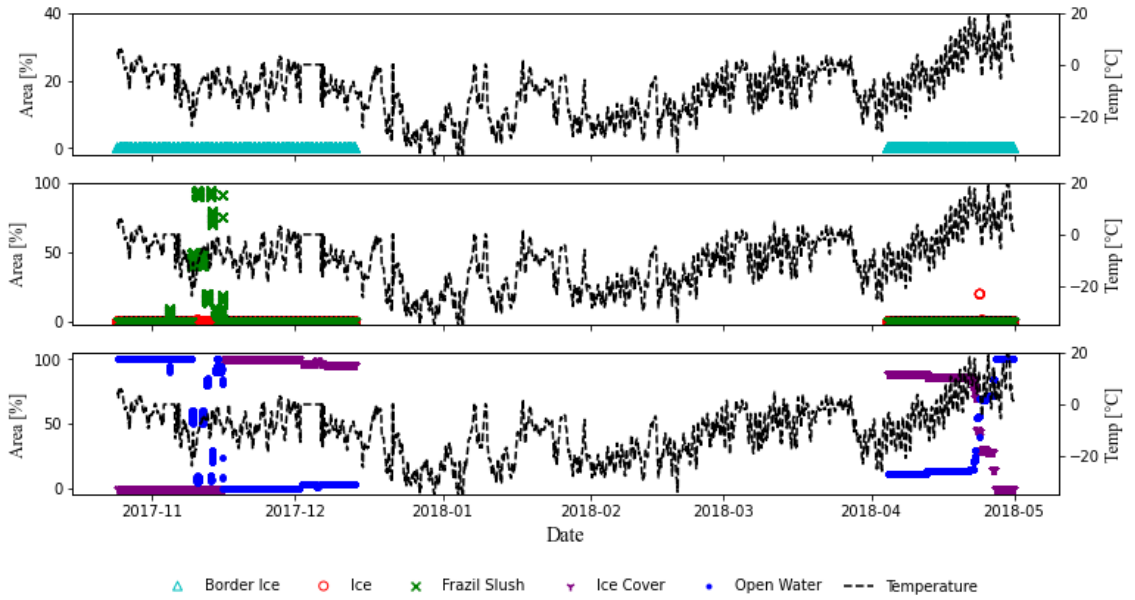

Figure 3-39 River ice concentrations of distinct ice classes, obtained from close-range imagery at DRLL07 during the 2017-18 winter, plotted with air temperature.

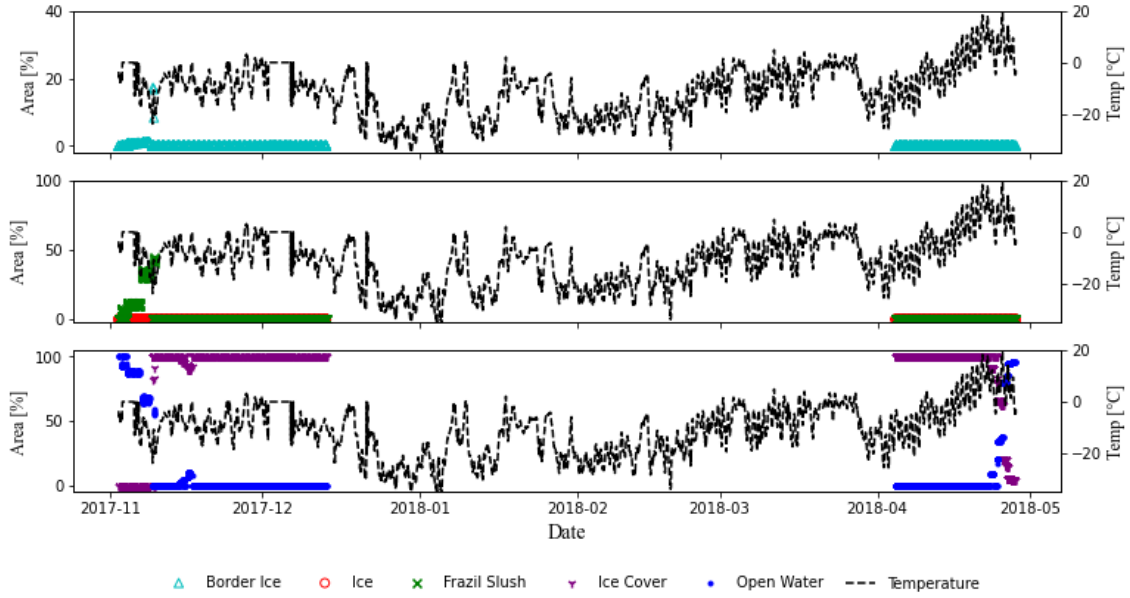

Figure 3-40 River ice concentrations of distinct ice classes, obtained from close-range imagery at DRLL08 during the 2017-18 winter, plotted with air temperature

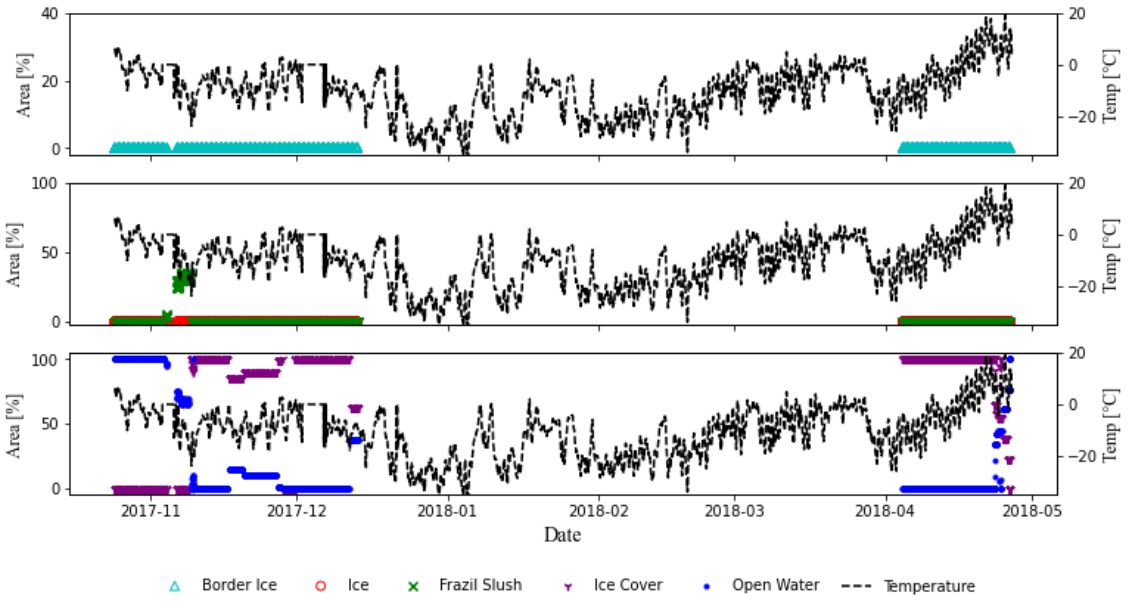

Figure 3-41 River ice concentrations of distinct ice classes, obtained from close-range imagery at DRLL08a during the 2017-18 winter, plotted with air temperature

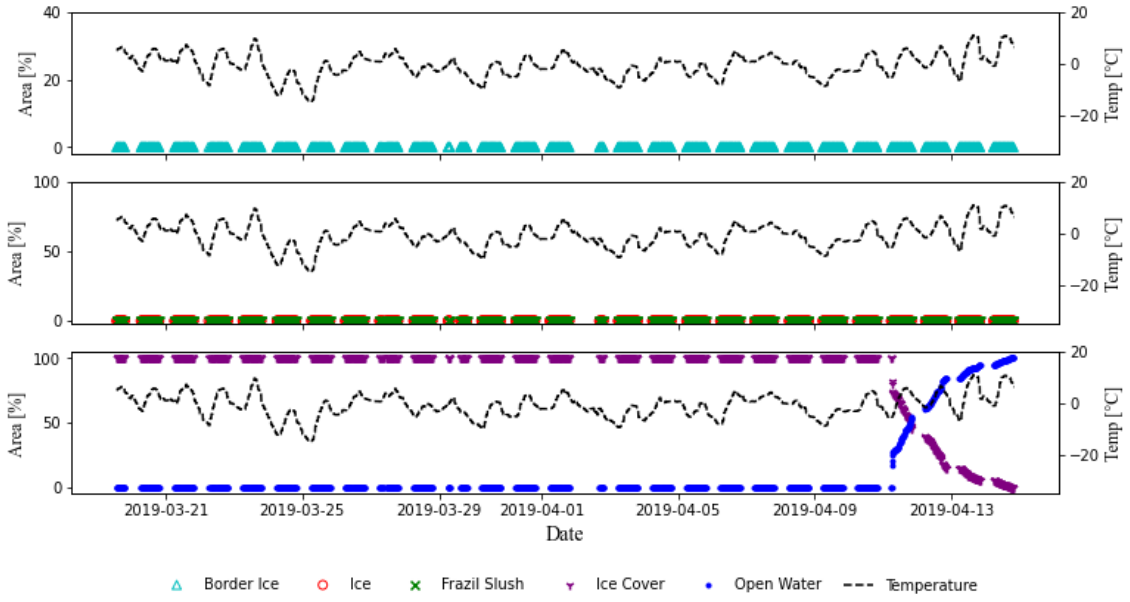

Figure 3-42 River ice concentrations of distinct ice classes, obtained from close-range imagery at DRLL03 during the 2018-19 winter, plotted with air temperature

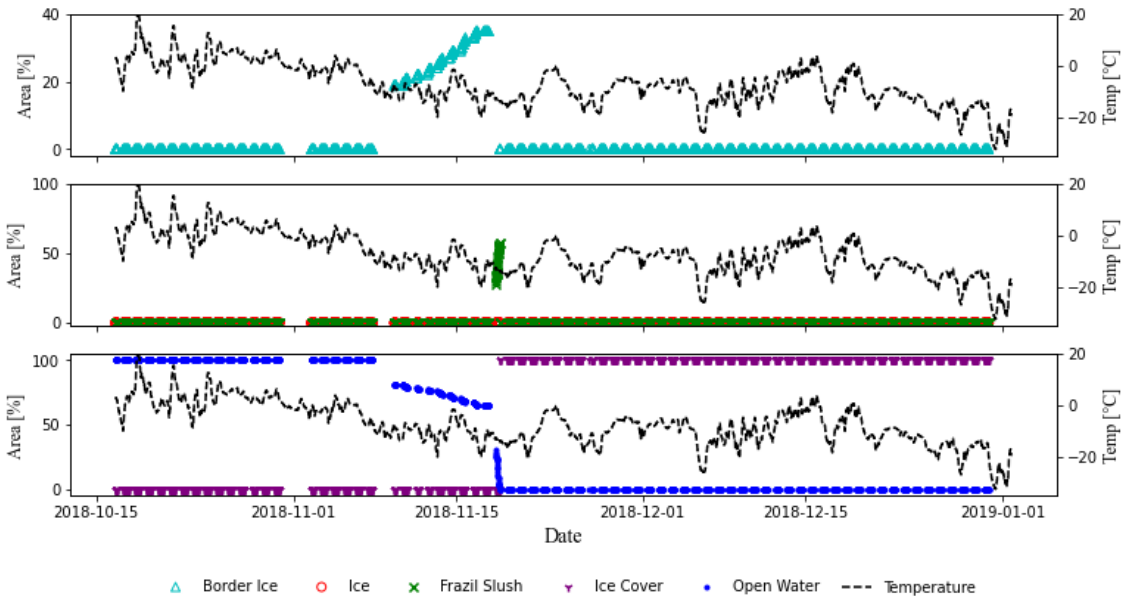

Figure 3-43 River ice concentrations of distinct ice classes, obtained from close-range imagery at DRLL04 during the 2018-19 winter, plotted with air temperature

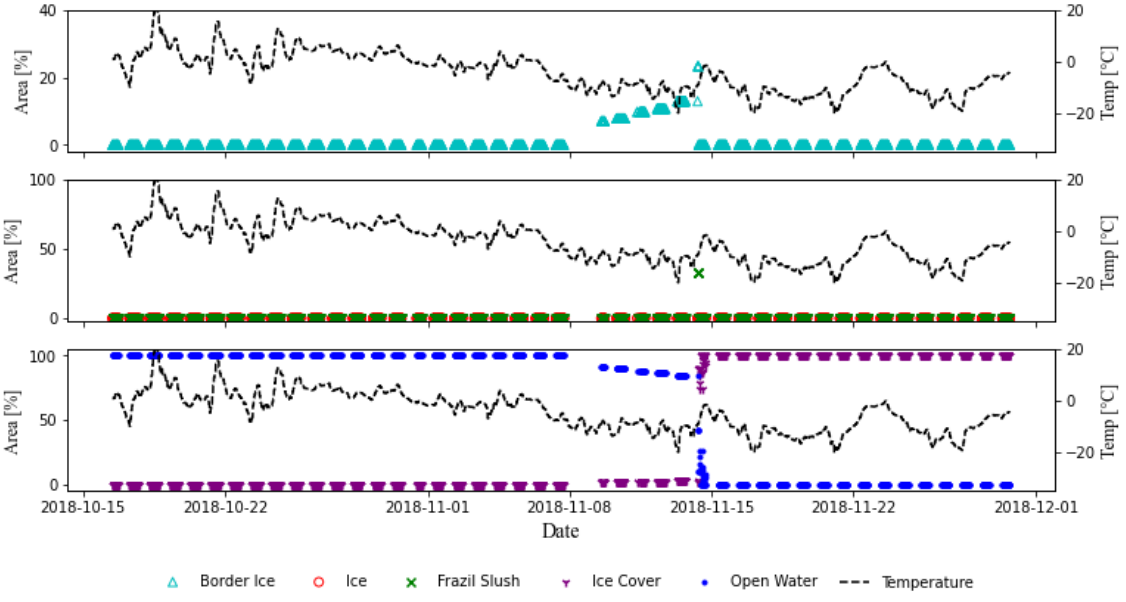

Figure 3-44 River ice concentrations of distinct ice classes, obtained from close-range imagery at DRLL05 during the 2018-19 winter, plotted with air temperature

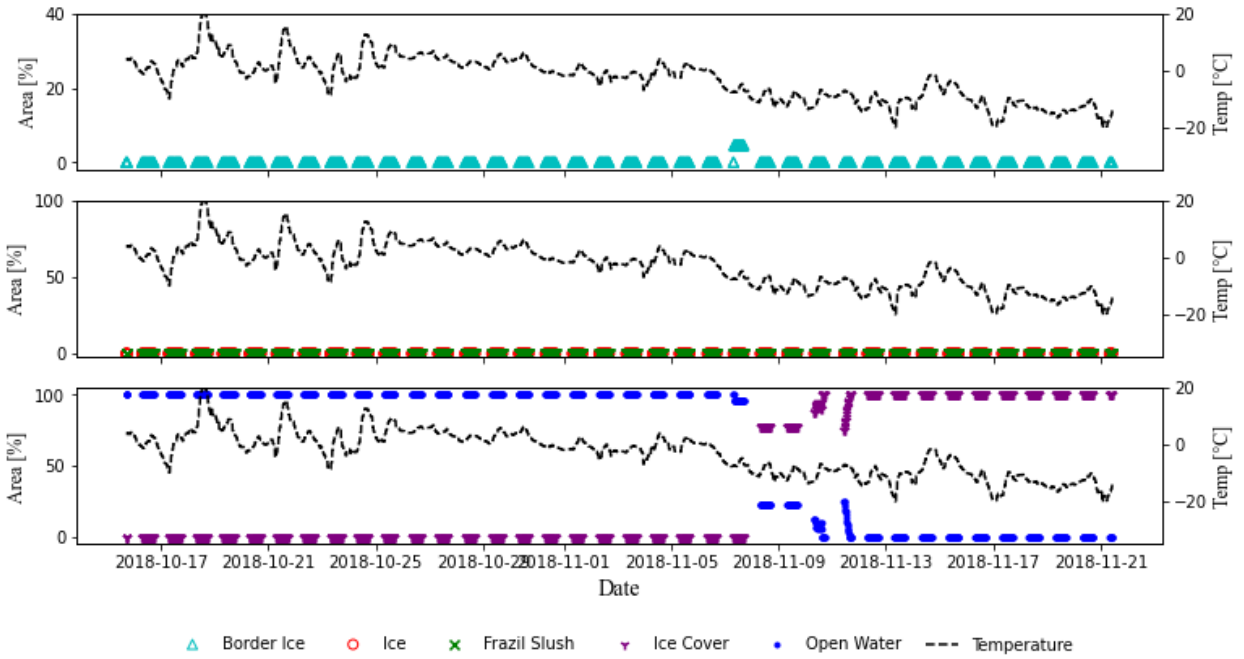

Figure 3-45 River ice concentrations of distinct ice classes, obtained from close-range imagery at DRLL06 during the 2018-19 winter, plotted with air temperature

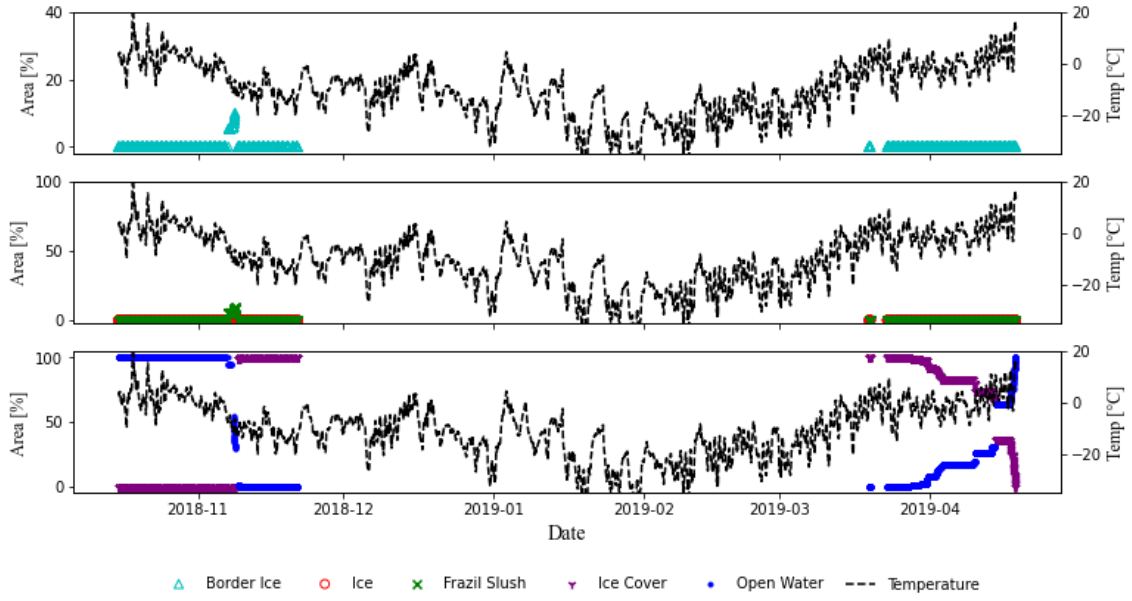

Figure 3-46 River ice concentrations of distinct ice classes, obtained from close-range imagery at DRLL07 during the 2018-19 winter, plotted with air temperature

3.3 Real-time classification of the sea ice interacting on a bridge pier using artificial intelligence techniques

Preprint of an article published in the proceedings of 25th IAHR International Symposium on Ice © IAHR

3.3.1 Introduction

Ice loading on the Confederation Bridge has been monitored by the University of Calgary (Brown, 2001, Brown *et al.,* 2010, Shrestha and Brown, 2018) and the NRC (Kubat *et al.,* 2000, and Poirier *et al.,* 2015) since its construction in 1997. This long term data record is the only one of its kind that provides ice loads on structures. The next longest comparable dataset is LOLEIF/STRICE which acquired 4 seasons of ice interactions against the Norströmsgrund lighthouse (Li *et al.,* 2016).

Visual examination of video data from the Confederation Bridge has provided researchers valuable information on the volume and type of ice interacting with the instrumented bridge piers, as well as the ice failure mechanisms. Visual observation is currently the most reliable means of ice characterization. However, this task is challenging, expensive and requires specialized training. New technologies in image processing and computer vision can be applied for this purpose. These would improve automation and reduce the time and effort required to collect these data. Attempts have previously been made for river ice detection and characterization using computer vision algorithms (Ansari *et al.,* 2017); machine learning methods (Kalke and Loewen, 2018) and deep learning techniques (Singh *et al.,* 2019) and (Ansari *et al.,* in prep.). In this study, an automated sea ice characterization algorithm was developed to detect and characterize the sea ice interacting with a bridge pier.

3.3.2 Study area and data

Confederation Bridge is the longest structure in the world constructed in ice-covered waters. The Confederation Bridge as part of the Trans-Canada Highway is the 13-kilometre linkage between the provinces of Prince Edward Island and New Brunswick across the Northumberland Strait. This bridge has 45 main spans, each 250 m long, that rest on a total of 44 piers (Poirier, Babaei and Frederking, 2015). Figure 3-47 illustrates the bridge and its location. As part of a comprehensive ice load monitoring program, two Sony SNC-EB632R cameras are installed to examine ice failures on two of the bridge piers. Cameras are connected to the network, and they are programmed to collect an image every 3 seconds. According to the Canadian Ice Service (CIS)

Gulf of St. Lawrence, the ice season in this location is between December 31st to April 15 (Johnston M.E. and Timco, G.W. 2008).

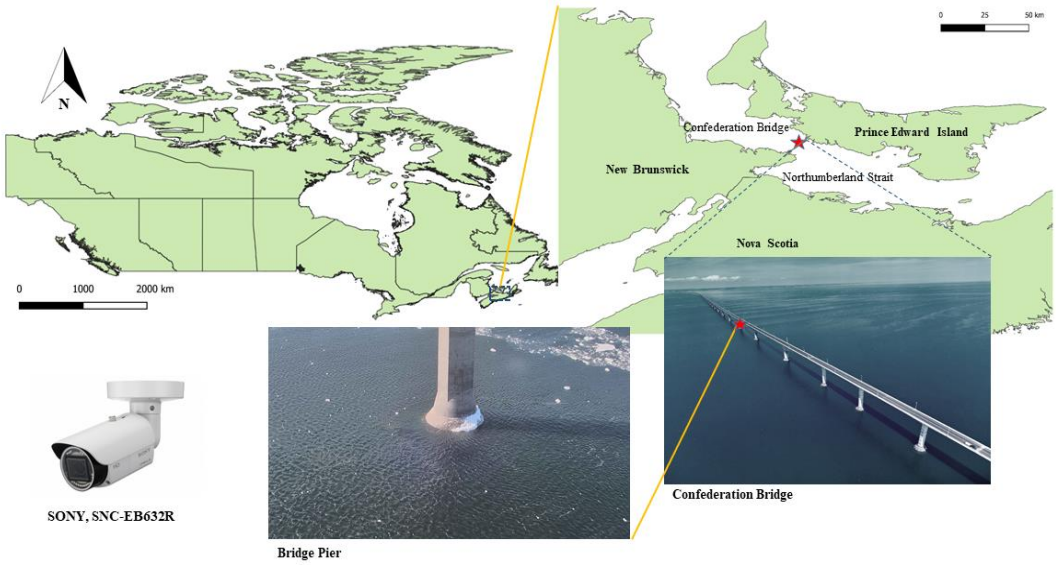

Figure 3-47 Project location, Confederation Bridge, and the SONY, SNC-EB632R

The vast number of images not only helps in the monitoring task but also provides the possibility of developing data-driven approaches for sea ice characterization. In this study, four different classes of sea ice have been defined for automatic recognition. These classes include Icefloe, Broken, Ridge, and Flex. The majority of the ice in any given image is ice floe (Icefloe). Icefloe is generally a piece of level ice that is at least half as large as the pier base, i.e., ≥ 5 m in diameter (Figure 3-48a). An Icefloe can also include deformed (ridged or rafted) ice. Broken sea ice is considered as the least imposing ice on a vessel or a structure. These are pieces of ice no larger than half of the pier base; in this dataset they are usually broken as a result of interacting with the bridge pier (Figure 3-48b). Deformed ice (ridged or rafted) is identified as Ridge (Figure 3-48c). Rafted ice occurs when two level ice sheets collide with each other and one is pushed over the other one leading to thickening of ice. Ridged ice, on the other hand, is when levelled ice interacts with an object, causing broken ice pieces to accumulate above or under the ice sheet. Finally, due to the conical shape of the bridge pier, ice interaction with the bridge leads to flexural failure; this is characterized as Flex in the presented algorithm (Figure 3-48d).

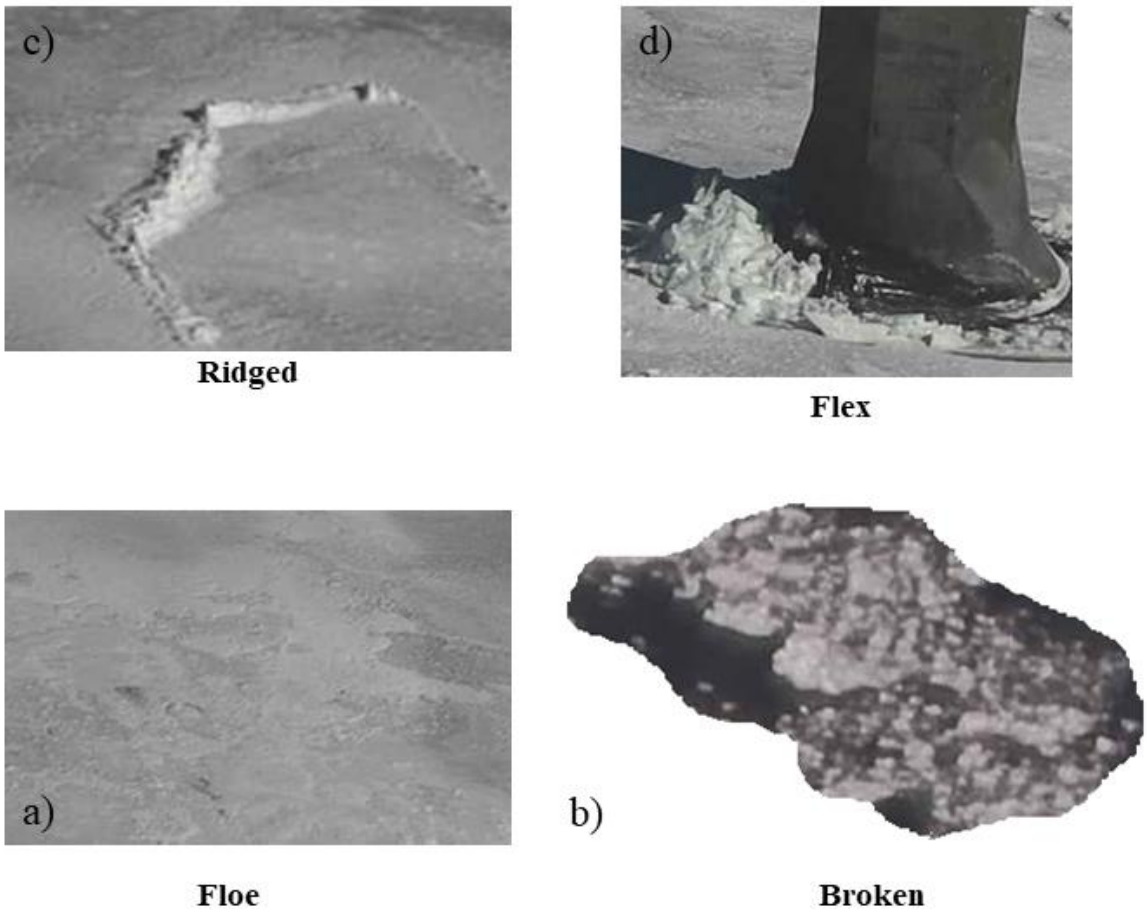

Figure 3-48 Different ice type classes; a) Floe; b) Broken ice; c)Ridged; d)Flex

3.3.3 Methodology

An instance image segmentation and object detection algorithm was employed to develop a real-time sea ice detection and classification algorithm. Mask RCNN model (He *et al.,* 2017) is the base model to establish the sea ice recognition algorithm. The Mask RCNN model used in this study was built on the Faster RCNN (Ren *et al.,* 2017) model. In the Mask RCNN a convolutional neural network first is used to generate object proposals within the image. An object proposal is essentially a rectangular area within the image that is identified to have a classifiable sea ice object within it. Then the Mask RCNN classifies the bounding boxes and adds an extra mask over the region of interest (RoI) (He *et al.,* 2017) to specify the polygon of the classified sea ice object. The architecture of the used model consists of a feature extraction model using a 101 layer Residual Neural Network (ResNet) (He *et al.,* 2006). After the feature extraction, the Region Proposal

Network (RPN) is used to generate the correct RoI. The generated RoIs are then classified using the RoI classification algorithm. In the next step, a bounding box regressor is used for refining the bounding boxes of the classes and another methodology named as RoIAlign based on a bilinear interpolation is used for pixel-wise prediction of the masks (He *et al.*, 2017). Figure 3-49 illustrates the developed algorithm used for automated classification of the sea ice interacting with the bridge pier.

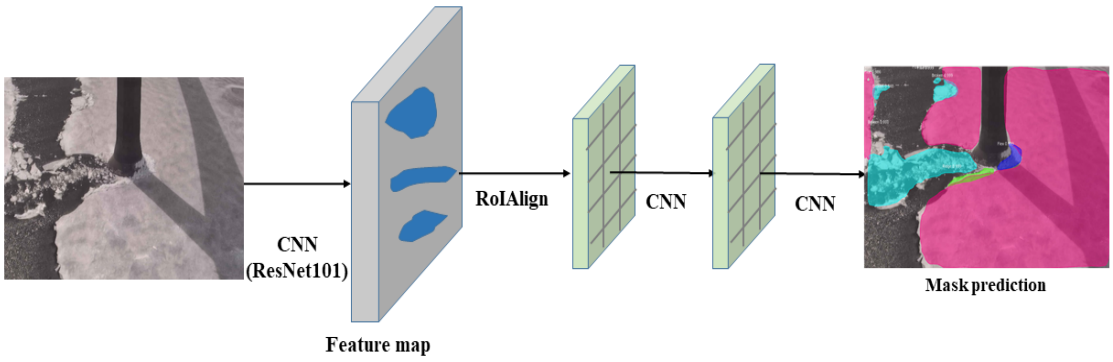

Figure 3-49 Architecture of the utilized improved version of the Mask-RCNN

3.3.4 Implementation

The developed algorithm utilizes the Mask RCNN model on TensorFlow (Abadi et al. 2015). The training of the model was conducted on a Graphics Processing Unit (GPU) equipped machine. Parallel GPU computing was utilized to accelerate the training process of the model. The training was performed on the backbone structure of ResNet101 (101 layers), with a batch size of 2 images with a training rate of 0.0015 and learning momentum of 0.88 and weight decay of 0.0002. The trained Mask RCNN model was performed on the pre-trained weights of the COCO data (Common Objects in Context) set (Lin *et al.*, 2014). 120 images with the size of 1920 × 1080 were annotated to be used in the training procedure. The image data set was split into 80 percent for training and 20 percent for validation. Moreover, in order to increase the generalization of the algorithm, simple data augmentation techniques such as random flips, left zoom, right zoom were employed in the model. The inference process was also conducted with a detection confidence of 70%.

The utilized model was optimized during the training process to evaluate the accuracy of the model and the sufficient number of the annotated images for the training process. The training process was performed with 100 epochs.

3.3.5 Results and discussion

After the investigation of the loss and validation parameters, the results indicate that validation loss values quickly reach their lowest after a few ephochs and then continue to fluctuate. However, training loss values continue to decend. This suggests that the model memorizes before the 20th epoch. Thus running the model for the 100 epochs does not give any advantage. Based on the validation loss increase no more than 20 epochs should be utilized, because otherwise the model is overfit to the training data-set. The reason for this is that the training process has been conducted on a weighted data set as a result of pertaining COCO dataset. Moreover, this is an indication of the insufficiency of the labelled images for the training process.

Figure 3-50 shows some results of the sea ice characterization algorithm. Four different classes of floe, broken, flex, and ridge have been detected. The detected ice types have been segmented with masks and their associated colors. The results show that the developed algorithm was able to detect, identify and characterize the four different classes accurately and with acceptable pixel-wise accuracy. While the results are promising, two sets of errors were discovered. Although the classification and detection tasks were conducted correctly the mask prediction has some errors. The errors include the marginal error in the boundaries of the masks and some overlaps in the mask prediction pixels. As this was predictable from the loss graphs in the optimization process, there is still a need to perform the manual labelling task on a greater number of images to ensure the reliability of the system.

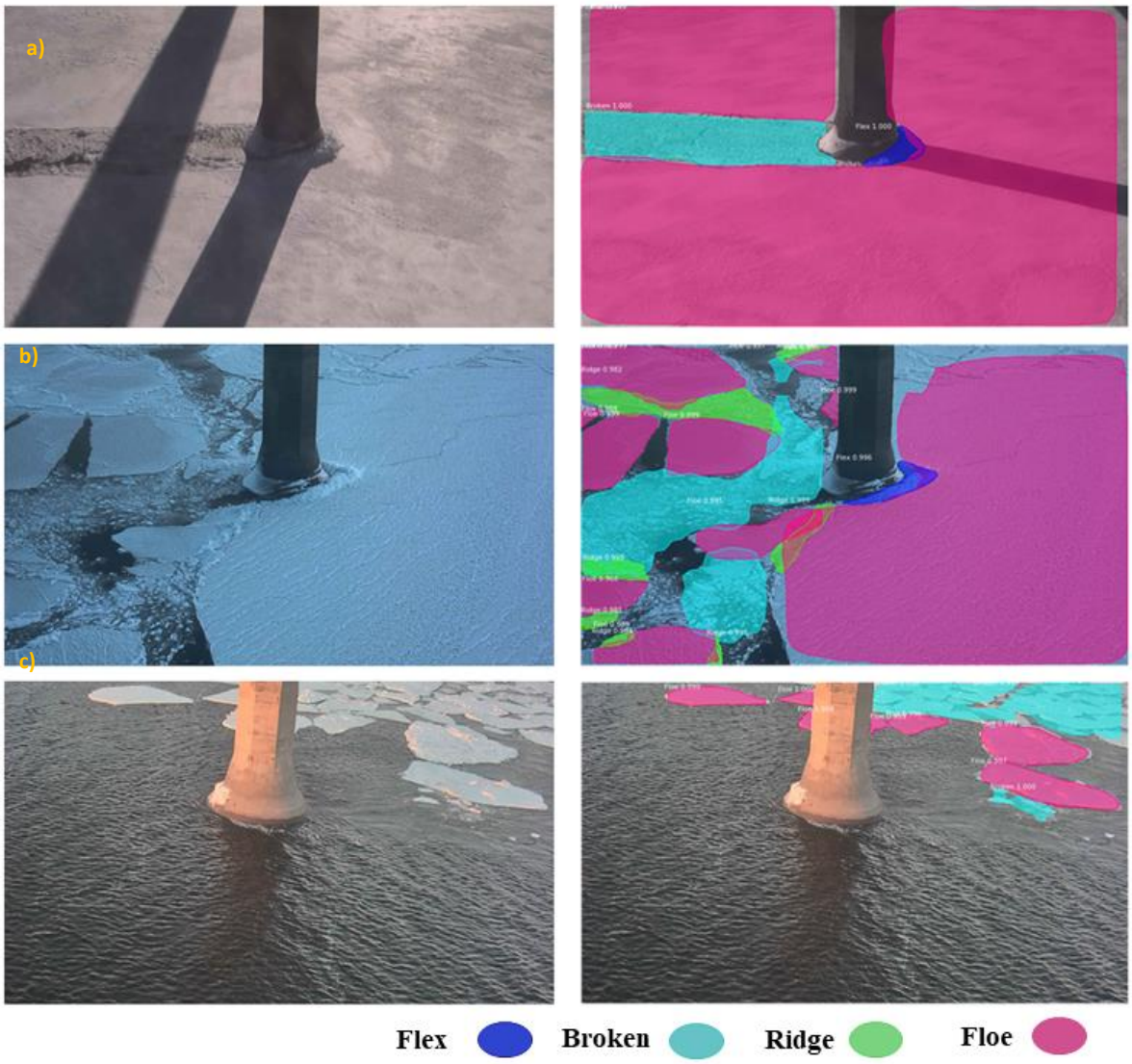

Figure 3-50 Sample results of the sea ice segmentation algorithm

3.3.6 Conclusion

As part of a comprehensive and automated monitoring network a sea ice characterization algorithm was developed to detect and recognize different classes of ice interacting with a bridge pier. With a changing climate, results of such a study are crucial, since monitoring, and specifically automated smart monitoring, is vital in providing the public with high-standard safe and reliable infrastructure. The developed algorithm employed an improved version of the Mask RCNN to improve sea ice characterization. The results indicated an acceptable outcome with some minor shortcomings, which should be investigated in future studies. Annotation of more images is a key factor in the generalization of the developed algorithm, which should be conducted in future work.

4. Photogrammetry techniques for surface velocimetry

4.1 RivQNet: Deep Learning based river discharge estimation using close-range water surface imagery

Preprint of an article printed in Water Resource Research © WILEY https://doi.org/10.1029/2021WR031841

4.1.1 Introduction

Streamflow data are of great importance in geoscience, hydraulic and hydrological research and engineering. In most open channels, streamflow measurements are performed using the velocity-area method utilizing velocity and depth measurements of a channel cross section (Rantz, 1982). Direct measurement of flow depth and velocity for streamflow can be difficult and expensive tasks that can also potentially be dangerous during extreme high flow or flooding events (Le Coz *et al.,* 2012; Tauro *et al.,* 2017). Therefore, it is common practice to establish routine discharge estimation using rating curves relating water level to flow (Rantz, 1982; Clarke, 1999; Le Coz *et al.,* 2012). Rating curves have been widely used for estimating continuous open channel flow. However, results derived from rating curves can be unreliable, due to various sources of error, such as cross section changes and bed movements. Moreover, since rating curves are mostly created using data acquired in low to moderate flow conditions, they may be inaccurate for high flow and flooding conditions (Kavetski *et al.,* 2006; McMillan *et al.,* 2010; Tauro *et al.,* 2017). The emergence of acoustic instrumentation for flow measurements such as the Acoustic Doppler Current Profiler (ADCP) improved rating curves by providing flow velocity throughout the entire cross section as well as more spatially intensive bathymetric data. Application of ADCPs for direct flow measurements has reduced rating curve derived discharge uncertainty due to more frequent and accurate discharge measurements. However, ADCP surveys in some cases can be expensive and laborious and not a suitable choice for flow measurement in flooding conditions or where continuous or timely discharge measurements are required, such as during rapidly changing conditions or in remote locations.

Non-contact river flow sensing mostly involves use of either high-frequency radar or optical imagery to measure velocity at a predefined location, which could be a single point, cross section or field of view. Non-contact flow measurement methodologies have several advantages with respect to the traditional methodologies: they do not disturb the flow, their application can be easier compared to the traditional methods, and they can also be conducted continuously and in various flow conditions (Aberle *et al.,* 2017). They also have several limitations that can be summarized as: measurement of velocity at only the water surface, and being subject to other environmental

considerations like wind, surface water texture, camera stability, and adequate lighting (Muste *et al.,* 2008; Muste *et al.,* 2014; Pearce *et al.,* 2020). Application of infrared cameras have addressed these issues to a great extent and have been introduced as a solution (Schweitzer et al. 2021). To estimate discharge from surface velocimetry, an index must be estimated to calculate depth-averaged velocity, and depth across the section must be known. There have been studies to estimate river bathymetry determined from surface turbulence metrics and remote estimation of velocity index (Johnson et al, 2016, 2017). Various applications of different radar technologies for flow measurement have been presented in several studies; Costa et al. (2000) utilized a fixed 10 GHz radar for flow measurements, Melcher et al. (2002) employed a helicopter mounted radar for river discharge measurements, and Costa et al. (2006) performed a comprehensive assessment of the technique. Nonetheless, surface velocity radar methods are still not universally deployed by hydrometric monitoring agencies.

The concurrent advent of high technology, cost-effective, commercial cameras with developments in image processing and computer vision has led to the vast application of close-range remote sensing in various geoscience and environmental engineering research studies. In the literature monitoring and data collection using radar, LiDAR, infrared and optical cameras that are conducted from a closer distance compared to satellite imagery are categorized as close-range remote sensing (e.g. Jakubauskas et al. (2000); Fraser, C.S. 2013). Flow visualization in fluid mechanics and hydraulics developed with several research works in the late 20th century (e.g. Clayton & Massey (1967); Werle (1973); Gadel Hak (1988); Adrian (1991); Freymuth (1993)). Most of these studies focused on flow structures in various flow conditions such as turbulent and laminar flows. With the advent of new imaging technologies, image-based surface velocimetry has developed rapidly as a non-contact, inexpensive technique over a wide range of spatial and temporal scales. Application of optical imagery for hydrometric measurements initiated with the application of particle tracking velocimetry (PTV) and large scale particle image velocimetry (LSPIV) approaches such as research works by Fujita et al. (1998, 2007). Application of these methodologies, especially LSPIV, gradually received a high acceptance and interest but has not yet been widely used by researchers and hydrometric practitioners. Additionally, alternative methods were also introduced such as the space-time image velocimetry (STIV) (Fujita *et al.,* 2007). Several studies on the application of close-range remote sensing (i.e. aerial/terrestrial) through optical imagery for surface velocimetry demonstrated its applicability in laboratory experimental studies (e.g. Jodeau *et al.,* 2017), flood monitoring (e.g. Le Coz *et al.,* 2010), long-term flow measurements in hydrometric stations (e.g. Ran *et al.,* 2016) as well as its application for shallow water flow measurements (e.g. Muste *et al.,* 2014). The extraordinary potential of

image-based surface velocimetry techniques for both long-term continuous and incident based flow monitoring, coupled with the emergence of Remotely Piloted Aircraft Systems (RPAS), made this technology a candidate for further development. Fast developments in image processing and computer vision techniques and image acquisition and storage software and hardware, along with the high interest of the hydrological community, have led to the development of several image-based surface velocimetry algorithms that are either open-source or proprietary (Perks *et al.*, 2020). The developed tools can generally be categorized into two different categories: correlation based techniques (e.g., Fudaa-LSPIV (Le Coz *et al.*, 2014), RIVeR (Patalano *et al.*, 2017), MATPIV (Sveen & Cowen, 2004), PIVlab (Thielicke & Stamhuis, 2014), PTVlab (Brevis *et al.*, 2011), Hydro-STIV (Fujita *et al.*, 2007)), and classical energy based optical flow approaches (e.g, OTV (Tauro *et al.*, 2018)). Although both software categories can provide relatively accurate results there are still some areas for enhancement, such as the requirement for user defined input both in pre- and post-processing stages can lead to user subjectivity and user-induced errors and thus flow estimation discrepancies (Kim *et al.*, 2008; Pearce *et al.*, 2020).

In this study a third category of image-based surface velocimetry algorithm based on deep learning approaches is introduced. The accuracy of the presented method is investigated using data sets acquired from a laboratory experiment and several field surveys. In all cases, in situ measurements of near surface velocities are used for validation. First, conventional optical flow routines (i.e. in computer vision methods that estimate motion) are reviewed, then RivQNet is introduced as a new surface velocimetry algorithm, based on recent deep learning optical flow approaches. The performances of RivQNet and conventional optical flow methods are then compared. The best deep learning approach for surface velocimetry and its superiority to conventional optical flow methods is determined through analysis of both the laboratory data and field cases. RivQNet with the preferred approach is then applied to several field cases and overall accuracy of deep learning surface velocity estimation is assessed. Finally, the calculated surface velocities for each case are used to estimate river discharge, and errors are assessed by comparison to in-situ discharge measurements. The entire deep learning procedure for discharge computation from surface imagery is coded as RivQNet.

4.1.1.1 Classical optical flow motion estimation

Optical flow methods are a group of methods to estimate motion and are based on the apparent flow field between two consecutive frames. In computer vision, optical flow is considered as a significant topic with various applications such as object detection (e.g. (Agarwal *et al.*, 2016)),

pose estimation (e.g. (Pfister *et al.*, 2015; Allan *et al.*, 2015)), action recognition (e.g., Wang & Schmid (2013); Sevilla-Lara et al. (2018); Wang et al. (2011)), autonomous driving (e.g. Bai et al. (2016); Siam et al. (2017)), and video gaming and editing (e.g. Jin et al. (2017)). In most classical optical flow methods, the apparent motion field is developed based on a variational methodology presented by Horn & Schunck (1981), who presented the pixel intensity conservation assumption known as the classical optical flow constraint equation (Equation 4-1).

$$\frac{\partial I}{\partial t}(\mathbf{x}, t) + \mathbf{u}(\mathbf{x}, t).\nabla I(\boldsymbol{x}, t) = 0 \tag{4-1}$$

Where I is pixel intensity, **u,** is the velocity field, *t* is time between two consecutive frames and ∇ is the spatial gradient (i.e. smoothness term) which assumes the consistency of the gray level of a particular pixel (i.e. $= (x, y)^T$) in two consecutive frames (Horn & Schunck, 1981). Resolving a two dimensional velocity field in isobrightness regions is not possible. In computer vision this is called the aperture problem. Horn & Schunck (1981) proposed an optimization approach to resolve the velocity field using the constraint equation (i.e. equation 4-1). This method is based on a minimization formulation consisting of a temporal pixel brightness consistency for motion estimation and a spatial smoothness term for smoothing neighboring pixels for similar motion (Horn & Schunck, 1981). The Horn-Schunck optical flow can be calculated based on an energy minimization approach that involves a data term, which encourages temporal brightness consistency, and a spatial smoothness term regularizing neighbouring pixels. The energy minimization formulation can be written as (Horn & Schunck, 1981; Hur & Roth, 2020):

$$E(\mathbf{u}) = \int (I_x u_x + I_y u_y + I_t)^2 + a^2 \left(\left|\left|\nabla u_x\right|\right|^2 + \left|\left|\nabla u_y\right|\right|^2 \right) dxdy \tag{4-2}$$

In equation (4-2), I_x, I_y, I_t are spatial and temporal pixel intensity derivatives and is the spatial gradient (i.e. smoothness term) which assumes the consistency of the gray level of a particular pixel in two consecutive frames (Horn & Schunck, 1981). The Horn and Schunck method (HS) is considered a global approach that is very sensitive to noise (defined as random variation of brightness and/or color intensity). In different image regions where the data term is lacking, the HS method performs an implicit interpolation leading to potentially unreliable data (Barron *et al.*, 1994). In a previous study Ansari et al. (2018) utilized an improved Horn-Schunck approach to detect and track surface boils of a steep bedrock canyon river, after applying some image

processing algorithms. Local optical flow approaches have addressed this issue with the application of matrix computations and thus are more robust to noisy data. Two widely used local optical flow techniques, Lucas-Kanade and Farneback, were utilized to investigate the applicability of optical flow approaches for surface velocimetry.

4.1.1.2 Lucas-Kanade

The Lucas-Kanade method (Lucas *et al.*, 1981), also known as a sparse optical flow method is considered a Lagrangian local approach. The brightness consistency equation (equation 4-1) can be written as:

$$\nabla I . u_0 = -\frac{\partial I}{\partial t} \tag{4-3}$$

To solve this equation additional constraints should be added. Lucas et al. (1981) proposed defining neighbouring windows with consistent pixel intensities for consecutive frames. This approach defines more equations than unknowns that can be solved by an iterative approach to minimize the sum of squared errors of the following equation.

$$(\nabla[I_0, I_1, \dots, I_{n-1}])^T . u_0 = -\frac{\partial I}{\partial t}[I_0, I_1, \dots, I_{n-1}]^T \tag{4-4}$$

The Lucas-Kanade method has been employed in various scientific fields for motion extraction such as in radar-based rainfall nowcasting (Woo & Wong, 2017), glacier motion extraction (Vogel *et al.*, 2012), measurement of bedload sediment transport (Blanckaert *et al.*, 2017), and measuring fine-scale sea ice drift (Karvonen, 2016). Moreover, a discharge estimation software based on the Lucas-Kanade algorithm has also been developed named OTV (Tauro *et al.*, 2018). In this study we utilize an improved feature extraction application (Shi *et al.*, 1994) of the Lucas-Kanade method, coded in OpenCV-Python.

4.1.1.3 Farneback

Two frame motion estimation based on a spatial polynomial expansion approach was proposed by Farneback (2003) for motion estimation. This approach estimates the motion field for every pixel

and is considered a dense Eulerian technique. For a pixel in a specific local coordinate vector (x) the neighbourhood approximation by a quadratic polynomial (Farneback, 2003) is considered as:

$$f_1(x) = x^T A_1 x + b_1^T x + c_1 \tag{4-5}$$

In this equation, *x* is the pixel coordinate in a local coordinate system, A_1 is a symmetric matrix, b_1 is vector and c_1 is a scalar. After constructing a new signal f_2 by a global displacement *d*, motion in a neighborhood is estimated by transforming the initial approximation using quadratic polynomials (Farneback, 2003):

$$\begin{aligned} f_2(x) = x^T A_2 x + b_2^T x + c_2 &= f_1(x - d) \\ &= x^T A_2 x + (b_1 - 2A_1 d)^T x + d^T A_1 d - b_1^T d + c_1 \end{aligned} \tag{4-6}$$

By equating the coefficients in the quadratic polynomials, displacement is calculated as:

$$d = -\frac{1}{2} A_1^{-1}(b_1 - b_2) \tag{4-7}$$

Although Equation 4-**Error! Reference source not found.** is initially a pixel-wise solution, it w as also recommended by Farneback (2003) to consider a neighbourhood of *x* to solve this equation for noise reduction. While there are some similarities between the Lucas-Kanade and Farneback methods, smoother results are expected for the Farneback solution due to the utilization of a quadratic polynominal approach. To the best knowledge of the authors there is no application of Farneback optical flow algorithm for image-based surface velocimetry and flow estimation. In this study, both the Lucas-Kanade and Farneback optical flow methods were coded in OpenCV-Python to be employed for surface velocimetry.

4.1.1.4 Optical Flow Estimation Using Convolutional Neural Networks

Recent advances in Convolutional Neural Networks (CNN) and their application in computer vision and especially in image classification (Krizhevsky *et al.*, 2017), have introduced new horizons for other computer vision applications such as in optical flow estimation. Application of CNN in optical flow estimation started with a combined approach. These methods combine classical optical flow methods with deep learning based approaches. They utilize CNN-based feature extraction to produce the data term for classical energy based optical flow i.e. Equation 4-

3 (Bai *et al.*, 2016; Gadot & Wolf, 2016; Guney & Geiger, 2016; Bailer *et al.*, 2017; Hur & Roth, 2020). On the other hand, other efforts have focused on the application of regression-based CNN architectures (Hur & Roth, 2020). These include end-to-end architectures that can directly estimate the motion between two consecutive pairs of images. FlowNet, with an encoder-decoder architecture is the first regression-based CNN approach for optical flow estimation (Fischer *et al.*, 2015). The original FlowNet algorithm includes two important subsections: one learning to detect image features, and one matching them at two different locations in two consecutive images to generate displacement (Fischer *et al.*, 2015). The FlowNet architecture was trained on a synthetic flying chair dataset of CAD models by Aubry *et al.*, 2014 and Fischer *et al.*, 2015. Two main architectures are defined for FlowNet end-to-end CNNs: FlowNetS and FlowNetC. FlowNetS is a straightforward encoder-decoder architecture i.e., an architecture where an input sequence in its entirety is transformed to a fixed-length internal representation. This means that image data is coarctated and then refined respectively in the contractive and expanding part of the network. After feeding the two consecutive images into the contractive part of the network as contracted data, the motion is estimated. In the decoder part of the network i.e. the expansive part, a series of up convolutions occur to increase resolution. FlowNetC, includes the correlation of feature maps (i.e. resultants of specific filters applied to an image; used in pattern recognition). In FlowNetC each consecutive image is fed into a series of processing networks to learn image features (such as edges). Then the correlation layer performs a patch comparison by comparing features obtained by each previous separate identical networks. The resultant of the comparison layer then is fed into an expansive layer that is otherwise similar to the expansive layer in FlowNetS (Figure 4-1).

In FlowNetS the input image pairs are fed into a rather general network that allows the network to process the image pair for motion calculation (Figure 4-1). In FlowNetC the architecture consists of two separate streams for the two image pairs that are combined on a higher level for matching. Patch level similarity comparison of the two feature maps yields a cost volume used for feature extraction is fed into a series of convolutions. The results of the patch comparison proceeds in a similar fashion to FlowNetS going through a refinement process to produce high resolution flow. The refinement section consists of upconvolutional layers and features from the contractive part. The refinement is performed four times given that further refinement does not improve the results (Fischer *et al.*, 2015). Although the end-to-end CNN architectures were able to directly predict the optical flow motion, at the time of emergence they

were lacking accuracy compared to some of the energy-based CNN methods such as Deepflow and EpicFlow (Weinzaepfel *et al.*, 2013; Revaud *et al.*, 2015).

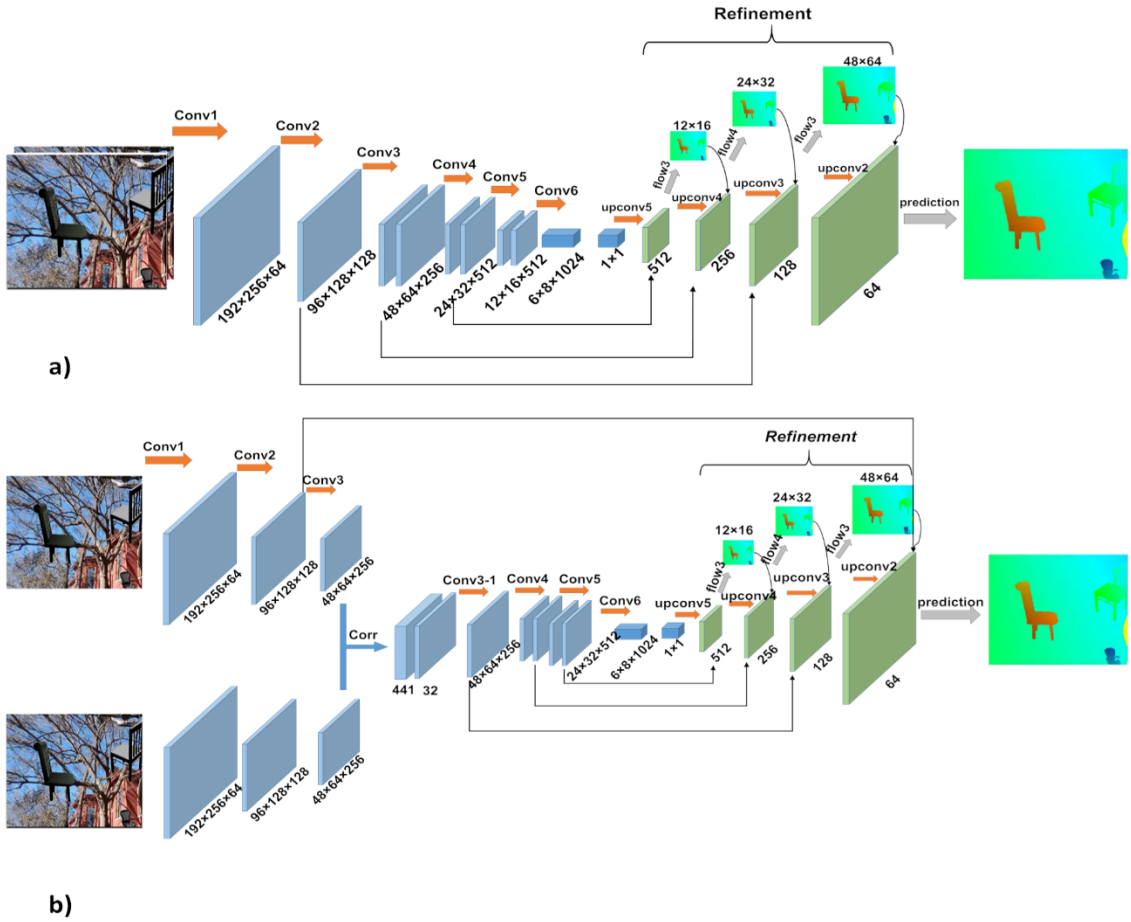

Figure 4-1 Two main FlowNet architectures - a) FlowNetSimple (FlowNetS) and b) FlowNetCorr (FlowNetC) - (adapted from Fischer et al. (2015))

Further development of novel architecture designs has led to new end-to-end CNN based optical flow estimation with higher accuracy. In an attempt to improve FlowNet optical flow estimation algorithms Ilg et al. (2017) introduced FlowNet2.0, which was created by stacking multiple FlowNet modules for training new models with higher accuracy. Moreover, Ilg et al. (2017) utilized larger synthetic datasets for training, and also performed pre-training and fine-tuning with a scheduled training starting with a less complex dataset and further proceeding to more complicated ones. Figure 4-2 illustrates the FlowNet2.0 neural network architecture. The complete FlowNet2.0 architecture includes one FlowNetC and two FlowNetS architectures that are stacked on top of each other (denoted as FlowNet2-CSS). This architecture is suitable for large displacements (i.e. displacements of larger than a few pixels where the matches of the pixels in two consecutive frames are not descriptive enough or their counterpart in the other image is missing). In this architecture the images are first fed into the first network and the subsequent networks receive the images along with the estimated flow in the previous network (Ilg *et al.*, 2017). To improve the flow estimation in the consequent networks the error is updated by warping the second image via the flow and a bilinear interpolation. This helps the next network to focus on the estimated error for an improved velocity field. Finally, a small network fuses (i.e., joining data from multiple modalities to extract better performing models) the previous stacked networks, FlowNet2CSS with a FlowNet2SD to account for small displacements.

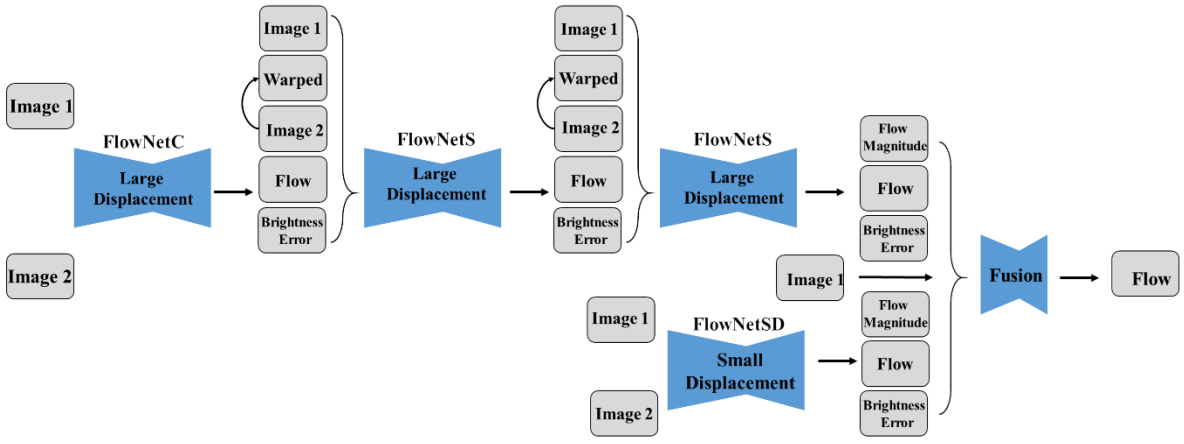

Figure 4-2. FlowNet2.0 architecture (adapted from Ilg et al. (2017))

4.1.2 RivQNet: A deep learning based river flow estimation algorithm using close-range water surface imagery

This study introduces RivQNet, a deep learning based river flow estimation algorithm using close-range water surface imagery. Various network architectures presented in Ilg et al. (2017), that were developed to find the most accurate FlowNet architecture for motion estimation in general applications, are implemented in RivQNet to be utilized for surface velocimetry and streamflow measurements. To the best knowledge of the authors there has been no study investigating the application of CNN based optical flow methods for stream flow measurements. The convolutional neural network architectures utilized and tested in **RivQNet** are: **FlowNet2C**, **FlowNet2S**, **FlowNet2CS**, **FlowNet2CSS**, **FlowNet2.0**. It should also be mentioned that initial assessments of FlowNet2SD led to excessively noisy results and therefore this network was eliminated from further investigations. A Pytorch (Paszke *et al.,* 2017) implementation of the FlowNet networks was used for flow field estimations (Ilg *et al.,* 2017; Reda *et al.,* 2017) on a GPU accelerated machine. To identify the preferred architecture for RivQNet, surface velocities computed using the different CNN architectures are assessed by comparison to contemporaneous laboratory and field data collected in situ. RivQNet with the preferred architecture is then used for further investigations and for discharge estimation.

The general workflow of the RivQNet is illustrated in Figure 4-3, which includes: image extraction, stabilization, lens distortion correction, orthorectification, surface velocity estimation, and discharge measurement. These steps are described in more detail below:

- The raw video footage is extracted into frames and video information such as frame rate and image size are recorded for future application.

- Camera information such as the intrinsic (i.e. focal length, effective sensor dimensions, image dimensions) and extrinsic (i.e. camera height and orientation) characteristics of the camera are given to the model as input for lens distortion removal and orthorectification. Lens distortion removal is necessary to reduce errors induced by obliqueness of the viewing angle.

- Stabilization is performed using a point feature mapping approach and tracking feature points between two consecutive frames (using Lucas-Kanade optical flow)

and utilizing the tracked features to estimate motion between frames and then compensating for the motion (Lee *et al.*, 2009).

- Two or three dimensional orthorectification is also performed using ground control points and camera intrinsic and extrinsic characteristics (Solem, 2012).

- Surface velocity is estimated using five different architectures of CNN based optical flow estimation: FlowNet2.0, FlowNet2C, FlowNet2S, FlowNet2CS and FlowNet2CSS. This is basically feeding consecutive frames of a video to the aforementioned models to produce velocity maps of the river flow.

- Surveyed cross section data is imported to the algorithm for discharge estimation. A velocity index approach was used to correlate RivQNet estimated surface velocity to depth-average velocity for discharge measurements using a correction factor of 0.85. The correction factor can be changed based on river characteristics (Creutin *et al.*, 2003, Hauet et al. 2018).

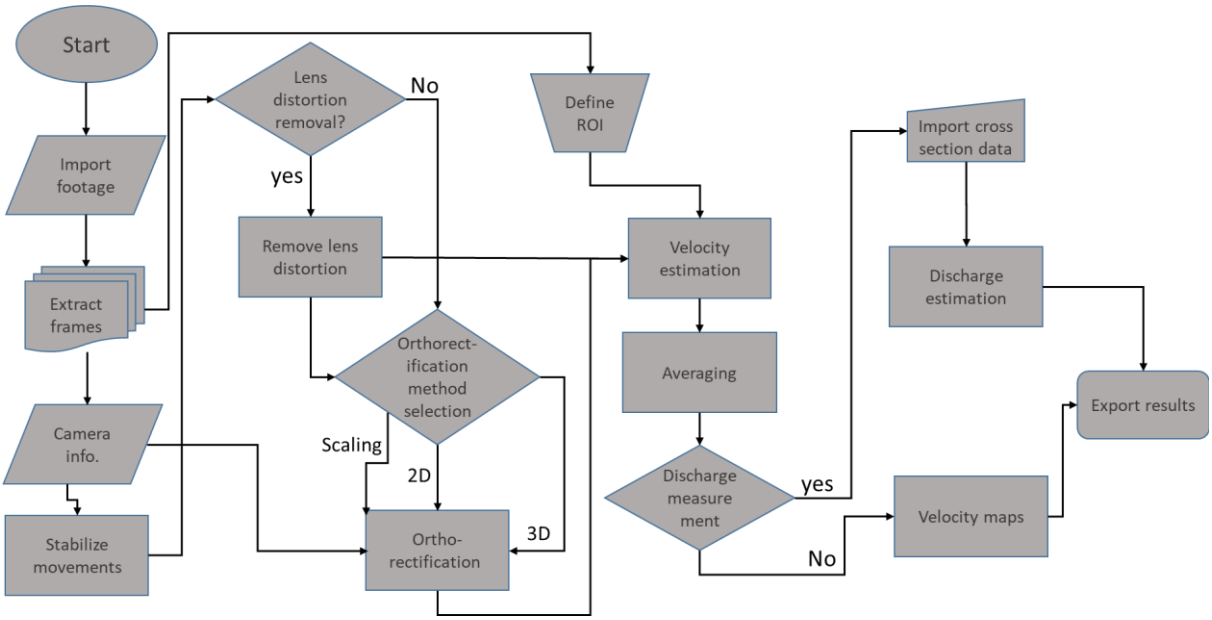

Figure 4-3. Main workflow of RivQNet, the image-based river flow estimation algorithm using deep learning based surface velocity estimation

4.1.3 Method validation

The application of RivQNet was investigated using measured laboratory and field data. The developed deep learning based algorithm was compared with the classical optical flow techniques. The evaluation of RivQNet performance was performed based on the criteria of root mean square error (RMSE) and mean absolute percentage error (MAPE) as defined in equations 4-8 and 4-9, respectively, where y_i is the verification data, x_i is the RivQNet estimated surface velocity using different methodologies and *n* is the total number of validation data.

$$RMSE = \sqrt{\frac{1}{n}\sum_{i=1}^{n}(y_i - x_i)^2} \tag{4-8}$$

$$MAPE = \frac{1}{n}\sum_{i=1}^{n}\left(\frac{|y_i - x_i|}{y_i}\right) \times 100 \tag{4-9}$$

Following this validation, RivQNet with the preferred FlowNet architecture was implemented for surface velocimetry and discharge measurement. ADCP measured verification data include variance induced by both turbulence and acoustic noise, which in this study was about 4 percent of the mean measured velocity, and the estimated MAPE would thus include this uncertainty as well as uncertainty induced by the image based surface velocity estimation.

4.1.3.1 Validation data

Laboratory

A validation laboratory experiment was carried out in a flume located in the Civil Engineering - Water Resources Engineering Laboratory at the University of Ottawa. The flume used in this experiment was 12 m long with a rectangular cross section of 1 m width and 0.9 m height. Laboratory experiments were conducted with a constant discharge and flow depth of 0.029 m^3s^{-1} and 18 cm, respectively. Instrumentation included a GoPro Hero5 camera fixed above the channel recording videos on a nadir angle. Instantaneous velocity measurements were conducted using a side-looking Nortek Vectrino (4-beam) Acoustic Doppler Velocimeter (ADV) mounted on a movable carriage orientated orthogonal to the flume walls. ADV data collection was conducted along the cross section and in 10 cm increments for two minutes and with a sampling rate of 200

Hz. The ADV probe was positioned such that the sampling volume was as close to the water surface as possible, which was measured at 2 cm below the water surface. The velocity data were used for comparison with the image-based surface velocimetry methodologies. Figure 4-4a,b shows the laboratory experiment setup and a sample frame of the recorded videos. A 30 second video with 30 frames per second was used for image-based velocimetry analysis.

Field

Field measurements were conducted on Castor and Salmon Rivers in order to investigate the application of the presented deep learning based optical flow methods for surface velocimetry in natural field environments. Table 4-1 lists a variety of aerial and shore-based imagery footage and the related flow conditions, footage and reference measurement data types collected at each site. The best FlowNet architecture to be used in RivQNet was identified using aerial imagery collected at the Castor River (March 11, 2020) and also the Salmon River (June 04, 2019). RivQNet with the preferred architecture was then used for further evaluation as well as discharge estimation for each of the remaining Castor River measurements listed in Table 4-1.

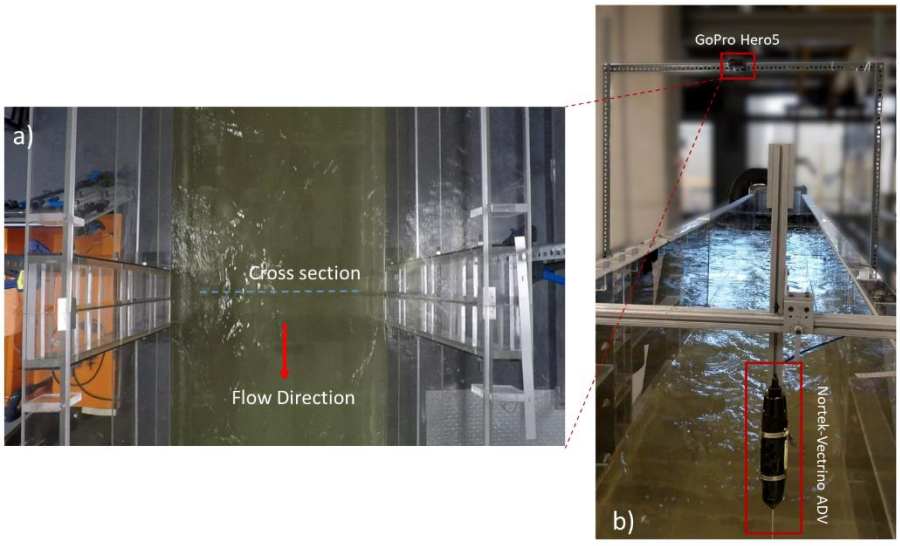

Figure 4-4. a) Field of view of the camera, b) Flume channel setup, GoPro Hero5 camera and the Nortek Vectrino ADV

Table 4-1. List of the field measurements used for validation of the developed algorithm

River	Date	Flow condition	Footage and camera type	Reference measurements
Castor River	April 04, 2020	High flow	Aerial (Mavic 2 Pro)	SonTek RiverSurveryor ADCP – M9
	March 11, 2020	High flow	Aerial (Phantom4) Shore-based (ACTi-A31)	Teledyne StreamPro ADCP
	November 29, 2019	Moderate to low	Aerial (Phantom4) Shore-based (ACTi-A31)	Teledyne StreamPro ADCP
	July 09, 2019	Low flow	Shore-based (ACTi-A31)	SonTek FlowTracker Handheld ADV
Salmon River	June 04, 2019	Low flow	Aerial (Phantom4)	SonTek FlowTracker Handheld ADV

Castor River

Castor River in eastern Ontario is an important tributary to South Nation River watershed that drains an area of about 739 km^2. Figure 4-5 shows the Castor River location. The Castor River hydrometric station at Russel (Water Survey of Canada (WSC) Station ID 02LB006) is located at 45°15' 45" North and 75°20' 37" West and has been operational for 73 years (Environment and Climate Change Canada, Wateroffice, 2021). The gross drainage area of the river at this location is about 439 km^2. Data utilized in this study were acquired using both RPAS aerial and fixed shore-based oblique imagery (Table 4-1). The videos were recorded in 8-bit depth and in mp4 format.

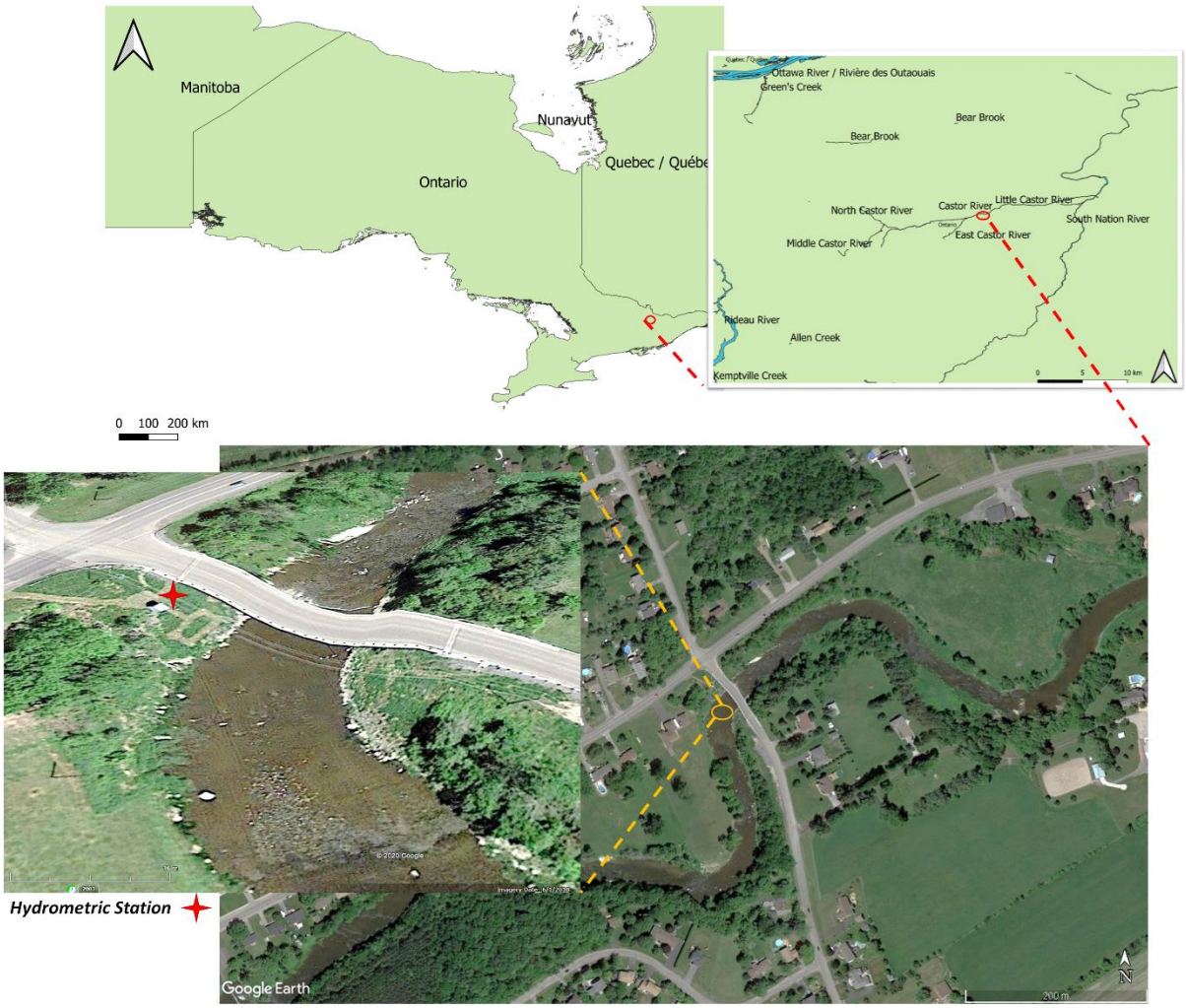

Figure 4-5. Castor River at Russel, Ontario, Canada

Salmon River

Salmon River in the north of Vancouver Island in British Columbia, Canada along with its main tributaries, White and Memekay Rivers, have a combined drainage area of 1210 km2. Data were collected at Salmon River (WSC Station ID 08HD006) on June 04, 2019. The aerial footage was acquired using a DJI Phantom 4 Pro RPAS at 50◦18' 444" North and 125◦54' 27" West downstream of the confluence between the Salmon River and the smaller White River (Figure 4-6). The videos were recorded in 8-bit depth and in mp4 format. The average depth of the river at the time of data collection was approximately 0.65 m with an average discharge of 22.9 m3s−1 and an average velocity of 0.65 ms−1 which is considered a low flow condition. A one minute video recorded at a 102 m elevation and with a frame rate of 24 Hz was used for the analysis. A FlowTracker handheld acoustic Doppler velocimeter was used to collect velocity data along a

single cross section at intervals of 3 m and they were sampled for 40 seconds at 1 Hz. Single point velocity measurements were obtained at 23 evenly spaced locations along the cross-section, at 60 percent of the depth. An adjustment coefficient of 1/0.85 was used to convert these velocities to surface velocity (Rantz, 1982). This Salmon River dataset is already available through Perks et al. (2020). Figure 4-6 shows the location of the river along with a sample frame of the recorded footage. The low flow conditions with the very clear water makes this a suitable example to verify the application of the presented method for such conditions.

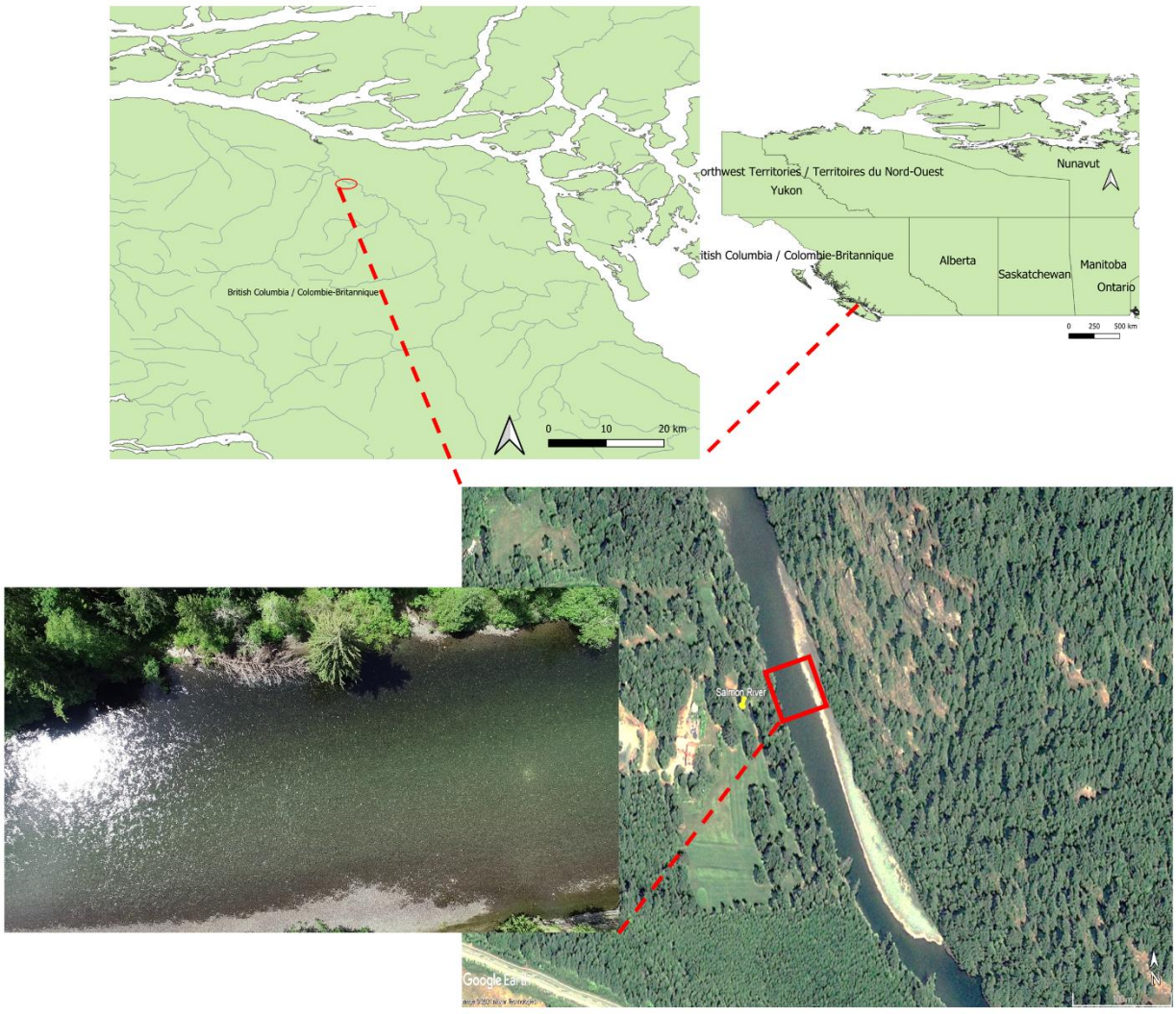

Figure 4-6. Salmon River, British Columbia, Canada

4.1.4 Validation results

4.1.4.1 Laboratory – accuracy of RivQNet

Measurement results for the same cross section shown in Figure 4-4a using the ADV and different deep learning based optical flow methods are illustrated in Figure 4-7 and Table 4-2. The RMSE and MAPE were calculated using the ADV point data and the corresponding FlowNet results along the transect. FlowNet2CSS and FlowNet2S with MAPE of 5.3 and 52.4 percent, respectively, yielded the best and the worst results compared to the ADV measurements. This was expected as FlowNetS has been reported to be highly sensitive to sudden brightness changes (Fischer *et al.*, 2015). FlowNet2C, FlowNet2CS and FlowNet2 respectively had MAPE of 19.1, 10.1, and 15.8 percent respectively.

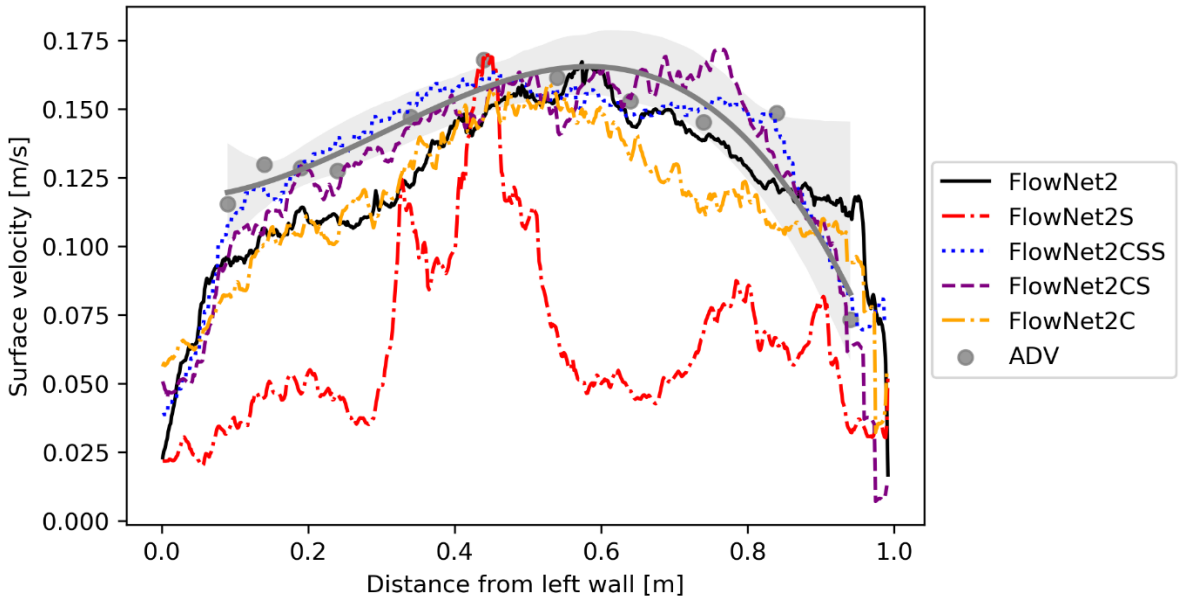

Figure 4-7. Validation of different FlowNet2 architectures implemented in RivQNet using laboratory data. A regression (gray line) with 95% confidence interval (shaded gray area) is fitted to the ADV data.

Table 4-2. Laboratory validation results of different FlowNet2 architectures implemented in RivQNet compared to ADV data.

Method	FlowNet2C	FlowNet2S	FlowNet2CS	FlowNet2CSS	FlowNet2
RMSE [m/s]	0.03	0.07	0.01	0.01	0.02
MAPE [%]	19.1	52.4	10.1	5.3	15.8

4.1.4.2 Field – selection of optimal CNN architecture

Castor River – March 11, 2020

March 11 survey data at Castor River was selected to evaluate RivQNet with different FlowNet architecture surface velocity estimation in high flow conditions. Water depth,discharge and average velocity on March 11, 2020 were 4.7 m, 54.8 m^3s^{-1} and 1.2 ms^{-1} respectively. The field survey included Teledyne StreamPro Acoustic Doppler Current Profiler (ADCP) measurements as well as RPAS flights using a DJI Phantom 4. The ADCP was operated on a The 30 second analyzed footage was recorded with a nadir view angle and a resolution of 3840×2160 pixels and 24 Hz frame rate. ADCP surveys were performed on two transects shown in Figure 4-8a, where transect 1 has an obstacle within the field of view. Average velocity of the two nearest bins to the water surface of the ADCP measurements (i.e. 0.18 m and 0.25 m below the water surface) was used for comparison with estimated surface velocity data. Figure 4-8b and 8c illustrate the measured and estimated surface velocity on the two cross sections, using the ADCP and seven different optical flow based surface velocimetry techniques (including both conventional and deep learning based techniques). Averaged spatial surface velocity distributions estimated using different FlowNet architectures are also shown in Figure 4-9.

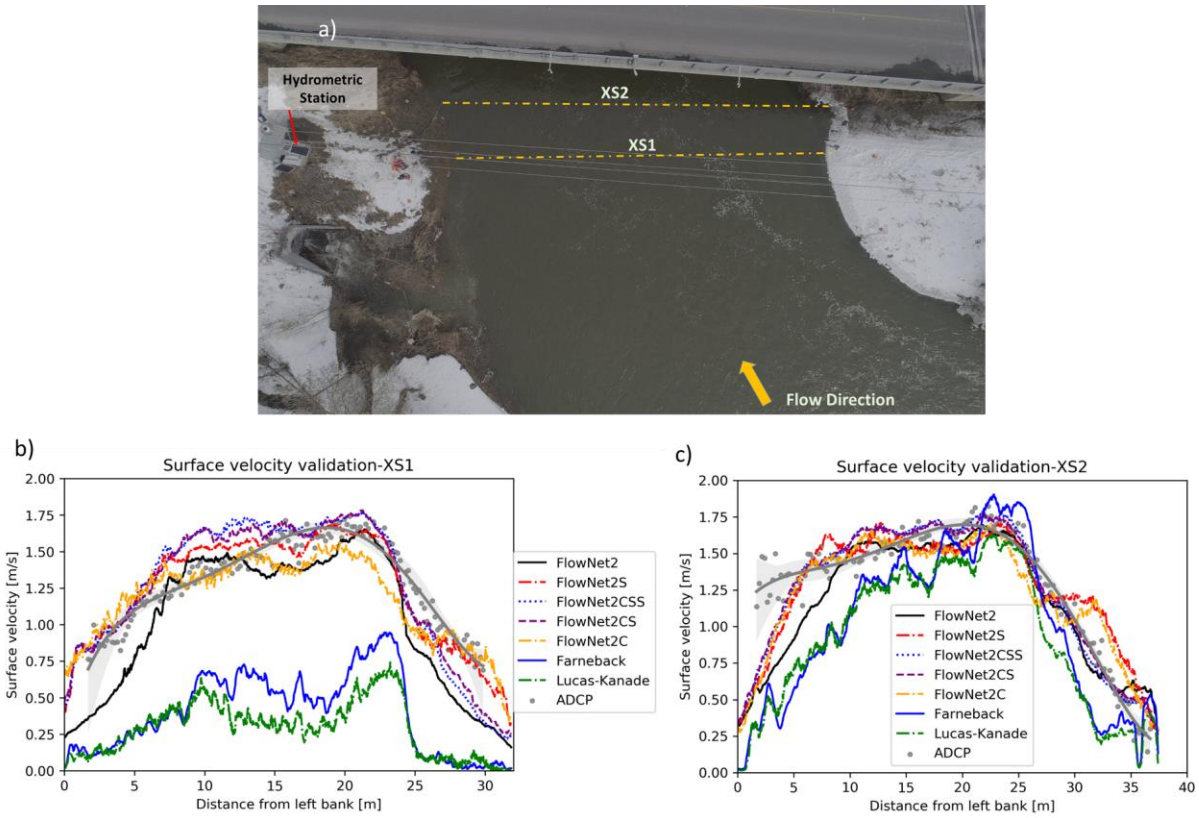

Figure 4-8. a) March 11, 2020 field measurement transects, b and c) Respectively cross sections 1 and 2, ADCP measurements along with extracted surface velocity using different optical flow methods implemented in RivQNet - ADCP measurements are shown in gray dots with spatial resolution of 20 cm, and regression lines with 95% confidence interval shown respectively with gray line and shading. The spatial resolution of the mage-based data is 16 mm.

Results show that generally the deep learning based optical flow methods yielded smoother spatial velocity distribution over the field of view of the camera. Visual comparison of the estimated and ADCP surveyed velocities shows that the investigated deep learning based optical flow methods yielded better results compared to the classical optical flow techniques. This is more apparent in Figure 4-8b, cross section 1, where the electricity cables are in the field of view of the camera. An error analysis was also performed for each of the surveyed cross sections shown in Figure 4-8a. Table 4-3 summarizes the error analysis of each transect using different optical flow techniques averaged for every 5 meters from the left bank. In all the analyzed cross sections, FlowNet2CSS with an estimation error varying from 8.4 to 9.9 percent for XS2 and XS1 and an RMSE of 0.13 to 0.17 ms^{-1} is the most accurate optical flow based surface velocity technique. The estimated velocity had the highest discrepancies on both left and right banks for all the analyzed methods. Lower water depth and velocity near to river banks can lead to both estimation and measurement errors in those areas. Figure 4-10 shows the extracted surface velocity and estimation error for every five meters along cross section 2 in accordance with river bathymetry. Each box plot

represents data from each 5m portion along the cross section. Data were analyzed in this way in order to find a distributed error along the cross section, to observe whether there is a describable relation between error and bathymetry.

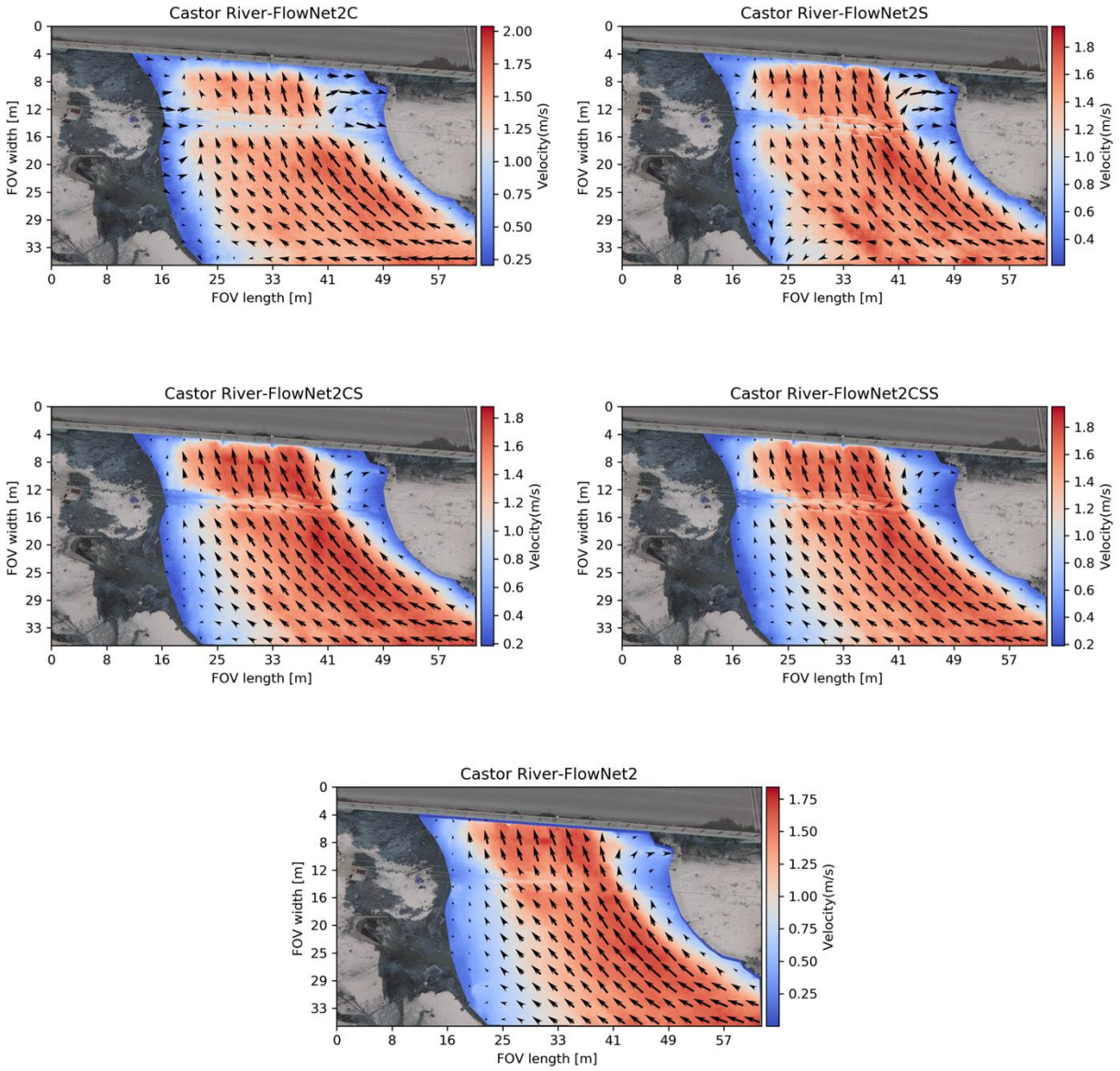

Figure 4-9. Averaged spatial surface velocity distribution estimated using different FlowNet architectures implemented in RivQNet, spatial resolution of the estimated velocity map data is 16 mm and vectors show averaged data for an area of 0.4 m.^{2}

Table 4-3. Error analysis for three transects estimated using different optical flow techniques using the aerial footage recorded on March 11, 2020

Cross Section	Method	Error analysis for defined increments from the left bank [m]– MAPE [%]								MAPE [%]	RMSE [m/s]
		1.5 - 5	5 - 10	10 - 15	15 - 20	20 - 25	25 - 30	30 - 35	35 - 36.5		
XS1	Lucas Kanade	82.7	68.6	72.3	80.4	65	92.1	---	---	76.6	1
	Farneback	81.9	68.6	56.2	68.2	52.1	93.7	---	---	69.5	0.9
	FlowNet2C	16.7	6.5	4.5	9.9	17.4	11.2	---	---	10.7	0.2
	FlowNet2	41.8	12.1	5.6	11.2	9.6	41.9	---	---	19.1	0.2
	FlowNet2S	9.1	16.9	16.5	4.9	6.5	29.6	---	---	14.1	0.2
	FlowNet2CSS	**9.1**	**12.4**	**8**	**4.1**	**6.3**	**10.9**	**---**	**---**	**8.4**	**0.1**
	FlowNet2CS	10.5	14.5	12.7	4.8	6.2	23.2	---	---	12	0.1
XS2	Lucas Kanade	61.3	38.3	17	14.4	10.1	24.1	53.5	67.3	31.9	0.4
	Farneback	65.1	40.2	12.3	10.5	9.1	14.7	44.8	86.4	29.5	0.4
	FlowNet2C	26.6	4.6	4.7	5.9	6.9	9.6	34	88.6	16.4	0.2
	FlowNet2	42.3	13.3	4.8	4.1	4.5	6.3	13.6	137.6	17.6	0.2
	FlowNet2S	29.1	6.3	4.9	5.2	5.7	7.6	44.9	124.1	19.6	0.2
	FlowNet2CSS	**21.8**	**6.2**	**9.1**	**7.7**	**2.9**	**5.6**	**9.9**	**36.4**	**9.9**	**0.1**
	FlowNet2CS	22.7	5.1	8.2	4.2	3.5	5.2	8	100.9	12.1	0.2

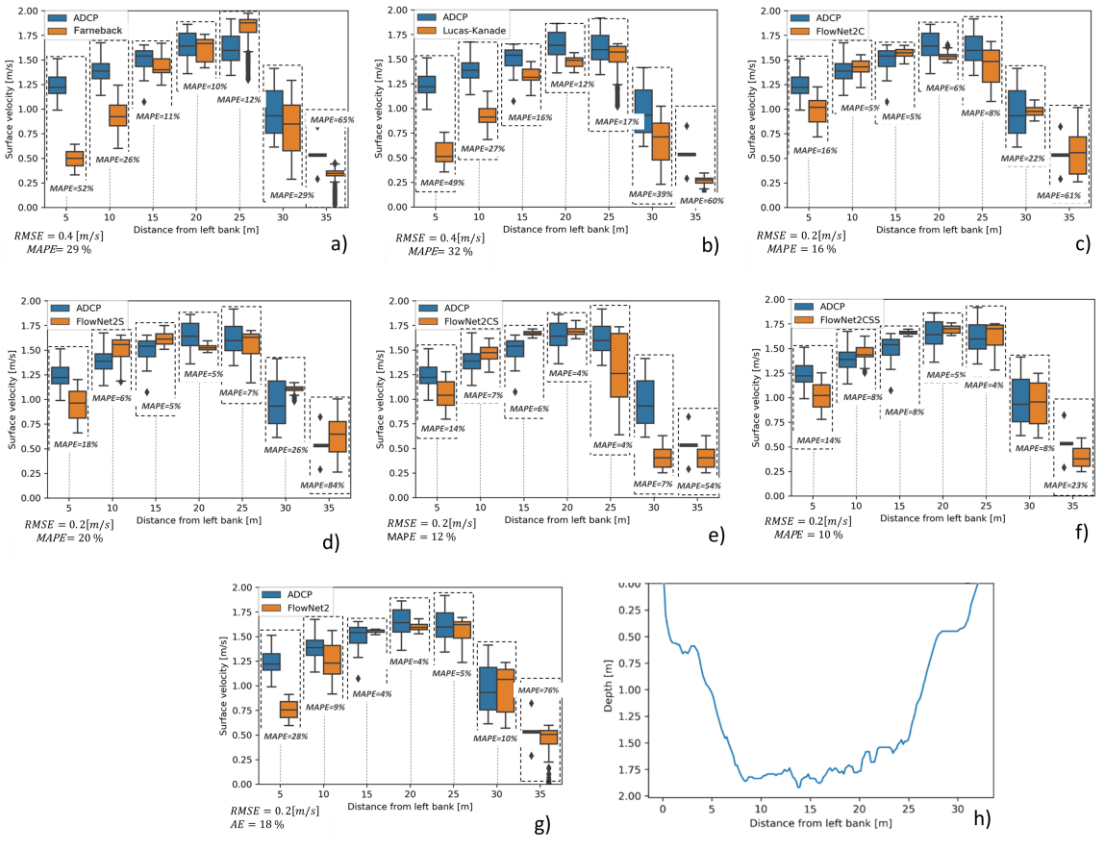

Figure 4-10. a-g) Surface velocity boxplots on XS2extracted using different optical flow techniques on - March 11, 2020. h) Surveyed cross section (XS2)- box plots represent the measured distribution for both ADCP and surface velocimetry methods. RMSE and MAPE are calculated from differences between coincident FlowNet2CSS and ADCP velocity values

Salmon River – June 04, 2019

To further investigate the application of the optical flow techniques in low flow conditions data from another field survey conducted on June 04, 2019 at Salmon River, British Columbia were used. Average depth, river flow and flow velocity at the time of data collection were 0.65 m, 22.9 m^3s^{-1} and 0.6 ms^{-1}, respectively. A 1 minute video was collected with a nadir angle and from an elevation of about 102 m. The first 30 seconds of the recorded footage was used for this analysis. The acquired footage resolution is about 1920×1080 pixels with a frame rate of 24 Hz. Figure 4-11 shows image-based estimated surface velocity using the acquired RPAS imagery at the ADV measured transect of the Salmon River. Further error analysis estimated for every 5 meters from the left bank of the measured transect of the Salmon River is also presented in Table 4-4. Results presented in Figure 4-11 and Table 4-4 show that where the classical optical flow methods underestimate surface velocity, generally the deep learning based optical flow techniques perform

better. FlowNet2CSS with a RMSE of 0.16 ms^{-1} and MAPE of 17.5 percent was the most accurate optical flow method among all tested techniques.

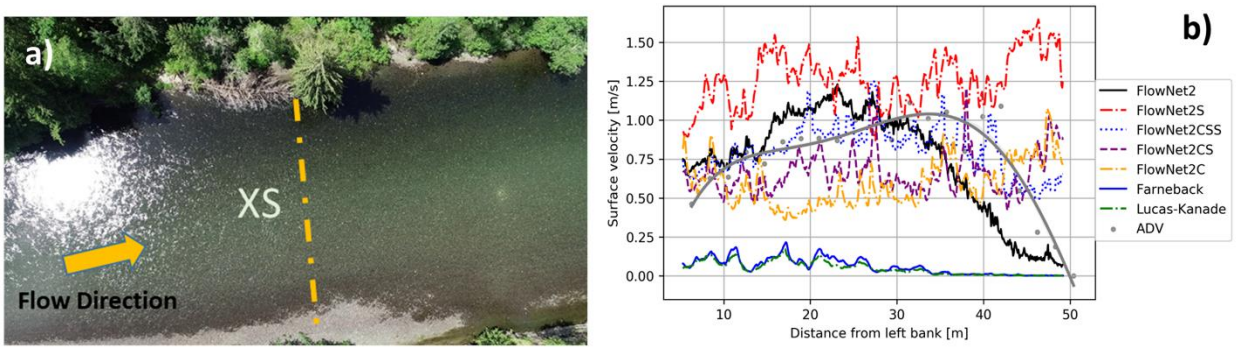

Figure 4-11. a) Sample frame of the aerial imagery of the Salmon River on June 04, 2019 and the ADV surveyed transect; b) Cross sectional ADV measurements along with extracted surface velocity using different optical flow methods - FlowTracker ADV measurements are shown in gray dots with spatial resolution of 2.1 m and regression line with 95% confidence interval shown respectively with gray line and shading. The spatial resolution of the image based data is 75 mm.

Table 4-4. Surface velocity estimation error evaluation for one cross section measured at Salmon River - June 04, 2019 (Low-flow conditions)

Cross Section	Method	Error analysis for defined increments from the left bank [m]– MAPE [%]									MAPE [%]	RMSE [m/s]
		3-10	10-15	15-20	20-25	25-30	30-35	35-40	40-45	45-50		
XS	Lucas Kanade	86.9	90.5	87.0	90.9	94.8	83.9	99.9	99.9	99.6	91.2	0.8
	Farneback	83.0	87.8	83.1	89.8	94.9	83.2	99.8	99.6	99.4	89.8	0.7
	FlowNet2C	25.2	35.0	49.4	44.5	43.1	26.0	50.5	111.8	319.1	46.1	0.4
	FlowNet2	27.1	11.3	20.2	22.4	13.5	26.5	66.1	64.9	53.6	28.6	0.3
	FlowNet2S	83.5	61.9	44.0	19.4	13.7	24.4	9.3	304.3	668.8	63.9	0.5
	FlowNet2CSS	**19.5**	**6.4**	**5.2**	**23.2**	**10.5**	**18.9**	**22.4**	**43.9**	**192.9**	**17.5**	**0.2**
	FlowNet2CS	13.9	20.3	9.6	18.2	39.9	29.5	41.4	105.2	400.0	32.5	0.3

The analysis and comparison of different classic and deep learning based optical flow techniques both for laboratory and field investigations in various flow conditions showed that generally RivQNet with deep learning based optical flow methods performed better with more accurate and smoother results compared to the classic optical flow methods. This can be due to the known sensitivity of classical optical flow methods (i.e. Farnback and Lucas and Kanade) to noise and pixel brightness and weakness to detect motion in smooth surfaces (i.e. low flow conditions). The comparison of different CNN based architectures also indicated that FlowNet2CSS provides more accurate results for river surface velocimetry. This conclusion differs from the results reported by Ilg et al. (2017), where FlowNet2 was reported as the most efficient approach for flow estimation of synthetic imagery. However, it should be acknowledged that the imagery was very different between these studies (i.e. natural flowing water surface vs synthetic flying chair). As well, the additional FlowNetSD that was added to FlowNet2CSS in the FLowNet2 architecture (to account for small displacements) makes the FlowNet2 architecture sensitive to noise that makes the accurate surface velocimetry difficult as the motion is measured in pixel size scale. Our investigations showed that FlowNet2CSS yields the most accurate results compared to the other architectures and hence was selected as the preferred architecture for RivQNet. Comparison of different optical flow architectures shows that FlowNet2C, which includes explicit correlation of the feature maps outperforms the FlowNet2S that is a straightforward encoder-decoder architecture. This is also confirmed previously by the results presented by Fischer *et al.,* 2015 and Ilg., *et al.,* 2017. By stacking FlowNet2C and FlowNet2S (i.e. FlowNet2CSS) more accurate surface velocity results were achieved. The application of FlowNet2CSS fine-tuned architecture to detect small-displacement (i.e. pixel size displacements) led to the most accurate results. It should be emphasized that in this study we have used pre-trained CNN models developed by Ilg., et al. 2017 for surface velocity measurements.

4.1.5 RivQNet results with preferred CNN architecture (FlowNet2CSS)

In this section, surface velocity and discharge of the previously introduced data set (Table 4-1) are estimated using the RivQNet algorithm with the preferred CNN architecture (i.e. FlowNet2CSS). The estimated results are then compared with the ADV or ADCP measured data. Evaluations in this section are presented in different categories of high-flow and low-flow conditions and for aerial RPAS and shore-based fixed camera imagery.

4.1.5.1 Castor River – multiple days

Castor River – March 11, 2020

Evaluations for high-flow conditions on March 11, 2020 are performed on the two transects introduced in Figure 4-8a. Figure 4-12 summarizes the acquired estimates of surface velocity using the RPAS aerial and fixed oblique imagery. A shore-based fixed camera recorded footage for surface velocimetry at the Castor River hydrometric station. A thirty seconds of footage acquired by an ACTi A31 fixed camera on March 11, 2020 with a resolution of 2048×1536 and a sampling rate of 30 Hz was analyzed to evaluate the newly presented RivQNet algorithm. Figure 4-12a shows a sample frame of the analyzed video. Results of the analysis along cross section 2 are shown in Figure 4-12b. Visual inspection of this plot shows that surface velocity estimated using RivQNet is within the range of the ADCP measured data.

Cross sectional error analysis of the software presented in Table 4-5 shows RMSE of 0.13 ms^{-1} and 0.11 ms^{-1} and MAPE of 8.42 and 9.94 percent for aerial imagery of cross sections 1 and 2 respectively. The RMSE of RivQNet estimated surface velocity from oblique imagery were 0.10 ms^{-1} and 0.16 ms^{-1} and the MAPE were 7.14 and 12.6 percent, respectively for cross sections 1 and 2 (as previously reported in Table 4-3). Results indicate that generally the accuracy is higher for velocities extracted from aerial nadir imagery, however in the case of cross section XS1 the shore based oblique imagery provided a higher accuracy estimated velocity due to the visual obstacles (Electricity cables) in the field of view of the nadir angle imagery. There is a relatively high discrepancy in the results of measured ADCP and RivQNet estimated surface velocity that can be related to the interference of acoustic reflection in shallower near-bank locations that may even be higher with the presence of conduit, cables and metal anchors that keep other gauge station sensors in place. Comparison of the aerial and nadir angle imager size shows that as long as the sufficient resolution captures the features of the water surface that can be tracked and used for image based velocimetry then the accuracies are similar, which is a similar finding to Le Boursicaude *et al.,* 2016. The surface velocity distribution obtained from oblique imagery is smoother and less detailed than that obtained from nadir imagery (cf. Liu et al. 2021). The distance to the camera sensor of river surface locations seen in the oblique image is different than in the drone imagery, thus the orthorectification procedure might introduce some error to the results. Moreover, due to the different distances for oblique and nadir imagery some smaller detailed surface patterns are lost in oblique imagery.

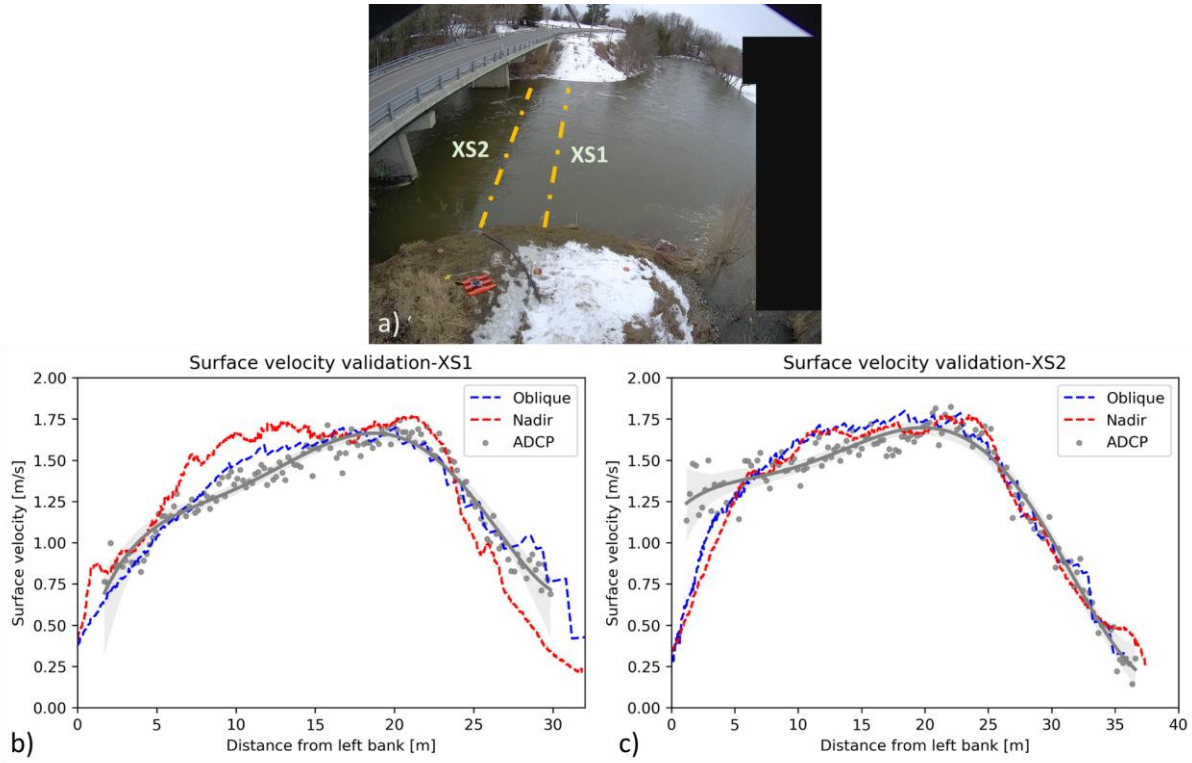

Figure 4-12 Sample frame of fixed shorebased camera at the Castor River. b) RivQNet estimated surface velocity using aerial and shore-based fixed camera installed at the Castor River hydrometric station – March 11, 2020 (High-flow conditions). ADCP measurements are shown in gray dots with spatial resolution of 20 cm and regression line with 95% confidence interval shown respectively with gray line and shading. The spatial resolution of RivQNet data is 16 mm.

Table 4-5. Error evaluation of RivQNet estimated surface velocity using aerial and shore-based imagery at the Castor River - March 11, 2020 (High-flow conditions)

Cross Section	Error analysis for defined increments from the left bank [m] – MAPE [%]								MAPE [%]	RMSE [m/s]
	1.5 - 5	5 - 10	10 - 15	15 - 20	20 - 25	25 - 30	30 - 35	35 - 36.5		
XS1 (Drone - Nadir)	9.13	12.43	8.02	4.08	6.32	10.92	---	---	8.42	0.13
XS1 (Shorebased - Oblique)	9.13	5.33	8.03	4.22	4.90	11.97	---	---	7.14	0.10
XS2 (Drone - Nadir)	21.87	6.25	9.07	7.74	2.88	5.65	9.93	36.41	9.94	0.11
XS2 (Shorebased - Oblique)	24.38	5.00	8.70	4.55	4.06	5.19	9.16	89.13	12.06	0.16

Castor River – April 04, 2020

Assessment of RivQNet image-based surface velocimetry algorithm in high flow conditions was further investigated with the data collected at Castor River on April 04, 2020. River water depth,

discharge and flow velocity on the survey day were 3.6 m, 13.5 m^3s^{-1}, 1.19 ms^{-1} respectively. Instantaneous velocity measurements were conducted using a SonTek m9 RiverSurveyor ADCP mounted on an Oceanscience trimaran riverboat. Mode of the ADCP operation was SmartPulse. The average of the nearest two bins to the water surface of the ADCP measurements was used for comparison with the estimated image-based surface velocity data (i.e. 20 cm below the water surface). The aerial footage was recorded using a DJI Mavic 2.0 Pro RPAS. The recorded footage had a resolution of 1632×1536 with a 30 Hz frame rate. A sample frame of the RPAS recorded aerial imagery used for the analysis is shown in Figure 4-13a. Estimated surface velocity using RivQNet and measured ADCP data are plotted in Figure 4-14b. Table 4-6 shows the error analysis of the RivQNet estimated surface velocity. It is shown that RivQNet estimated the surface velocity with an RMSE of 0.14 ms^{-1} and MAPE of 7.21 percent.

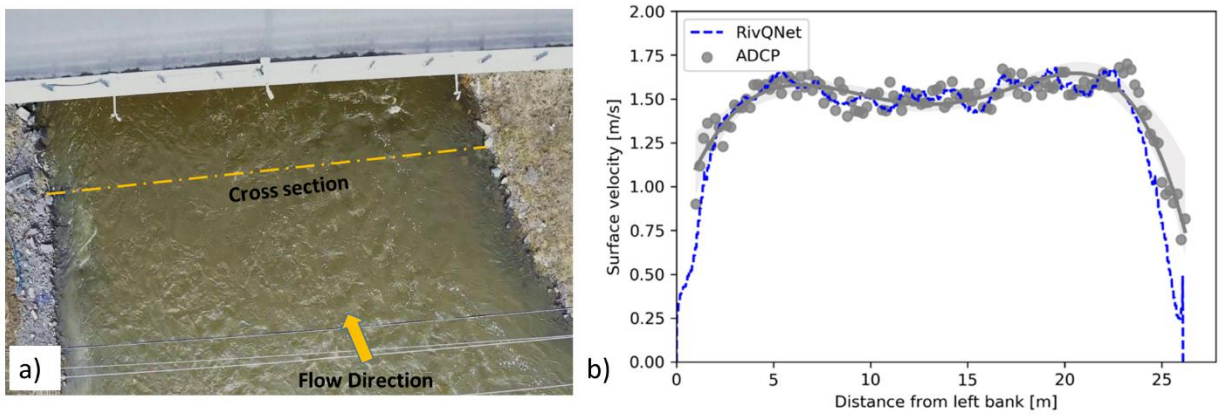

Figure 4-13. a) Sample frame of aerial footage at the Castor River. b) RivQNet estimated surface velocity using aerial imagery at the Castor River hydrometric station - April 04, 2020 (High-flow conditions). ADCP measurements are shown in gray dots with spatial resolution of 20 cm and regression line with 95% confidence interval shown respectively with gray line and shading. The spatial resolution of the RivQNet data is 19 mm.

Table 4-6. Error evaluation of RivQNet estimated surface velocity using aerial imagery at the Castor River – April 04, 2020 (High-flow conditions)

Cross Section	Error for defined increments from left bank [m] – MAPE [%]						MAPE [%]	RMSE [m/s]
	1.5 - 5	5 - 10	10 - 15	15 - 20	20 - 25	25 - 26		
XS	7.48	3.10	3.35	3.56	8.16	50.69	7.21	0.14

Castor River – July 09, 2019

Image-based surface velocimetry algorithms generally provide a weaker performance in low flow shallow water conditions (Meselhe *et al.*, 2004). Therefore, investigating the performance of RivQNet in moderate and low flow conditions with minimal surface texture was considered in three sets of data collected at Castor River (i.e. July 09 and November 29, 2019) and Salmon River (June 04, 2019 – results presented in section 3.2.2). A 30 second video cut to 27 seconds due to camera movements recorded on July 09, 2019 was used to estimate surface velocity in Castor River. The analyzed video was recorded using a ACTI A31 IP camera, mounted at an oblique angle and approximately 8.5 m above water surface. This dataset is already available through Perks *et al.*, (2020). 4a shows a sample frame of the recorded video. The water level, river discharge, and flow velocity at the time of the survey were 3.128 m, 0.93 m^3s^{-1} and 0.13 ms^{-1} respectively. Reference velocity data were collected using a FlowTracker 2 handheld ADV. Figure 4-14b illustrates the estimated surface velocity using the RivQNet algorithm and the measured surface velocity at four points across the cross section. Overall surface velocity estimation error (MAPE) calculated using the reference measurements was around 16 percent.

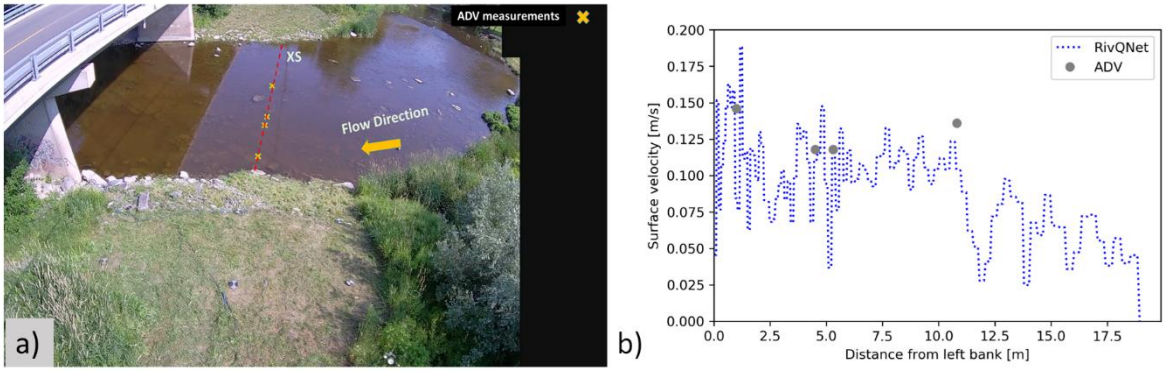

Figure 4-14. a) Sample frame of shore-based footage at the Castor River. b) RivQNet estimated surface velocity using shore-based imagery at the Castor River hydrometric station - July 09, 2019 (Low-flow conditions). ADV measurements are shown in gray dots. The spatial resolution of the RivQNet data is 24 mm.

Castor River – November 29, 2019

A field survey was conducted at Castor River on November 29, 2019. Water depth, river flow and flow velocity on the survey day were 3.15 m, 10.37 m^3s^{-1} and 0.8 ms^{-1}, respectively. Field survey included moving boat ADCP measurements. The average of the nearest two bins to the water surface of the averaged four transects was used for comparison (i.e. 20 cm below the water surface). Aerial footage acquired by RPAS fights and oblique shore-based video recorded using an Acti A31 fixed camera mounted on the hydrometric station 8.5 m above water surface. The

aerial and the shore-based footage used for the analysis had a resolution of 3840×2160 and 2048×1536 respectively with a duration of 30 seconds and a frame rate of 30 Hz. Figure 4-15a and b show a sample frame of the aerial footage and shore-based imagery; Figure 4-15c illustrates the measured and estimated surface velocimetry along the surveyed cross section. It is shown that the RivQNet estimated surface velocity is in the range of the measured ADCP data. The cross sectional error evaluation conducted on this dataset is presented in Table 4-7. The evaluation shows that surface velocity estimated using the RivQNet algorithm had a RMSE of 0.15 ms^{-1} 0.17 ms^{-1} and MAPE of 13.3 and 17 percent respectively for aerial and shore-based imagery.

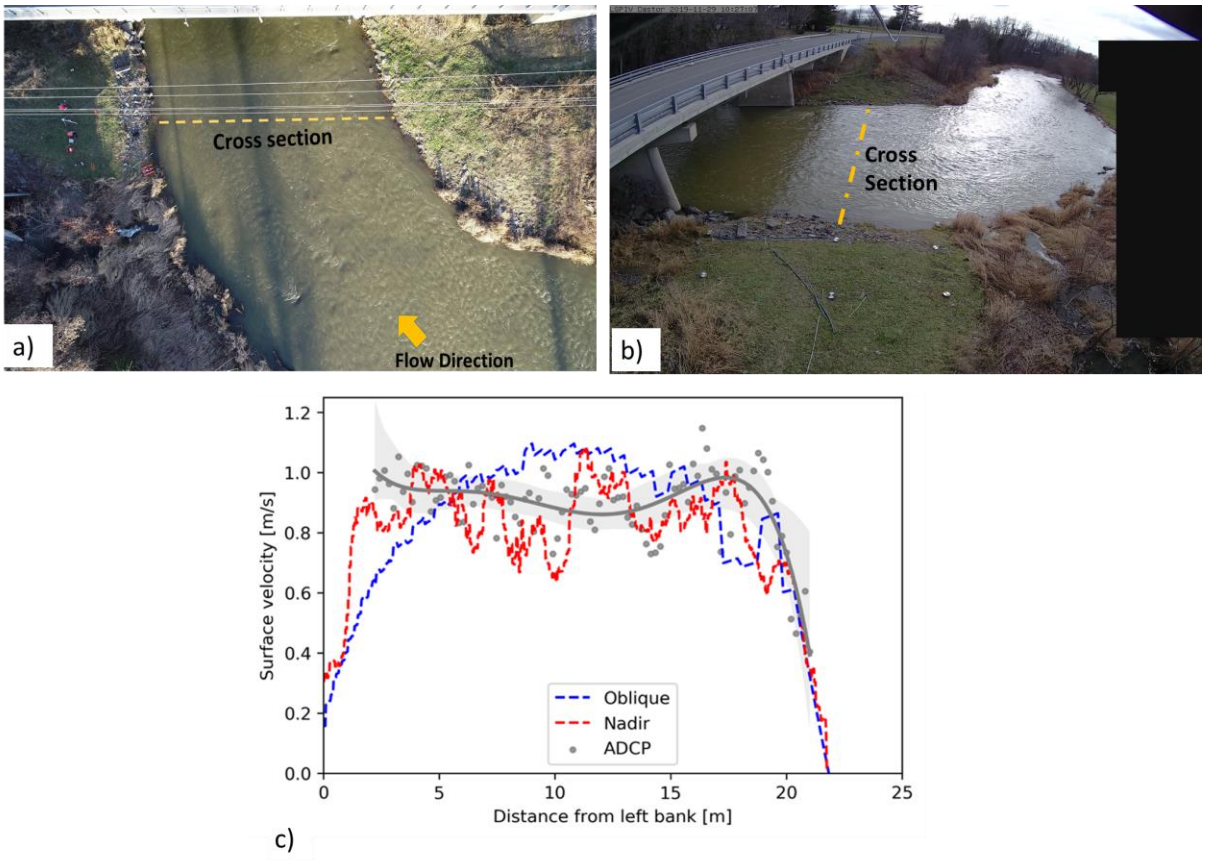

Figure 4-15. a) Sample frame of aerial footage at the Castor River. b) Sample frame of oblique shore-based footage at the Castor River. c) RivQNet estimated surface velocity using aerial and shore-based imagery at the Castor River hydrometric station - November 29, 2020 2019 (low to medium flow conditions). Near surface ADCP velocity measurements are shown in gray dots with spatial resolution of 20 cm and regression line with 95% confidence interval shown respectively with gray line and shading. The spatial resolution of the RivQNet data is 16 mm.

Table 4-7, Error evaluation of RivQNet estimated surface velocity using aerial imagery at the Castor River - November 29, 2020 2019 (medium-flow conditions)

Cross Section	Error Analysis for defined increments in meters from left bank [%]					MAPE [%]	RMSE [m/s]
	2 - 5	5 - 10	10 - 15	15 - 20	20 - 22		
XS (Drone - Nadir)	9.66	12.89	10.17	17.78	21.07	13.30	0.15
XS (Shorebased - Oblique)	18.99	14.33	18.76	16.60	17.96	17.01	0.17

The data collection campaigns included hourly video file collection for a continuous period of around two years. This sampling intensity and data transmission requirements necessitated collection of videos of reasonable duration, thus 30 s was selected. The 30 second video records were found to be sufficient for surface velocimetry and discharge measurement. To investigate impact of record duration on surface velocity estimation two of the videos for different durations less than the full 30 seconds were analyzed. Figure 4-16 a and b for laboratory and field measurements show that using a shorter video duration and thus shorter sampling period does not have significant effects on the surface velocities calculated by RivQNet.

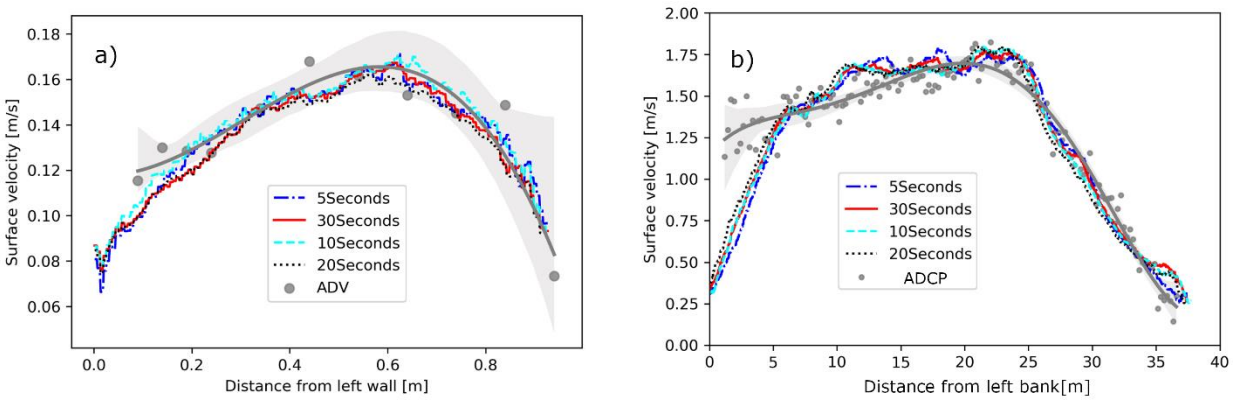

Figure 4-16. a) surface velocity estimated for different record times (Lab experiment) b) surface velocity estimated for different record times (Castor River – March 11 – XS2)

4.1.6 Discharge estimation

RivQNet estimated surface velocity data was used to estimate discharge for the surveyed days. A coefficient of 0.85 was used to relate the surface velocity to average velocity for discharge measurements. Previous studies show that a coefficient of 0.85 resulted in errors up to +/-5% in discharge measurements (Hulsing *et al.*, 1966), which is consistent with discharge measurement errors shown in Table 4-8. The estimated average velocity and the midsection cross section

measurements were used for discharge measurements. Results of these analyses are shown in Table 4-8. RivQNet estimated discharge error compared to ADCP and ADV measured data ranges from 1 to 5.9 percent. The lowest error was for the aerial footage analysis on March 11, 2020 and the highest error for the fixed shore-based oblique imagery for low flow conditions on July 09, 2019.

Table 4-8. Error analysis RivQNet estimated discharge

Date	Location	Footage type	Measured Discharge	Estimated Discharge	MAPE [%]
			ADCP/ADV [cms]	RivQNet [cms]	
March 11, 2020	Castor River	Aerial	54.8	56.44	2.9
		Fixed camera		57.62	5.1
April 04, 2020	Castor River	Aerial	19.2	19.4	1.0
July 09, 2019	Castor River	Fixed camera	0.92	0.98	5.9
November 29, 2019	Castor River	Aerial	10.06	9.84	2.2
		Fixed camera		9.85	2.1
June 04, 2019	Salmon River	Aerial	22.9	22.21	3.0

4.1.7 Discussion

RivQNet was introduced as an accurate novel application of CNN based optical flow approach for water surface velocimetry. Five different FlowNet architectures were implemented and tested in RivQNet for surface velocity estimation. Comparison of the deep learning and conventional optical flow techniques using laboratory and field experiments revealed the higher accuracy of the CNN based methods for this application. Conventional optical flow methodologies are based on the concept of brightness consistency and smoothness, and thus the flow estimation using these methodologies can be erroneous in varying brightness and illumination condition. On the other hand, CNN based approaches do not require image intensities and gradients or other user defined feature extractors and instead they utilize trained models for feature extraction and thus are less sensitive to variance and brightness change. Five different architectures were tested, and the FlowNet2CSS was determined to be the preferred architecture for RivQNet deep learning based surface velocimetry and discharge measurement. RivQNet was evaluated for different flow conditions and different camera orientation. It was shown that while this software provides its highest accuracy in high flow conditions with a higher resolution it can also provide accurate flow

estimation for moderate and moderate to low flow regimes. It was also shown that RivQNet can provide reliable surface velocity data in different illumination and brightness conditions and for poor quality footage. The developed algorithm provided accurate surface velocity data for low flow conditions with clear water and minimum surface texture, however future research attempts should focus on a detailed assessment and further enhancement of the software for the application of the RivQNet for low flow conditions where water surface texture is minimal. RivQNet is also capable of providing robust data in conditions where obstacles such as electricity cables are partially blocking the field of view of the camera. RivQNet can estimate surface velocity even for videos subject to glare, however this is not recommended as the sudden pixel intensity variation caused by glare may lead to discrepancies. Similar to other image based surface velocimetry methodologies accurate estimation on river banks seems to also be challenging using RivQNet. These challenges both include accuracy of the validation data (i.e. measured with other instruments such as ADCP or ADV) and challenges associated with input imagery such as slower flow velocity (i.e. smooth water surface with no/few featurs) or vegetation on river banks that may lead to discrepancies between validation and image based surface velocimetry). Overall, RivQNet can provide dense and smooth spatially distributed surface velocity data with a high accuracy.

Wind induced waves is considered as another influencing parameter in image-based surface velocimetry. In this study efforts have been made to perform the analysis in no wind conditions, which reduced the effect of wind induced waves in surface velocity estimation. Future work should also address this issue to further enhance RivQNet algorithm and perform a sensitivity analysis addressing this issue.

One of the main goals of this work was the development of an enhanced automated tool for flow measurement to minimize the need of user input that potentially increases uncertainty. Variational LSPIV methods require predefined interrogation and search areas to be defined by the user for processing. STIV methods typically require manual correction of the STIs which can drastically change the results. Conversely, RivQNet does not require any user defined input for the processing step as the recoded footage is going through a previously trained model without requirement for user identified input. Despite the fact that RivQNet proved to be efficient, accurate and robust for image-based surface velocimetry and flow estimation, future work should include the development of fully automated image-based discharge estimation tools that can continuously collect river flow data with minimal supervision and intervention.

4.1.8 Conclusion

An imaged based surface velocimetry scheme, RivQNet, was developed for remote stream flow sensing. RivQNet encompasses 2D and 3D image georectification, lens correction, image stabilization and a novel deep learning based optical flow estimation algorithm to be utilized for river surface velocimetry as well as discharge measurements. The presented algorithm was tested in laboratory and diverse field and stream flow conditions and both for aerial RPAS footage as well as fixed shore-based imagery. It was shown that RivQNet can robustly estimate surface velocity in different visibility, brightness and shade and for footage with different qualities. The comparison of the ADCP/ADV measured and RivQNet estimated discharge also indicated that the presented algorithm has an acceptable performance with a strong potential of real-time application for continuous data collection at hydrometric stations.

4.2 Comparing correlation-Based and Deep Learning-Based Optical Flow Surface Velocimetry Techniques

Preprint of an article submitted to 40th IAHR World Congress © IAHR

4.2.1 Introduction

Surface velocimetry techniques have gained greater importance in recent years as an essential tool for flow measurement in various natural and urban environments. These non-intrusive methods measure the water velocity at or near the surface, providing valuable data for understanding and managing water resources, including rivers, streams, canals, and coastal areas (Aberle *et al.,* 2017). In this context, surface velocimetry techniques offer several advantages over traditional flow measurement methods, making them indispensable in the field of hydrology and water resource management. Traditional flow measurement techniques, such as current meters, acoustic Doppler current profilers (ADCP), and pressure sensors, often require direct contact with the water or the installation of equipment within the water body (Aberle *et al.,* 2023). These intrusive methods can be time-consuming, labor-intensive, and costly, and sometimes challenging to conduct especially during floods. Surface velocimetry techniques, such as particle image velocimetry (PIV), large-scale particle image velocimetry (LSPIV), and remote sensing-based methods, use optical or radar-based sensors to track the movement of naturally occurring or artificially introduced tracers (or surface texture) on the water surface (Fujita *et al.,* 1998). By analyzing these tracers' movement, surface velocimetry can accurately determine the flow velocity without the need for physical contact with the water body. This non-intrusive approach allows for more rapid and cost-effective data collection, particularly in challenging environments like remote or hazardous locations, where traditional methods may be impractical or dangerous.

Another significant advantage of surface velocimetry techniques is their ability to provide spatially distributed velocity measurements. Traditional methods typically measure velocity at discrete points or limited area, which may not capture the complexity and variability of the flow field, particularly in turbulent or rapidly changing conditions. Surface velocimetry, on the other hand, can provide detailed velocity maps over large areas, enabling a more comprehensive understanding of the flow dynamics and their spatial variations. This information is vital for various applications, such as flood forecasting, sediment transport modeling, engineering e.g. bridge design and habitat assessment. Surface velocimetry techniques have also proven essential in monitoring and understanding the impacts of climate change on water resources (Al-mamari *et al.,* 2019). With increasing global temperatures and changing precipitation patterns, rivers and streams are experiencing more frequent and severe flood events, as well as periods of drought.

Surface velocimetry can help monitor and predict these changes by providing real-time data on velocities and flows, enabling more accurate flood forecasting and early warning systems. This information is critical for the development of effective mitigation and adaptation strategies to safeguard communities and infrastructure from the devastating effects of floods. The development and implementation of surface velocimetry techniques have also fostered interdisciplinary research and collaboration. By combining expertise from fields like hydrology, remote sensing, computer vision, and artificial intelligence, researchers have developed advanced algorithms and methodologies for more accurate and efficient flow measurements. These innovations have further expanded the applicability of surface velocimetry in various domains, such as flood protection and urban planning (Yang *et al.,* 2019), and coastal engineering (Holland and Kooney 2001).

Large Scale Image Velocimetry (LSPIV) and Space Time Image Velocimetry (STIV) are two widely recognized and frequently employed image-based surface velocimetry methods. Both LSPIV and STIV utilize image processing and cross-correlation techniques to calculate surface velocity, and as explained in the subsequent section, they necessitate a certain degree of user input, which could potentially influence the final estimated outcomes. RivQNet, a recently introduced approach, aims to address this problem and facilitate the automation of surface velocimetry through computer vision and artificial intelligence techniques (Ansari *et al.,* 2023). In this research, RivQNet is evaluated for the first time against the traditional surface velocimetry methods of LSPIV and STIV.

4.2.2 Methodology

4.2.2.1 Large Scale Particle Image Velocimetry (LSPIV)

Large Scale Particle Image Velocimetry (LSPIV) is a conventional and well-known image-based surface velocimetry technique that has been widely accepted and used in river flow measurements (e.g. Ettema et al. (1997), Fujita et al. (1998), Fujita and Aya. (2000), Creutin et al. (2003), Meselhe et al.(2004) and Muste et al. (2004)). LSPIV is used to study flow patterns and velocities in open-channels, rivers and streams. The basic principle behind LSPIV techniques is tracking the motion of detectable tracer particles (e.g., naturally forming tracers such as foam or debris, or manually seeded particles). The LSPIV technique usually utilizes a cross-correlation algorithm to track the motion of the tracer particles across consecutive images or video frames. LSPIV was first used by Fujita et al. (1994), to estimate surface velocity in rivers using aerial imagery. In particle image velocimetry techniques each image is divided into a uniform grid of

subarrays, which are known as interrogation areas. The tracking procedure in LSPIV takes place within the length of the specified interrogation area and it is very important to define an area with a uniform velocity distribution (Adrian, 1991). The size of the interrogation area is a very important factor in velocity estimation and as a rule of thumb it should be decided based on the size of flow patterns (Creutin *et al.,* 2003). Each interrogation area is examined in a pair of successive images captured within a known time interval. The most probable displacement of visible features on the water surface is determined by identifying the maximum cross-correlation coefficient calculated between two groups of gray scale pixels in the interrogation areas (Le Coz *et al.,* 2010). Several algorithms have been created based on LSPIV techniques for surface velocimetry and river discharge measurement utilizing close-range imagery, such as Fudaa-LSPIV (Le Coz *et al.,* 2014), RIVeR (Patalano *et al.,* 2017), MAT PIV (Sveen & Cowen, 2004), PIVlab (Thielicke & Stamhuis, 2014), and PTVlab (Brevis *et al.,* 2011).

4.2.2.2 Space-time image velocimetry (STIV)

Space-Time Image Velocimetry (STIV) is an advanced optical measurement technique used to analyze fluid flow patterns and velocities first introduced by Fujita et al. (2007). STIV is an extension of the Particle Image Velocimetry (PIV) and Large-Scale Particle Image Velocimetry (LSPIV) methods. The primary concept behind STIV is to analyze the movement of tracer particles (e.g., natural debris or artificially introduced seeding particles) in the fluid by constructing a space-time image, which is a two-dimensional representation of the fluid motion along a specified path or line over time. The acquired images are processed to construct a space-time image by extracting pixel intensity values along a specified path or line in each frame and stacking these values in consecutive columns of a two-dimensional space-time image matrix. Patterns or features, such as streaks, are identified in the space-time image, which represent the motion of tracer particles over time. The slope or angle of the identified streaks or features in the space-time image represents the velocity of the tracer particles, and hence, the underlying motion (Fujita et al., 2007). The identification of the streak is a crucial step in this method and often is the main source of error as it is sometimes required even with the automated streak detections within these algorithms.

4.2.2.3 Deep learning based surface velocimetry (RivQNet)

The RivQNet deep learning method for surface velocity measurement and discharge estimation utilizes close-range water surface imagery and depends on trained models for feature

extraction, making it more resistant to fluctuations and alterations in brightness. This approach employs a novel deep learning-based optical flow estimation algorithm, which eliminates the need for image intensities, gradients, or other user defined feature extractors. The algorithm was tested using five different architectures, and FlowNet2CSS was determined to be the best option for RivQNet's deep learning-based surface velocimetry and discharge evaluation (Ansari *et al.,* 2023). The algorithm's performance was assessed under a variety of flow conditions and camera angles in the field, proving its ability to provide consistent flow estimates for low to high flow regimes, reliable surface velocity information in various lighting and brightness environments, and the capability to manage low quality videos. Moreover, the application of this algorithm is different from LSPIV or STIV methods as they don't require any user defined input data such as selecting the interrogation window size in LSPIV or manually identifying the STI angle or slope. Additionally, the implementation of this algorithm differs from the LSPIV or STIV methods, as it does not necessitate any user defined input data, such as the interrogation window size and STIV line direction identification respectively for LSPIV and STIV.

4.2.2.4 Data

In this research, three separate datasets are used to evaluate RivQNet's performance compared to the conventional techniques of LSPIV and STIV. The data includes aerial imagery gathered with a drone at two locations in Canada, Castor River in Ontario and Salmon River in British Columbia, under both high and low flow conditions. The data for this analysis was obtained from Ansari *et al.,* 2023 for Castor River and Perks *et al.,* 2020 for Salmon River. The dataset for analysis contains aerial images of the Castor River from March and April 2020, which were used to examine high-flow conditions. Additionally, the dataset includes images from June 2019 of the Salmon River to assess the algorithm's effectiveness under low-flow conditions.

4.2.3 Results and discussion

A comparison of traditional LSPIV and STIV methods with the recently developed deep learning-based surface velocimetry technique RivQNet was conducted using data from moderate and high-flow situations at Castor River on March 11, 2020, and April 04, 2020 (Ansari *et al.,* 2023), as well as low-flow conditions at Salmon River on June 04, 2019 (Perks *et al.,* 2020). Sample frames from aerial images utilized for this assessment are displayed in Figure 4-17a, Figure 4-18a, and Figure 4-19a, showing drone footage from Castor River and Salmon River. The performance evaluation of LSPIV, STIV, and RivQNet was based on the root mean square error (RMSE) and mean absolute percentage error (MAPE) criteria, as described in Equations 4-10 and

4-11. Here, yi represents the verification data, xi is the surface velocity estimated by using the three surface velocimetry methods, (i.e. LSPIV, STIV and RivQNet) and n denotes the total number of validation data points obtained through concurrent ADCP measurements. Furthermore, a visual comparison of results derived from both traditional and deep learning-based surface velocimetry is provided in the cross-sectional surface velocity estimations displayed in Figure 4-17b, Figure 4-18b, and Figure 4-19c.

$$RMSE = \sqrt{\frac{1}{n}\sum_{i=1}^{n}(y_i - x_i)^2} \tag{4-10}$$

$$MAPE = \frac{1}{n}\sum_{i=1}^{n}\left(\frac{|y_i - x_i|}{y_i}\right) \times 100 \tag{4-11}$$

4.2.3.1 High-flow conditions

The assessment of algorithm performance under high-flow conditions was carried out using aerial imagery at the Castor River. Situated in eastern Ontario, Canada, Castor River is a significant tributary to the South Nation River watershed, covering a drainage area of approximately 739 km2. Figure 4-17a displays a sample frame of the survey section of the river located at 45°15'45" North and 75°20'37" West Castor River at this location has a total drainage area of about 439 km2. The video footage acquired here is in 8-bit depth mp4 format. On March 11, 2020, the water depth, discharge, and average velocity were 4.7 m, 54.8 m3s-1, and 1.2 ms-1, respectively. Fieldwork involved Teledyne StreamPro Acoustic Doppler Current Profiler (ADCP) near surface measurements and drone flights using a DJI Phantom 4. The ADCP was deployed on a transect displayed in Figure 4-17a, which was utilized for comparison purposes. The 30-second analyzed video was captured at a nadir viewing angle, with a resolution of 3840x2160 pixels and a frame rate of 24 Hz (Ansari *et al.*, 2023).

The outcomes of this analysis are displayed in Figure 4-17b and Table 1. These findings indicate that the RivQNet algorithm surpasses both LSPIV and STIV algorithms, with an MAPE of 9.9% and an RMSE of 0.1 m/s. A visual comparison of cross-sectional surface velocity estimates

using LSPIV, STIV, and RivQNet algorithms, as seen in Figure 4-17b and Table 4-9, reveals that the majority of the error occurs near the left and right banks. This could be attributed to errors linked to the ADCP measurements in the shallower parts of the river. The comparison of the results show that the STIV algorithm performs better when compared to the LSPIV methodology.

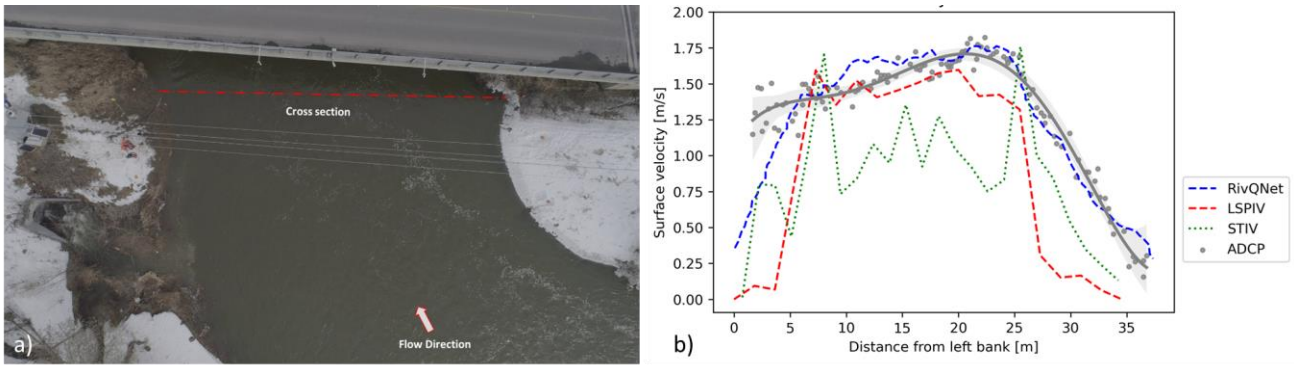

Figure 4-17 a: Aerial imagery of Castor River on March 11, 2020 and ADCP measured validation transect (Ansari et al, 2023); b: ADCP measurements along with extracted surface velocity using different methodologies of LSPIV, STIV and RivQNet.

Table 4-9 Comparison of conventional surface velocimetry and RivQNet through error evaluation of one measured cross sections at Castor River - March 11, 2020 (High-flow conditions)

Method	**Error analysis for defined distances from the left bank [m]– MAPE [%]**								**MAPE [%]**	**RMSE [m/s]**
	1.5 - 5	**5 - 10**	**10 - 15**	**15 - 20**	**20 - 25**	**25 - 30**	**30 - 35**	**35 - 36.5**		
STIV	35.6	41.3	40.3	27.7	45.5	13.7	24	28.5	32.07	0.5
LSPIV	94.5	16.5	3.5	5	10.7	53.7	72.2	89.5	43.2	0.4
RivQNet	**21.8**	**6.2**	**9.1**	**7.7**	**2.9**	**5.6**	**9.9**	**36.4**	**9.9**	**0.1**

The accuracy of the RivQNet image-based surface velocimetry algorithm in comparison to the LSPIV and STIV methods was further examined in high-flow conditions at Castor River on April 4, 2020. On the day of the survey, river water depth, discharge, and flow velocity were 3.6 m, 13.5 m3s-, and 1.19 ms-1, respectively (Ansari *et al.*, 2023). Instantaneous near surface velocity measurements were carried out using a SonTek m9 RiverSurveyor ADCP attached to an Oceanscience trimaran riverboat, with the ADCP operating in SmartPulse mode (Ansari *et al.*, 2023). Aerial footage was captured using a DJI Mavic 2.0 Pro RPAS, featuring a resolution of

1632×1536 and a 30 Hz frame rate. Figure 4-18a presents a sample frame of the drone-recorded aerial imagery utilized for the analysis. Figure 4-18b shows the estimated surface velocity using measured ADCP data, RivQNet and surface velocity estimates from LSPIV and STIV. Table 4-10 provides the error analysis of surface velocity estimates from LSPIV, STIV, and RivQNet, demonstrating that RivQNet outperformed both the LSPIV and STIV. RivQNet estimated the surface velocity with an RMSE of 0.14 ms-1 and a MAPE of 7.21 percent, whereas the LSPIV and STIV estimated surface velocity had an MAPE of 19 and 27.8 percent, respectively. While the RivQNet algorithm estimated surface velocity with a higher accuracy, the LSPIV algorithm performed better compared to STIV. The reason for this can be associated to the high variation of pixel intensities in this drone imagery that can potentially be considered as the error source of identifying streaks.

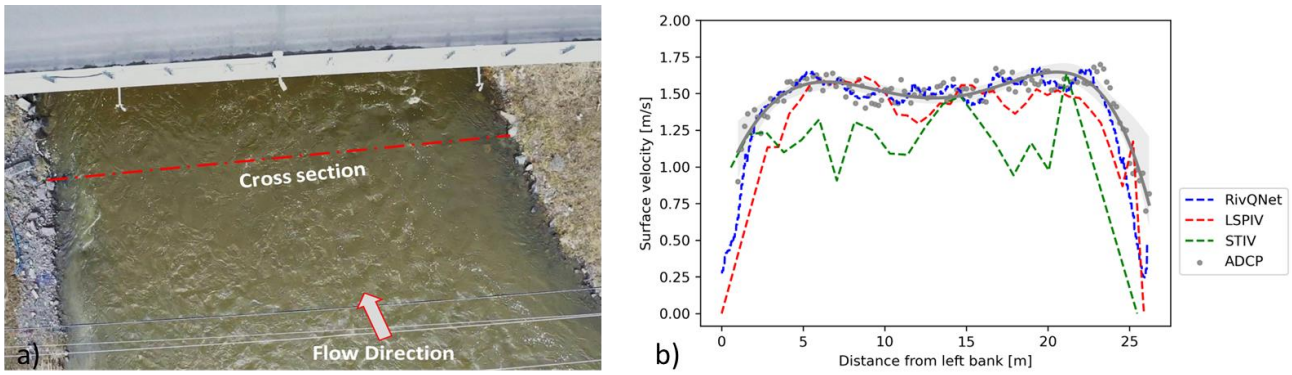

Figure 4-18 a: Aerial imagery of Castor River on April 04, 2020 and ADCP measured validation transect(Ansari et al, 2023); b: ADCP measurements along with extracted surface velocity using different methodologies of LSPIV, STIV and RivQNet.

Table 4-10 Comparison of conventional surface velocimetry and RivQNet through error evaluation of one measured cross sections at Castor River - April 04, 2020 (Mode-flow conditions)

Method	**Error for defined distances from left bank [m] – MAPE [%]**						**MAPE [%]**	**RMSE [m/s]**
	1.5 - 5	**5 - 10**	**10 - 15**	**15 - 20**	**20 - 25**	**25 - 26**		
STIV	20.7	21.3	17	23.5	30.3	54.2	27.8	0.4
LSPIV	8	1.4	6.3	5.4	18.5	74.3	19	0.22
RiVQNet	**7.5**	**3.1**	**3.35**	**3.56**	**8.2**	**50.7**	**7.21**	**0.14**

4.2.3.2 Low-flow conditions

The RivQNet, LSPIV, and STIV algorithms were also compared for surface velocity estimation in low-flow conditions using data from another field survey conducted on June 4, 2019, at Salmon River, British Columbia. The drone imagery utilized for this comparison was sourced from Perks *et al.*, 2020 and also used in the introduction of the RivQNet in Ansari *et al.*, 2023. At the time of data collection, the average depth, river flow, and flow velocity were 0.65 m, 22.9 $m3s^{-1}$, and 0.6 ms^{-1}, respectively. A 1-minute video was captured at a nadir angle from an elevation of approximately 102 m (Perks *et al.*, 2020). The obtained footage has a resolution of 1920×1080 pixels and a frame rate of 24 Hz. Figure 4-19a and b illustrates the image-based estimated surface velocity using RivQNet, LSPIV, and STIV, along with the acquired drone imagery at the ADV-measured transect of Salmon River. Additional error analysis, estimated every 5 meters from the left bank of the measured transect of Salmon River, is presented in Table 4-11. The results indicate that RivQNet outperformed the other two methods with an RMSE of 0.16 ms-1 and a MAPE of 17.5 percent. This dataset also shows that STIV performed better than the LSPIV algorithm, with an RMSE of 34.8 percent and a MAPE of 0.3 ms^{-1}.

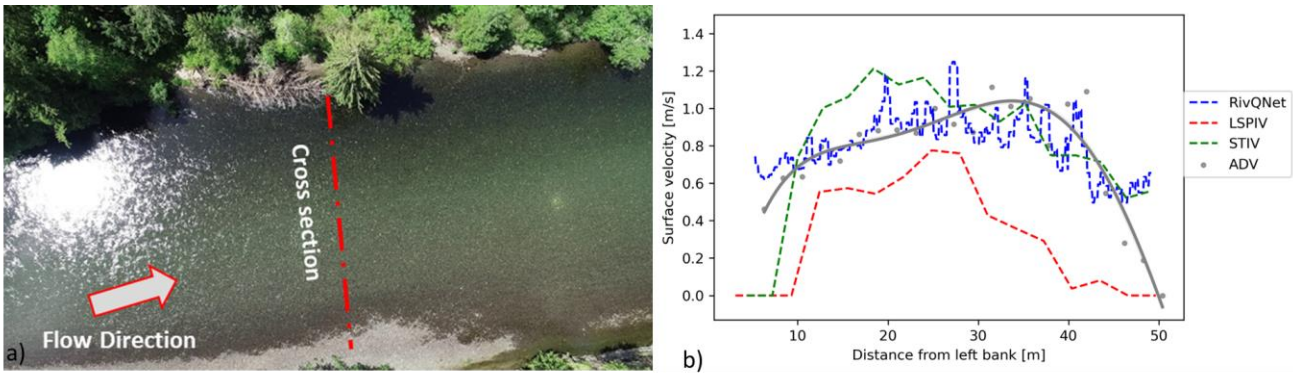

Figure 4-19 a: Aerial imagery of Salmon River on June 04, 2019 and ADV measured validation transect(Ansari et al, 2023); b: ADV measurements along with extracted surface velocity using different methodologies of LSPIV, STIV and RivQNet.

Table 4-11 Comparison of conventional surface velocimetry and RivQNet through error evaluation of one measured cross sections at Salmon River - June 04, 2019 (Low-flow conditions)

Method	Error analysis for defined distances from the left bank [m]– MAPE [%]									MAPE [%]	RMSE [m/s]
	3 - 10	10 - 15	15-20	20-25	25-30	30-35	35-40	40-45	45-50		
LSPIV	100	25.3	28.7	20.2	12.41	59	81.6	96	100	58.1	0.6
STIV	100	21.4	47.5	34.25	23.9	1.7	25	26	33.6	34.8	0.3
RivQNet	**19.5**	**6.4**	**5.2**	**23.2**	**10.5**	**18.9**	**22.4**	**43.9**	**192.9**	**17.5**	**0.2**

4.2.4 Conclusions

This study focused on the accuracy of the recently introduced deep learning-based RivQNet algorithm for surface velocimetry, emphasizing its comparison to other traditional image-based surface velocimetry techniques. The results demonstrated that RivQNet can reliably estimate surface velocity in varying visibility, brightness, and shade conditions, as well as for footage of different qualities. To provide a comprehensive evaluation, RivQNet was compared to the widely used image-based surface velocimetry methods, LSPIV and STIV using imagery and river data for high and low flow conditions. The findings indicated that RivQNet outperformed the other methods in all tested conditions. Furthermore, RivQNet was the most automated approach with minimal required user input, showcasing the potential of the RivQNet algorithm for automated hydrometric applications.

4.3 Shore-based Monitoring of Flow Dynamics in a Steep Bedrock

Preprint of an article published on the proceedings of the 9th International Conference on Fluvial Hydraulics © IAHR

4.3.1 Introduction

Surface processes can drastically influence landscape evolution. Bedrock canyon erosion is one of the critical factors affecting landscape dynamics. This phenomenon occurs by various interconnected interior and exterior earth processes in the long-term. Various geological processes affect the bedrock erosion, including bedrock blocks plucking as well as abrasion by saltating bedload and suspended load in a highly turbulent flow. Understanding river hydraulics processes in bedrock canyons is crucial in a comprehensive understanding of the incision processes. A better understanding of this phenomenon can lead to the development of robust sediment transport models in steep bedrock canyon conditions. Field observations and flow measurements, as well as long-term continuous monitoring of river processes, are essential for better analysis of these processes. Application of the close-range photogrammetry has been recognized as a reliable method for surface flow velocity estimation; thus, with a known surface velocity, it can also be a very suitable tool for turbulent flow measurements. The utilization of these methods to identify and measure turbulent structures in a bedrock canyon can be of interest due to the difficulty and potential danger of in-situ acoustic measurements and the capability of long-term monitoring. This study focuses on the development of a robust algorithm for turbulent flow measurements. A comprehensive study including concurrent utilization of shore-based imagery and Acoustic Doppler Current Profiler (ADCP) survey was used to investigate the turbulent flow structures observed in the black canyon of the Fraser River.

4.3.2 Study area

A comprehensive study was conducted on the Black Canyon of the Fraser River. As the longest river in British Columbia, flowing for 1,375 km, this river starts in the Rocky Mountains and discharges to the Strait of Georgia (Figure 4-20). The draining watershed of this river has an area of about 228,000 km^2, and the mean discharge at the river mouth is about 3550 m^3/s. The Fraser River includes both alluvial and bedrock sections. Alluvial sections are mostly dominant in the river's length downstream of Hope. On the other hand, upstream of Hope the river mostly includes bedrock canyons (Ham, 2005). The bedrock bound reaches, which include Black Canyon, comprise about 18% of the total length of the river (Venditti *et al.*, 2014).

In a previous study conducted by Venditti *et al.*, 2014 on the Fraser River to study flow characteristics in a steep canyon, it was found that flow entering a bedrock canyon plunges towards the bed and the wall which causes a velocity inversion. The formed lateral circulation then causes upwelling and eruption of surface boils along the canyon walls (Figure 4-20). Development of a monitoring system to track and quantify these boils and as a resultant measurement of the turbulent flow coherent structures of the flow is the main motivation of this study. As the in situ field surveys by ADCP at this location are only possible during the low flow season, the development of such an algorithm can assist in a better understanding of the flow structures during high and extreme flow situations.

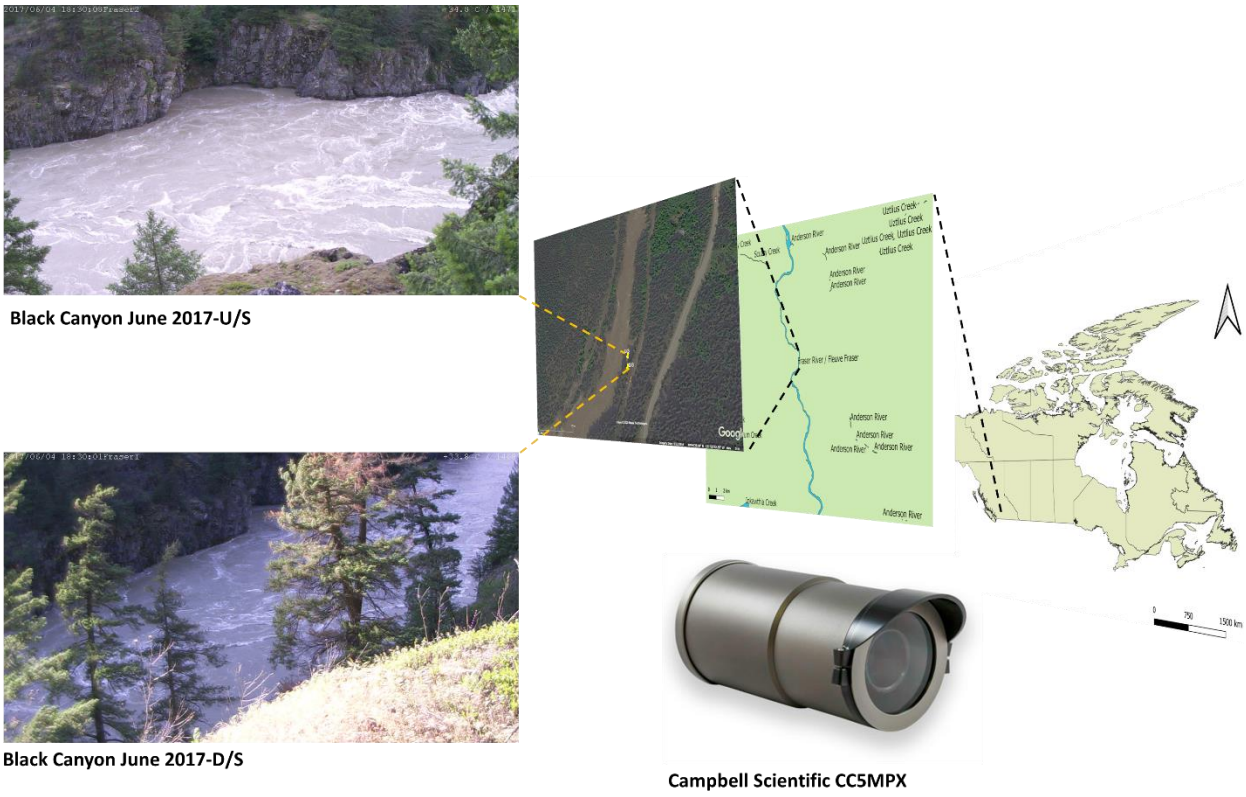

Figure 4-20 Study area, Fraser River, Campbell Scientific CC5MPX camera and its field of view

4.3.3 Instrumentation

Field-work conducted in this study includes ADCP survey along with long-term shore-based monitoring. A 1200 kHz WorkHorse Rio Grande ADCP (RD Instruments, Inc.) was used from a

moving boat for the ADCP measurements. Two Campbell Scientific CC5MPX cameras were used for the long-term shore based monitoring of the Black Canyon. The cameras were programmed to capture still images and record one-minute video files during daylight. Camera specifications are summarized in Table 4-12. The field of view of the monitoring camera is also provided in Figure 4-20.

Table 4-12 Campbell Scientific CC5MPXspecifications

Diameter: 9.3 cm	Length: 22cm
Weight: 1.06 Kg	Power: 9 to 16 Vdc
Operating temperature range: -40 to +60 ˚C	Standard lens:4 to 12 mm (27° to 80° FOV)
Zoom lens: 10 to 40 mm (9° to 35° FOV)	

4.3.4 Methodology

An automated video processing algorithm was developed to analyze the recorded video files. The main goal of this algorithm is to extract quantitative results from water surface boils. The extracted quantified results are then used to resolve turbulent flow structures for better understanding of the secondary circulation patterns and flow structures in a large steep river bedrock canyon. The steps of the developed algorithm are illustrated in a flowchart presented in Figure 4-21. The developed algorithm can be divided into three major subsections; pre-processing and image enhancement, surface boil detection and tracking, real-world velocity estimation.

Figure 4-21 illustrates the flowchart of the developed video analysis algorithm. This algorithm includes four main subsections; pre-processing, geo-rectification, detection and tracking surface boils, and real-world velocity estimation. Different subroutines of the developed video analysis algorithm are illustrated in Figure 4-21.

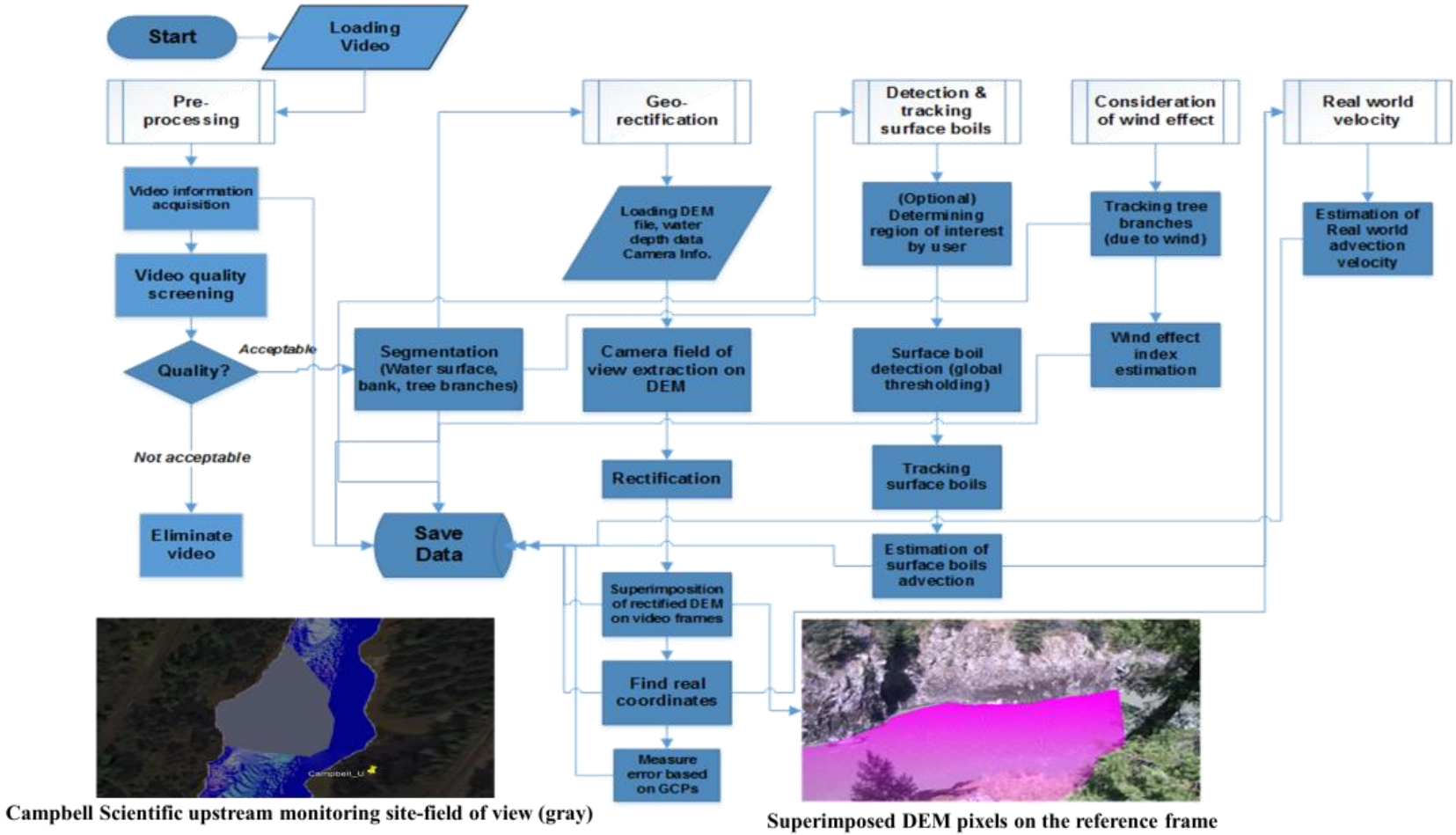

Figure 4-21 Developed video processing algorithm in a pipeline. Figures on the bottom right and left show the superimposed camera FOV and the camera field of view (gray), respectively

4.3.4.1 Pre-processing

Due to the large number of the collected video image data, and in order to increase the quality of the collected imagery, a pre-processing step was introduced to the algorithm to decrease the processing time. An image quality classification algorithm was also developed and utilized in this step to eliminate the poor quality video files from processing and increase the quality of the remaining imagery.

4.3.4.2 Geo-rectification

Extracting quantified data from shore-based imagery requires real-world coordinates of the image pixels. A geo-rectification pipeline was utilized to perform the image transformation. In this subroutine, a reference image corresponding to the collected imagery is used for the rectification algorithm. The calculated rectification matrix is then used to calculate the real-world coordinates of the pixels of the whole image data set. The calculated real-world coordinates are used in the final step of the developed algorithm to calculate the real-world velocity that is employed in turbulence flow measurements. Details on the utilized image rectification algorithm are elaborated in (Bourgault, 2008) and (Ansari *et al.*, 2017). A sample image of the geo-rectification algorithm is illustrated as a superimposition of the Digital Elevation Model (DEM) on a reference image (Figure 4-21).

4.3.4.3 Tracking surface

Detection and tracking of the surface boils are the basic objective of the developed algorithm. A global thresholding optimization algorithm was developed for better detection of the surface boils. The developed threshold optimization algorithm was based on the pixel intensity histogram and the record time. Once the boils were detected, different surface velocity estimation methods were utilized and tested to estimate the velocity of the boils.

Different optical flow methods were among the various methods used for surface velocity estimation for this application. The basics of the optical flow rely on the pixel intensity consistency change in a sequence of images described by the following equation:

$$\frac{\partial I}{\partial t} + \nabla I . w = 0 \qquad (4\text{-}13)$$

Spatial gradient of the image intensity function in the above equation illustrates by $\nabla I = [I_x, I_y]^T$ and velocity function is shown by $w = [u, v]^T$. As described in section 4.2.5 several methods have been presented to solve this equation, which describes different optical flow methods. Figure 4-22 illustrates a sample result of the surface boil velocity estimated by (B. K. P. Horn and Schunck, 1981) method. As future work, several other optical flow methods should be tested and employed for surface boil velocity estimation.

4.3.4.4 Wind effect

Wind drift can affect detected surface boils and velocity estimation accuracy. A comparison of the results showed that under similar discharge conditions, the estimated surface boils showed a higher velocity. Video files that displayed tree branch vibration were corrected for the wind effect. This was conducted by selecting reference video files in correspondence to similar discharge conditions. The reference video files had the least tree movements (wind drift). A wind drift correction factor was calculated by the comparison of the video files with the reference video under the same flow conditions.

4.3.4.5 Real-world velocity estimation

As a final step for the surface boil velocity estimation, the estimated surface boil velocities in pixel coordinates were transformed to real-world velocity using the image georectification matrix developed in earlier steps of the algorithm.

4.3.5 Preliminary results

The developed video analysis algorithm for surface boil velocity estimation based on (Horn and Schunck, 1981) was applied to a series of oblique shore-based recorded video files. Unlike other large-scale particle image velocimetry methods, the developed algorithm used a masking technique to detect and solely focus on the surface boils. Figure 4-22 illustrates a sample result of the video processing algorithm applied to a selected Region of Interest (RoI), of a section close to the right wall of the Black Canyon. Figure 4-22-B shows the same ROI at T=0 s, and the second set of images (Figure 4-22-C) shows the same ROI after 0.5 s. Each set of pictures (Figure 4-22B and C) illustrate the selected region of interest. The second binary image is the result of tracked detected boils. Vectors on the binary images are the indication of the direction and magnitude of the velocity of the surface boil. The last figure in each set illustrates the estimated boil velocity. Single eddies and their advection velocity can be recognized in the pictures. A comparison of

different frames allows for the calculation of the velocity and the advection acceleration of the boils. The whole frame size could be analyzed using the developed method; however, focusing on a specific region of interest may lead to better analysis and a better understanding of upwelling occurrence in the canyon.

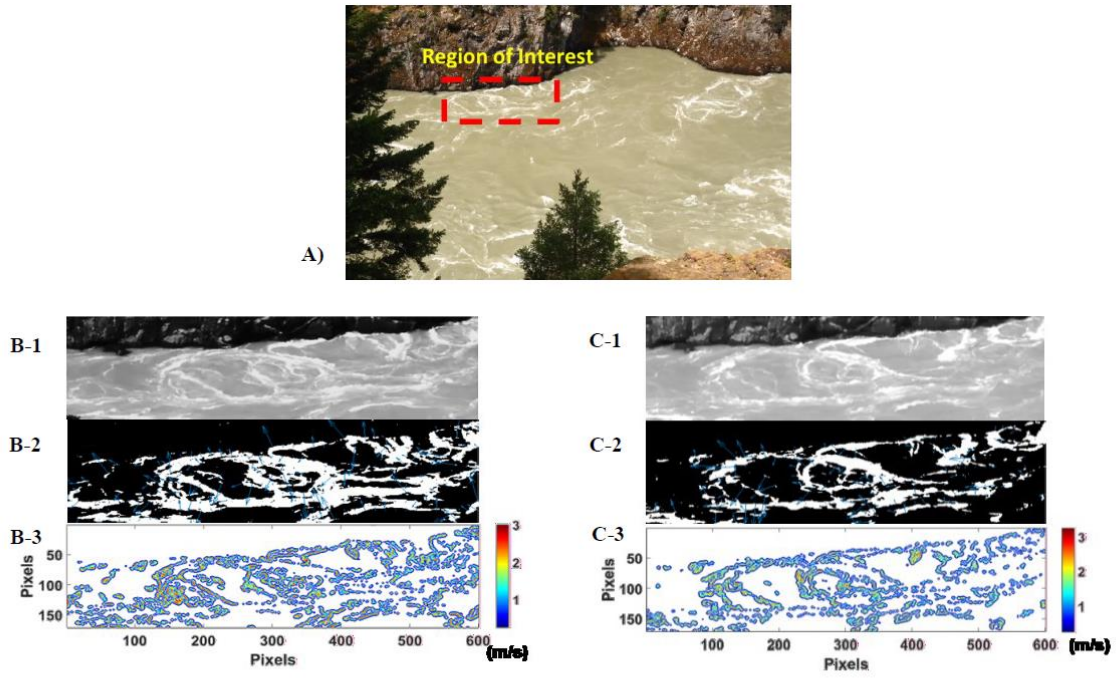

Figure 4-22 Selected RoI including the detected surface boils and estimated surface boil velocity (m/s) - A) at T= 0 Sec B) at T=0.5 Sec

5. Conclusions and Recommendations for Future Work

5.1 Conclusions

The advancements made throughout this PhD research have made a substantial impact on the field of river and sea ice monitoring and river discharge estimation. The developed algorithms harness the power of deep learning techniques and remote sensing technologies to transform our understanding of river ice processes and river hydraulics. These contributions ultimately lead to better decision-making and hazard mitigation.

The IceMaskNet algorithm, based on the Mask R-CNN architecture, was proven to be highly effective at detecting and classifying river ice from aerial imagery. Its high accuracy in ice detection and classification can significantly improve the efficiency and accuracy of river ice studies, numerical models, and hazard prevention strategies. River ice detection and classification are essential monitoring and data collection steps that can highly improve modeling complex ice processes that can affect various aspects of a river system. These processes include the formation, progression, recession, and breakup of ice, all of which can have extensive impacts on river hydraulics, sediment transport, water quality, and morphology. By applying the IceMaskNet algorithm to aerial photography collected from the Dauphin River, the research demonstrates its effectiveness in various field conditions. Aerial imagery provides a unique perspective on river ice processes, allowing researchers to monitor large areas of ice cover and identify changes over time. This information is instrumental in developing and validating numerical models that simulate ice processes, ultimately helping to improve our understanding of the dynamic nature of river ice.

Furthermore, the adaptation of IceMaskNet to oblique shore-based photography from cost-effective trail cameras has expanded its applicability, providing valuable quantitative data from long-term monitoring efforts. The ability to extract this data from shore-based imagery enables researchers and decision-makers to better understand and manage river ice processes, ultimately leading to improved hazard prevention and mitigation strategies. This is particularly important in cold regions, where ice jams can cause flooding and damage to infrastructure. By monitoring river ice processes and characterizing ice types accurately, the developed algorithms can help inform the design and implementation of effective flood hazard prevention and mitigation measures. Moreover, this information can help in better prediction of ice jam induced flooding events.

The sea ice characterization algorithm developed in this research has addressed a critical need for monitoring and classifying different types of sea ice interacting with bridge piers, especially as climate change increases the urgency of maintaining safe and reliable infrastructure. Different ice types can have varying impacts on the navigability of a vessel or the loads on a structure, making accurate monitoring and classification essential for ensuring the safety and functionality of infrastructure in ice-prone regions. This algorithm's high accuracy and real-time capabilities enhance the existing ice load monitoring systems, paving the way for more automated, efficient, and reliable monitoring networks. This is especially important in areas where climate change may result in increased variability in ice conditions, making it essential for infrastructure to be able to withstand a range of ice loads and types.

Lastly, the RivQNet algorithm has demonstrated the potential for revolutionizing river discharge estimation through the use of deep learning techniques and close-range water surface imagery. River discharge measurements are critical for hydrologic and hydraulic research, modeling, and design studies, as well as for water resource management and flood forecasting. Traditional methods of river discharge measurement often involve contact-based techniques, such as current meters or acoustic Doppler current profilers, which can be time-consuming, labor-intensive, and subject to various sources of error. The development of RivQNet has addressed the need for a robust and user independent method for river discharge estimation. This innovative approach has shown promise in providing accurate, dense spatial distributions of surface velocities, with strong potential for real-time application at hydrometric stations. By leveraging deep learning techniques and close-range water surface imagery, the RivQNet algorithm overcomes many of the limitations of traditional discharge measurement methods, offering a more efficient and accurate means of obtaining essential streamflow data.

5.2 Recommendations for Future Work

The research efforts presented herein showcase the potential of innovative artificial intelligence and close-range remote sensing techniques for obtaining high-quality, cost-effective, classified, real-time, and/or long-term data on river ice and river flow. To further refine these methodologies and develop more comprehensive and automated algorithms, the following research activities are recommended:

- Enhance the river ice segmentation and recognition algorithms by incorporating datasets from various rivers to validate the comprehensiveness of the developed algorithm and further improve its robustness and accuracy if needed.

- To obtain more accurate results from the RivQNet surface velocity algorithm, it is crucial to assess its performance for surface velocimetry and discharge measurements under varying wind conditions.
- A significant research gap remains in exploring the use of surface velocity for a better understanding of river hydrodynamics, including insights into turbulence in rivers and deriving river bathymetry from surface velocity data.
- Address the limitation of a single camera's field of view for comprehensive river process monitoring by deploying multiple cameras to expand the coverage area, benefiting both river ice recognition and flow measurement.
- Utilize stereovision to extract more detailed data and information about river ice processes and hydrodynamics. The following are some applications of stereovision for river ice and hydrodynamics:

    a. Generate relatively high-accuracy point clouds using stereo vision, which can be used to create a three-dimensional point cloud of the ice surface for estimating ice roughness.

    b. Combine stereo vision with surface velocimetry to measure vertical flow velocity, thereby enhancing our understanding of river hydrodynamics.

    c. Employ stereo vision to develop bathymetric data.

    d. Generally, 2-D surface velocimetry measures water velocity in two directions. However, using stereo vision to estimate surface velocity in 3 dimensions can improve discharge measurements by accommodating uneven surfaces with significant curvatures.

6. References

Abadi, M., Agarwal, A., Barham, P., Brevdo, E., Chen, Z., Citro, C., . . . Zheng, X. (2015). Large-scale machine learning on heterogeneous systems, Software available from tensorflow.org.

Aberle, J., Rennie, C., Admiraal, D., Muste, M., (2017). *Experimental HydraulicsII: Methods, Instrumentation, Data Processing and Management: Volume II: Instrumentation and Measurement Techniques.* CRC Press.

Adrian, R. J. (1991) 'Particle-image techniques for experimental fluid mechanics', *Annual Review of Fluid Mechanics*, 23, pp. 261–304. doi: 10.1146/annurev.fl.23.010191.001401.

Agarwal, A., Gupta, S. and Singh, D.K., 2016, December. Review of optical flow technique for moving object detection. In *2016 2nd international conference on contemporary computing and informatics (IC3I)* (pp. 409-413). IEEE.

Al-mamari, M.M., Kantoush, S.A., Kobayashi, S., Sumi, T. and Saber, M., 2019. Real-time measurement of flash-flood in a wadi area by LSPIV and STIV. Hydrology, 6(1), p.27.

Allan, M., Chang, P.L., Ourselin, S., Hawkes, D.J., Sridhar, A., Kelly, J. and Stoyanov, D., 2015. Image based surgical instrument pose estimation with multi-class labelling and optical flow. In *Medical Image Computing and Computer-Assisted Intervention--MICCAI 2015: 18th International Conference, Munich, Germany, October 5-9, 2015, Proceedings, Part I 18* (pp. 331-338). Springer International Publishing.

Anantharaman, R., Velazquez, M. and Lee, Y., 2018, December. Utilizing mask R-CNN for detection and segmentation of oral diseases. In *2018 IEEE international conference on bioinformatics and biomedicine (BIBM)* (pp. 2197-2204). IEEE.

Ansari, S., Ghareh, S., Zare, A., Ousmane, S., Rennie, C. and Malenchak, J., 2016. River ice dynamics determined from time series photo analysis. In 23rd IAHR International Symposium on Ice. Ann Arbor, Michigan.

Ansari, S. *et al.* (2017) 'Automated monitoring of river ice processes using shore-based imagery', *Cold Regions Science and Technology*. Elsevier, 142(June), pp. 1–16. doi: 10.1016/j.coldregions.2017.06.011.

Ansari, S. *et al.* (2019) 'Application of a fast superpixel segmentation algorithm in river ice classification', *Proceedings of the 20th Workshop on the Hydraulics of Ice Covered Rivers*, p. 9.

Ansari, S., Rennie, C.D., Clark, S.P. and Seidou, O., 2021. IceMaskNet: River ice detection and characterization using deep learning algorithms applied to aerial photography. *Cold Regions Science and Technology*, *189*, p.103324.

Ansari, S., Rennie, C.D., Jamieson, E.C., Seidou, O. and Clark, S.P., 2023. RivQNet: Deep Learning Based River Discharge Estimation Using Close-Range Water Surface Imagery. Water Resources Research, 59(2), p.e2021WR031841.

Arbeláez, P. *et al.* (2011) 'Contour detection and hierarchical image segmentation', *IEEE*

Transactions on Pattern Analysis and Machine Intelligence. IEEE, 33(5), pp. 898–916. doi: 10.1109/TPAMI.2010.161.

Ashton, G.D., 1986. River and lake ice engineering. Water Resources Publication.

Assur, A., 1980. Some promising trends in ice mechanics. In Physics and Mechanics of Ice: Symposium Copenhagen, August 6–10, 1979, Technical University of Denmark (pp. 1-15). Springer Berlin Heidelberg.

Bai, M., Luo, W., Kundu, K. and Urtasun, R., 2016. Exploiting semantic information and deep matching for optical flow. In *Computer Vision–ECCV 2016: 14th European Conference, Amsterdam, The Netherlands, October 11-14, 2016, Proceedings, Part VI 14* (pp. 154-170). Springer International Publishing.

Bailer, C., Varanasi, K., & Stricker, D. (2017). CNN-based patch matching for optical flow with thresholded hinge embedding loss. In Proceedings of the IEEE conference on computer vision and pattern recognition (pp. 3250–3259).

Banfield, J. D. and Raftery, A. E. (1992) 'Ice floe identification in satellite images using mathematical morphology and clustering about principal curves', *Journal of the American Statistical Association*, 87(417), pp. 7–16. doi: 10.1080/01621459.1992.10475169.

Barker, R., Dixon, L. and Hooke, J. (1997) 'Use of terrestrial photogrammetry for monitoring and measuring bank erosion', *Earth Surface Processes and Landforms*, 22(13), pp. 1217–1227. doi: 10.1002/(SICI)1096-9837(199724)22:13<1217::AID-ESP819>3.0.CO;2-U.

Bastiaanssen, W.G., (1998) Remote sensing in water resources management: the state of the art. International Water Management Institute.

Bates, P. D. and De Roo, A. P. J. (2000) 'A simple raster-based model for flood inundation simulation', *Journal of Hydrology*, 236, pp. 54–77.

Bearman, A. *et al.* (2016) 'What's the point: Semantic segmentation with point supervision', *In European conference on computer vision*, pp. 549–565. doi: 10.1007/978-3-319-46478-7_34.

Beltaos (1993) 'Numerical computation of river ice jams', *Canadian Journal of Civil Engineering*, 20(1), pp. 88–99.

Beltaos, S., 1995. Ice jam processes. River Ice Jams, pp.71-104.

Beltaos, S. and Burrell, B. C. (2003) 'Climatic change and river ice breakup', *Canadian Journal of Civil Engineering*, 30(1), pp. 145–155. doi: 10.1139/l02-042.

Beltaos, S., (2012). Canadian Geophysical Union Hydrology Section Committee on River Ice Process-es and the Environment: Brief History. Journal of Cold Regions Engineering, 26(3), pp.71-78. https://doi.org/10.1061/(ASCE)CR.1943-5495.0000046

Beltaos, S. (2013) *River ice formation*. Committee on river ice processes and the environment, Canadian geophysical union hydrology section.

Beltaos, S. and Burrell, B.C., 2016. Transport of suspended sediment during the breakup of the ice cover, Saint John River, Canada. Cold Regions Science and Technology, 129, pp.1-13.

Becket, M.A., Dow, K.E. and Clark, S.P., 2021. Development of an ice jam database and prediction tool for the Lower Red River. Canadian Water Resources Journal/Revue canadienne des ressources hydriques, 46(1-2), pp.73-86.

Bennett, K.E. and Prowse, T.D., 2010. Northern Hemisphere geography of ice-covered rivers. *Hydrological Processes: An International Journal*, *24*(2), pp.235-240.

Blanckaert, K., Heyman, J., & Rennie, C. D. (2017). Measuring bedload sediment transport with an acoustic Doppler Velocity Profiler. Journal of Hydraulic Engineering, 143(6), 04017008. https://doi.org/10.1061/(asce)hy.1943-7900.0001293

Bokeh Development Team, 2014. Bokeh: Python library for interactive visualization.

Biron, P. M., Buffin-Bélanger, T. and Martel, N. (2018) 'Mixing processes at an ice-covered river confluence', in *E3S Web of Conferences*, pp. 1–8. doi: 10.1051/e3sconf/20184005037.

Bjerklie, D. M. *et al.* (2003) 'Evaluating the potential for measuring river discharge from space', *Journal of Hydrology*, 278(1–4), pp. 17–38. doi: 10.1016/S0022-1694(03)00129-X.

Bourgault, D. (2008) 'Shore-based photogrammetry of river ice', *Canadian Journal of Civil Engineering*, 35, pp. 80–86. doi: 10.1139/L07-087.

Brevis, W., Niño, Y. and Jirka, G.H., 2011. Integrating cross-correlation and relaxation algorithms for particle tracking velocimetry. *Experiments in Fluids*, *50*, pp.135-147.

Brown, T.G., 2001. Four years of ice force observations on the Confederation Bridge. In *Proceedings of the International Conference on Port and Ocean Engineering Under Arctic Conditions*.

Brown, T.G., Tibbo, J.S., Tripathi, D., Obert, K. and Shrestha, N., 2010. Extreme ice load events on the Confederation Bridge. *Cold regions science and technology*, *60*(1), pp.1-14.

Calmant, S., Seyler, F. and Cretaux, J.F., 2008. Monitoring continental surface waters by satellite altimetry. *Surveys in geophysics*, *29*, pp.247-269.

Calkins, J. (1983) 'Ice jams in shallow rivers with floodplain flow', *Canadian Journal of Civil Engineering*, 10(3), pp. 538–548.

Chen, L., Armstrong, C. W. and Raftopoulos, D. D. (1994) 'An investigation on the accuracy of three-dimensional space reconstruction using the direct linear transformation technique', *Journal of Biomechanics*, 27(4), pp. 493–500. doi: 10.1016/0021-9290(94)90024-8.

Chollet, F., et al., 2015. Keras, GitHub. Available at https://github.com/fchollet/keras

Clark, P. E. and Hardegree, S. P. (2005) 'Quantifying Vegetation by Point Sampling Langdscape Photography Time Series', *Rangeland Ecology & Management*, 58(6), pp. 588–597.

Clark, S.P., Wall, A., 2016. Freeze-up monitoring on the Dauphin River, Manitoba, Canada. In: Pro-ceedings of the 23rd International Symposium on Ice. International Association of Hydro-Environment Engineering and Research, Ann Arbor, Michigan, pp. 10.

Clarke, R.T., 1999. Uncertainty in the estimation of mean annual flood due to rating-curve indefinition. *Journal of Hydrology*, *222*(1-4), pp.185-190.

Clayton, B. R. and Massey, B. S. (1967) 'Flow visualization in water: A review of techniques', *Journal of Scientific Instruments*, 44(1), pp. 2–11. doi: 10.1088/0950-7671/44/1/302.

Cortes, C. and Vapnik, V. (1995) 'Support-Vector Networks', *Machine Learning*, (20(3)), pp. 273–297.

Costa, J. E. *et al.* (2000) 'Measuring stream discharge by non-contact methods: A proof-of-concept experiment', *Geophysical Research Letters*, 27(4), pp. 553–556. doi: 10.1029/1999GL006087.

Costa, J. E., Cheng, R. T., Haeni, F. P., Melcher, N., Spicer, K. R., Hayes, E., et al. (2006). Use of radars to monitor stream discharge by noncontact methods. Water Resources Research, 42(7), W07422. https://doi.org/10.1029/2005WR004430

Cowen, E. a. and Monismith, S. G. (1997) 'A hybrid digital particle tracking velocimetry technique', *Experiments in Fluids*, 22, pp. 199–211. doi: 10.1007/s003480050038.

Creutin, J., Muste, M., Bradley, A., Kim, S., & Kruger, A. (2003). River gauging using PIV techniques: A proof of concept experiment on the Iowa River. Journal of Hydrology, 277(3–4), 182–194. https://doi.org/10.1016/s0022-1694(03)00081-7

Csurka, G., Larlus, D. and Perronnin, F. (2013) 'What is a good evaluation measure for semantic segmentation?', in *BMVC 2013 - Electronic Proceedings of the British Machine Vision Conference 2013*. doi: 10.5244/C.27.32.

Dai, J., He, K. and Sun, J. (2015) 'BoxSup: Exploiting bounding boxes to supervise convolutional networks for semantic segmentation', *Proceedings of the IEEE International Conference on Computer Vision*, 2015 Inter, pp. 1635–1643. doi: 10.1109/ICCV.2015.191.

Daly, S. F. and Vuyovich, C. (2007) 'Overview of Ice Jams in Three Major US Rivers Overview of Ice Jams in Three Major US Rivers', in *2CGU HS Committee on River Ice Processes and the Environment 17th Workshop on River Ice Edmonton, Alberta*.

Dempsey, J. P. (2000) 'Research trends in ice mechanics', *International Journal of Solids and Structures*, 37(1–2), pp. 131–153. doi: 10.1016/S0020-7683(99)00084-0.

Deng, J., Dong, W., Socher, R., Li, L.J., Li, K. and Fei-Fei, L., 2009, June. Imagenet: A large-scale hierarchical image database. In 2009 IEEE conference on computer vision and pattern recognition (pp. 248-255). Ieee.

Döll, P., Douville, H., Güntner, A., Müller Schmied, H. and Wada, Y., (2016). Modelling freshwater resources at the global scale: challenges and prospects. *Surveys in Geophysics*, *37*, pp.195-221.

Dramais, G. *et al.* (2011) 'Advantages of a mobile LSPIV method for measuring flood discharges and improving stage-discharge curves', *Journal of Hydro-Environment Research*, 5(4), pp. 301–312. doi: 10.1016/j.jher.2010.12.005.

Duguay, C.R., Bernier, M., Gauthier, Y. and Kouraev, A., 2015. Remote sensing of lake and river ice. Remote sensing of the cryosphere, pp.273-306.

Durand, M. *et al.* (2016) 'An intercomparison of remote sensing river discharge estimation

algorithms from measurements of river height, width and slope', *water Reources Research*, 52(6), pp. 4527–4549. doi: 10.1111/j.1752-1688.1969.tb04897.x.

Dutta, A. and Zisserman, A., 2019, October. The VIA annotation software for images, audio and video. In *Proceedings of the 27th ACM international conference on multimedia* (pp. 2276-2279).

Eigen, D. and Fergus, R. (2015) 'Predicting depth , surface normals and semantic labels with a common multi-scale convolutional architecture', in In Proceedings of the IEEE international conference on computer vision, pp. 2650–2658. doi: 10.1109/ICCV.2015.304.

Ettema, R. et al. (1997) 'Particle-image velocimetry for whole-field measurement of ice velocities', Cold Regions Science and Technology, 26, pp. 97–112.

Ettema, R., (2002) Review of alluvial-channel responses to river ice. Journal of Cold Regions Engineering, 16(4), pp.191-217.

Ettema, R. and Zabilansky, L., (2004) Ice influences on channel stability: Insights from Missouri's fort peck reach. Journal of Hydraulic Engineering, 130(4), pp.279-292.

Farnebäck, G. (2003). Two-frame motion estimation based on polynomial expansion. In Scandinavian conference on image analysis (pp. 363–370).

Felzenszwalb, P. F. *et al.* (2009) 'Object Detection with Discriminatively Trained Part Based Models', in *IEEE transactions on pattern analysis and machine intelligence*, pp. 1627–1645. doi: 10.1109/MC.2014.42.

Fischer, P., Dosovitskiy, A., Ilg, E., H¨ausser, P., Hazırba ş, C., Golkov, V., et al. (2015). Flownet: Learning optical flow with convolutional networks. arXiv preprint arXiv:1504.06852.

Fonstad, M. A. and Marcus, W. A. (2005) 'Remote sensing of stream depths with hydraulically assisted bathymetry (HAB) models', *Geomorphology*, 72(1–4), pp. 320–339. doi: 10.1016/j.geomorph.2005.06.005.

Fraser, C.S., 2013. Automatic camera calibration in close range photogrammetry. *Photogrammetric Engineering & Remote Sensing*, *79*(4), pp.381-388.

Freymuth, P. (1993) 'Flow visualization in fluid mechanics', *Review of Scientific Instruments*, 64(1), pp. 1–18. doi: 10.1063/1.1144433.

Fujita, I., Muste, M. and Kruger, A. (1998) 'Large-scale particle image velocimetry for flow analysis in hydraulic engineering applications', *Journal of Hydraulic Research*, 36(3), pp. 397–414. doi: 10.1080/00221689809498626.

Fujita, I. and Aya, S. (2000) 'Refinement of LSPIV technique for monitoring river surface flows', *In Building Partnerships*, 16, pp. 1–9.

Fujita, I., Watanabe, H. and Tsubaki, R. (2007) 'Development of a non-intrusive and efficient flow monitoring technique: The space-time image velocimetry (STIV)', *International Journal of River Basin Management*, 5(2), pp. 105–114. doi: 10.1080/15715124.2007.9635310.

Gleason, C.J. and Durand, M.T., (2020) Remote sensing of river discharge: A review and a framing for the discipline. Remote Sensing, 12(7), p.1107.

Gad-el-Hak, M. (1988) 'Visualization techniques for unsteady flows: An overview', *Journal of Fluids Engineering, Transactions of the ASME*, 110(3), pp. 231–243. doi: 10.1115/1.3243539.

Geman, S. and Geman, D. (1984) 'Stochastic Relaxation, Gibbs Distributions, and the Bayesian Restoration of Images', *IEEE Transactions on Pattern Analysis and Machine Intelligence*, PAMI-6(6), pp. 721–741. doi: 10.1109/TPAMI.1984.4767596.

Ghareh Aghaji Zare, S. *et al.* (2016) 'Boundary Shear Stress in an Ice-Covered River during Breakup', 142(4), pp. 1–14.

Ghobrial, T.R. and Loewen, M.R., 2021. Continuous in situ measurements of anchor ice formation, growth, and release. The Cryosphere, 15(1), pp.49-67.

Girshick, R. *et al.* (2014) 'Rich feature hierarchies for accurate object detection and semantic segmentation', *Proceedings of the IEEE Computer Society Conference on Computer Vision and Pattern Recognition*, 1, pp. 580–587. doi: 10.1109/CVPR.2014.81.

Girshick, R. (2015) 'Fast R-CNN', *Proceedings of the IEEE International Conference on Computer Vision*, 2015 Inter, pp. 1440–1448. doi: 10.1109/ICCV.2015.169.

Govender, M., Chetty, K. and Bulcock, H. (2007) 'A review of hyperspectral remote sensing and its application in vegetation and water resource studies', *Water SA*, 33(2), pp. 145–151. doi: 10.4314/wsa.v33i2.49049.

Güney, F., & Geiger, A. (2017). Deep discrete flow. In Asian conference on computer vision (pp. 207–224). Springer International Publishing. Hauet, A., Morlot, T., & Daubagnan, L. (2018). Velocity profile and depth-averaged to surface velocity in natural streams: A review over a large sample of rivers. In Proceedings of river flow 2018, (Vol. 40, p. 06015). EDP Sciences.

Guo, Q. (2002) 'Applicability of criterion for onset of river ice breakup', *Journal of Hydraulic Engineering*, 128(11), pp. 1023–1026. doi: 10.1061/(ASCE)0733-9429(2002)128:11(1023).

Guo, Y. *et al.* (2018) 'A review of semantic segmentation using deep neural networks', *International Journal of Multimedia Information Retrieval*. Springer London, 7(2), pp. 87–93. doi: 10.1007/s13735-017-0141-z.

Ham, D. (2005) 'Morphodynamics and sediment transport in a wandering gravel-bed channel : Fraser River , British Columbia', *Phd diss.*,.

Härer, S. *et al.* (2013) 'PRACTISE – Photo Rectification And ClassificaTIon SoftwarE (V.1.0)', *Geosci. Model Dev*, 6, pp. 837–848. doi: 10.5194/gmd-6-837-2013.

Hartley, R. and Zisserman, A., 2003. Multiple view geometry in computer vision. Cambridge university press.

Hauet, A., Morlot, T., & Daubagnan, L. (2018). Velocity profile and depth-averaged to surface velocity in natural streams: A review over a large sample of rivers. In Proceedings of river flow 2018, (Vol. 40, p. 06015). EDP Sciences.

He, K. *et al.* (2006) 'Deep Residual Learning for Image Recognition', in *IEEE conference on computer vision and pattern recognition*, pp. 1951–1954. doi: 10.1002/chin.200650130.

He, K. *et al.* (2016) 'Identity mappings in deep residual networks', in *In European conference on*

computer vision. Springer, pp. 630–645. doi: 10.1007/978-3-319-46493-0_38.

He, K. *et al.* (2017) 'Mask R-CNN', in *Proceedings of the IEEE International Conference on Computer Vision (ICCV)*. Venice, Italy, pp. 2980–2988. doi: 10.1109/ICCV.2017.322.

Hirpa, F. A. *et al.* (2013) 'Upstream satellite remote sensing for river discharge forecasting: Application to major rivers in South Asia', *Remote Sensing of Environment*. Elsevier Inc., 131, pp. 140–151. doi: 10.1016/j.rse.2012.11.013.

Holden, A. J. *et al.* (2006) 'Reducing the Dimensionality of', 313(July), pp. 504–507.

Holland, K.T., Puleo, J.A. and Kooney, T.N., 2001. Quantification of swash flows using video-based particle image velocimetry. *Coastal Engineering*, *44*(2), pp.65-77.

Horn, B. K. P. and Schunck, B. G. (1981) 'Determining optical flow', *Artificial Intelligence*, 17(1–3), pp. 185–203. doi: 10.1016/0004-3702(81)90024-2.

Horn, B. and Schunck, B. (1981) '"Determining optical flow"', *Artificial Intelligence*, 17(1–2), pp. 185–203. doi: 10.1016/0004-3702(93)90173-9.

Horritt, M S and Bates, P. D. (2001) 'Effects of spatial resolution on a raster based model of flood flow', *Journal Hydrology*, 253, pp. 239–249.

Horritt, M. S. and Bates, P. D. (2001) 'Predicting floodplain inundation: Raster-based modelling versus the finite-element approach', *Hydrological Processes*, 15(5), pp. 825–842. doi: 10.1002/hyp.188.

Hosseini, N., Chun, K.P., Wheater, H. and Lindenschmidt, K.E., 2017. Parameter sensitivity of a surface water quality model of the lower South Saskatchewan River—Comparison between ice-on and ice-off periods. *Environmental Modeling & Assessment*, *22*, pp.291-307.

Hu, S., Wang, T., Xu, S., Ma, L., Sun, X. and Wang, T., 2022. Distributions of nitrogen and phospho-rus in ice-covered water systems and comprehensive evaluation of water quality in reservoirs during the freezing period. Chemistry and Ecology, 38(3), pp.265-283. https://doi.org/10.1080/02757540.2022.2032001

Hulsing, H., Smith, W., & Cobb, E. D. (1966). Velocity-head coefficients in open channels. (No. (1869)). US Government Printing Office.

Hur, J., & Roth, S. (2020). Optical flow estimation in the deep learning age. arXiv preprint arXiv:2004.02853.

Hussain, A. K. M. F. 1983. "Coherent Structures—reality and Myth." *Physics of Fluids* 26(10): 2816. http://scitation.aip.org/content/aip/journal/pof1/26/10/10.1063/1.864048.

Huusko, A.R.I., Greenberg, L., Stickler, M., Linnansaari, T., Nykänen, M., Vehanen, T., Koljonen, S., Louhi, P. and Alfredsen, K., 2007. Life in the ice lane: the winter ecology of stream salmonids. *River research and applications*, *23*(5), pp.469-491.

Ilg, E., Mayer, N., Saikia, T., Keuper, M., Dosovitskiy, A., & Brox, T. (2017). Flownet 2.0: Evolution of optical flow estimation with deep networks. In Proceedings of the IEEE conference on computer vision and pattern recognition (pp. 2462–2470).

Jaccard, P., 1908. Nouvelles recherches sur la distribution florale. *Bull. Soc. Vaud. Sci. Nat.*, *44*, pp.223-270.

Jakubauskas, M., Kindscher, K., Fraser, A., Debinski, D. and Price, K.P., 2000. Close-range remote sensing of aquatic macrophyte vegetation cover. *International Journal of Remote Sensing*, *21*(18), pp.3533-3538.

Jędrzychowski, K. and Kujawski, A. (2014) 'Method of image analysis in the process of assessment of ice occurrences', *ZESZYTY NAUKOWE Akademia Morska w Szczecinie*, 37(109), pp. 45–49.

Jin, B., Segovia, M. V. O. and Süsstrunk, S. (2017) 'Webly supervised semantic segmentation', in *Proceedings of the IEEE Conference on Computer Vision and Pattern Recognition*, pp. 3626–3635. doi: 10.1109/CVPR.2017.185.

Jin, H., Chen, Z., Cohen, S. D., Yang, J., & Lin, Z. (2016). Video denoising using optical flow. Google Patents. (US Patent 9,311,690).

Jodeau, M., Hauet, A., Coz, J.L.E., Bercovitz, Y., Lebert, F., Edf, D.T.G. and Hhly, U.R., 2017, March. Laboratory and field LSPIV measurements of flow velocities using Fudaa-LSPIV a free user-friendly software. In *Proceedings of the HydroSensoft Conference, HydroSenSoft, International Symposium and Exhibition on Hydro-Environment Sensors and Software, Madrid, Spain* (pp. 1-3).

Johnson, E.D. and Cowen, E.A., 2016. Remote monitoring of volumetric discharge employing bathymetry determined from surface turbulence metrics. *Water resources research*, *52*(3), pp.2178-2193.

Johnson, E.D. and Cowen, E.A., 2017. Remote determination of the velocity index and mean streamwise velocity profiles. *Water Resources Research*, *53*(9), pp.7521-7535.

Johnston, M.E. and Timco, G.W., 2008, July. Guide for understanding and identifying old ice in summer. In *SNAME International Conference and Exhibition on Performance of Ships and Structures in Ice* (p. D031S012R001). SNAME.

Kalke, H., McFarlane, V., Schneck, C. and Loewen, M., 2017. The transport of sediments by released anchor ice. Cold Regions Science and Technology, 143, pp.70-80.

Kalke, H. and Loewen, M. (2018) 'Support vector machine learning applied to digital images of river ice conditions', *Cold Regions Science and Technology*. Elsevier, 155(September 2017), pp. 225–236. doi: 10.1016/j.coldregions.2018.08.014.

Karvonen, J. (2016). Virtual radar ice buoys–a method for measuring fine-scale sea ice drift. The Cryosphere, 10(1), 29–42. https://doi.org/ 10.5194/tc-10-29-2016

Kaufmann, V. (2012) 'The evolution of rock glacier monitoring using terrestrial photogrammetry: The example of Ausseres hochebenkar rock glacier (Austria)', *Austrian Journal of Earth Sciences*, 105(2), pp. 63–77.

Kavetski, D., Kuczera, G. and Franks, S.W., 2006. Bayesian analysis of input uncertainty in hydrological modeling: 2. Application. *Water resources research*, *42*(3).

Kavukcuoglu, K. *et al.* (2009) 'Learning invariant features through topographic filter maps', *2009 IEEE Computer Society Conference on Computer Vision and Pattern Recognition Workshops, CVPR Workshops 2009*. IEEE, 2009 IEEE, pp. 1605–1612. doi: 10.1109/CVPRW.2009.5206545.

Kempema, E.W. and Ettema, R., 2011. Anchor ice rafting: observations from the Laramie River. *River research and applications*, *27*(9), pp.1126-1135.

KGS Group, North/South Consultants, 2014. Emergency Reduction of Lake Manitoba and Lake St. Martin Water Levels.

Khoreva, A. *et al.* (2017) 'Simple does It: Weakly supervised instance and semantic segmentation', *Proceedings - 30th IEEE Conference on Computer Vision and Pattern Recognition, CVPR 2017*, 2017-Janua, pp. 1665–1674. doi: 10.1109/CVPR.2017.181.

Kim, Y., Muste, M., Hauet, A., Krajewski, W. F., Kruger, A., & Bradley, A. (2008). Stream discharge using mobile large-scale particle image velocimetry: A proof of concept. Water Resources Research, 44(9), W09502. https://doi.org/10.1029/2006wr005441

Kluyver, T., Ragan-Kelley, B., Pérez, F., Granger, B.E., Bussonnier, M., Frederic, J., Kelley, K., Hamrick, J.B., Grout, J., Corlay, S. and Ivanov, P., 2016. Jupyter Notebooks-a publishing format for reproducible computational workflows. *Elpub*, *2016*, pp.87-90.

Krizhevsky, A., Sutskever, I. and Hinton, G. E. (2012) 'ImageNet Classification with Deep Convolutional Neural Networks', in *InAdvances in neural information processing systems*, pp. 1097–1105. doi: 10.1201/9781420010749.

Krizhevsky, A., Sutskever, I. and Hinton, G.E., 2017. Imagenet classification with deep convolutional neural networks. Communications of the ACM, 60(6), pp.84-90.

Kubat, I., Frederking, R. and Hayakawa, T., 2000, June. Response of the Confederation Bridge to ice action. In *Proceedings CSCE 2000 Conference, London, Canada* (pp. 434-441).

Le Boursicaud, R. *et al.* (2016) 'Gauging extreme floods on YouTube: Application of LSPIV to home movies for the post-event determination of stream discharges', *Hydrological Processes*, 30(1), pp. 90–105. doi: 10.1002/hyp.10532.

Le Coz, J., Camenen, B., Peyrard, X. and Dramais, G., 2012. Uncertainty in open-channel discharges measured with the velocity–area method. *Flow Measurement and Instrumentation*, *26*, pp.18-29.

Lecun, Y. *et al.* (1998) 'Gradient-based learning applied to document recognition', *Proceedings of the IEEE 86*, 86(11), pp. 2278–2324. Available at: http://ieeexplore.ieee.org/document/726791/#full-text-section.

Lecun, Y., Bengio, Y. and Hinton, G. (2015) 'Deep learning', *Nature*, 521(7553), pp. 436–444. doi: 10.1038/nature14539.

Lee, K.-Y., Chuang, Y.-Y., Chen, B.-Y., & Ouhyoung, M. (2009). Video stabilization using robust feature trajectories. In 2009 IEEE 12th international conference on computer vision (pp. 1397–1404). IEEE.

Lees, K., Clark, S.P., Malenchak, J. and Chanel, P., (2023) A novel methodology to quantify hydraulic conveyance through an ice-impacted lake-outlet system. *Cold Regions Science and Technology, 206*, p.103713.

Lettenmaier, D.P., Alsdorf, D., Dozier, J., Huffman, G.J., Pan, M. and Wood, E.F., (2015) Inroads of remote sensing into hydrologic science during the WRR era. *Water Resources Research, 51*(9), pp.7309-7342.

Lin, T. *et al.* (2014) 'Microsoft COCO : Common Objects in Context', pp. 740–755.

Lindenschmidt, K.E., 2017. RIVICE—A non-proprietary, open-source, one-dimensional river-ice model. *Water, 9*(5), p.314.

Lloyd, P. M., Stansby, P. K. and Ball, D. J. (1995) 'Unsteady surface-velocity field measurement using particle tracking velocimetry', *Journal of Hydraulic Research*, 33(4), pp. 519–534. doi: 10.1080/00221689509498658.

Liu, W. C., Lu, C. H., & Huang, W. C. (2021). Large-scale particle image velocimetry to measure streamflow from videos recorded from unmanned aerial vehicle and fixed imaging system. Remote Sensing, 13(14), 2661. https://doi.org/10.3390/rs1314266

Long, J., Shelhammer, E. and Darrell, T. (2015) 'Fully Convolutional Adaptation Networks for Semantic Segmentation', in *Proceedings of the IEEE Computer Society Conference on Computer Vision and Pattern Recognition*, pp. 3431–3440. doi: 10.1109/CVPR.2018.00712.

Lucas, B. D. and Kanade, T. (1981) 'An Iterative Image Registration Technique with an Application to Stereo Vision', in *Proceedings of Image Understanding Workshop*, pp. 121–130. doi: 10.1109/HPDC.2004.1323531.

MANICE, C., 2005. Manual of standard procedures for observing and reporting ice conditions. *Environment Canada: Ottawa, ON, Canada*.

Melcher, N.B., Costa, J.E., Haeni, F.P., Cheng, R.T., Thurman, E.M., Buursink, M., Spicer, K.R., Hayes, E., Plant, W.J., Keller, W.C. and Hayes, K., 2002. River discharge measurements by using helicopter-mounted radar. *Geophysical Research Letters*, *29*(22), pp.41-1.

Mermoz, S., Allain-Bailhache, S., Bernier, M., Pottier, E., Van Der Sanden, J.J. and Chokmani, K., 2013. Retrieval of river ice thickness from C-band PolSAR data. IEEE Transactions on Geoscience and Remote Sensing, 52(6), pp.3052-3062.

Meselhe, E. A., Peeva, T., & Muste, M. (2004). Large scale particle image velocimetry for low velocity and shallow water flows. Journal of Hydraulic Engineering, 130(9), 937–940. https://doi.org/10.1061/(asce)0733-9429(2004)130:9(937)

McMillan, H., Freer, J., Pappenberger, F., Krueger, T. and Clark, M., 2010. Impacts of uncertain river flow data on rainfall-runoff model calibration and discharge predictions. *Hydrological Processes: An International Journal*, *24*(10), pp.1270-1284.

McMillan, H. *et al.* (2017) 'How uncertainty analysis of streamflow data can reduce costs and promote robust decision in water management applications', *Water Resources Research*, 53(7),

pp. 5220–5228. doi: 10.1002/2015WR017200.A.

Muste, M. *et al.* (2004) 'Practical aspects of ADCP data use for quantification of mean river flow characteristics; Part II: Fixed-vessel measurements', *Flow Measurement and Instrumentation*, 15(1), pp. 17–28. doi: 10.1016/j.flowmeasinst.2003.09.002.

Muste, Marian *et al.* (2004) 'Validation and Extension of Image Velocimetry Capabilities for Flow Diagnostics in Hydraulic Modeling', *Journal of Hydraulic Engineering*, 130(3), pp. 175–185. doi: 10.1061/ASCE0733-9429200413031175.

Muste, M., Fujita, I., & Hauet, A. (2008). Large-scale particle image velocimetry for measurements in riverine environments. Water Resources Research, 44(4), W00D19. https://doi.org/10.1029/2008wr006950

Muste, M., Hauet, A., Fujita, I., Legout, C., & Ho, H.-C. (2014). Capabilities of large-scale particle image velocimetry to characterize shallow free-surface flows. Advances in Water Resources, 70, 160–171.

Nafziger, J., She, Y. and Hicks, F., 2016. Celerities of waves and ice runs from ice jam releases. *Cold Regions Science and Technology*, *123*, pp.71-80.

Nafziger, J., She, Y. and Hicks, F., 2019. Dynamic river ice processes in a river delta network. *Cold Regions Science and Technology*, *158*, pp.275-287.

Nyantekyi-Kwakye, B., Essel, E.E., Dow, K., Clark, S.P. and Tachie, M.F., 2021. Hydraulic and turbulent flow characteristics beneath a simulated partial ice-cover. *Journal of Hydraulic Research*, *59*(3), pp.392-403.

P.A. Chambers, G.J. Scrimgeour, A. Pietroniro, J.M. Culp, I. L. (1993) 'Oxygen Modelling Under River Ice Covers'. Proceedings of the workshop on Environmental Aspects of River Ice, T.D. Prowse, pp. 235–260.

Papandreou, G. *et al.* (2015) 'Weakly-and semi-supervised learning of a deep convolutional network for semantic image segmentation', *Proceedings of the IEEE International Conference on Computer Vision*, 2015 Inter, pp. 1742–1750. doi: 10.1109/ICCV.2015.203.

Paszke, A., Gross, S., Chintala, S., Chanan, G., Yang, E., DeVito, Z., et al. (2017). Automatic differentiation in pytorch.

Patalano, A., García, C.M. and Rodríguez, A., 2017. Rectification of Image Velocity Results (RIVeR): A simple and user-friendly toolbox for large scale water surface Particle Image Velocimetry (PIV) and Particle Tracking Velocimetry (PTV). *Computers & Geosciences*, *109*, pp.323-330.

Pearce, S., Ljubičić, R., Peña-Haro, S., Perks, M., Tauro, F., Pizarro, A., Dal Sasso, S.F., Strelnikova, D., Grimaldi, S., Maddock, I. and Paulus, G., 2020. An evaluation of image velocimetry techniques under low flow conditions and high seeding densities using unmanned aerial systems. *Remote Sensing*, *12*(2), p.232.

Perks, M.T., Dal Sasso, S.F., Hauet, A., Jamieson, E., Le Coz, J., Pearce, S., Peña-Haro, S., Pizarro, A., Strelnikova, D., Tauro, F. and Bomhof, J., 2020. Towards harmonisation of image velocimetry techniques for river surface velocity observations. *Earth System Science*

Data, *12*(3), pp.1545-1559.

Pei, C., She, Y. and Loewen, M., 2023. Deep learning based river surface ice quantification using a distant and oblique-viewed public camera. *Cold Regions Science and Technology*, *206*, p.103736.

Pfister, T., Charles, J. and Zisserman, A., 2015. Flowing convnets for human pose estimation in videos. In *Proceedings of the IEEE international conference on computer vision* (pp. 1913-1921).

Pilechi, A. *et al.* (2015) 'In situ spatially distributed field measurements of transverse dispersion of a wastewater effluent in an extended natural meandering river', *Journal of Hydraulic Research*, 53(1), pp. 20–35. doi: 10.1080/00221686.2014.950611.

Pinheiro, P.O., Collobert, R. and Dollár, P., 2015. Learning to segment object candidates. *Advances in neural information processing systems*, *28*.

Pitts, W. and McCulloch, W. S. (1947) 'How we know universals the perception of auditory and visual forms', *The Bulletin of Mathematical Biophysics*, 9(3), pp. 127–147. doi: 10.1007/BF02478291.

Poirier, L., Babaei, H. and Frederking, R., 2015. Statistical Analysis of the Ice Loading Events on the Confederation Bridge. In *Proceedings of the International Conference on Port and Ocean Engineering Under Arctic Conditions*.

Prasad, A. K. *et al.* (1992) 'Experiments in Fluids Effect of resolution on the speed and accuracy of particle image velocimetry interrogation *', *Experiments in Fluids*, 13, pp. 105–116. Available at: https://link.springer.com/content/pdf/10.1007%2FBF00218156.pdf (Accessed: 20 May 2018).

Prowse, T. D. and Marsh, P. (1989) 'Thermal budget of river ice covers during breakup', *Canadian Journal of Civil Engineering*, 16(1), pp. 62–71. doi: 10.1139/l89-008.

Prowse, T. D. and Beltaos, S. (2002) 'Climatic control of river-ice hydrology: A review', *Hydrological Processes*, 16(4), pp. 805–822. doi: 10.1002/hyp.369.

Prowse, T.D. and Culp, J.M., (2003) Ice breakup: a neglected factor in river ecology. Canadian Journal of Civil Engineering, 30(1), pp.128-144.

Prowse, T.D., Wrona, F.J., Reist, J.D., Gibson, J.J., Hobbie, J.E., Lévesque, L.M. and Vincent, W.F., (2006) Climate change effects on hydroecology of Arctic freshwater ecosystems. AMBIO: A Journal of the Human Environment, 35(7), pp.347-358. https://doi.org/10.1579/0044-7447(2006)35[347:CCEOHO]2.0.CO;2

Prowse, Terry, B. R. Bonsal, C. R. Duguay, and M. P. Lacroix. (2007) "River-Ice Break-up/Freeze-up: A Review of Climatic Drivers, Historical Trends and Future Predictions." Annals of Glaciology 46 (c): 443–51. https://doi.org/10.3189/172756407782871431.

Raffel, M., Willert, C.E., Scarano, F., Kähler, C.J., Wereley, S.T., Kompenhans, J., Raffel, M., Willert, C.E., Scarano, F., Kähler, C.J. and Wereley, S.T., 2018. Stereoscopic PIV. Particle Image Velocimetry: A Practical Guide, pp.285-307.

Ran, Q. H. *et al.* (2016) 'Application of an automated LSPIV system in a mountainous stream for continuous flood flow measurements', *Hydrological Processes*, 30(17), pp. 3014–3029. doi: 10.1002/hyp.10836.

Rango, A. (1994) 'Application of remote sensing methods to hydrology and water resources', *Hydrological Sciences Journal*, 39(4), pp. 309–320. doi: 10.1080/02626669409492752.

Ranjie, H. O. U. and Huimin, L. I. (1987) 'Modelling of BOD-DO dynamics in an ice-covered river in Northern China', *Water Research*, 21(3), pp. 247–251.

Rantz, S.E., 1982. *Measurement and computation of streamflow* (Vol. 2175). US Department of the Interior, Geological Survey.

Reda, F., Pottorff, R., Barker, J., & Catanzaro, B. (2017). flownet2-pytorch: Pytorch implementation of flownet 2.0: Evolution of optical flow estimation with deep networks. Retrieved from https://github.com/NVIDIA/flownet2-pytorch. GitHub

Ren, X. and Malik, J. (2003) 'Learning a Classification Model for Segmentation', in *IEEE*, p. 10.

Ren, S. *et al.* (2017) 'Faster R-CNN: Towards Real-Time Object Detection with Region Proposal NEtworks', *IEEE Transactions on Pattern Analysis and Machine Intelligence*, 39(6), pp. 1137–1149. doi: 10.1109/TPAMI.2016.2577031.

Revaud, J., Weinzaepfel, P., Harchaoui, Z., & Schmid, C. (2015). Epicflow: Edge-preserving interpolation of correspondences for optical flow. In Proceedings of the ieee conference on computer vision and pattern recognition (CVPR).

Saleh, F. *et al.* (2016) 'Built-in foreground/background prior for weakly-supervised semantic segmentation', *European Conference on Computer Vision*, pp. 413–432. doi: 10.1007/978-3-319-46484-8_25.

Schweitzer, S.A. and Cowen, E.A., 2021. Instantaneous river-wide water surface velocity field measurements at centimeter scales using infrared quantitative image velocimetry. *Water Resources Research*, *57*(8), p.e2020WR029279.

Sen, M., Kiran Bhaganagar, and V. Juttijudata. (2007) "Application of Proper Orthogonal Decomposition (POD) to Investigate a Turbulent Boundary Layer in a Channel with Rough Walls." *Journal of Turbulence* 8: 1–21.

Sevilla-Lara, L., Liao, Y., Güney, F., Jampani, V., Geiger, A. and Black, M.J., 2019. On the integration of optical flow and action recognition. In *Pattern Recognition: 40th German Conference, GCPR 2018, Stuttgart, Germany, October 9-12, 2018, Proceedings 40* (pp. 281-297). Springer International Publishing.

Shen, H. T., Su, J. and Liu, L. (2000) 'SPH Simulation of River Ice Dynamics', *Journal of Computational Physics*, 165(2), pp. 752–770. doi: 10.1006/jcph.2000.6639.

Shi, J. (1994). Good features to track. In 1994 proceedings of ieee conference on computer vision and pattern recognition (pp. 593–600). Siam, M., Mahgoub, H., Zahran, M., Yogamani, S., Jagersand, M., & El-Sallab, A. (2017). Modnet: Moving object detection network with motion and appearance for autonomous driving. arXiv preprint arXiv:1709.04821.

Shrestha, N. and Brown, T.G., 2018. 20 years of monitoring of ice action on the Confederation Bridge piers. *Cold Regions Science and Technology*, *151*, pp.208-236.

Siam, M., Mahgoub, H., Zahran, M., Yogamani, S., Jagersand, M. and El-Sallab, A., 2017. Modnet: Moving object detection network with motion and appearance for autonomous driving. *arXiv preprint arXiv:1709.04821*.

Simoes, J. and Clark, S. P. (2019) 'Quantification of Border Ice Growth on the Assiniboine River', *Journal of Cold Regions Engineering*, 34(1), p. 04019016. doi: 10.1061/(ASCE)CR.1943-5495.0000200.

Simonyan, K. and Zisserman, A. (2014) 'Very deep convolutional networks for large-scale image recognition', *3rd International Conference on Learning Representations, ICLR 2015 - Conference Track Proceedings*, pp. 1–14.

Singh, A. *et al.* (2019) 'River Ice Segmentation with Deep Learning', *arXiv preprint*, p. 1901.04412.

Siyal, A. A. *et al.* (2017) 'Ice-Cover and Jamming Effects on Inline Structures and Upstream Water Levels', in *World Environmental and Water Resources Congress*, pp. 270–279. Available at: https://earthexplorer.usgs.gov/.

Smith, D.G., 1979. Effects of channel enlargement by river ice processes on bankfull discharge in Alberta, Canada. *Water Resources Research*, *15*(2), pp.469-475.

Smith, L. C., Isacks, B. and Bloom, A. (1996) 'Estimation of discharge from three braided rivers using synthetic aperture radar satellite imagery: Potential application to ungauged basins', *Water Resources Research*, 32(7), pp. 2021–2034. doi: 10.1029/96WR00752.

Smith, Brennan T., and Robert Ettema. "Flow resistance in ice-covered alluvial channels." *Journal of hydraulic engineering* 123, no. 7 (1997): 592-599.

Smith, L. C. (1997a) 'Satellite remote sensing of river inundation area, stage, and discharge: a review', *Hydrological Processes*, 11(10), pp. 1427–1439. doi: 10.1002/(SICI)1099-1085(199708)11:10<1427::AID-HYP473>3.3.CO;2-J.

Smith, L. C. (1997b) 'Satellite remote sensing of river inundation area, stage, and discharge: A review', *Hydrological Processes*, 11(10), pp. 1427–1439. doi: 10.1002/(sici)1099-1085(199708)11:10<1427::aid-hyp473>3.0.co;2-s.

Sola, D. and Scott, K.A., 2022. Efficient Shallow Network for River Ice Segmentation. *Remote Sensing*, *14*(10), p.2378.

Solem, J. E. (2012). Programming computer vision with python: Tools and algorithms for analyzing images. O'Reilly Media, Inc. Sveen, J. K., & Cowen, E. A. (2004). Quantitative imaging techniques and their application to wavy flows. PIV and water waves, 1–49.

Sorokin, A., 2018. Lesion analysis and diagnosis with mask-rcnn. *arXiv preprint arXiv:1807.05979*.

Stumpf, A. *et al.* (2016) 'Photogrammetric discharge monitoring of small tropical mountain rivers: A case study at Riviere des Pluies Reunion Island', *Journal of the American Water*

Resources Association, 52(6), pp. 4550–4570. doi: 10.1111/j.1752-1688.1969.tb04897.x.

Sveen, J. K., & Cowen, E. A. (2004). Quantitative imaging techniques and their application to wavy flows. PIV and water waves, 1–49.

Sveen, J. K. (2013) *Laser Doppler anemometry (LDA) and particle image velocimetry (PIV) for marine environments*, *Subsea Optics and Imaging*. Woodhead Publishing Limited. doi: 10.1533/9780857093523.3.353.

Tang, Y. (2013) 'Deep Learning using Linear Support Vector Machines'. doi: /S0102-311X2006000600002.

Tang, G., Zhu, Y., Wu, G., Li, J., Li, Z.L. and Sun, J., 2016. Modelling and analysis of hydrodynamics and water quality for rivers in the northern cold region of China. *International Journal of Environmental Research and Public Health*, *13*(4), p.408.

Tauro, F., Petroselli, A. and Arcangeletti, E. (2016) 'Assessment of drone-based surface flow observations', *Hydrological Processes*, 30(7), pp. 1114–1130. doi: 10.1002/hyp.10698.

Tauro, F., Piscopia, R., & Grimaldi, S. (2017). Streamflow observations from cameras: Large-scale particle image velocimetry or particle tracking velocimetry? Water Resources Research, 53(12), 10374–10394. https://doi.org/10.1002/2017wr020848

Tauro, F., Tosi, F., Mattoccia, S., Toth, E., Piscopia, R., & Grimaldi, S. (2018). Optical tracking velocimetry (OTV): Leveraging optical flow and trajectory-based filtering for surface streamflow observations. Remote Sensing, 10(12), 2010. https://doi.org/10.3390/rs10122010

Thielicke, W., and Stamhuis, E., 2014. PIVlab–towards user-friendly, affordable and accurate digital particle image velocimetry in MATLAB. *Journal of open research software*, *2*(1), p.30.

Thomee, B. *et al.* (2008) 'Large scale image copy detection evaluation', *Proceedings of the 1st International ACM Conference on Multimedia Information Retrieval, MIR2008, Co-located with the 2008 ACM International Conference on Multimedia, MM'08*, pp. 59–66. doi: 10.1145/1460096.1460108.

Thota, S. D. *et al.* (2013) 'Comparison Between The Optical Flow Computational Techniques', 4(10), pp. 4507–4511.

Tsuji, I. *et al.* (2019) 'Development of Aerial Space Time Volume Velocimetry for Measuring Surface Velocity Vector Distribution from UAV', in.

Tsung-yi, L. *et al.* (2017) 'Feature Pyramid Networks for Object Detection', in *InProceedings of the IEEE conference on computer vision and pattern recognition*, pp. 1019–1022. doi: 10.1017/S0025315411000634.

Turcotte, B. and Morse, B. (2011) 'Ice processes in a steep river basin', Cold Regions Science and Technology. Elsevier B.V., 67(3), pp. 146–156. doi: 10.1016/j.coldregions.2011.04.002.

Turcotte, B., Burrell, B. C. and Beltaos, S. (2019) 'The Impact of Climate Change on Breakup Ice Jams in Canada : State of knowledge and research approaches', *20th Workshop on the Hydraulics of Ice Covered Rivers*, (May), p. 30.

Uijlings, J. R. R. *et al.* (2013) 'Selective search for object recognition', *International Journal of*

Computer Vision, 104(2), pp. 154–171. doi: 10.1007/s11263-013-0620-5.

Venditti, J. G. *et al.* (2014) 'Flow in bedrock canyons', *Nature*. Nature Publishing Group, 513(7519), pp. 534–537. doi: 10.1038/nature13779.

Vogel, C., Bauder, A., & Schindler, K. (2012). Optical flow for glacier motion estimation. ISPRS Annals of Photogrammetry Remote Sensing and Spatial Information Sciences, I-3, 359–364. https://doi.org/10.5194/isprsannals-i-3-359-2012

Vuola, A.O., Akram, S.U. and Kannala, J., 2019, April. Mask-RCNN and U-net ensembled for nuclei segmentation. In *2019 IEEE 16th international symposium on biomedical imaging (ISBI 2019)* (pp. 208-212). IEEE.

Wang, H., Klaser, A., Schmid, C. and Cheng-Lin, L., 2011, June. Action recognition by dense trajectories. Computer Vision and Pattern Recognition (CVPR). In *2011 IEEE Conference on* (pp. 3169-3176).

Wang, H. and Schmid, C., 2013. Action recognition with improved trajectories. In *Proceedings of the IEEE international conference on computer vision* (pp. 3551-3558).

Wazney, L., Clark, S.P. and Wall, A., (2017) July. Freeze-up jam observations on the Dauphin River. In Proceedings of the 19th Workshop on the Hydraulics of Ice Covered Rivers (p. 21). Com-mittee on River Ice Processes and the Environment Whitehorse, Yukon, Canada.

Wazney, L., Clark, S.P. and Wall, A.J., (2018) Field monitoring of secondary consolidation events and ice cover progression during freeze-up on the Lower Dauphin River, Manitoba. Cold Re-gions Science and Technology, 148, pp.159-171.

Wazney, L., Clark, S. P. and Malenchak, J. (2019) 'Effects of freeze-up consolidation event surges on river hydraulics and ice dynamics on the Lower Dauphin River', *Cold Regions Science and Technology*. Elsevier, 158(June 2018), pp. 264–274. doi: 10.1016/j.coldregions.2018.09.003.

Wazney, L., Clark, S.P. and Malenchak, J., (2019) Laboratory investigation of the consolidation resistance of a rubble river ice cover with a thermally grown solid crust. Cold Regions Science and Technology, 157, pp.86-96.

Wei, Y. *et al.* (2016) 'Learning to segment with image-level annotations', *Pattern Recognition*. Elsevier, 59, pp. 234–244. doi: 10.1016/j.patcog.2016.01.015.

Weinzaepfel, P., Revaud, J., Harchaoui, Z., & Schmid, C. (2013). Deepflow: Large displacement optical flow with deep matching. In Proceedings of the ieee international conference on computer vision (pp. 1385–1392).

Werle, H. (1973) 'Hydrodynamic Flow Visualization', *Annual Review of Fluid Mechanics*, 5(1), pp. 361–386. doi: 10.1146/annurev.fl.05.010173.002045.

Westerweel, J. (1999) 'Fundamentals of digital particle image velocimetry', *Measurement Science and Technology*, 8(12), pp. 1379–1392. doi: 10.1088/0957-0233/8/12/002.

Westoby, M. J. *et al.* (2012) '"Structure- from- Motion" photogrammetry: A low- cost, effective tool for geoscience applications', *Geomorphology*, 179, pp. 300–314. doi: 10.1016/j.geomorph.2012.08.021.

Woo, W.-C., & Wong, W.-K. (2017). Operational application of optical flow techniques radar-based rainfall nowcasting. Atmosphere, 8(3), 48. https://doi.org/10.3390/atmos8030048

Yang, S.K., Kang, B.S. and Kang, M.S., 2019, December. Estimation of the Flood Discharge Considering the Hydrological Characteristics of Urban Stream in Island area. In *AGU Fall Meeting Abstracts* (Vol. 2019, pp. H41N-1902).

Zare, S.G.A., Moore, S.A., Rennie, C.D., Seidou, O. and Ahmari, H., 2013. Estimating the influence of river ice break-up on suspended sediment transport using acoustic techniques. In *Proceedings of Canadian hydrotechnical conference*.

Zhang, W., Witharana, C., Liljedahl, A.K. and Kanevskiy, M., 2018. Deep convolutional neural networks for automated characterization of arctic ice-wedge polygons in very high spatial resolution aerial imagery. *Remote Sensing*, *10*(9), p.1487.

Zhang, X., Jin, J., Lan, Z., Li, C., Fan, M., Wang, Y., Yu, X. and Zhang, Y., 2020. ICENET: A semantic segmentation deep network for river ice by fusing positional and channel-wise attentive features. *Remote Sensing*, *12*(2), p.221. https://doi.org/10.3390/rs12020221

Zhang, X., Zhou, Y., Jin, J., Wang, Y., Fan, M., Wang, N. and Zhang, Y., 2021. ICENETv2: A Fine-Grained River Ice Semantic Segmentation Network Based on UAV Images. *Remote Sensing*, *13*(4), p.633.

Zhao, Z. Q. *et al.* (2019) 'Object Detection with Deep Learning: A Review', *IEEE Transactions on Neural Networks and Learning Systems*. IEEE, 30(11), pp. 3212–3232. doi: 10.1109/TNNLS.2018.2876865.

7. Appendix

Summary table of IceMaskNet execution steps:

Step No.	Description	Required Input/Parameters	Expected Output/Result
1	Set up the environment	-	Environment setup
2	Install required libraries and dependencies	-	Libraries like TensorFlow, Keras, pycocotools, etc. installed
3	Load pre-trained weights/model (for fine-tuning)	Path to pre-trained weights file	Initialized Mask R-CNN model for fine-tuning
4	Load training and validation data	Paths to training/validation datasets	Datasets loaded into memory
5	Configure hyperparameters for training	Learning rate, epochs, batch size, etc.	Customized training parameters
6	Train Mask R-CNN from scratch or perform fine-tuning	Training data (from annotated images), validation data, config settings	Updated model weights
7	Save trained/fine-tuned model	Destination path for model weights	Model weights saved
8	Load test image(s) or video(s)	Path to test image(s)/video(s)	Media loaded into memory
9	Perform object detection and segmentation (River ice) on test data	Test media, trained/fine-tuned model	Bounding boxes, class labels, segmentation masks
10	Visualize and/or evaluate results	Object detection and segmentation results	Annotated media with boxes, labels, masks, evaluation metrics
11	Save or export results (optional)	Desired save path, format preferences	Saved annotations and results

Library Dependencies:

TensorFlow (2.x recommended): Primary deep learning library.
Keras: High-level neural networks API (usually comes bundled with TensorFlow 2.x).
pycocotools: Utilities for the COCO dataset, especially for evaluation.
NumPy, SciPy: Libraries for numerical operations.
Pillow (PIL): For image processing.
OpenCV: For certain image/video processing tasks.
matplotlib: For visualization.

Summary table of RivQNet execution steps:

Step No.	Description	Required Input/Parameters	Expected Output/Result
1	Set up the environment	-	Environment ready for processing
2	Install required libraries and dependencies	-	Libraries like Torch, CUDA, torchvision, etc., installed
3	Extract image series from video	Path to the video	Video extracted to images (OpenCV)
4	Stabilize images	Path to the extracted images	Images stabilized (OpenCV)
5	Geo-rectification (in oblique imagery)	Path to surveyed GCPs-Camera intrinsic and extrinsic Parameters	Images georectified (OpenCV-NumPy)
6	Load pre-trained weights/model	Path to pre-trained weights	Initialized FlowNet2CSS model
7	Define region of interest (ROI)	Path to the reference image	ROI coordinates loaded into memory
8	Load image pairs for optical flow estimation	Path to image folder	Image pairs loaded into memory
9	Perform optical flow estimation on image sequences	Test image pairs, trained/fine-tuned model	Optical flow maps of surface velocity
10	Averaging	Estimated surface velocity maps	Averaged surface velocity
11	Visualize averaged optical flow maps (if needed)	Averaged surface velocity super imposed on the reference image	Visual representations of velocity, e.g., color-coded maps
12	Save or export optical flow results (optional)	Desired save path, format preferences	Saved optical flow maps

Library Dependencies:

Torch: To implement FlowNet2
CUDA: For GPU acceleration.
NumPy: For numerical operations.
OpenCV: Essential for image and video processing tasks.
matplotlib: For visualization.